Emitter-wrap-through solar cells:
Processing, characterization, device modeling

Von der Fakultät für Elektrotechnik und Informatik
der Gottfried Wilhelm Leibniz Universität Hannover
zur Erlangung des Grades
Doktor der Naturwissenschaften
Dr. rer. nat.
genehmigte Dissertation
von
Dipl.-Phys. Christian Ulzhöfer
geboren am 22. August 1979 in Wertheim.

2013

Referent: Prof. Dr. N.-P. Harder
Korreferent: PD Dr. P. P. Altermatt
Tag der Promotion: 21. März 2013

Erklärung der Selbstständigkeit

Hiermit versichere ich, die vorliegende Arbeit mit dem Titel:

"Emitter-wrap-through solar cells: Processing, characterization, device modeling"

selbstständig verfasst und keine anderen als die angegebenen Quellen und Hilfsmittel benutzt sowie die Zitate deutlich kenntlich gemacht zu haben.

Christian Ulzhöfer
Wertheim, Dezember 2012

Abstract

The present thesis covers experimental and theoretical results of emitter-wrap-through (EWT) solar cells. EWT devices feature a front and a rear emitter both conductively connected by diffused EWT-via holes. Due to the existing *pn*-junctions at the front and rear side, EWT solar cells profit from short transport paths of photogenerated minority carriers and, hence, low recombination losses at short-circuit conditions. Compared to industrial front junction solar cells with a full area back surface field, the EWT solar cell unit exhibits long majority carrier transport paths that induce resistive losses and resistance induced recombination at external voltages around the maximum power point. In this thesis, critical EWT cell components and efficiency losses are discussed by three device models.

A diode network is designed that models the I-V-curve by means of the total device recombination and resistance. Furthermore, the model reveals the specific FF-loss magnitude based on the recombination and the resistances of single device components.

A one-dimensional numerical EWT model, generated by means of the device simulator PC1D, discusses the internal current transport and the recombination of EWT devices. It is shown that the current along the EWT-via (resistance) increases the injection of minority carriers for external voltages around the maximum power point (MPP). This leads to higher recombination losses compared to a virtual EWT scenario with a negligible EWT-via resistance.

A three-dimensional numerical EWT device model, designed by means of the simulation software SENTAURUS, respects the EWT geometry and all device recombination parameters. The model calculates the SRH and Auger recombination currents, as well as the total I-V-curves of EWT devices. At MPP, the high internal majority carrier currents can result in spatially distributed, high voltage drops depending on the local device series resistances. At open circuit conditions (V_{oc}), these internal currents and the resulting voltage drops are strongly reduced. The injection of minority carriers between MPP and V_{oc} is disturbed compared to those of a perfect diode. As a result, the total I-V-characteristics, mainly composed of SRH and Auger recombination, is disturbed and the fill factor of the EWT solar cell is reduced.

The resistances of the EWT-via and the base are identified as critical EWT parameters by means of experiments and device modeling. Three process sequences propose technological approaches for increasing the device efficiency of EWT solar cells.

If the solar cell base contributes to large series resistances of the device, the application of highly boron-doped silicon wafers is a superior strategy in terms of fill factor gains compared to the application of a strong EWT-via emitter diffusion. A disadvantage of this approach is the low bulk lifetime of highly boron-doped Czochralski grown silicon that exhibits higher recombination losses at J_{sc}-conditions based on the boron-oxygen complex.

In this thesis, the integration of a full area back-surface field (BSF) featuring a high conductivity is identified as the best technological approach for improving the FF of EWT devices. The BSF constitutes an additional current path connected in parallel to the base and strongly reduces the base series resistance. Moderately or lowly doped Cz-Si featuring high bulk lifetimes can be applied in order to reduce recombination losses at any operation point.

The scientific findings are used to simulate and to fabricate a 21.6 % -efficient EWT device featuring the highest fill factor (FF=80.8 %) that has been published so far. The device is fabricated on n-type Cz-Si with a low wafer resistivity (ρ=1.6 Ωcm) and a high bulk lifetime (τ_{bulk}=1000 µs) due to the absence of boron-oxygen complexes. The boron diffused emitter and the phosphorus-diffused BSF are passivated by aluminum oxide and thermally grown silicon dioxide, respectively. The saturation current densities of the emitter and BSF account for 50 fA/cm^2 and 120 fA/cm^2, respectively.

Keyword: solar cell, EWT, n-type

Kurzzusammenfassung

Die vorliegende Dissertation behandelt experimentelle und theoretische Ergebnisse von Emitter-wrap-through (EWT) Solarzellen. EWT-Zellen besitzen einen Vorder- und Rückseitenemitter, die über diffundierte EWT-Löcher verbunden sind. Durch die vorder- und rückseitigen *pn*-Übergänge sind die resultierenden Strompfade für photogenerierte Minoritätsladungsträger kurz und die damit verbundenen Rekombinationsverluste unter Kurzschlussbedingungen gering. Verglichen mit vorderseitensammelnden Solarzellen, besitzt die EWT-Zelle lange Strompfade für Majoritäten, die Widerstandsverluste und widerstandsinduzierte Rekombinationsverluste um den maximalen Arbeitspunkt (MPP) erzeugen können. In dieser Arbeit werden kritische EWT-Solarzellenbestandteile und Wirkungsgradverluste mit Hilfe von drei Modellen diskutiert.

Die Solarzellenkennlinie wird durch ein Diodennetzwerk modelliert. Das Modell ermöglicht die Identifizierung spezifischer Füllfaktorverluste, die durch die Rekombination und den Widerstand einzelner Solarzellenkomponenten zu Stande kommen.

Ein mit PC1D erstelltes, eindimensionales EWT-Modell diskutiert den internen Stromtransport und spezifische Rekombinationen von EWT-Solarzellen. Unter anderem wird gezeigt, dass der EWT-Lochstrom die Injektion von Minoritätsladungsträgern um den maximalen Arbeitspunkt erhöht. Dies führt zu höheren Rekombinationsverlusten im Vergleich zu einem virtuellen EWT-Szenario ohne Lochwiderstand.

Ein dreidimensionales, numerisches EWT-Modell wird mit der Simulationssoftware Sentaurus erstellt. Sämtliche EWT-Geometrie-, Diffusions- und Rekombinationsparameter werden berücksichtigt. Das Modell berechnet die SRH- und Auger-Rekombinationsströme, sowie die Kennlinie der EWT-Zelle. Hohe, interne Majoritätenströme können in Kombination mit kritischen Serienwiderständen großen Spannungsabfällen um den *MPP* erzeugen. Unter offenen Klemmen (V_{oc}-Bedingungen), sind genau diese Ströme und die verbundenen Spannungsabfälle klein. Im Vergleich zu einer perfekten Diode ohne Serienwiderstände ist die Minoritäteninjektion zwischen *MPP* und V_{oc} erhöht. Die resultierende Kennlinie ist verzerrt und der Füllfaktor reduziert.

Drei vorgestellte Solarzellenprozesse präsentieren Vorschläge zur Steigerungen des Wirkungsgradpotentiales von EWT-Solarzellen. Der EWT-Lochwiderstand sowie einzelne Basiswiderstandskomponenten der Solarzelle werden mit Hilfe von Experimenten und Modellen als kritische Parameter identifiziert.

Die Verwendung von hochdotiertem Siliziumwafer im EWT-Solarzellenprozess ist dann vorteilhaft, wenn der Hauptanteil der Serienwiderstände in der Basis liegt. Im Vergleich zur Implementierung von starken EWT-Lochdiffusionen, können mit dieser Strategie höhere Füllfaktoren und Wirkungsgrade erzielt werden. Hoch bordotiertes Czochralski Silizium (Cz-Si) besitzt allerdings geringe Volumenlebensdauern aufgrund des Borsauerstoffkomplexes und damit höhere Rekombinationsverluste unter Kurzschlussbedingungen.

In dieser Arbeit wird die Integration eines vollflächigen und hochleitenden "Back-surface field's" (BSF) als bester technologischer Ansatz identifiziert, um den Füllfaktor und den Wirkungsgrad zu steigern. Das BSF ist ein zusätzlicher, parallel zur Basis geschaltener Strompfad, der den Gesamtbasiswiderstand der Solarzelle reduziert. Mittel- oder schwachdotiertes Cz-Si mit hohen Volumenlebensdauern kann in Kombination mit dem BSF verwendet werden, um Widerstands- und Rekombinationsverluste zu minimieren.

Sämtliche theoretischen und experimentellen Ergebnisse werden zusammengeführt, um eine EWT-Zelle mit einem Wirkungsgrad von 21.6 % herzustellen. Der gemessene Füllfaktor von 80.8 % ist der höchste bis jetzt publizierte. Das Bauteil ist auf *n*-Type Cz-Si hergestellt mit einem spezifischen Waferwiderstand von 1.6 Ωcm. Durch die Abwesendheit des Borsauerstoffkomplexes beträgt die Volumenlebensdauern hohe 1000 µs. Der Boremitter wird mit Aluminiumoxid, das Phosphor-BSF mit thermisch gewachsenem Siliziumoxid passiviert. Die Sättigungsstromdichten des Emitters beträgt 50 fA/cm^2, die des BSF 120 fA/cm^2.

Schlagworte: Solarzelle, EWT, *n*-Typ

Contents

Abstract i

Kurzzusammenfassung iii

Glossary ix

1 Introduction 1

2 Historical view of EWT solar cells 5

3 Recombination, generation and I-V-characteristics 7
- 3.1 Carrier densities and carrier lifetimes 7
- 3.2 Carrier transport 9
- 3.3 Mechanisms of recombination 9
  - 3.3.1 Auger recombination 9
  - 3.3.2 Radiative recombination 10
  - 3.3.3 Shockley-Read-Hall recombination 10
  - 3.3.4 Surface recombination 11
- 3.4 Lifetime measurement 12
- 3.5 Effective lifetime τ_{eff} 14
- 3.6 I-V-characteristics 15
  - 3.6.1 Diode recombination and dark I-V-characteristics 15
  - 3.6.2 Illuminated I-V-characteristics 16
- 3.7 Illuminated I-V-characteristic shifted by the short-circuit current 19
- 3.8 Impact of series resistances on the illuminated I-V-curve 20
- 3.9 J_{sc}-V_{oc}-characteristics and R_s-determination 24

4 Modeling of EWT solar cells 25
- 4.1 Introduction 25
- 4.2 Two-diode model 25
  - 4.2.1 EWT-network model considering front and rear emitter 26
- 4.3 Diode network model considering series resistances and injection dependent lifetimes 27
  - 4.3.1 Determination of series resistances for single EWT device components 28
- 4.4 Numerical EWT device modeling 36
  - 4.4.1 One-dimensional numerical EWT-model designed by means of PC1D 36
  - 4.4.2 Three-dimensional numerical EWT-model 37

5 Didactical approach to EWT solar cells: One-dimensional model 39
- 5.1 Motivation 39
- 5.2 Experimental results of EWT cells 39
- 5.3 Device model and simulation parameters 40
- 5.4 One-dimensional simulation results 42
  - 5.4.1 Short-circuit current density 43
  - 5.4.2 Fill factor 45
  - 5.4.3 Open-circuit voltage 50
  - 5.4.4 Cell efficiency 52
- 5.5 One-dimensional model of a front junction solar cell 53
- 5.6 Conclusion 55

6 Investigations on the internal current transport of EWT devices by varying the wafer resistivity 57
6.1 Introduction 57
6.2 Solar cell fabrication 57
6.3 Solar cell characterization 59
6.4 Discussion of the EWT fill factor by means of a diode network 62
6.5 Device simulation 66
6.5.1 Short-circuit current-density 66
6.5.2 Open-circuit voltage 67
6.5.3 Loss mechanisms of the fill factor 67
6.5.4 Simulated internal current transport and recombination currents 67
6.5.5 Comparative simulation with lower EWT-via sheet resistances 71
6.6 Discussion of the minority carrier transport 72
6.6.1 Resistive interpretation of the internal current transport 72
6.7 Conclusions 74

7 Back surface fields:
An approach for improving the fill factor and the efficiency of EWT solar cells 77
7.1 Introduction 77
7.2 Solar cell fabrication 77
7.3 Solar cell characterization 80
7.3.1 Short-circuit current-density 81
7.3.2 Open circuit voltage 82
7.3.3 Fill factor 83
7.3.4 Efficiency 88
7.4 Device simulation 88
7.4.1 Model description 88
7.5 Simulation results: 3.5 Ωcm boron-doped Cz-Si device 89
7.5.1 External voltage range from 0 to 400 mV 89
7.5.2 External voltage around 530 mV 95
7.5.3 External voltages around V_{oc} 96
7.6 Simulation results: 0.8 Ωcm boron-doped Cz-Si device 96
7.6.1 External voltage range from 0 to 400 mV 97
7.6.2 External voltage around 530 mV 98
7.6.3 External voltages around V_{oc} 99
7.7 Conclusion 99

8 EWT solar cell fabricated on
n-type Czochralski silicon 101
8.1 Introduction 101
8.2 Solar cell fabrication 101
8.3 Experimental investigations 103
8.3.1 EWT-via emitter sheet resistance 103
8.3.2 Boron emitter recombination 105
8.4 Solar cell characterization 106
8.4.1 Short-circuit current 108
8.4.2 Open circuit voltage 109
8.4.3 Fill factor 110
8.4.4 Efficiency 112

8.5 Device simulation 112
8.5.1 Introduction 112
8.5.2 Short-circuit 114
8.5.3 Maximum power point 114
8.5.4 Open circuit 115
8.6 Conclusion 116

9 Conclusion and perspective 117

A Measured IV-curves of full area BSF cell fabricated on 0.8 Ω cm boron-doped Cz-Si 131

B List of publications 133
B.1 Refereed journal papers 133
B.2 Refereed conference papers 133
B.3 Given talks 134

C Danksagung 135

D Wissenschaftlicher Werdegang 137

Glossary

Notation	**Unit**	**Definition**
$1/p$		weighting factor for recombination currents
A	m^2	area
Al_2O_3		aluminum oxide
α	rad	angle
B_sO_{2i}		boron-oxygen complex
B_s		substitutional boron
b_x	m	base width
BBr_3		boron tribromide
C_{rad}	m^3s^{-1}	coefficient of radiative recombination
C_n	m^6s^{-1}	Auger coefficient of *eeh*-recombination process
C_p	m^6s^{-1}	Auger coefficient of *ehh*-recombination process
Cz		Czochralski
d	m	ditch depth
D	m^2s^{-1}	diffusion constant
d_{LFC}	m	distance between LFC contacts
d_y	m	EWT-via distance parallel to rear emitter finger
$\Delta\sigma$	$\Omega^{-1}m^{-1}$	excess conductivity
ΔFF		fill factor difference
Δh	m^{-3}	excess hole density
ΔJ_{rec}	A/m^2	difference of recombination current densities
ΔJ_{via}	A/m^2	difference of EWT-via current densities
Δn	m^{-3}	excess electron carrier density
Δn_{av}	m^{-3}	averaged excess carrier density
Δn_{bulk}	m^{-3}	excess carrier density in the bulk
Δn_{local}	m^{-3}	local excess carrier density
Δp	m^{-3}	excess hole carrier density
ΔV_{base}	V	voltage drop in the base
ΔV_{em}	V	voltage drop along the emitter
dR	Ω	differential of series resistances
d_{SiO2}	m	thickness of silicon dioxide layers
e^-		electron carrier
E_C	eV	conduction band energy
E_d	eV	energy of defect level in silicon band gap
$E_{F,h}$	eV	hole quasi-Fermi level
$E_{F,n}$	eV	electron quasi-Fermi level
$E_{Fn,front}$	eV	electron quasi-Fermi level in the base at front *pn*-junction
$E_{Fn,rear}$	eV	electron quasi-Fermi level in the base at rear *pn*-junction
$E_{Fp,front}$	eV	hole quasi-Fermi level in the base at front *pn*-junction
$E_{Fp,rear}$	eV	hole quasi-Fermi level in the base at rear *pn*-junction
E_{photon}	eV	photon energy
E_{pulse}	J	laser pulse energy

Notation	**Unit**	**Definition**
E_t	eV	energy of trap level in silicon band gap
E_V	eV	valence band energy
E_i	eV	intrinsic Fermi level energy
e_x	m	rear emitter width
η		efficiency
EWT		emitter-wrap-through
FF		fill factor
FF_{imp}		fill factor of J_{sc}-shifted implied I-V-characteristics
FF_{Pseudo}		fill factor of J_{sc}-shifted J_{sc}-V_{oc}-characteristics
FJ		front junction
G	A/m^3	generation rate
G_{av}	A/m^3	averaged generation rate
h	m	depth of photogeneration
h^+		hole carrier
h_p	eVs	Planck constant
I		current; relation: illumination intensity/1 sun intensity
I-V		current-voltage relation
I_0	A/m^2	EWT-via current density injected into front emitter
i_{rc}	m	edge length of a rectangle
i_x	m	EWT index: sum of emitter and base finger width
ISFH		Institut für Solarenergieforschung Hameln
J	A/m^2	current density
J_0	A/m^2	saturation current density
$J_{0,i}$	A/m^2	saturation current density of a certain device component
J_{01}	A/m^2	saturation current density of the "first diode"
J_{02}	A/m^2	saturation current density of the "second diode"
$J_{02,edge}$	A/m^2	saturation current density of the damaged emitter edge
J_{1sun}	A/m^2	current density density of I-V-characteristic at 1 sun illumination
$J_{0,Al2O3}$	A/m^2	saturation current density of Al_2O_3-passivated surfaces
$J_{0,base}$	A/m^2	saturation current density of the base
$J_{0,BSF}$	A/m^2	saturation current density of back surface fields
$J_{0,bulk}$	A/m^2	saturation current density of the bulk
$J_{0,const}$	A/m^2	saturation current density with constant local ideality factor
$J_{0,e}$	A/m^2	saturation current density of the emitter
$J_{0,front}$	A/m^2	saturation current density in front part of EWT solar cell
j_{diff}	A/m^2	diffusion current density
J_{gen}	A/m^2	generation current density
$J_{loss,b}$	A/m^2	recombination current density in the base
$J_{loss,e}$	A/m^2	recombination current density in the emitter
$J_{loss,e,front}$	A/m^2	recombination current density in the front emitter
J_{mpp}	A/m^2	device current density at maximum power point
$J_{ref,loss}$	A/m^2	reflexion losses

Notation	**Unit**	**Definition**
$J_{rec,0}$	A/m^2	recombination current density in the dark at V_{ext}= 0mV
$J_{rec,1sun,0}$	A/m^2	recombination current density under illumination at V_{ext}=0 mV
$J_{rec,1sun}$	A/m^2	recombination current density under illumination
$J_{rec,planar}$	A/m^2	emitter recombination current density, planar surface
$J_{rec,text}$	A/m^2	emitter recombination current density, textured surface
J_{rec}	A/m^2	recombination current density
$J_{rec,edge}$	A/m	recombination current density of the damaged emitter edge
$J_{sc,1sun}$	A/m^2	short-circuit current density at 1 sun illumination
J_{sc}	A/m^2	short-circuit current density
J_{total}	A/m^2	total recombination current density
J_{via}	A/m^2	EWT-via current density
$J_{rec,i}$	A/m^2	recombination current density of a certain device component
J_L	A/m^2	light generated current density
k_B	eV/K	Boltzmann constant
λ	m	wavelength
LFC		laser-fired contact
m		gettering factor for B_sO_{2i} complexes
MPP		maximum power point
μ_h	m^2/Vs	hole mobility
μ_n	m^2/Vs	electron mobility
MWT		metal-wrap-through
n	m^{-3}	electron density, ideality factor, refractive index
N		total number of EWT-vias
n-type		conductive for electrons
N_A	m^{-3}	doping density of acceptor atoms
N_C	m^{-3}	effective state densities of electrons in the conduction band
N_d	m^{-3}	density of one defect species in the silicon band gap
N_{dop}	m^{-3}	density of dopant atoms
$N(E)$	$m^{-3}eV^{-1}$	state density per volume and energy unit
n_f	m^{-3}	electron density at the front surface of a wafer/precursor
n_i	m^{-3}	intrinsic carrier density
n_{local}	m^{-3}	local electron density
n_{MPP}		local ideality factor at the maximum power point
N_{peak}	m^{-3}	peak concentration of diffusion profiles at surfaces
n_{pn}	m^{-3}	electron density inside the base at pn-junction
n_r	m^{-3}	electron density at the rear surface of a wafer/precursor
ns		nanosecond
N_V	m^{-3}	effective state densities of holes in the valence band
N_{via}		number of EWT-vias in one EWT-unit area
n_0	m^{-3}	electron density in thermal equilibrium
n_1		local ideality factor of the "first diode"
n_2		local ideality factor of the "second diode"

Notation	**Unit**	**Definition**
∇	m^{-1}	nabla operator
$\nabla\phi$	V/m	gradient of electric potential
$\nabla E_{F,h}$	eV/m	gradient of hole quasi-Fermi level
$\nabla E_{F,n}$	eV/m	gradient of electron quasi-Fermi level
O_i	m^{-3}	interstitial oxygen density
$\phi(\lambda)$	$\mathrm{s}^{-1}\mathrm{m}^{-3}$	photon flux density
p	m^{-3}	hole density
P	W	electric power
PECVD		plasma enhanced chemical vapor deposition
ps		pico-second
p-type		conductive for holes
$P^{BSF}_{base,par}$	W	power dissipation: parallel transport in base, BSF-device
$P^{BSF}_{base,ver}$	W	power dissipation: vertical transport in base, BSF-device
$P^{BSF}_{BSF,par}$	W	power dissipation: parallel transport in BSF, BSF-device
$P^{LFC}_{base,par}$	W	power dissipation: parallel transport in base, LFC-device
$P^{LFC}_{base,rad}$	W	power dissipation: radial transport in base, LFC-device
$P^{LFC}_{base,ver}$	W	power dissipation: vertical transport in base, LFC-device
$P_{em,par}$	W	power dissipation: parallel transport in front emitter
$P_{em,rad}$	W	power dissipation: radial transport in front emitter
$P_{em,via}$	W	power dissipation: transport in EWT-via emitter
P_{mpp}	$\mathrm{W/m}^2$	electric power at *MPP*
P_{solar}	$\mathrm{W/m}^2$	area weighted irradiated solar power
p_0	m^{-3}	hole density in thermal equilibrium
pn-junction		junction between the p- and n-type semiconductor
$\mathrm{POCl_3}$		phosphorus oxychloride
q	C	unit charge
R	$\Omega\mathrm{m}^2$	area weighted resistance
R_{base}	$\Omega\mathrm{m}^2$	area weighted base series resistance
$R^{BSF}_{base,par}$	$\Omega\mathrm{m}^2$	area weighted resistance: parallel transport in base, BSF-device
$R^{BSF}_{base,ver}$	$\Omega\mathrm{m}^2$	area weighted resistance: vertical transport in base, BSF-device
$R^{BSF}_{BSF,par}$	$\Omega\mathrm{m}^2$	area weighted resistance: parallel transport in BSF, BSF-device
$R^{LFC}_{base,par}$	$\Omega\mathrm{m}^2$	area weighted resistance: parallel transport in base, LFC-device
$R^{LFC}_{base,rad}$	$\Omega\mathrm{m}^2$	area weighted resistance: radial transport in base, LFC-device
$R^{LFC}_{base,ver}$	$\Omega\mathrm{m}^2$	area weighted resistance: vertical transport in base, LFC-device
$R_{bulk,r}$	$\Omega\mathrm{m}^2$	area weighted minority carrier resistance in the bulk
$R_{em,f}$	$\Omega\mathrm{m}^2$	area weighted resistance: front emitter
$R_{em,par}$	$\Omega\mathrm{m}^2$	area weighted resistance: parallel transport in EWT front emitter
$R_{em,rad}$	$\Omega\mathrm{m}^2$	area weighted resistance: radial transport in EWT front emitter
$R_{em,via}$	$\Omega\mathrm{m}^2$	area weighted resistance: transport in EWT-via
R_{front}	$\Omega\mathrm{m}^2$	area weighted sum of resistances: front collecting current path
$R(\lambda)$		wavelength dependent reflexion coefficient
r_{LFC}	m	radius of LFC point contact

Notation	**Unit**	**Definition**
$R_{s,light}$	Ωm^2	area weighted lumped series resistance: illuminated solar cell
R_s	Ωm^2	area weighted series resistance
R_{sh}	Ωm^2	area weighted shunt resistance
R_{sq}	Ω	sheet resistance
R_{sum}	Ωm^2	area weighted sum of resistances
R_{total}	Ωm^2	area weighted total resistance
R_{via}	Ω	sheet resistance: EWT-via emitter
$R_{via,total}$	Ω	total resistance of N EWT-via emitters connected in parallel
r_{via}	m	EWT-via radius
r_{vir}	m	virtual radius of EWT-via with non-circle geometry
ρ	Ωm	resistivity
S_{eff}	m/s	effective surface recombination velocity
$S_{eff,f}$	m/s	effective surface recombination velocity: front side
$S_{eff,r}$	m/s	effective surface recombination velocity: rear side
$S_{eff,SiN}$	m/s	effective recombination velocity: SiN passivated surface
S_{n0}	m/s	SRH-S_{eff} parameter for electrons
S_{p0}	m/s	SRH-S_{eff} parameter for holes
σ	$\Omega^{-1}m^{-1}$	conductivity
σ_n	m^2	capture cross section of electron carriers
σ_p	m^2	capture cross section of holes carriers
SiN_x		PECVD-deposited silicon nitride
SiO_2		thermally grown silicon dioxide
SiO_x		evaporated silicon oxide
SRH		Shockley-Read-Hall
T	K	absolute temperature
τ	s	carrier lifetime
$\tau_{Fe,i}$	s	minority carrier lifetime limited by interstitial iron
τ_{n0}	s	SRH capture times for electrons
τ_{p0}	s	SRH capture times for holes
τ_{Aug}	s	minority carrier lifetime limited by Auger recombination
τ_{bulk}	s	bulk carrier lifetime of minority carriers
τ_{eff}	s	effective minority carrier lifetime
τ_{pulse}	s	laser pulse duration
τ_{rad}	s	minority carrier lifetime limited by radiative recombination
τ_{SRH}	s	minority carrier lifetime limited by SRH recombination
τ_{surf}	s	minority carrier lifetime limited by surface recombination
τ_i	s	minority carrier lifetime in a certain device component
U	m	EWT-via perimeter
$U\,(\Delta n)$	$m^{-3}s^{-1}$	recombination rate
U_{Auger}	$m^{-3}s^{-1}$	Auger recombination rate
$U_{Auger,front}$	$m^{-3}s^{-1}$	Auger recombination rate in front part of EWT device
U_{Rad}	$m^{-3}s^{-1}$	radiative recombination rate

Notation	**Unit**	**Definition**
U_{SRH}	$\mathrm{m}^{-3}\mathrm{s}^{-1}$	SRH recombination rate
U_{surf}	$\mathrm{m}^{-2}\mathrm{s}^{-1}$	surface recombination rate
V	V	voltage
$V_{base,par}^{BSF}$	V	local voltage: parallel transport in base, BSF-device
$V_{base,ver}^{BSF}$	V	local voltage: vertical transport in base, BSF-device
$V_{BSF,par}^{BSF}$	V	local voltage: parallel transport in BSF, BSF-device
$V_{base,par}^{LFC}$	V	local voltage: parallel transport in base, LFC-device
$V_{base,rad}^{LFC}$	V	local voltage: radial transport in base, LFC-device
$V_{base,ver}^{LFC}$	V	local voltage: vertical transport in base, LFC-device
V_{base}	V	local voltage in the base
$V_{em,par}$	V	local voltage: parallel transport in front emitter
$V_{em,rad}$	V	local voltage: radial current transport in front emitter
$V_{em,via}$	V	local voltage: transport in EWT-via emitter
V_{em}	V	local voltage in the emitter
V_{ext}	V	externally applied voltage
V_{imp}	V	implied voltage
$V_{oc,imp,1sun}$	V	implied open-circuit voltage at 1 sun illumination
V_{local}	V	local voltage
$V_{local,dark}$	V	local voltage at the *pn*-junction in the dark
V_{mpp}	V	external voltage at maximum power point
$V_{oc,imp}$	V	implied open-circuit voltage
V_{oc}	V	open-circuit voltage
V_{Shift}	V	voltage at which demarcation area begins to shift
v_{th}	V	thermal velocity
V_{th}	V	thermal voltage
v_x	m	EWT-via width in x-direction
v_y	m	EWT-via width in y-direction
$\vec{E}$	V/m	vectorial electric field
$\vec{j}_n$	$\mathrm{A/m}^2$	vectorial electron current density
$\vec{j}_p$	$\mathrm{A/m}^2$	vectorial hole current density
W	m	wafer thickness
$W_{current}$	m	height of current transport around LFC
z	m	depth inside a semiconductor

1 Introduction

Semiconductor solar cells may be categorized by various basic concepts: having front collecting and/or rear collecting junctions [1], having metal contacts at both the front and the rear side [2, 3], or only at the rear [4, 5] - and this categorization can be combined with various concepts for lateral structuring such as point contacts [6, 7], buried emitters [8] or buried contacts [9].

The market share of silicon wafer based solar cells on the total photovoltaic energy production has been greater than 85% in 2010 [10]. Over all years, the "workhorse" of this photovoltaic segment has been a solar cell fabricated on boron-doped multi- or monocrystalline silicon wafers which are used as absorber material with a typical thickness of 150 to 210 µm [2]. The device features a phosphorus-diffused front emitter [2]. The front side metalization is fabricated by a grid of silver paste that covers 5-8% of the front surface. At the rear side, a screen printed aluminum paste covers the total device area [11]. This certain type of solar cell exhibits efficiencies of 14-16.5% on multicrystalline and 16-18.5% on mononcrystalline silicon wafers in industrial production lines.

The highest efficiency of a silicon wafer based solar cell is reported by Zhao [12]. The respective front-junction device is fabricated on a boron-doped float-zone silicon wafer and exhibts an efficiency of 25.0%.

The gap between theoretical conversion limits and experimental results is due to technological issues depending on the solar cell process, the device concept and the quality of the applied substrate [13].

A front side metalization scheme results in reflexion losses of the incident light. Depending on the metalization coverage, the referring optical losses account for 5-8% for an industrially fabricated device. Further optical losses are caused by the antireflexion layer onto the front side. The magnitude of these losses depend on the front side topography, the deposited dielectrical layers and the encapsulate layers in the photovoltaic modul.

Impurities and crystallographic defects can induce energy states in the forbidden bandgap of a semiconductor. Electrons and holes are captured by these states and recombine which leads to reduced bulk lifetimes and bulk diffusion lengths of photogenerated minority carriers. The recombination rate for one energy state in the bandgap has been statistically described by the Shockley-Read-Hall recombination (SRH) [14, 15]. In multicrystalline silicon which is commonly used in photovoltaic solar cell production, metallic impurities like iron [16, 17, 18, 19, 20, 21], chromium [22, 23] and crystallographic defects limit the carrier lifetimes. In boron-doped Czochralski grown silicon [24], two interstitial oxygen atoms and one substitutional boron atom form the boron-oxygen complex that also limits the lifetime of photogenerated minority carriers [25, 26, 27, 28, 29]. Surfaces are interruptions of the periodical crystal structure of a semiconductor. Silicon atoms bordering the surface exhibit non-saturated bonds that can generate a spectrum of energy states in the semiconductor bandgap. The resulting surface SRH recombination respects the entire spectrum of energy states at the surface. Technologically, the surface recombination rate is minimized by dielectric passivation layers that lower the concentration of defect states and/or exhibit charges repelling one carrier species [30, 31].

Shunt resistances that short-circuits the n- and p-type side of the semiconductor of a solar cell also contribute to efficiency losses. The specific shunt type can exhibit an ohmic behavior or a diode-like recombination characteristic [32, 33]. In all scenarios, a shunt results in lower fill factors and, hence, a reduced device efficiency. Usually, shunts are caused by technological issues. One possible origin is the silver paste which is printed on top of the front side of a solar cell. The penetration of silver crystals into the semiconductor can damage the front pn-junction during the final firing fabrication step of the industrial solar cell process [34].

A further loss mechanism is joule power dissipation in device resistances that exhibit majority carrier currents. Diffused (e.g. emitter) and non-diffused (e.g. base) device components, contact resistances of the semiconductor-metal interface, and the metalization of the solar cell exhibit series resistances and, hence, induce resistive losses.

In this thesis, a concept is investigated which is commonly called "emitter-wrap-through" (EWT). Figure 1.1 shows an illustrative side-view of an EWT solar cell fabricated on a *p*-type wafer substrate. In this exemplary scenario, electrons are minority and holes are majority carriers. The cell has an emitter at both the front and rear side, but the metal contacts are restricted to the rear, so the front emitter must "wrap through" fabricated EWT-vias (holes) in the cell to connect with the rear emitter. Consequently, some of the photogenerated minority carriers in the base diffuse to the front emitter, where they become majority carriers and drift through the EWT-vias to the rear emitter. The other minority carriers diffuse directly to the rear emitter. As a result, the transport paths of photogenerated minority carriers (suffering from recombination) are shorter than in solar cells featuring a single front or rear emitter. The partition of front and rear collecting minority carriers depends on the place of photogeneration, the device geometry, the base dopant density and further parameters discussed in this thesis.[1]

In 1993, Gee et al. proposed the EWT solar cell concept featuring laser-drilled EWT-vias. EWT solar cells have been discussed to be a next step in the development of photovoltaic devices since they offer a higher efficiency potential than common industrial screen-printed solar cells [36]. The highest efficiency of 21.6% of an EWT solar cell has been reported by Hermann et al. [37]. The referring solar cell is fabricated on float-zone silicon wafers and has been developed on a laboratory scale in order to demonstrate the high efficiency potential. With the EWT concept, a combination of three advantages is desired:

- Materials with a short minority carrier diffusion length relative to cell thickness can be used [38]. The solar cell exhibits low recombination losses at externally applied voltages of 0 mV which results in high short-circuit current densities of the device. As a consequence for the current collection at short-circuit, EWT devices are less sensitive for impurities limiting the bulk lifetime of photogenerated carriers compared to front or rear junction devices.

- No metalization scheme is necessary to contact the front emitter. All discussed EWT solar cells in this thesis feature an aluminum metalization at the rear side that is evaporated in one single process step [39]. The aluminum contacts both, the emitter and the base.

- No shading and/or reflexion by front metalization occurs which results in an increased generation current inside the device and, finally, larger short-circuit currents compared with front contacted solar cells.

As a disadvantage, EWT cells are known for low fill factors which is an indication for a series resistance issue. In contrast to the reduced recombination of minority carriers in the base, the resistance losses of majority carrier are greater compared to industrial front junction devices. At short-circuit conditions the largest partition of photogenerated minority carriers is collected at the front *pn*-junction. These carriers are transported as majority carriers through the resistance of the EWT-front and -via emitter to the rear emitter contacts. Inside the base, majority carriers suffer from resistive losses due to their long lateral transport paths from their place of photogeneration to the rear base contacts. Until now, a challenge has been the optimization of the EWT fill factor. To this day, the strategy has been a reduction of the EWT-via emitter sheet resistance [40, 41, 39]. A proposed fabrication sequence for improving the fill factor involves a selective emitter concept. In the EWT-via, a strong emitter diffusion with a high dopant concentration and, consequently, a low sheet resistance has been applied. Additionally, at the front and rear side, a weak emitter diffusion

---

[1] A further example of a high efficiency solar cell structure are rear junction devices that achieve very high efficiencies of 24.2% [35]. These cells exclusivly feature rear collecting junctions. A rather long minority carrier diffusion length is required to maintain good collection efficiency, because about 80% of the free carriers are photogenerated in the first 20 µm below the front surface, and must travel to the rear side.

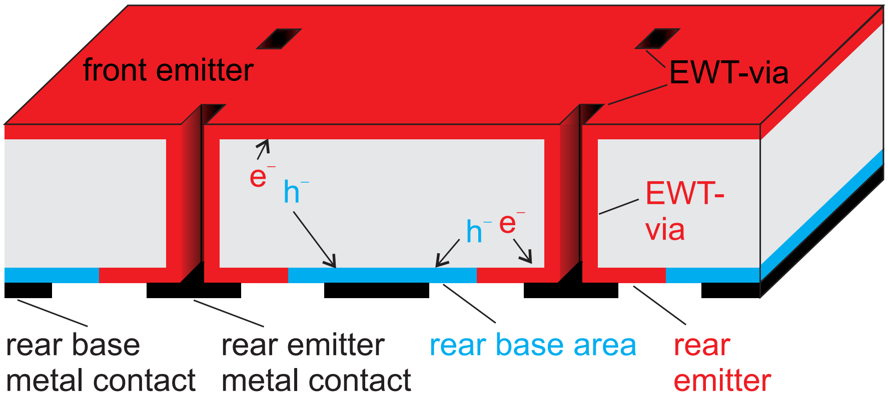

Figure 1.1: Illustrative side-view of an EWT solar cell fabricated on a *p*-type wafer substrate.

with a lower dopant concentration and a higher sheet resistance is the proposed device component for improving the efficiency. By means of this strategy, three advantages are achieved:

- The current collection at the weakly diffused front emitter (e.g. 100 Ω/□) is less sensitive for recombination losses compared to the scenario of a strongly diffused emitter diffusion (e.g. 50 Ω/□). The front emitter recombination is reduced and the short-circuit current is increased compared to the emitter concept that involves a single diffusion with a higher dopant concentration and a lower sheet resistance.
- The total saturation current of the device is reduced. The large area partition of the front and rear emitter substantially reduces the device recombination. Due to the small area partition of the EWT-via, a strong via-diffusion is negligible in terms of recombination losses. Finally, the open-circuit voltage is increased.
- The resistance of the EWT-via emitter is reduced which is the emitter component that exhibits the highest current densities and, hence, is critical in terms of resistive losses.

However, one finds that these measures do not lead to substantially improved fill factors in practice. It is shown in Chapter 7 that this is because the primary resistance-induced losses stem from mechanisms that are not targeted by the selective EWT emitter design. The *FF*- issue is not eliminated.

Another consequence of series resistances, compared to a scenario with a resistance of zero, is an increased recombination of minority carriers at external voltages smaller than V_{oc}. Majority carrier currents induce voltage drops along device resistances. The resulting local *pn*-junction voltage is increased compared to the external voltage which leads to a higher minority carrier injection across the *pn*-junction, and, hence a higher recombination current compared to the comparative scenario with a series resistance of zero. In order to optimize the fill factor and the efficiency of EWT solar cells, all series resistances of the referring device components have to be minimized since resistive and recombination losses are coupled.

The aim of this thesis is the identification and analysis of fill factor loss mechanisms of EWT devices. The EWT-via emitter does not contribute the only resistance that reduces the *FF*. In the scenario of moderately or lowly doped silicon wafers, the base series resistances are even more critical if majority carriers are forced to be transported long distances inside the base toward the rear contacts. The present thesis investigates the resistance-induced losses of EWT solar cells. The fill factor issue is picked up and solved by identifying the resistances and recombination currents of single device components. A short description of the single chapters is presented in the following:

Chapter 2 provides a review of published EWT results. The review also includes historical facts and developments in relation to EWT devices.

Chapter 3: Basic semiconductor equations are briefly discussed. This catalog is used as a reference for the discussion of theoretical and experimental results. The chapter also comprises a more profound discussion of the solar cell I-V-curves. The relation between recombination, series resistances and solar cell I-V-curve is explained.

Chapter 4: Three models are presented in order to describe the physics of EWT solar cells. Firstly, a one-dimensional EWT model designed by means of the device simulator PC1D allows a discussion of the internal current transport. Secondly, a network is applied that respects the total device recombination and the total series resistance in order to calculate the I-V-curve of an EWT solar cell. Furthermore, the network calculates the impact of the recombination characteristic and series resistance of single device components on the total device I-V-curve. Thirdly, a three-dimensional EWT model is presented that has been designed by means of the simulation software SENTAURUS. The model respects the device geometry, the series resistances, the spatially distributed internal current transport and the recombination parameters of all device components.

Chapter 5: The one-dimensional EWT model is applied to discuss the internal current transport along the EWT-via emitter. By means of this PC1D-model, it is possible to qualitatively determine the impact of the series resistance on the device I-V-characteristic.

Chapter 6 presents the effect of absorber doping in EWT solar cells. Boron-doped Czochralski silicon wafers are used as substrates. The chapter discusses the recombination characteristics and resistive losses in the scenario of lowly and highly doped substrates.

Chapter 7 reveals the FF improvement of EWT devices induced by the implementation of a back-surface field (BSF) that covers the total base area. A BSF is a conductive channel connected in parallel to the solar cell base. The total base series resistance is sustainably reduced in the scenario of moderately or lowly doped silicon substrates.

Chapter 8 discusses the technology and the experimental results for an n-type EWT solar cell. The solar cell gains an efficiency of 21.6% and a fill factor of 80.8%, which is the highest I-V-curve parameter of an EWT solar cell, so far.

2 Historical view of EWT solar cells

The concept of having a front emitter as well as a rear emitter evolved from the earliest days of silicon solar cells because, at that time, only materials with small minority carrier diffusion lengths were available and no metal fingers had been developed to contact the front surface. To overcome this limitation, concepts of contacting the front and rear side of the cells as well as fabricating vias in the cells to contact the front emitter from the rear side evolved over time. The EWT development process should be considered as a part of the entire solar cell development and not as an independent line section. Separately developed techniques like selective emitter diffusion and screen printing have been adapted to fabricate EWT solar cells. The following historical view seizes single steps of the solar cell development related to EWT solar cells.

1954: The three scientists D.M. Chapin, C.S. Fuller, and G.L. Pearson develop the first Si cells with efficiency levels above 1% [42]. The emitter wrap around their edges of the solar cell and both contacts are at the rear. Lateral conduction within the wrapped-around emitter poses severe limitations on cell size. Very long current paths induced high voltage drops that cause detrimental series resistance and recombination losses.

1975: George J. Pack fills the vias with metal, called the "metal-wrap-through" design. This metal may serve to "pin-up" the cells to the module frame [43].

1980: R.N. Hall and T.J. Soltys possibly realizes the first approach for wrapping the emitter through the vias, instead of filling the vias with metal [44]. The via-holes are pyramidally etched inside the wafer. The wider part of the pyramids is situated at the rear and the narrow pyramid heads are situated at the front side of the solar cell. The conduction between front and rear side is realized by a phosphorus diffusion that forms the emitter. The pyramid shape of the vias originates from the different crystal planes of silicon that exhibit different etching rates in alkaline solutions. A solar cell efficiency of 10.5% was achieved.

1988: Sinton et al. present a self-adjusting metalization technique for rear-contacted solar cells. The metalization is realized by aluminum with a thickness of 3 µm covered by a 300 nm layer of titan [45]. The aluminum is evaporated on the stepped rear side of a solar cell. The higher (lower) part of the steps represent the emitter or base areas of the solar cell, respectively, depending on the individual solar cell layout. Along the edge of the steps, the evaporated aluminum exhibits a columnar growth with a rough surface that cannot be fully covered by titan. The aluminum can be removed along these edges of the steps in a following wet chemical etching step. This results in a contact separation between the emitter and base area of the solar cell.

1993: Gee et al. defines the expression "emitter wrap-through solar cell" and is the first to fabricate the vias with lasers, instead of using etchants [46]. His laser-based EWT-via drilling concept is adopted by all the following researcher in this historical view. Over the years, various concepts of EWT and back-junction solar cells are developed which is discussed in Ref. [5].

2001: Glunz et al. reports on EWT solar cells fabricated on *p*-type FZ-Si with an efficiency of 21.4% [47].

2002: Neu et al. fabricates screen-printed EWT devices featuring a selective emitter diffusion. The solar cells exhibit efficiencies of 14.2% on multicrystalline (mc) *p*-type silicon and 16% on Czochralski-grown (Cz) *p*-type silicon [48].

2003: Kray et al. reports on EWT solar cells fabricated on Czochralski-grown *p*-type silicon. The cell process features some high-efficiency approaches like selective emitter diffusions and an inverted pyramid texturization at the front side in order to increase the light trapping. After light induced degradation, the efficiency of the solar cell is 18.7% [49].

2005: Engelhart applied the metalization technique of Sinton (published in 1988) for highly efficient silicon solar cells. The technique comprises one single aluminum evaporation step at the rear side. This concept was applied to EWT cells fabricated on *p*-type FZ-Si wafers. The efficiency of the discussed solar cell is 20% [50].

2006: Advent Solar launches the first production line of EWT solar cells. The industrial devices were fabricated on boron-doped mc-Si and feature screen-printed metalization at the rear side [51].

2008: Hermann and Harder present a 21.6% efficient p-type FZ-Si EWT cell featuring a selective emitter diffusion [37].

2009: Hacke et al. present an mc-Si EWT cell with an efficiency of 17%. The refering device is fabricated at Advent Solar and features a screen-printed metalization at the rear side [52].

2010: Mingirulli publishes an EWT process sequence featuring a firing stable passivation scheme for the emitter and base area at the rear side. The referring solar cell is metalized by screen-printing technology and has an efficiency of 18.5% on 0.5 Ωcm p-type FZ-Si [53].

2010: Hermann et al. present an EWT solar cell fabricated on a large-scale (12.5×12.5 cm^2) boron-doped Cz-Si wafer [54]. The device has an efficiency of 19.0% and 18.1% before and after light-degradation, respectively. The EWT device profits from an optimized edge design which results in a FF-increase of 2.8% absolute compared to the first results in this cell development project.

2011: Among other results in this thesis, a 21.6% efficient EWT solar cell is presented. The device is fabricated on a n-type Cz-Si wafer that suits the low-cost industrial needs. The cell features a boron-diffused emitter and a phosphorus-diffused back surface field passivated by aluminium oxide and silicon dioxide layers, respectively. The emitter and base areas are contacted by evaporated aluminum at the rear side.

3 Recombination, generation and I-V-characteristics

In this chapter, important equations on semiconductor physics are summarized to discuss the results of this thesis. Profound discussions are found in textbooks on photovoltaics or semiconductor technologies [55, 56, 57, 58, 59]. The units of all used variables and parameters are listed in the Glossary on page ix. The units of Eq. 3.19 differ from those of the glossary. This equation has been emperically found and is applied with the units which are shown by means of a quotient: *physical variable*/unit.

3.1 Carrier densities and carrier lifetimes

The generation of free carriers in a semiconductor denotes the transition of electrons from the valence band into the conduction band. As a result, a free hole and electron carrier is generated in the valence and conduction band, respectively. The recombination denotes the inverse process. A free hole in the valence band captures a free electron from the conduction band.

In thermodynamic equilibrium, the probability to occupy an energy state E with an electron is defined by the Fermi-distribution $f(E)$:

$$f(E) = \frac{1}{1 + exp(\frac{E-E_F}{k_b T})}, \tag{3.1}$$

where E_F is the Fermi-energy (Fermi-level) in thermodynamic equilibrium, T the absolute temperature and k_B the Boltzmann constant. Assuming temperatures greater than zero Kelvin (T>0°K), the Fermi-distribution always extends into the conduction band.

In thermodynamic equilibrium of a non-illuminated and intrinsic semiconductor, the concentration of thermally generated electrons n_0 and holes p_0 equals which is defined by the law of mass action:

$$n_0 p_0 = n_i^2, \tag{3.2}$$

with n_i the intrinsic carrier density [60, 61, 62]. The density of thermally generated electrons in the conduction band is calculated from:

$$n_0 = \int_{E_C}^{\infty} f(E) N(E) dE, \tag{3.3}$$

where E_C is the energy of the conduction band edge and $N(E)$ the state density per volume and energy unit [59]. A similar relation holds for holes in the valence band with the Fermi-distribution $1 - f(E)$. Assuming a state density $N(E) \propto \sqrt{E - E_C}$ and $E - E_F >> k_B T$, n_0 and p_0 can be calculated from:

$$n_0 = N_C exp\left(\frac{E_F - E_C}{k_B T}\right), \tag{3.4}$$

$$p_0 = N_V exp\left(\frac{E_V - E_F}{k_B T}\right). \tag{3.5}$$

N_C and N_V denote the effective state densities of electrons and holes in the conduction and valence band, respectively.

The carrier densities in a non-intrinsic semiconductor also depend on the dopant concentration beside the parameters discussed above. On condition that all dopant atoms are ionized in thermal equilibrium, it is $n_0 = N_D$ in a n-type semiconductor and $p_0 = N_A$ in a p-type semiconductor, with

N_D and N_A the dopant concentration of donor and acceptor atoms, respectively.

The thermodynamic equilibrium of a semiconductor is displaced by the illumination with light or, alternatively, by the application of an external voltage. In this scenario, the product of the electron density n and the hole density p is greater than n_i^2 and can be calculated from:

$$np = (n_0 + \Delta n)(p_0 + \Delta p) = n_i^2 e^{V/V_{th}} = n_i^2 e^{(E_{F,n} - E_{F,h})/qV_{th}}, \tag{3.6}$$

with Δn and Δp the excess carrier densities of electrons and holes, respectively, and V_{th} the thermal voltage. Mathematically, the displacement of the thermal equilibrium in Eq. 3.6 is described by the existence of a separate electron and hole Fermi-level. V denotes the local voltage. Multiplying this voltage with the unit charge results in the splitting of the electron quasi-Fermi-level $E_{F,n}$ and the hole quasi-Fermi-level $E_{F,h}$ at a certain position in the semiconductor.

The generation and recombination of electrons and holes is a pairwise process. In the scenario of a semiconductor that exhibits no energy states inside the band gap, it is $\Delta n = \Delta p$ for flat energy bands. Scenarios with $\Delta n \neq \Delta p$ are caused by energy states in the band gap that temporarily trap electrons or holes as explained in Refs. [63, 64]. In the following scenario, we consider a p-type semiconductor with $\Delta n = \Delta p$. The excess carrier density can be derived from Eq. 3.6:

$$\Delta n = -\frac{n_0 + N_A}{2} + \sqrt{n_i^2 \left(e^{V/V_{th}} - 1\right) + \left(\frac{n_0 + N_A}{2}\right)^2}. \tag{3.7}$$

For low level injection (LLI) with $\Delta n << N_A$ [56] and for high level injection (HLI) with $\Delta n >> N_A$ [65], the excess carrier density in a p-type semiconductor Eq. 3.7 can be approximated by:

$$\Delta n = \frac{n_i^2}{N_A} \left(e^{V/V_{th}} - 1\right) \quad (LLI), \tag{3.8a}$$

$$\Delta n = n_i \left(e^{V/2V_{th}} - 1\right) \quad (HLI), \tag{3.8b}$$

where V denotes the local voltage. Similar relations are derived for an n-type semiconductor by calculating Δp from Eq. 3.6.

After generation ending, excess carriers recombine with a net recombination rate $U(\Delta n)$:

$$U\left(\Delta n\right) = \frac{\partial \Delta n(t)}{\partial t}. \tag{3.9}$$

On condition that $U\left(\Delta n\right)$ is proportional to Δn, a basic solution of Eq. 3.9 is $\Delta n(t) = \Delta n(0) e^{-\frac{t}{\tau}}$, with τ the carrier lifetime. If different recombination processes do not interact, the net-recombination rate $U\left(\Delta n\right)$ is the sum of all contributing recombination rates in a semiconductor. In this scenario, the carrier lifetime τ is given by the sum of all single recombination lifetimes τ_i:

$$\tau = \frac{\Delta n}{U\left(\Delta n\right)} = \left(\sum_i \frac{1}{\tau_i}\right)^{-1}. \tag{3.10}$$

3.2 Carrier transport

The electron and hole QFL is the sum of the electrochemical and the electric potential. The net-current is defined by the product of the QFL gradient and the local conductivity [57]:

$$\vec{j} = \frac{\sigma}{q} \nabla E_F, \tag{3.11}$$

which holds for the current transport of electrons or holes with respect to the referring QFL. The sum of the electron and hole current represents the total current at a certain point in a semiconductor. The Einstein relation defines the diffusion constant D of free carriers to be proportional to the mobility μ of one carrier species:

$$D = \frac{\mu k_B T}{q} \tag{3.12}$$

and where k_B is the Boltzmann constant, T the absolute temperature and q the electric charge. The mobility μ is a determining parameter in terms of the semiconductor conductivity of electrons or holes [66, 67]. The local conductivity of a semiconductor for one type of carrier is calculated from:

$$\sigma = q \mu n \tag{3.13}$$

and where n is the carrier concentration of holes or electrons.

3.3 Mechanisms of recombination

3.3.1 Auger recombination

Auger recombination is an intrinsic recombination process that exists in every semiconductor. The emitted energy of an electron-hole recombination process is transfered to a free electron in the conduction band (*eeh*-process) or to a free hole in the valence band (*ehh*-process). This third particle relaxes within the energy band toward the band edge. The energy of the recombination process is transfered by phonons to the crystal lattice. Neglecting the interaction of free carriers, the net-Auger recombination rate in highly doped silicon is calculated from [68]:

$$U_{Auger} = \underbrace{C_n \left(n^2 p - n_i^2 n_0 \right)}_{eeh-process} + \underbrace{C_p \left(n p^2 - n_i^2 p_o \right)}_{ehh-process}, \tag{3.14}$$

with C_n and C_p the Auger coefficients of the respective *eeh*- and *ehh*- process [69]. Altermatt et al., Hangleitner et al. and Schmidt et al. developed more sophisticated Auger recombination models that involve the interaction of free carriers in crystalline silicon [70, 71, 72]. Kerr et al. developed a "General parameterization of Auger recombination in crystalline silicon" [73] which is straightforward to apply in order to estimate the Auger lifetime limit based on the dopant and carrier densities.

Auger recombination is sensitive for high doping densities and/or high carrier densities in high level injection. The specific scenario of high level injection can be induced by concentrated sunlight that is focused on a solar cell, by high externally applied voltages or, alternatively, by very low base doping densities (N_A<1×10^{14} cm^{-3}) which also results in high carrier densities for high externally applied voltages. Auger recombination rates are increased by highly diffused layers, e.g. the emitter or a back-surface field.

3.3.2 Radiative recombination

Radiative recombination is the second intrinsic recombination mechanism in a semiconductor [74]. A free electron in the conduction band is captured by a free hole in the valence band. The recombination energy is emitted by a photon. The recombination rate is proportional to the *pn*-product:

$$U_{Rad} = C_{rad} np, \tag{3.15}$$

with C_{rad} the coefficient of the radiative recombination which depends on the excess carrier density as described in Ref. [75]. Silicon is an indirect semiconductor with a minimum energy of the conduction band and a maximum energy of the valence band that exhibit different crystal momentums. Due to the thermalization of free electrons and holes in the conduction and valence band, respectively, the referring carriers are located in these minimum or maximum energy states. A radiative recombination process involves the absorption or the emission of phonons whose sum of momentum corresponds to those of the crystal lattice between the energy states of the electrons and holes. The emitted photon energy E_{photon} is calculated from:

$$E_{photon} = h_p f_{photon} = \mathit{\Delta} E \pm E_{phonon}, \tag{3.16}$$

with f_{photon} the frequency of the emitted photon, $\mathit{\Delta} E$ the energy difference of electrons and holes in the conduction and valence band, respectively, and E_{phonon} the total energy of phonons.

Compared to Auger and Shockley-Read-Hall recombination (explained in the following section), radiative recombination is not the limiting loss mechanism of the solar cells in this thesis.

Concrete example: Assuming a *p*-type wafer with a boron-dopant density of $4{\times}10^{15}$ cm^{-3}, an excess carrier density of $1{\times}10^{15}$ cm^{-3} which relates to a local voltage of 631 mV in the silicon semiconductor and a coefficient of the radiative recombination of $4.73{\times}10^{-15}$ cm^{-3}/s [76], the radiative and Auger recombination rates (calculated by means of the parameterization of Ref. [73]) account for $2.4{\times}10^{16}$ cm^{-3}s^{-}1 and $5.6{\times}10^{16}$ cm^{-3}s^{-}1, respectively. The excess carrier density is chosen to achieve a local voltage similar to a typical open-circuit voltage of an industrially fabricated screen-printed solar cell. The respective minority carrier lifetimes limited by radiative and Auger recombination account for 42.3 ms and 17.7 ms, respectively. Typical Shockley-Read-Hall recombination lifetimes in the bulk of a solar cell account for 10 µs up to 2 ms which is several magnitudes lower than radiative recombination and, hence, has a much stronger impact on the device recombination.

Radiative recombination increases for large *pn*-products at a certain point in the semiconductor. Hence, radiative recombination is sensitive for high local voltages which means high carrier densities. In this thesis, all solar cells operate under non-concentrated sunlight and exhibit moderate local carrier densities resulting in low rates for radiative recombination.

3.3.3 Shockley-Read-Hall recombination

Contaminants and defects in the crystal lattice can generate energy states in the band gap of a semiconductor. W. Shockley, W.T. Read [14] and R.N. Hall [15] developed a statistical model for an extrinsic type of recombination. Electrons from the conduction band and holes from the valence band are captured by an energy state in the band gap and recombine. Assuming one defect state with a constant energy E_d in the band gap, the Shockley-Read-Hall (SRH) recombination rate is calculated from:

$$U_{SRH} = \frac{\sigma_n \sigma_p v_{th} N_d \left(np - n_i^2\right)}{\sigma_n \left[n + n_i e^{\frac{E_d - E_i}{kT}}\right] + \sigma_p \left[p + n_i e^{\frac{E_i - E_d}{kT}}\right]} \tag{3.17}$$

with v_{th} the thermal velocity, N_d the density of the defect state and σ_n and σ_p the capture cross sections of the defect for electrons and holes, respectively.

The SRH carrier lifetime can be calculated from:

$$\tau_{SRH} = \frac{\tau_{p0}\left(n_0 + N_C e^{\frac{E_d - E_C}{kT}} + \Delta n\right) + \tau_{n0}\left(p_0 + N_V e^{\frac{E_V - E_d}{kT}} + \Delta n\right)}{n_0 + p_0 + \Delta n} \tag{3.18}$$

with $\tau_{n0} = (\sigma_n v_{th} N_d)^{-1}$ and $\tau_{p0} = (\sigma_p v_{th} N_d)^{-1}$ the electron and hole capture times of the defect, respectively.

Boron-oxygen complex

Czochralski-grown silicon wafers [24] are frequently used substrates for industrial cell production. Excess carrier lifetimes τ of boron-doped Cz-Si wafers are limited by boron-oxygen complexes B_sO_{2i}, whose densities are proportional to the wafer doping density N_A [25]. By illuminating the wafer, two interstitial oxygen atoms and one substitutional boron atom form the boron-oxygen complex which has a ten times higher capture cross section for electrons than for holes. As a result, the SRH carrier lifetime is decreased and exhibits an injection-dependent characteristic. In low level injection, carrier lifetimes are ten times lower than in high level injection. This state is defined as degraded state with low lifetimes [77, 78, 79]. The density of the complexes is reduced by an annealing step at 300°C, e.g. on a hot plate. This leads to high τ of the so-called annealed state.

The SRH recombination parameters of the boron-oxygen complex are defined as [29, 27]:

$$\left(\frac{\tau_{n0}}{s}\right) = 4.0202 \times 10^{39} \left(\frac{N_A}{cm^{-3}}\right)^{-0.824} \left(\frac{O_i}{cm^{-3}}\right)^{-1.748} m, \tag{3.19a}$$

$$\tau_{p0} = 10\tau_{n0}, \tag{3.19b}$$

$$E_T = E_C - 0.41\ eV, \tag{3.19c}$$

where O_i is the interstitial oxygen density in Si and m is an improvement factor [29] which may be related to the density of O_i dimers, a responsible constituent for the lifetime limitation. Equation 3.19 can be used to approximate the injection-dependent τ_{SRH} as follows:

$$\tau_{SRH} = \tau_{p0}\left(\frac{1}{N_A/\Delta n + 1} + \frac{1}{10}\right). \tag{3.20}$$

An approach for reducing the density of boron-oxygen complexes is the application of boron doped magnetically-confined Cz-Si [80] which has a lower interstitial oxygen concentration. This specific type of Cz-Si is not yet commercially available. Another approach is the use of gallium-doped Cz-Si, showing no light-induced lifetime degradation and enabling high cell efficiencies [81].

3.3.4 Surface recombination

Surfaces are interruptions in the periodical crystal lattice. In the band gap of a semiconductor, this causes a spectrum of energy states. The specific state distribution depends on the surface topography and on dielectric passivation layers on top of the surface [30, 82, 83]. Passivation defines the approach to reduce the surface recombination which is done by:

- reducing the density of defect states, and/or
- reducing the density of one carrier species at the recombination loaded surface.

The first approach is done, e.g. by a thin layer of thermally grown silicon oxide (SiO_2) that is covered by a layer of hydrogen containing silicon nitride (SiN). An annealing step increases the mobility of hydrogen atoms in the SiN that can diffuse through the SiO_2-layer to the SiO_2-Si-interface. The hydrogen atoms saturate defects and reduce the surface recombination rate [84].

The second approach can be realized by a field effect passivation. The deposition of positive (negative) charges onto the surface induces an electric field that repels hole (electron) carriers. As a result, the density of one carrier species is decreased leading to a lower recombination rate by defect states at the surface. A deposition of PECVD-SiN (**p**lasma-**e**nhanced **c**hemical **v**apor **d**eposition) containing positive charges [85, 86, 87] or aluminum-oxide (Al_2O_3) containing negative charges [31, 88] are technical approaches for field effect passivation.

Diffusing the surface with dopant atoms also reduces the concentration of one carrier species as explained by Eq. 3.6. In photovoltaic technology, diffused surfaces can act as an emitter for carrier collection, or as a back-surface and front-surface fields [89] that offer additional conductivities for the current transport inside the solar cell [90].

The deposition of charges and/or the diffusion of dopant atoms result in a bending of the conduction and valence band near the surface. In this scenario, the concentration of electrons and hole carriers depends on the local band bending in the semiconductor. For this reason, an effective surface is defined that includes the narrow volume with band bending at the real surface. The sum of all recombination processes in this volume and at the real surface is combined as an effective surface recombination rate U_{surf}. The excess carrier density Δn in the bulk with flat energy bands bordering the effective surface is used to define an effective surface recombination velocity S_{eff}:

$$S_{eff}\left(\Delta n\right) = \frac{U_{surf}\left(\Delta n\right)}{\Delta n}. \tag{3.21}$$

Eq. 3.21 also holds for an uncharged and undiffused surface. In this scenario, Δn and U_{surf} denote the excess carrier density and the net-recombination rate, respectively, both taken at the real surface of the semiconductor.

3.4 Lifetime measurement

The temporal variation of the excess carrier density in a semiconductor is given by the continuity equation for electrons [57]:

$$\frac{\partial \Delta n\left(t\right)}{\partial t} = G_n\left(t\right) - U_n\left(t\right) + \frac{1}{q}\nabla \vec{J_n}, \tag{3.22}$$

and holes:

$$\frac{\partial \Delta p\left(t\right)}{\partial t} = G_p\left(t\right) - U_p\left(t\right) - \frac{1}{q}\nabla \vec{J_p}, \tag{3.23}$$

with $G_n\left(t\right)$ and $G_p\left(t\right)$ the generation rates, $U_n\left(t\right)$ and $U_p\left(t\right)$ the recombination rates and J_n and J_p the current densities for electrons and holes, respectively.

Nagel et al. solved the continuity equation by assuming an averaged generation rate $G_{av}(t)$ and an averaged excess carrier density $\Delta n_{av}(t)$ in the volume of a semiconductor, e.g. a silicon wafer with a certain thickness W [91]. The calculated effective carrier lifetime is:

$$\tau_{eff}(t) = \frac{\Delta n_{av}(t)}{G_{av}(t) - \frac{\partial \Delta n_{av}(t)}{\partial t}}. \tag{3.24}$$

The average excess carrier density Δn_{av} can be deduced from the excess conductivity $\Delta\sigma$. By subtracting the conductivity in the dark at thermal equilibrium from the conductivity at or after carrier generation, the excess conductivity can be calculated from:

$$\Delta\sigma = q\mu_n(n - n_0) + q\mu_p(p - p_0) = q\mu_n \Delta n + q\mu_p \Delta p. \tag{3.25}$$

and with μ_n and μ_p the mobilities of electrons and holes, respectively.

A widespread method for the determination of the effective carrier lifetime has been developed by Sinton et al. [92]. The so-called "**q**uasi-**s**teady-**s**tate **p**hoto**c**onductance" (QSSPC) technique uses a light pulse for the carrier generation. A reference diode is used to measure the temporal illumination intensity. The generated current inside the sample can be calculated from its optical properties. By coupling a changing magnetic field at the wafer, circular currents are induced whose magnitude depend on the temporal wafer conductivity and, hence, on the the temporal excess carrier density. The analysis of the QSSPC method assumes the equality of electron and hole excess carriers ($\Delta n = \Delta p$). The average excess carrier density is calculated from the the excess conductivity of a wafer:

$$\Delta n_{av} = \frac{\Delta\sigma}{q\left(\mu_n + \mu_p\right)}. \tag{3.26}$$

Deviations of the carrier equality can be caused by energy states inside the semiconductor band gap that can trap minority carriers temporarily [93]. In this scenario, Equation 3.26 does not hold for the calculation of excess carriers and must be adjusted in order to calculate the carrier lifetime which has been investigated in several studies [94, 63, 93, 95, 17, 64, 96, 97, 98].

If the decay time of the light pulse duration is greater than the effective carrier lifetime, the net-recombination rate U is about the average generation rate: $U \approx G_{av}$. The term "quasi" in the abbreviation "QSSPC" denotes the quasi-statical equality of generation and recombination. For the specific case of constant generation, Eq. 3.24 simplifies to:

$$\tau_{eff} = \frac{\Delta n_{av}}{G_{av}}. \tag{3.27}$$

The averaged generation G_{av} rate is determined by a calibrated reference cell. G_{av} depends on the optical properties of the sample, on the illumination intensity and on the illumination spectrum. The time-dependent generation rate is calculated from:

$$G_{av}(t) = \frac{I(t) f_{abs} J_{sc,1sun}}{qW}, \tag{3.28}$$

with $I(t)$ the illumination intensity detected by the reference cell, $J_{sc,1sun}$ the short-circuit current density of the reference cell and W the wafer thickness of the sample. The absorption coefficient f_{abs} depends on the optical properties of the sample and is set as an input parameter.

If the net-recombination differs from the generation ($U \neq G$), a correction term $\frac{\partial \Delta n}{\partial t}$ has to be inserted as described in Ref. [91].

3.5 Effective lifetime τ_{eff}

The net-recombination rate and, consequently, the effective carrier lifetime τ_{eff} is calculated from the sum of all contributing recombination rates:

$$\frac{1}{\tau_{eff}} = \frac{1}{\tau_{SRH}} + \frac{1}{\tau_{Aug}} + \frac{1}{\tau_{rad}} + \frac{1}{\tau_{surf}} \tag{3.29}$$

and where τ_{surf} is the lifetime limited by surface recombination. By solving the transport equations, Fischer introduced an expression for τ_{surf} of a semiconductor wafer [99]:

$$\frac{1}{\tau_{surf}} = \frac{\Delta n_f S_{eff,f}}{\Delta n_{av} W} + \frac{\Delta n_r S_{eff,r}}{\Delta n_{av} W}, \tag{3.30}$$

with $S_{eff,r}$ and $S_{eff,f}$ the effective surface recombination velocities at the front and rear side, respectively. n_f and n_r denote the carrier densities in the volume without band bending adjoining the effective front and rear surfaces, respectively. Note that S_{eff} includes all contributing recombination mechanisms (Auger, SRH and radiative) of the effective surface.

In the scenario of similar surface recombination velocities and similar carrier densities at the front and rear side, Eq. 3.30 simplifies to:

$$\frac{1}{\tau_{surf}} = \frac{2S_{eff}}{W}. \tag{3.31}$$

The effective surface recombination velocity is proportional to the saturation current density J_0 of the surface:

$$S_{eff} = \frac{J_0}{qn_i^2}(N_{dop} + \Delta n) \tag{3.32}$$

where N_{dop} denotes the concentration of dopant atoms of the wafer.

In the following scenario, we assume similar and constant surface saturation current densities for the front and rear side. The difference of the inverse effective lifetime and the inverse Auger lifetime is plotted as a function of the excess carrier density. This results in a linear slope in high level injection which is used to calculate the saturation currents J_0 of the surface:

$$\frac{1}{\tau_{eff}} - \frac{1}{\tau_{Aug}} = \frac{1}{\tau_{SRH}} + \frac{2J_0}{qn_i^2 W}(N_{dop} + \Delta n), \tag{3.33}$$

with W wafer the thickness. The factor 2 in Eq. 3.33 denotes the fact of similar saturation current densities at both sides of the wafer. SRH lifetimes are constant in high level injection. Hence, τ_{SRH} does not disturb the linear characteristics of $\frac{1}{\tau_{eff}} - \frac{1}{\tau_{Aug}}$.

An alternative method to discuss single recombination contributions of a device is the measurement of the injection dependent recombination current density $J_{rec}(\Delta n)$. We assume a lifetime sample that corresponds to a certain solar cell component. The respective recombination current is calculated from:

$$J_{rec}(\Delta n_{av}) = \frac{qW\Delta n_{av}}{\tau_{eff}}. \tag{3.34}$$

By using Eq. 3.6, the averaged QFL splitting (local voltage) of the lifetime sample is calculated from the measured excess carrier density. Hence, the recombination current can be plotted as a function of the internal voltage which results in an implied I-V-characteristic [100]. In the scenario of negligible or non-existing internal majority carrier currents, the lifetime measurements and the implied I-V-characteristics, are not affected by series resistances. Summarizing the implied I-V-characteristics of every lifetime sample that corresponds to a solar cell components, this can be understood as an approximation of the solar cell I-V-curve without the impact of series resistances.

First concrete example: The effective lifetime of a float-zone silicon wafer featuring a passivated emitter on both sides is measured as a function of the excess carrier density. The resulting $\tau_{eff}(\Delta n)$ is used to calculate the recombination current density of the lifetime sample. In this scenario, the impact of τ_{SRH} can be neglected since the substrate quality of float-zone silicon and the bulk lifetime is high. The emitter recombination determines the effective lifetime.

Second concrete example: If the substrate quality is low and τ_{SRH} limits τ_{eff}, the calculated recombination current density considers SRH recombination. The area weighted recombination current density accounts for the surface and for the bulk recombination. In this scenario, the wafer thickness of the sample and the cell must be equal to obtain similar magnitudes of SRH recombination currents inside the bulk.

3.6 I-V-characteristics

3.6.1 Diode recombination and dark I-V-characteristics

In the dark, the excess carrier density and the resulting recombination current of a diode is zero at V_{ext}=0 mV. The application of an external voltage increases the splitting of the QFL at the pn-junction. Electrons and holes are injected across the pn-junction which results in increased excess carrier densities in the semiconductor (see Eq. 3.7). A diode with a constant saturation current density J_0 exhibits a recombination current density J_{rec} which is calculated from [56]:

$$J_{rec} = J_0(e^{\frac{V}{nV_{th}}} - 1) \tag{3.35}$$

with V the voltage in the semiconductor diode and n the local ideality factor. n can be considered as the inverse slope of the recombination characteristic that is semi-logarithmically plotted as a function of the voltage. The local ideality factor n is calculated from:

$$n = \frac{V_2 - V_1}{V_{th} ln\,(J_2/J_1)} \tag{3.36}$$

and where (J_1,V_1) and (J_2,V_2) are two neighboring points of the characteristics. In the exemplary case of an ideal diode, the local ideality factor is constant and accounts for unity (n=1) for all externally applied voltages. This is achieved for the following conditions:

- The increase of the excess carrier density must be proportional to $e^{\frac{V_{ext}}{V_{th}}}$ in every point of the device.
- The effective carrier lifetime τ_{eff} and/or the total saturation current density J_0 of the diode is constant and does not depend on the excess carrier density.

The resulting net-recombination rate (Eq. 3.9) and, finally, the net-recombination current is proportional to $e^{\frac{V_{ext}}{V_{th}}}$.

In the dark, a current J_{rec} is injected from outside by applying an external voltage. Injected electrons and holes recombine before they enter the external circuit. Due to series resistances of the device structure, the diode current J induces a voltage drop between the external circuit and the solar cell. As a result, the local voltage inside the device is **lower** than the external voltage. Assuming a lumped series resistance R_s of the device, the local voltage at the pn-junction is calculated from:

$$V_{local,dark} = V_{ext} - |JR_s| \tag{3.37}$$

In the scenario of a dark (and illuminated) solar cell, excess carriers recombine with a recombination rate that is proportional to the excess carrier density and the inverse effective lifetime. The recombination current density can be calculated from:

$$J_{rec}(V) = \frac{q}{A} \int\limits_{Vol} \frac{\Delta n(\vec{x})}{\tau_{eff}(\Delta n,\vec{x})} dx^3, \tag{3.38}$$

with A the total device area, $\vec{x}$ the position inside the diode, dx^3 a volume element and Vol the total device volume.

3.6.2 Illuminated I-V-characteristics

The illumination with light generates excess carriers with a rate $G(z)$ that depends on the depth z inside the semiconductor. The total generation current density inside a wafer or a solar cell J_{gen} is calculated from:

$$J_{gen} = q \int\limits_{0}^{W} G(z) dz, \tag{3.39}$$

where W denotes the wafer depth. Generally, the illuminated I-V-characteristic of a solar cell is defined as the difference of generation and recombination:

$$J_{1sun}(V_{ext}) = -(|J_{gen}| - J_{rec,1sun}(V_{ext})), \tag{3.40}$$

where J_{1sun} and $J_{rec,1sun}$ denotes the I-V-curve and the recombination current densities at 1 sun illumination. The generation current does not depend on the external voltage but on the optical properties of the device, the illumination intensity and the illumination spectrum (see Fig. 3.1(b)). By definition, the sign of the generation current is negative and the sign of the recombination current is positive. Any illumination intensity can be applied to measure the I-V-curve of a solar cell. The standard test conditions for solar cell measurements are defined for the am 1.5g spectrum at an illumination intensity of 100 mW/cm^2 [101], simply denoted as "1 sun" in this thesis. The illuminated I-V-characteristic has negative signs between J_{sc} and V_{oc} (see Fig. 3.1(b)). In order to calculate the recombination current under illumination, Eq. 3.38 or 3.35 can be used for the respective carrier densities and local voltages. In the following example, we assume a solar cell with a total saturation current density of 600 mA/cm^2 that is used to calculate the currents in Fig. 3.1. In contrast to the dark scenario, the illumination with light generates excess carriers which results in recombination current $J_{rec,1sun}$ greater than zero at V_{ext}=0 mV ($J_{rec,1sun}$=1.1 mA/cm^2 in Fig. 3.1(a)).

The short-circuit current density J_{sc} can be calculated from:

$$J_{sc} = J_{1sun}(V_{ext} = 0mV) = -(|J_{gen}| - J_{rec,1sun,0}), \tag{3.41}$$

where $J_{rec,1sun,0}$ denotes the recombination current density under illumination at V_{ext}=0 mV.

By increasing the external voltages, the excess carrier density exponentially increases referring to Eq. 3.7. In the dark and illuminated scenario, this leads to an increased recombination current with a magnitude of several mA/cm^2 for external voltages greater than 500 mV (see Fig. 3.1(a)). The exponentially increasing carrier injection and the resulting recombination currents determine

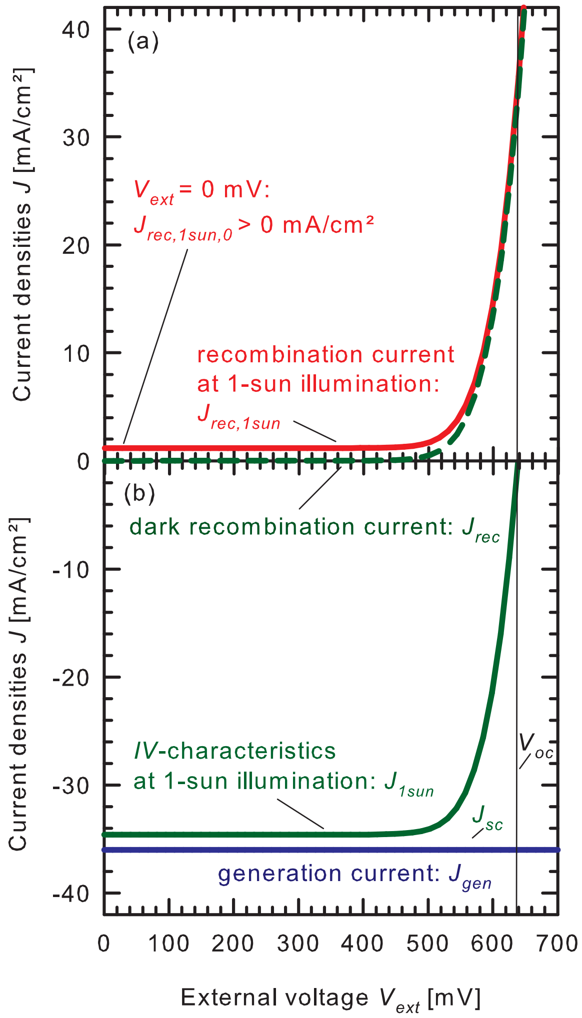

Figure 3.1: (a) Recombination current densities of a solar cell at 1 sun illumination and in the dark. In the dark, the injection of holes and electrons across the *pn*-junction exclusively increases the carrier density inside the device. The recombination current is zero at V_{ext}=0 mV. Under illumination, the excess carrier density and the resulting recombination currents are greater than zero at V_{ext}=0 mV. In both scenarios, the excess carrier density at the *pn*-junction exponentially increases by increasing the external voltage (Eq. 3.7). This leads to a strongly increased recombination in the dark and illuminated scenario for V_{ext}>500 mV. (b) The generation current density is constant in the entire injection regime. J_{gen} depends on the optical device properties and the incident light spectrum. The I-V-curve is defined as the difference of generation and recombination currents.

the typical shape of a solar cell I-V-curve.

A concept to describe the I-V-curve of a solar cells is the superposition principle. It assumes the illuminated I-V-characteristic as the sum of the short-circuit current and the recombination current in the dark:

$$J = J_{rec} - J_{sc}. \tag{3.42}$$

The great advantage of this theoretical concept is the simple relation between the illuminated and dark I-V-curve. In the illuminated device, the superposition principle assumes the quasi-Fermi levels to be constant in the depletion region. In fact, this assumption does not hold and leads to departures of the superposition principle as described in Refs. [102, 103, 104]. However, the departures appear at low external voltages at which the gradients of the QFL extend into the depletion region. The impact on the I-V-parameters is small or even negligible as long as the maximum power point of the solar cell is not affected [103]. This holds for all solar cells in this thesis.

In the case of an illuminated solar cell, photogenerated currents inside the device flow toward the semiconductor-metal contacts where they enter the external circuit. On this way due to series resistances of the device structure, the current induces a voltage drop between the device and the external circuit. As a result, the local voltage inside the device is **higher** than the external voltage as long as the net-current flows into the external circuit. This scenario holds between J_{sc} and V_{oc}:

$$V_{local,1sun} = V_{ext} + |JR_s| . \tag{3.43}$$

Assuming similar external voltages, the local voltage at the pn-junction inside the device is increased in the illuminated scenario compared to the dark scenario. Assuming the superposition principle and an ideal diode whose recombination current is expressed by Eq. 3.35, the I-V-characteristic of the illuminated solar cell can be calculated from:

$$J(V_{ext}) = J_0(e^{\frac{V_{ext}+|JR_s|}{V_{th}}} - 1) - J_{sc}. \tag{3.44}$$

Note that the local voltage inside the illuminated device is greater than zero for V_{ext}=0 mV, due to the voltage drop that is induced by the current transport from the device into the external circuit.

At open-circuit conditions (V_{oc}), there is no solar cell current entering the external circuit: $J(V_{oc}) = 0$. In the exemplary case of an ideal diode, the open circuit voltage is calculated from:

$$V_{oc} = V_{th} ln\left(\frac{J_{sc}}{J_0} + 1\right). \tag{3.45}$$

Equation 3.45 is often used to estimate the V_{oc} of a solar cell. The fabrication of lifetime samples that represent certain device components (emitters, passivated surfaces, etc.) allows the measurement of the respective saturation currents $J_{0,i}$, e.g. by QSSPC measurement. By summarizing all contributing saturation currents, a total saturation current J_0 is calculated to estimate the V_{oc} by means of Eq. 3.45.

At the maximum power point MPP, the largest output power of a solar cell $P_{mpp} = V_{mpp}J_{mpp}$ is transfered into the external circuit, with V_{mpp} the referring external voltage and J_{mpp} the current-density of the device. The relation of P_{mpp} and the J_{sc}-V_{oc}-product is defined as the fill factor FF of a solar cell:

$$FF = \frac{J_{mpp}V_{mpp}}{J_{sc}V_{oc}}. \tag{3.46}$$

The solar cell efficiency η is a comparative parameter that relates the largest output power P_{mpp} with the irradiated solar power P_{solar}: $\eta = \left|\frac{J_{mpp}V_{mpp}}{P_{solar}}\right|$.

Using Eq. 3.46, the parameters J_{sc}, V_{oc}, FF and the solar power define an efficiency formula that is most often used:

$$\eta = \left|\frac{V_{oc}J_{sc}FF}{P_{solar}}\right|. \tag{3.47}$$

The fill factor and the efficiency do not exhibit dimensions or units as shown by the equations above. However, the common linguistic usage "defines" the "unit" percent for both variables. In this thesis, percent is used, too. Hence, a solar cell efficiency calculated by Eq. 3.47 of 0.2 is similar to a 20 % percent solar cell. The same procedure holds for the fill factor.

3.7 Illuminated I-V-characteristic shifted by the short-circuit current

The J_{sc}-shifted illuminated I-V-curve is commonly used to discuss the impact of series and shunt resistances or injection dependent lifetimes. By subtracting the short-circuit current from the illuminated I-V-curve, the characteristic is shifted into the first quadrant of the coordinate system. The respective current density and the external voltage exhibit positive signs as shown in Fig. 3.2(a). Using Eqs. 3.40 and 3.41, the J_{sc}-shifting of the illuminated I-V-curve is similar to the shifting of the total recombination current by the recombination current $J_{rec,1sun,0}$ at V_{ext}=0 mV. Both operations result in similar characteristics:

$$J_{1sun} - J_{sc} = J_{rec,1sun} - J_{rec,1sun,0} \tag{3.48}$$

In the present thesis, recombination currents are used to reproduce the measured J_{sc}-shifted I-V-characteristics of fabricated devices. The shape of the J_{sc}-shifted I-V-curve is expressed by the local ideality factor n (see Eq. 3.36). Local ideality factors greater than unity (n>1) indicate deviations of the ideal diode characteristic which results in reduced *FF*. A real device exhibits series or shunt resistances that always disturb the perfect diode characteristic as discussed in the next section.

Similar to the total recombination, every single recombination contribution of the device (e.g. Auger or SRH recombination) can be shifted by its value $J_{rec,1sun,0}$ at V_{ext}=0 mV. Then, the sum of all shifted recombination currents is equal to the J_{sc}-shifted illuminated I-V-curve:

$$J_{1sun} - J_{sc} = \sum_{i}^{N} \left(J_{rec,1sun,i} - J_{rec,1sun,i,0}\right). \tag{3.49}$$

The magnitude of a recombination contribution determines its impact on the total I-V-curve. Figure 3.2(a) depicts the J_{sc}-shifted I-V-curve of a solar cell and the $J_{rec,1sun,0}$ shifted Auger- and SRH recombination currents, all as a function of the external voltage. Auger recombination exhibits a large magnitude and, hence, strongly affects the total device characteristic. In contrast, SRH recombination is about one order of magnitude lower and has a minor impact. The respective local ideality factors of all three curves are depicted in Fig. 3.2(b). The *FF* is sensitive for increased local ideality factors in the voltage range around *MPP* to V_{oc}. In the present scenario, it is Auger recombination that determines the shape of the total I-V-characteristic and, hence, the local ideality factors for external voltages between *MPP* and V_{oc}. The large ideality factors of the shifted SRH recombination are less detrimental due to the low recombination magnitude. High local ideality factors for voltages less than 400 mV in Fig. 3.2(b) are caused by the "photogenerated current perturbing the carrier concentrations across the depletion region compared to their values in the dark." [103]. Robinson et. al investigated this effect that reminds on a shunt resistance. However, its impact on the *FF* is negligibly small at 1 sun illumination and for solar cells with a *pn*-junction that covers not less than one side of the wafer. Both conditions hold for all solar cells in this thesis.

A discussion of local ideality factors is a curve sketching that reveals no physical aspects. The origin of n>1 has to be found by analyzing the recombination currents and the carrier transports inside the device. This can be done by diode networks or simulation models that identify the loss mechanisms. Efficiency improvement strategy must focus on the recombination loaded device components that contribute the dominant losses.

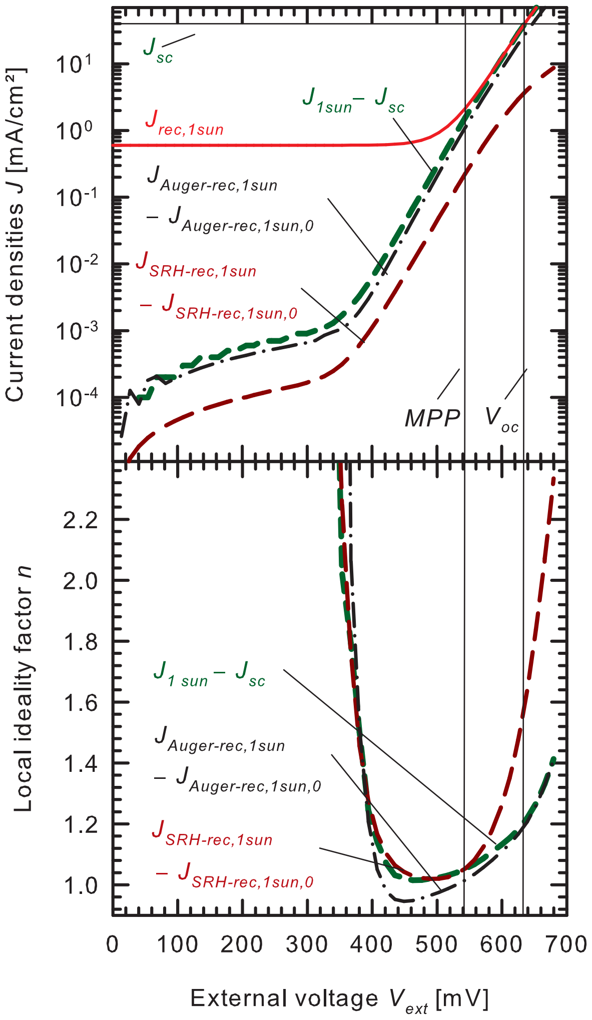

Figure 3.2: (a) J_{sc}-shifted illuminated 1 sun *I*-*V*-curve ($J_{1sun} - J_{sc}$) and the SRH and Auger recombination currents shifted by the respective recombination currents at V_{ext}=0 mV (e.g. $J_{Auger-rec,1sun} - J_{Auger-rec,1sun,0}$). The total recombination current density $J_{rec,1sun}$ is depicted to illustrate the consequences of the $J_{rec,1sun,0}$-shifting on the shape of the shifted *I*-*V*-curves. The higher the magnitude of a certain type of recombination, the stronger its impact on the *I*-*V*-curve. (b) Local ideality factors of the shifted *I*-*V*-curve and shifted recombination currents. In the present example, it is Auger recombination that determines the shape of the *I*-*V*-curve. The local ideality factors of the total *I*-*V*-characteristics and the the shifted Auger recombination exhibit similar values between *MPP* and V_{oc}.

3.8 Impact of series resistances on the illuminated *I*-*V*-curve

In the scenario of an illuminated solar cell, series resistances R_s induce voltage drops that result in increased *pn*-junction voltages (see Eq. 3.43). This causes higher carrier injection and, hence, higher recombination currents compared to a scenario with R_s=0. In addition to ohmic power dissipation ($P = RJ^2$), series resistances increase the excess carrier densities and the recombination losses for a defined external voltage compared to a virtual solar cell without series resistances. In order to discuss different scenarios of solar cells, the numerical one-dimensional device simulator PC1D [105] is applied to calculate the recombination currents and the *I*-*V*-curve of three exemplary devices. A more detailed discussion of PC1D is given in the next chapter. All solar cells feature a single front side emitter and a total saturation current density of 800 fA/cm². The series resistance is situated between the external circuit and the emitter of the device. All photogenerated carriers collected at the *pn*-junction are transported across the series resistance in order to enter the external circuit. The generation current is 35.3 mA/cm^2. The first device has a large lumped R_s of 1 Ωcm^2, the second device has a low lumped R_s of 0.4 Ωcm^2 and the third device is an exemplary cell with R_s=0 Ωcm^2. To keep nomenclature simple, the solar cells are simply called "1 Ωcm^2", "0.4 Ωcm^2" or "0 Ωcm^2 solar cell".

Figure 3.3(a) depicts the recombination currents of the solar cells as a function of the external voltage. The recombination current density at V_{ext}=0 mV accounts for 1.2 mA/cm^2 in the 0 Ωcm^2 scenario. The impact of the voltage drops on the recombination currents of the 0.4 and 1 Ωcm^2 devices can be estimated as described in the following.

Figure 3.3(b) shows the illuminated *I*-*V*-curves of the solar cells as function of the the external voltage. The short-circuit current density is similar for all devices (J_{sc}=34.2 mA/cm^2). The local *pn*-junction voltage inside the device can be estimated by using Eq. 3.43. At V_{ext}=0 mV, it accounts for 34.2 mV, 13.7 mV and 0 mV in the 1 Ωcm^2, 0.4 Ωcm^2 and 0 Ωcm^2 device, respectively. The increased recombination current densities due to internal voltage drops are calculated from Eq. 3.35. They account for 0 mA/cm^2 (0 Ωcm^2 device), 7.3$\times$10^{-10} mA/cm^2 (0.4 Ωcm^2 device) and 2.2$\times$10^{-9} mA/cm^2 (1 Ωcm^2 device). In the chosen scenarios, the series resistance induced voltage drops and the increased recombination currents at V_{ext}=0 mV have no practical impact on J_{sc} which is several magnitudes larger.

The recombination current around the maximum power point is affected by different series resistances. The solar cells featuring a lumped R_s of 1 Ωcm^2 and 0.4 Ωcm^2 exhibit increased recombination currents compared to the 0 Ωcm^2 scenario. This becomes obvious for external voltages greater than 500 mV (Fig. 3.3(a)). In this injection regime, the excess carrier densities are strongly increased compared to J_{sc}-conditions. Furthermore, the device currents around *MPP* exhibit similar magnitudes compared to J_{sc}-conditions. The currents induce high voltage drops in the 1 Ωcm^2 scenario ($\Delta V(V_{ext} = 500mV) = 33\ mV$) and comparatively lower voltage drops in the 0.4 Ωcm^2 scenario ($\Delta V(V_{ext} = 500mV) = 13\ mV$).

Mathematically, a simple expression can be deduced that relates the higher local voltage inside the device to an increased excess carrier density Δn_{local} and, finally, to a higher recombination compared to a scenario with R_s=0. The starting point for this derivation is given by Eq. 3.7 which defines the exponential behavior of the excess carrier density as a function of the local voltage at the *pn*-junction.

In a first step, the excess carrier density Δn_{local} inside the device is related to the reference excess carrier density Δn in the scenario with R_s=0. The following relation holds for $e^{\frac{V}{V_{th}}} >> 1$, this means, for external voltages greater than 200 mV:

$$\frac{\Delta n_{local}}{\Delta n} = \frac{e^{\frac{V_{local}}{V_{th}}}}{e^{\frac{V_{ext}}{V_{th}}}}. \tag{3.50}$$

$V_{local} = V_{ext} + \Delta V$ is inserted in Eq. 3.50 leading to the relation:

$$\frac{\Delta n_{local}}{\Delta n} = e^{\frac{\Delta V}{V_{th}}}, \tag{3.51}$$

which describes the multiplication factor of the carrier density at the *pn*-junction for internal voltage drops.

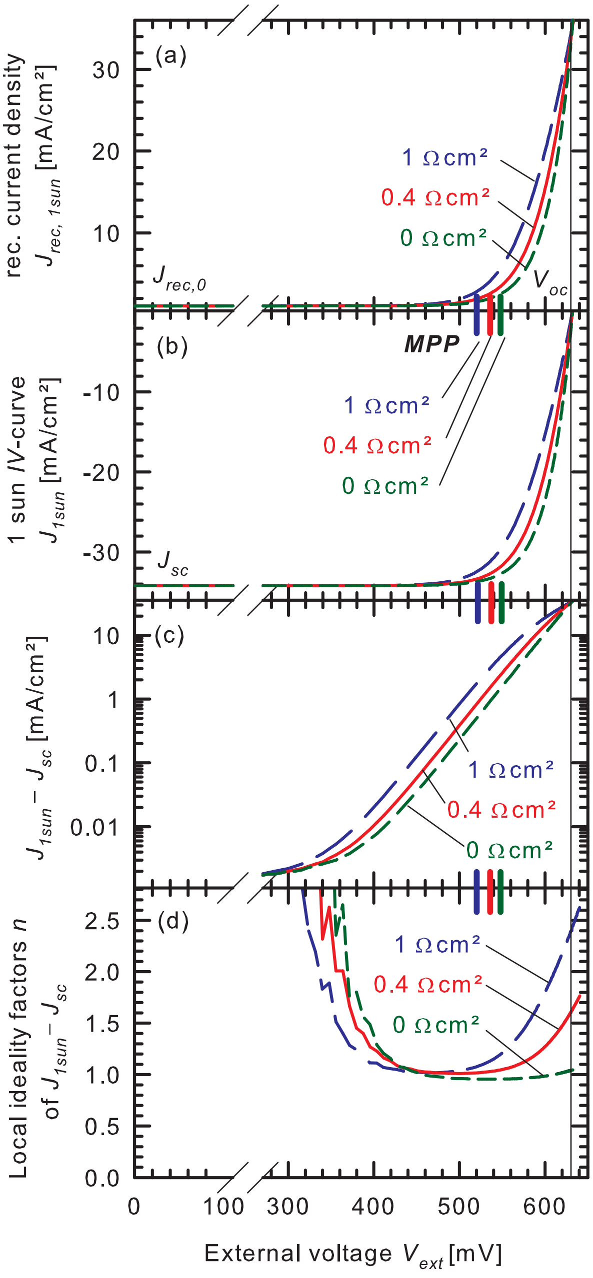

Figure 3.3: (a) Recombination currents at 1 sun illumination of three solar cells featuring similar saturation and generation currents. The lumped series resistance of the three devices accounts for 1 Ωcm², 0.4 Ωcm² and 0 Ωcm², respectively. (b) *I*-*V*-characteristics of the referring cells. The larger the series resistance, the stronger the shifting of *MPP* to smaller external voltages. (c) J_{sc}-shifted *I*-*V*-curves. The semilogarithmic plot illustrates the impact of different R_s (voltage drops) on the shape of the *I*-*V*-curve. (d) Local ideality factors of the J_{sc}-shifted *I*-*V*-characteristics. The impact of R_s is typically found for external voltages around *MPP* up to V_{oc}. The larger the series resistance the larger the local ideality factors in this voltage regime.

At V_{ext}=500 mV, the 1 Ωcm² and the 0.4 Ωcm² device exhibit a 3.6 and 1.7 times increased carrier density at the *pn*-junction compared to the scenario with R_s=0. Assuming constant effective lifetimes (saturation currents), these factors can be multiplied with the respective recombination current densities. In the present simulation study, the saturation current densities are set to be constant in all devices. At V_{ext}=500 mV, the recombination current densities account for 0.83 mA/cm² (1 Ωcm² device), 0.39 mA/cm² (0.4 Ωcm² device) and 0.25 mA/cm² (0 Ωcm² device) (see

Fig. 3.3(a)). The higher the series resistance, the higher the recombination currents at one defined external voltage. Hence, the absolute current density of the I-V-characteristics is stronger reduced for high R_s (Fig. 3.3(b)). As a result, the I-V-characteristic is more deformed, the MPP is shifted to smaller external voltages and the FF is reduced. The single FF account for 77.9 % (1 Ωcm^2 device), 80.4 % (0.4 Ωcm^2 device) and 82.8 % (0 Ωcm^2 device).

The open-circuit voltage of all devices (V_{oc}=632 mV) is not affected by series resistances. At V_{oc}, the device currents and the voltage drops converge to zero. The pn-junction voltage, the injection of carriers and, hence, the recombinations currents are similar in all scenarios.

The J_{sc}-shifted illuminated I-V-curves are semi-logarithmically plotted as a function of the external voltage (see Fig. 3.3(c)). For V_{ext}<300 mV, the different curves exhibit similar shapes and magnitudes. Firstly, the subtracted recombination contributions at V_{ext}=0 mV are similar in all scenarios. Secondly, in this voltage regime, the total recombination is mainly based on photogenerated excess carriers since the carrier injection across the pn-junction is comparatively small. For V_{ext}>400 mV, the total excess carrier density is increased by the carrier injection across the pn-junction.

The J_{sc}-shifted I-V-curve can be considered as the $J_{rec,1sun,0}$-shifted total recombination current. The $J_{rec,1sun,0}$-term is a constant recombination current. By substracting this term from the total recombination, a recombination current is calculated which exponentially increases as it is described by means of Eq. 3.35. For this reason, the local ideality factors of the J_{sc}-shifted I-V-curve are used in order to analyze the specific diode behavior of a solar cell. Local ideality factors greater (or smaller) than unity indicate deviations of the perfect diode characteristic with local ideality factors of unity. The shape of the J_{sc}-shifted I-V-curve is sensitive for voltage drops induced by the current flow along series resistances inside the device. Futhermore, shunt currents can be easily identified by analyzing the J_{sc}-shifted I-V-curve.

The adaption from high internal voltage drops between J_{sc} and MPP to low or non-existing internal voltage drops at V_{oc} results in a recombination characteristic that increases in a sub-exponential pace. The J_{sc}-shifted I-V-curve exhibits local ideality factors greater than unity as described in the following. The multiplication factor of the excess carrier density $e^{\Delta V/V_{th}}$ has a maximum for large voltage drops (device currents) which is the case for external voltages up to V_{mpp}. At V_{ext}= 500 mV, the multiplication factors of the excess carrier density $e^{\Delta V/V_{th}}$ account for 3.6 and 1.7 in the 1 Ωcm^2 and 0.4 Ωcm^2 scenario, respectively. By increasing the external voltage, the majority carrier currents of the device decrease. For external voltages near V_{oc}, the current densities and ΔV converge to zero. Consequently, $e^{\Delta V/V_{th}}$ converges to unity. The voltage drop adaption and the adaption of increased to non-increased recombination rates is large for the 1 Ωcm^2 device and comparatively reduced in the 0.4 Ωcm^2 solar cell.[1] However, the 1 Ωcm^2 and 0.4 Ωcm^2 device recombinations launch at strongly and slightly increased rates at J_{sc}, respectively, compared to the exemplary 0 Ωcm^2 scenario. At V_{oc}, the recombination rates are equal in all scenarios. As a result, the increase of recombination rates and currents from J_{sc} to V_{oc} is strongly (slightly) affected in the 1 Ωcm^2 (0.4 Ωcm^2) device, respectively.

Local ideality factors describe the variations of the recombination rates. Figure 3.3(d) depicts the local ideality factors of J_{sc}-shifted I-V-curves as a function of the external voltage. For V_{ext}<400 mV, high local ideality factors are caused by the effect described in Ref. [103]. However, this has no detrimental impact on the FF or the efficiency of a device. Between MPP and V_{oc}, the 1 Ωcm^2 solar cell exhibits the largest ideality factors compared to the other devices. This difference is caused by the variations of the recombination rates and currents as explained above. Discussing the local ideality factors is an easy method in order to determine deviations of the recombination rates. By considering the recombination magnitude of a device component and its recombination rate

---

[1] Note that recombination rates always increase for increasing external voltages. This holds for all three scenarios.

evolution (⇒ local ideality factors), it is straight-forward to analyze the impact on the I-V-curve.

3.9 J_{sc}-V_{oc}-characteristics and R_s-determination

The J_{sc}-V_{oc}-curve is an approximation to the J_{sc}-shifted illuminated I-V-curve of the device with eliminated series resistances. The V_{oc} and the J_{sc} is measured for different illumination intensities. If R_s is reasonably low and, hence, does not affect J_{sc} and if V_{oc} is unaffected by internal currents, the composition of both measured values creates an I-V-characteristic without disturbing series resistances. Hence, the J_{sc}-V_{oc}-curve is not affected by increased pn-junction voltages as in the scenario of an illuminated I-V-curve. The J_{sc}-V_{oc}-curve can be considered as a $J_{rec,1sun,0}$ -shifted recombination characteristic without the impact of series resistances (see Eq. 3.41).

Assuming one defined current density of the J_{sc}-V_{oc}- and the illuminated I-V-characteristic, the voltage drop between both curves can be explained by a lumped series resistance R_s of the entire device structure. R_s is calculated from [106, 107]

$$R_{s,light} = \frac{V_{J_{sc}V_{oc}} - V_{1sun}}{-J}, \tag{3.52}$$

where $J = J_{J_{sc}V_{oc}} = J_{1sun}$.

4 Modeling of EWT solar cells

4.1 Introduction

Emitter-wrap-through solar cells feature a front and a rear emitter. Either, photogenerated minority carriers are collected at the front *pn*-junction and transported as majority carriers through the front and EWT-via emitter, or they are transported as minority carriers through the base and collected at the rear *pn*-junction. Figure 4.1 shows a side view of a *p*-type EWT device. Inside the base, electrons e^- are minority carriers and holes h^+ are majority carriers. Due to the both-side collecting structure of an EWT cell, the recombination loaded transport paths of minority carriers are short. This leads to lower recombination losses at J_{sc}-conditions compared to front-junction cells with single front emitter.

An attribute of EWT solar cells is the existence of longer current paths of majority carriers compared to front junction devices. Electrons in the front emitter and holes in the base are transported longer distances before they enter the metal contacts at the rear side (see Fig. 4.1). Furthermore, EWT devices suffer from resistive losses induced by high local current densities.

Two approaches are found in literature for modeling the I-V-curve of EWT solar cells.

- Networks have been designed that consider different diodes, series resistances and shunt resistances all referring to single components of EWT devices.
- Numerical simulation models have been developed that include the present semiconductor models. As an advantage, the distributed nature of internal current transports of EWT devices is considered. As a disadvantage, all presented models exclusively focus on the periodically EWT unit cell without considering boundary areas of real devices, e.g. the busbars.

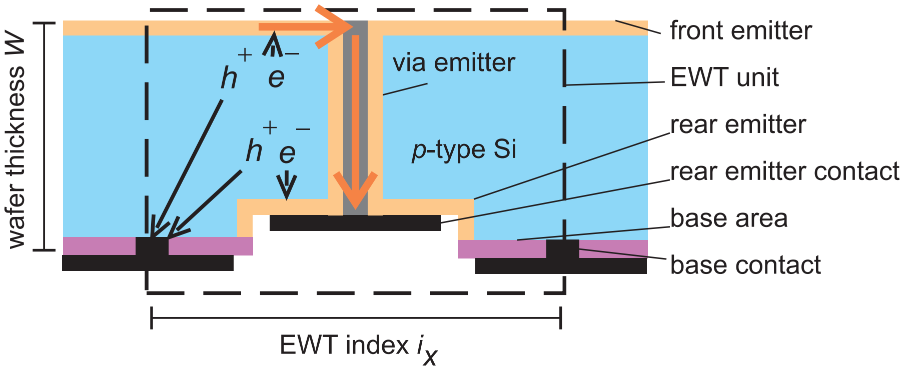

Figure 4.1: Side view of a *p*-type Si EWT solar cell structure (not drawn to scale) featuring front, EWT-via and rear emitter. The base area and base contacts are situated at the left and right hand side of the rear emitter. Minority carriers (electrons in the present scenario: e^-) are collected at the front or rear emitter depending on their place of photogeneration. Either electrons are transported as majority carriers along the front and EWT-via emitter to the rear contacts or they are transported as minority carriers through the base to the rear emitter. Photogenerated majority carriers (holes in the present scenario) possess one current path. They are transported through the base to their rear contacts.

4.2 Two-diode model

The two-diode model is frequently used to calculate the I-V-characteristics of front junction or MWT solar cells that feature a screen-printed metalization. The referring network is depicted in Fig. 4.2. Device components with constant saturation current densities and constant ideality factors of n_1=1 are represented by the "J_{01}"-diode. The "J_{02}"-diode considers recombination currents in the depletion region. It has a constant saturation current density, too, but exhibits a constant local ideality factor greater than unity. Frequently, the local ideality factor of the "J_{02}"-diode is set as n_2=2 resulting in SRH recombination currents of the second diode which are proportional to $e^{\frac{V}{2V_{th}}}$ [108].

The I-V-characteristic of the two-diode model is calculated from:

$$J = J_{01}(e^{\frac{V_{ext}-JR_s}{n_1V_{th}}}) + J_{02}(e^{\frac{V_{ext}-JR_s}{n_2V_{th}}}) + \frac{V_{ext}-JR_s}{R_{sh}} - J_L, \tag{4.1}$$

where J_L is the light generated current. Note that the device current J has a negative sign for external voltages smaller than V_{oc}[1].

The device current is transported across the lumped series resistance R_s resulting in a voltage drop of $\Delta V = JR_s$ between the external circuit and the pn-junction. The ohmic shunt resistance R_{sh} is connected in parallel to the diodes. In the scenario of an illuminated solar cell, the light induced current J_L is considered as a current source connected in parallel to the diodes.

Engelhart et. al used this network to discuss the I-V-curve of EWT solar cells [39]. FF-losses were explained by series resistances and J_{02}-recombination currents [50]. In his analysis, the J_{02}-recombination is interpreted as a deviation of the ideal diode characteristic with a constant local ideality factor of unity (n=1). The spatially resolved origin of the J_{02}-contribution cannot be explained in detail by the two-diode model since it does not respect the geometrical structure of EWT devices.

Other publications in the field of EWT solar cells associate the J_{02}-loss current with a laser-induced damage in the EWT-vias or at the rear side [109]. Recent investigations showed that alkaline etching solutions effectively remove the laser damage in the EWT-vias. Boron-doped silicon wafers were perforated by laser power, variably etched in potassium hydroxide solution and phosphorus diffused in a tube furnace. Depending on the applied laser system, the measured implied I-V-characteristics showed negligible J_{02} contributions for etching times shorter than 2 minutes [110].

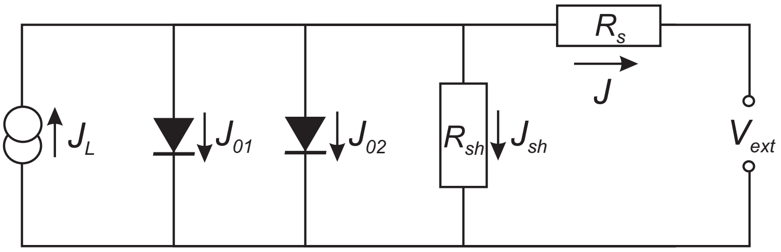

Figure 4.2: Two-diode model of a solar cell. The diodes J_{01} and J_{02} feature different saturation current densities and different local ideality factors. The photogenerated current is considered by the current source J_L. A lumped series resistance R_s combines all series resistance contributions of the device. The ohmic shunt resistance R_{sh} is connected in parallel to the diodes.

4.2.1 EWT-network model considering front and rear emitter

Smith et al. developed a sophisticated network for EWT solar cells [111]. The model considers the front and rear emitter by the integration of two opposed diodes. Furthermore, the model features an additional diode connected with the network by a lumped series resistances. This coupled circuit represents the edges of a real EWT device that exhibit even longer current paths for majority carriers than the periodical EWT cell structure. Smith applied his model to optimize the geometry

---

[1] Concrete example: A screen printed solar cells can suffer from damages inside the depletion region between the front emitter and the base. This is due to the silver paste and the firing step at elevated temperatures (T>800°C) used to form the contact between the metal and the phosphorus diffused emitters at the end of the process [34].

and the fabrication of EWT devices resulting in experimental efficiencies and fill factors of 18.2 % and 77.6 %, respectively.

4.3 Diode network model considering series resistances and injection dependent lifetimes

The influence of the EWT device series resistance on the I-V-curve can be estimated by a basic diode model. We apply a network that is related to the two-diode model in Fig. 4.2. The model does not consider "J_{02}-diodes" that would represent recombination currents in the space charge region. Shunt resistances are not included since they are mostly due to processing issues.

Figure 4.3 depicts the applied diode network that assumes the superposition principle. The first diode comprises all types of recombination with constant saturation current densities $J_{0,const}$ and constant local ideality factors n=1. The resulting recombination current can be calculated from Eq. 3.35. As an example, phosphorus emitters are represented by this type of recombination since they usually exhibit constant J_0 [112].

The second diode respects recombination rates that depend on the excess carrier density. A concrete example is the injection dependent bulk lifetime of boron-doped Cz-Si wafers (see Eq. 3.20). Further injection dependent recombination mechanisms can be considered by additional diodes connected in parallel. The recombination currents of these diodes are calculated by means of Eq. 3.34.

The voltage drop between the external circuit and the pn-junction of the device is induced by a lumped series resistance: $\mathit{\Delta} V = JR_s$. The illuminated I-V-curve is calculated from:

$$J = J_{0,const}(e^{\frac{V_{ext}-JR_s}{V_{th}}}) - J_{sc} + \sum_i qW\frac{\mathit{\Delta} n}{\tau_i(\mathit{\Delta} n)}, \tag{4.2}$$

where $\tau_i(\mathit{\Delta} n)$ is the injection dependent lifetime of a certain device component and W the wafer thickness. The excess carrier density is deduced from Eq. 3.7. By using the short circuit current density J_{sc} in Eq. 4.2, recombination losses at V_{ext}=0 mV are respected (see Eq. 3.41). Note that using J_{sc} is not a characteristic for the present calculation but also common for the one- or two-diode model. The generation current J_{gen} cannot be identified by means of a diode network and, hence, is an unknown parameter not used for the present calculation.

FF-losses due to series resistances of the EWT device can be easily estimated by using Eq. 4.2. These results can be comparatively discussed with findings of numerical simulation models.

In the present diode model, it is assumed that the total device current of majority carriers is transported across the lumped series resistance. In a real three-dimensional EWT device at J_{sc} conditions, about 90 % of the photogenerated carriers inside the base diffuse to the front side. Here, these carriers are collected by the front emitter and are transported as majority carriers through

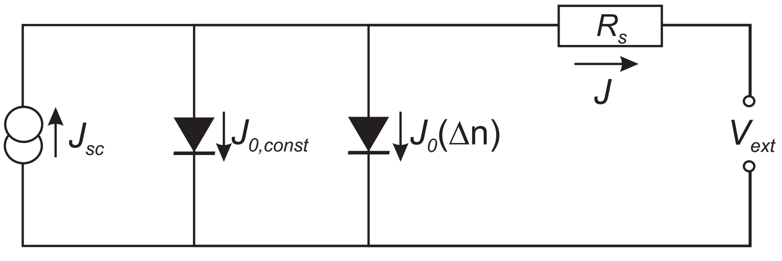

Figure 4.3: Diode network applied to calculate the I-V-curve of EWT solar cells. The diode $J_{0,const}$ features a constant saturation current density and a constant ideality factor of n=1. The diode $J_0(\mathit{\Delta} n)$ considers injection dependent recombination currents, e.g. of the bulk in boron-doped Cz-Si wafers. The short-circuit current density J_{sc} respects recombination losses at V_{ext}=0 mV. A lumped series resistance R_s combines all series resistance contributions of the device.

the front emitter and EWT-via emitter to the rear emitter contacts. This current path is sensitive for resistive losses. 10 % of the photogenerated carriers inside the base diffuse to the rear emitter without suffering from resistive losses in the front or EWT-via emitters. However, these carriers are sensitive for recombination losses. Hence, the resistive losses in the present diode network represent an upper limit for an EWT solar cell since all the photogenerated majority carriers are transported across the lumped series resistance. In a real device, it is only about 90 % of the carriers.

4.3.1 Determination of series resistances for single EWT device components

The current flow in certain device components of EWT solar cells is of a distributed nature. In order to respect the spatially distributed currents, we calculate the series resistances R_s by means of the ohmic power dissipation as described in Ref. [55]:

$$R_s = \frac{P}{I^2}, \tag{4.3}$$

where P denotes the ohmic power loss and I the current in the respective device component. The ohmic power dissipation P is calculated from:

$$P = \int I^2 dR, \tag{4.4}$$

where dR denotes the differential of the ohmic series resistance. The voltage drop $\varDelta V$ along the series resistance loaded current path of majority carriers is calculated from:

$$\varDelta V = \int I dR. \tag{4.5}$$

In order to calculate the ohmic power dissipation and the series resistances, the knowledge of majority carrier trajectories is anticipated. Simulations results based on a three-dimensional simulation model will reveal the nature of the trajectories in the following chapters. We use these results in order to calculate the R_s contributions of single device components. Finally, we can estimate the impact of each R_s contribution on the FF.

In the following calculations, we assume a circular EWT-via that exhibits a defined radius r_{via}. However, the calculations can be approximated for any other EWT-via geometry with a certain perimeter U. The virtual radius r_{vir} of an EWT-via can be calculated from: $2\pi r_{vir} = U \rightarrow r_{vir} = U/2\pi$. Usually, the EWT-via diameter is much smaller than the EWT-via distance. Hence, the current flow is approximately radial toward rectangular or triangular EWT-vias that also exist after laser processing and etching [113]. On that condition, the following calculations hold for any type of EWT-via geometry.

EWT-via emitter series resistance

The EWT-via emitter exhibits a parallel and constant current flow (see vertical arrow in Fig. 4.1). The photogenerated current collected at the front pn-junction is transported through the EWT-via to the rear emitter. The EWT-via resistance can be considered as a lumped series resistance that is simply deduced from the geometrical device parameters [114]:

$$R_{em,via} \approx \frac{R_{sq} i_x d_y W}{U N_{via}}, \tag{4.6}$$

where R_{sq} is the emitter sheet resistance, W the EWT-via height (similar to the wafer thickness above the rear emitter), i_x the emitter index (distance between two vias perpendicular to the rear emitter fingers), d_y the EWT-via index (distance between two vias parallel to the rear emitter fingers) and U the perimeter of an EWT-via whose shape depends on the combination of laser-drilling and KOH-edging [113]. The product of i_x and d_y can be considered as the EWT unit area. If there are several EWT-vias in one EWT unit area, it is sensible to consider i_x and d_y as the edge lengths of a rectangle that comprises all EWT-vias with a certain number N_{via} in one unit cell [1].

Front emitter series resistances

Figure 4.4 depicts a schematic top view of an EWT solar cell. The current collected at the front *pn*-junction is transported through the front emitter. Due to its two-dimensional geometry, the current flow exhibits a distributed character.

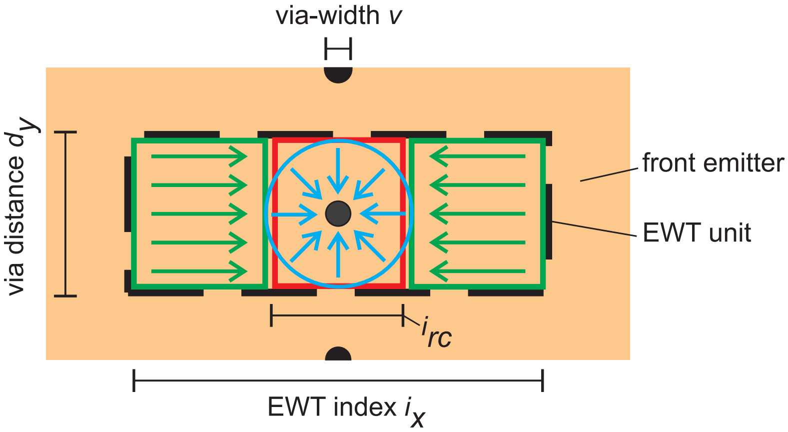

Figure 4.4: Top view of an EWT solar cell structure (not drawn to scale). The current transport in the front emitter can be approximated by a parallel (green arrows) and a radial partition (blue arrows). As a constraint, the area of the radial current flow (blue circle) equals the area of the red rectangle which is the EWT unit area (dashed rectangle) less the area of the parallel current.

In our series resistance model, this current transport is split into a radial partition near the EWT-via and into a parallel partition more distant to the EWT-via. The respective areas of the parallel or radial transport are indicated by two green rectangles ("1") or by a blue circle ("2") in Fig. 4.4, respectively. The diameter of the blue circle equals the distance of EWT-vias parallel to the rear emitter fingers and is denoted as d_y. As a constraint, the area of the radial current (blue circle) is the difference of the EWT unit area (dashed rectangle) and the area of the parallel current (both green rectangles). Figure 4.4 depicts this difference as a red rectangle which equals the area of the blue circle. Due to this constraint, the edge length of the red rectangle i_{rc} (perpendicular to the rear emitter fingers) can be deduced from the EWT-via distance and accounts for $i_{rc} = d_y\pi/4$ (see Fig. 4.4).

The ohmic power dissipation based on the parallel current transport in the front emitter is

---

[1] In this thesis, i_x and d_y are the distances between single EWT-vias in x- (perpendicular) and y-direction (parallel) referring to the pattern of the rear emitter and base fingers. There is no EWT device that features several EWT-vias in one unit cell. Hence, N_{via} is "1" in all calculations.

calculated from:

$$\begin{aligned} P_{em,par} &= \frac{R_{sq}}{d_y} \int\limits_{0}^{(i_x - d_y\pi/4)/2} (Jd_y x)^2 dx \\ &= \frac{J^2 d_y R_{sq}}{1536} \left(4i_x - d_y\pi\right)^3, \end{aligned} \tag{4.7}$$

where J is the photogenerated current density collected at the front pn-junction. Equation 4.7 only considers the loss in one of the two rectangles in Fig. 4.4. The series resistance $R_{em,par}$ of the parallel current transport in the front emitter is calculated from:

$$\begin{aligned} R_{em,par} &= P_{em,par} A/I^2 \\ &= \frac{R_{sq}}{192} (d_y\pi - 4i_x)^2 \\ &\text{with } A = d_y \left(\frac{i_x}{2} - \frac{d_y\pi}{8}\right) \text{ and } I = Jd_y \left(\frac{i_x}{2} - \frac{d_y\pi}{8}\right). \end{aligned} \tag{4.8}$$

The respective voltage drop along the parallel current transport in the front emitter is defined as:

$$\begin{aligned} V_{em,par} &= \frac{R_{sq}}{d_y} \int\limits_{0}^{(i_x - d_y\pi/4)/2} Jd_y x dx \\ &= \frac{JR_{sq}}{128} (d_y\pi - 4i_x)^2. \end{aligned} \tag{4.9}$$

$$\tag{4.10}$$

In order to calculate the ohmic power dissipation of the radial current transport, we consider a scenario of a current I_0 that is injected from the EWT-via emitter into the front emitter (blue circle in Fig. 4.4). In terms of power dissipation, there is no difference if a current is injected from the EWT-via into the front emitter or the inverse case of a current that is collected by the front emitter and subsequently transported to the EWT-via. The power dissipation of a current path that flows in radial direction from the small EWT-via emitter radius r_{via} to the large radius $d_y/2$ (radius of the blue circle in Fig. 4.4) and which decreases with a constant current density J is calculated from:

$$\begin{aligned} P_{em,rad} &= \frac{R_{sq}}{\alpha} \int\limits_{r_{via}}^{d_y/2} \left(I_0 - \frac{\alpha}{2\pi} J\pi r^2\right)^2 \frac{dr}{r} \\ &= R_{sq} \left[\frac{I_0^2}{\alpha} ln\left(\frac{d_y}{2r_{via}}\right) - \frac{I_0 J}{2}\left(\left(\frac{d_y}{2}\right)^2 - r_{via}^2\right) + \frac{J^2\alpha}{16}\left(\left(\frac{d_y}{2}\right)^4 - r_{via}^4\right)\right] \\ &\text{with } I_0 = \frac{\alpha}{2\pi} J(i_x d_y - \pi r_{via}^2), \end{aligned} \tag{4.11}$$

and with α the angle of the circle's sector in which the current is injected. In the present scenario, $\alpha = \pi$ in order to respect the current flow in a semi-circle, J is the photogenerated current density and I_0 the referring total current both collected at the front pn-junction. The resulting series resistance $R_{em,rad}$ along the radial current transport in the front emitter is calculated from:

$$\begin{aligned} R_{em,rad} =& P_{em,rad} A/I^2 \qquad (4.12)\\ =& \frac{R_{sq}}{256\alpha A}\left(\alpha\left(-32A\left(d_y^2-4r_{via}^2\right)+\alpha\left(d_y^4-16r_{via}^4\right)\right)+256A^2 ln\left(\frac{d_y r_{via}}{2}\right)\right)\\ &\text{with } A=\frac{1}{2\pi}\left(i_x d_y-\pi r_{via}^2\right),\ I=JA, \text{ and } \alpha=\pi. \qquad (4.13)\end{aligned}$$

The voltage drop along the radial current transport in the front emitter is calculated from:

$$\begin{aligned} V_{em,rad} =& \frac{R_{sq}}{\alpha}\int_{r_{via}}^{d_y/2}\left(I_0+\frac{\alpha}{2\pi}J\pi\left(r_{via}^2-r^2\right)\right)\frac{dr}{r}\\ =& R_{sq}\left[\left(\frac{I_0}{\pi}+\frac{J}{2}r_{via}^2\right)\left(ln(d_y/2)-ln(r_{via})\right)-\frac{J}{2}\left((d_y/2)^2-r_{via}^2\right)\right]\\ &\text{with } \alpha=\pi \text{ and } I_0=\frac{J}{2}\left(i_x d_y-\pi r_{via}^2\right). \qquad (4.14)\end{aligned}$$

Base series resistance in the scenario of base point contacts

The current transport inside the base is of a three-dimensionally distributed nature. Figure 4.5 depicts a side-view of a semi-EWT structure with the rear emitter at the right hand side and the base area at the left hand side. Photogenerated majority carriers in the base exhibit long transport paths until the reach the base contacts situated in the lower left corner.

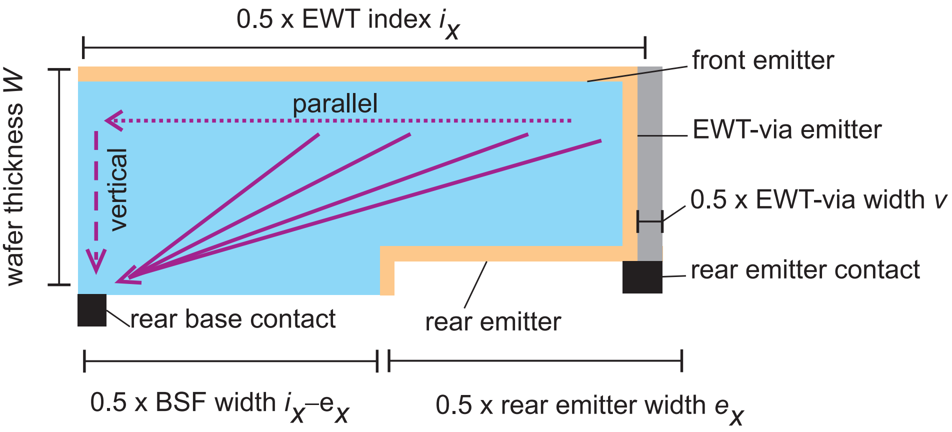

Figure 4.5: Side view of a semi-EWT structure featuring (laser fired) point contacts (not drawn to scale). Photogenerated majority carriers in the base exhibit long transport paths (solid lines) until they reach the rear base contacts. The current transport in the base can be approximated by a parallel (dotted arrow) and a vertical component (dashed arrow).

In the following model, we split the current transport into a component parallel to the front surface and into a vertical component which is perpendicular to the front and rear surface (see Fig. 4.5). Furthermore, we assume both components to be independent from each other. Three expressions for the base series resistance can be deduced.

In the scenario of a vertical current transport inside the base, the base series resistance is calculated from [55]:

$$R_{base,ver}^{LFC} = \rho W, \qquad (4.15)$$

where ρ denotes the wafer resistivity and W the wafer thickness. The referring voltage drop between the front and rear side is defined as:

$$V^{LFC}_{base,ver} = \rho W J, \tag{4.16}$$

with J the current density. In this thesis, EWT devices are discussed that feature base point contacts fabricated by laser power. The single point contacts exhibit a certain radius and distance to each other. Both values are used as free parameters in the following discussion. In the present scenario, a line of point contacts is formed at the base area.

We assume the point contacts to be parallel to the base and emitter fingers at the rear side of the device. Hence, the scenario is very similar to those of the front emitter which exhibits the EWT-via emitter as a "point contact". In order to calculate the single R_s contributions of the parallel current transport inside the base, we consider the similar model of a parallel and a radial current as used to describe the current transport in the front emitter. The referring variables of the front emitter (EWT-via distance, radius, etc.) are exchanged by those of the LFC geometry.

More distant to the LFC contacts, we assume a current flow which is parallel to the front side. The series resistance contribution of the parallel current transport inside the base is calculated from:

$$R^{LFC}_{base,par} = \frac{\rho}{192W}(d_{LFC}\pi - 4i_x)^2, \tag{4.17}$$

where d_{LFC} denotes the distance between single LFC point contacts and i_x the EWT-index. The voltage drop due to the parallel current transport inside the base is defined as:

$$V^{LFC}_{base,par} = \frac{J\rho}{128W}(d_{LFC}\pi - 4i_x)^2. \tag{4.18}$$

The series resistance contribution of the radial current transport around the laser fired point contacts is calculated from:

$$\begin{aligned} R^{LFC}_{base,rad} = & \frac{\rho\left(\alpha\left(d^2_{LFC} - 4r^2_{LFC}\right)\left(\alpha d^2_{LFC} - 16 d_{LFC} i_x + 4\alpha r^2_{LFC} + 16\pi r^2_{LFC}\right)\right)}{128 W_{current}\alpha\left(d_{LFC} i_x - \pi r^2_{LFC}\right)} \\ & + \frac{\rho\left(64\left(d_{LFC} i_x - \pi r^2_{LFC}\right)^2 ln\left(\frac{d_{LFC}}{2}\right) - 64\left(d_{LFC} i_x - \pi r^2_{LFC}\right)^2 ln\left(r_{LFC}\right)\right)}{128 W_{current}\alpha\left(d_{LFC} i_x - \pi r^2_{LFC}\right)}, \end{aligned} \tag{4.19}$$

where r_{LFC} is the radius of a single LFC and $W_{current}$ is the height of the current flow around the LFC. In this scenario, $W_{current}$ is introduced in order to describe the current crowding around the base point contacts. Note that Eq. 4.19 would underestimate the real value of the radial series resistance, if the real wafer thickness W were used.

In the front emitter, the current flow of majority carriers fills the total emitter volume. Hence, the total conductance (= inverse resistance) of the highly doped emitter layer is used for the current transport. For this reason, the emitter sheet resistance R_{sq} can be applied to calculate the resistance of the radial current path in the front emitter (see Eq. 4.13).

In the scenario of base point contacts, the current around these contacts only fills a small volume of the solar cell base. This effect can be understood as a current crowding: the current is focused in a smaller volume or area. Hence, there are increased local current densities which are transported in a small part of the base volume. Hence, it is **not** the entire base conductivity that contributes to this current transport but only a small portion of it. The referring height $W_{current}$ of the current transport above the LFC is smaller than the wafer thickness W. As a result, the effective sheet resistance of the base around the LFC contacts is increased: $R_{sq}(around\ LFC) \approx \frac{\rho}{W_{current}} > \frac{\rho}{W} = R_{sq}(base)$, where ρ is the wafer resistivity. This effect can be understood as a current crowding around the point contacts. In order to calculate $R^{LFC}_{base,rad}$, two- or three-dimensional device simulations can be applied to investigate the current flow that fills the thickness $W_{current}$ above the LFC. Alternatively, the sum of all calculated series resistances of the single device components except $R^{LFC}_{base,rad}$ can be subtracted from the measured device series resistance. Then, the difference is mainly due to the contact resistances and the radial current transport around the LFC. Finally, the calculated R_s difference can be used to adjust $W_{current}$ in Eq. 4.19 and to estimate the effect of the current crowding around the LFC. This point is taken into account when solar cell results are discussed.

The calculation of the voltage drop along the radial transport path around the LFC is also based on a similar model as the scenario of the radial current transport in the front emitter (see 4.14):

$$\begin{aligned} V^{LFC}_{base,rad} &= \frac{\rho}{W_{current}\alpha} \int\limits_{r_{LFC}}^{d_{LFC}/2} \left(I_0 + \frac{\alpha}{2\pi} J\pi \left(r^2_{LFC} - r^2\right)\right) \frac{dr}{r} \\ &= \frac{\rho}{W_{current}} \left[\left(\frac{I_0}{\pi} + \frac{J}{2} r^2_{LFC}\right) \left(ln(d_{LFC}/2) - ln(r_{LFC})\right) - \frac{J}{2} \left(\left(d_{LFC}/2\right)^2 - r^2_{LFC}\right)\right] \\ &\text{with } \alpha = \pi \text{ and } I_0 = \frac{J}{2} \left(i_x d_{LFC} - \pi r^2_{LFC}\right), \end{aligned} \tag{4.20}$$

where I_0 denotes the initial current that is injected from the LFC into the base. Similar to the front emitter scenario, only one half of the area of the radial current transport is considered in order to calculate the injected current. Again, Eq. 4.20 will slightly underestimate the real voltage drop due to the current crowding effect around the LFC.

Base series resistance in the scenario of a full area back surface field

The aim of a back surface field (BSF) integration is the reduction of resistive losses of majority carriers. In the scenario of a *p*-type (*n*-type) semiconductor, a BSF is a highly *p*- (*n*-) conductive layer at the rear side that offers a lower resistance than the solar cell substrate. Usually, a BSF adjoins the rear metal contacts at the base. Photogenerated majority carriers are preferably transported inside the BSF toward the base contacts. The sheet resistance of the BSF should be smaller than those of the wafer substrate in order to profit from an increased device conductivity.

Figure 4.6 depicts a semi-EWT structure featuring a BSF that covers the total base area. Compared to the LFC scenario in Fig. 4.5, the current transport of majority carriers in the base is modified due to the high conductivity of the BSF. As mentioned above, we anticipate the knowledge of the current trajectories that are calculated by means of a three-dimensional numerical EWT model. The depicted current trajectories in Fig. 4.6 simplify the real nature. The goal is an estimation of the impact of single EWT device component resistances on the *I*-*V*-curve and the *FF*. This is achieved by the simplified model presented in the following.

Above the rear emitter (right hand side in Fig. 4.6), we assume a transport of majority carriers parallel to the front side. The current flows to the left toward the rear base contacts.

Above the base region (left hand side in Fig. 4.6), the majority carrier current is vertically transported toward the BSF. Furthermore, we assume this current transport to be parallel.

All the photogenerated majority carriers are collected by the BSF. This holds for the parallel and the vertical current components (referring to the front surface) in the right and left hand side of Fig. 4.6, respectively.

A BSF is a highly conductive device component that offers a lower resistance than the solar cell substrate. Photogenerated majority carriers are preferably transported inside the BSF. Similar to the scenario in the front emitter, the current transport in the BSF can be split into a parallel component more distant to the contacts and into a radial component around the rear base contacts.

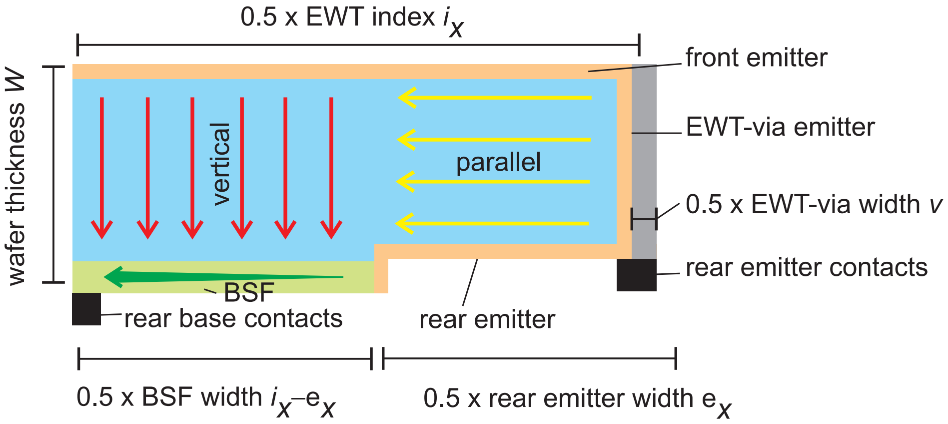

Figure 4.6: Side view of a semi-EWT structure featuring a full area back surface field at the base region. In the base above the rear emitter, we assume a current flow which is parallel to the front side (yellow arrows). The current transport in the base above the BSF is approximately vertical toward the rear side (red arrows). All the photogenerated majority carriers in the base are collected by the BSF and transported toward the rear base contacts (green arrow).

For simplicity, we assume a current inside the BSF which is exclusively transported parallel to the rear base contacts. The radial component is neglected. This approximation holds for small distances between the base contacts and for low sheet resistances of the BSF. Assuming both conditions, the radial current transport around the point contacts suffers from very low resistive losses. This scenario holds for all solar cells featuring a BSF in this thesis.

First, we derive the ohmic power dissipation of the current transport inside the base above the rear emitter. This current component is parallel to the front surface:

$$\begin{aligned} P_{base,par}^{BSF} &= \frac{\rho}{d_y W} \int_0^{e_x/2} (J d_y x)^2 \, dx \\ &= \frac{J^2 \rho d_y e_x^3}{24W}, \end{aligned} \tag{4.21}$$

with e_x the rear emitter width, d_y the EWT-via distance, W the wafer thickness, ρ the wafer resistivity and J the current density of photogenerated majority carriers. The series resistance $R_{base,par}^{BSF}$ in the parallel current path inside the base is calculated from:

$$\begin{aligned} R_{base,par}^{BSF} &= P_{base,par}^{BSF} A / I^2 \\ &= \frac{\rho e_x^2}{12W} \\ &\text{with } I = \frac{J d_y e_x}{2} \text{ and } A = \frac{d_y e_x}{2}, \end{aligned} \tag{4.22}$$

where A denotes the semi-area of a BSF. The voltage drop $V_{base,par}^{BSF}$ along the referring current path accounts for:

$$\begin{aligned} V_{base,par}^{BSF} &= \frac{\rho}{W d_y} \int\limits_0^{e_x/2} J d_y x dx \\ &= \frac{J \rho e_x^2}{8W}. \end{aligned} \tag{4.23}$$

The series resistance $R_{base,ver}^{BSF}$ along the vertical current transport inside the base above the BSF (left hand side in Fig. 4.6) has a similar form than Eq. 4.15:

$$R_{base,ver}^{BSF} = \rho W, \tag{4.24}$$

where ρ denotes the wafer resistivity and W the wafer thickness. The referring voltage drop between the front and rear side is defined as:

$$V_{base,ver}^{BSF} = \rho W J. \tag{4.25}$$

In the present model, we assume that the parallel current above the rear emitter flows into the BSF. Furthermore, we assume that this current is not focused into a smaller device volume near the BSF but virtually collected by the base cross section as depicted in Fig. 4.6. In a real device, the respective position at which the current is focused into the BSF is the base volume above the *pn*-junction between the rear emitter and the BSF. Here, the "real" current density is increased which leads to higher resistive losses and voltage drops compared to those in present model. However, the present estimation holds since the base current is not focused into a small area, as it is the case for the base point contacts, but into the large BSF. Hence, current crowding is not as detrimental as it is in the scenario of point contacts.

In order to calculate the ohmic power dissipation $P_{BSF,par}^{BSF}$ of the current inside the BSF, we assume the total parallel and vertical current component to be collected by this highly diffused layer:

$$\begin{aligned} P_{BSF,par}^{BSF} &= \frac{R_{sq}}{d_y} \int\limits_0^{(i_x - e_x)/2} \left(J d_y \frac{e_x}{2} + J d_y x \right)^2 dx \\ &= \frac{J^2 R_{sq} d_y}{24} \left(i_x^3 - e_x^3 \right). \end{aligned} \tag{4.26}$$

The series resistance of the BSF is calculated from:

$$\begin{aligned} R_{BSF,par}^{BSF} &= P_{BSF,par}^{BSF} A / I^2 \\ &= \frac{R_{sq} \left(i_x^2 - e_x^3 \right)}{12 i_x} \\ &\text{with } I = J d_y \frac{i_x}{2} \text{ and } A = \frac{i_x}{2} d_y. \end{aligned} \tag{4.27}$$

The voltage drop along the BSF field is defined as:

$$\begin{aligned} V_{BSF,par}^{BSF} &= \frac{R_{sq}}{d_y} \int\limits_0^{(i_x - e_x)/2} \left(J d_y \frac{e_x}{2} + J d_y x \right) dx \\ &= \frac{J R_{sq}}{8} \left(i_x^2 - e_x^2 \right) . \end{aligned} \tag{4.28}$$

4.4 Numerical EWT device modeling

Beside the application of diode networks that calculate the I-V-curve of EWT solar cells, numerical device models have been designed in order to understand the loss mechanisms of EWT devices. An often used software for device modeling is PC1D that only respects a one-dimensional current transport. In 2003, the first approach of a more-dimensional (two-dimensional) EWT model is introduced by Dicker in Ref. [114]. In 2009, Hilali used a two-dimensional model to investigate multicrystalline EWT solar cells [115].

4.4.1 One-dimensional numerical EWT-model designed by means of PC1D

PC1D is a one-dimensional numerical device simulator that solves the fully coupled set of non-linear, partial van Roosbroeck differential equations of second order [116] numerically and self-consistently [105]. PC1D has been applied by various solar cell developers in order to model emitter-wrap-through solar cells [114, 117, 118, 113].

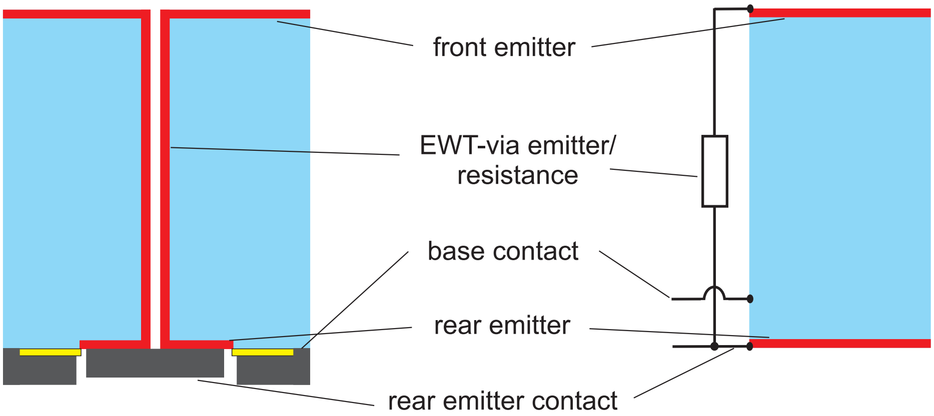

Figure 4.7: Cross-sectional view of an EWT-solar cell (left) and corresponding PC1D simulation model (right).

Figure 4.7 illustrates a schematic cross section of an EWT device and the corresponding PC1D model. The one-dimensional model features a front and rear emitter both connected by a series resistance. The model respects the both-sided minority carrier collection and the EWT-via resistance. As a disadvantage, the lateral transport of carriers in the front and rear emitter, as well as in the base region is not included. These current paths can exhibit large series resistances and are critical in terms of FF-losses. In the PC1D model, the EWT-via resistance $R_{em,via}$ is the only critical EWT-parameter in terms of FF-losses. The one-dimensional model qualitatively calculates the internal current transport and the FF-loss mechanism of EWT solar cells. However, PC1D only reproduces low EWT-FF for very high $R_{em,via}$ which are untypical for real devices [118]. The referring results are presented in Chapter 5.

4.4.2 Three-dimensional numerical EWT-model

In order to analyze EWT devices by a more-dimensional numerical model in this thesis, the fully coupled semiconductor equations [116] are numerically solved in the drift-diffusion approximation in three dimensions with the software SENTAURUS [119] running eight threads on a dual-core linux server with 16 GB RAM. The physical models and input parameters are listed and referenced in Tab. 4.1. In contrast to many binary logic devices, the current-densities of EWT-solar cells need to be modeled with high precision, and the effective intrinsic carrier density [62, 120] strongly influences device behavior (in contrast to majority carrier devices), etc.

A unit cell of the EWT design is shown in Fig. 4.8. The expression "unit cell" implies the possibility to pursue the structure in space by sliding the unit parallel (perpendicular) to the EWT-vias. The length of the translation vector corresponds to the EWT-via distance d_y (i_x). The unit cell itself comprises the three-dimensional simulation domain (upper left quarter in Fig. 4.8) which can be pursued in space by mirroring the structure at the edges. It includes all recombination mechanisms and internal current transports. Lateral currents within the Al finger contacts along the metalized rear side of the solar cell are not considered. The simulation domain is discretized by applying the finite-difference method. Furthermore, the pyramidally etched front surface is approximated using a planar geometry. The electronic properties can be closely approximated to the real conditions as explained in Refs. [121] and [122]. A texturized front emitter features extended current paths compared to a planar emitter. The relation of the area cross section of a textured and planar diffused surfaces are similar to the extension factor of the current paths. For this reason, the sheet resistances are similar in both scenarios. However, textured surfaces are larger and surface recombination velocities must be adjusted to obtain similar magnitudes compared to planar emitters [123]. In the optical model, the effects of pyramids are fully included by using the 3D Monte Carlo ray tracer SUNRAYS [124]. The photogenerated current-densities J_{gen} of the solar cells are numerically simulated using the am1.5g solar spectrum [101], the silicon absorption data from Ref. [125] and in-house ellipsometric measurements of the refractive indices and extinction coefficients of the SiN antireflection layer. In this way, the measured front reflectance spectrum is reproduced.

Table 4.1: Models and parameters used in the numerical model.

Temperature	300 K
Carrier statistics	Fermi
Intrinsic carrier density	9.65×10^{9} cm^{-3} [62]
Band gap narrowing	Schenk's model [120]
SRH recombination-bulk	Eqs. 3.20
Surface	SiN- and SiO$_2$-specific model [122, 126]
Auger recombination	Coulomb-enhanced model [70]
Radiative recombination	Coulomb-enhanced model [76, 75]
Carrier mobility	Klaassen's model [127]
Si/metal contact Resistance	1 mΩcm^{2}
Illumination spectrum	Most recent am1.5gstandard [101]
Si band-band Absorption	Green's compilation of 2008 [125]

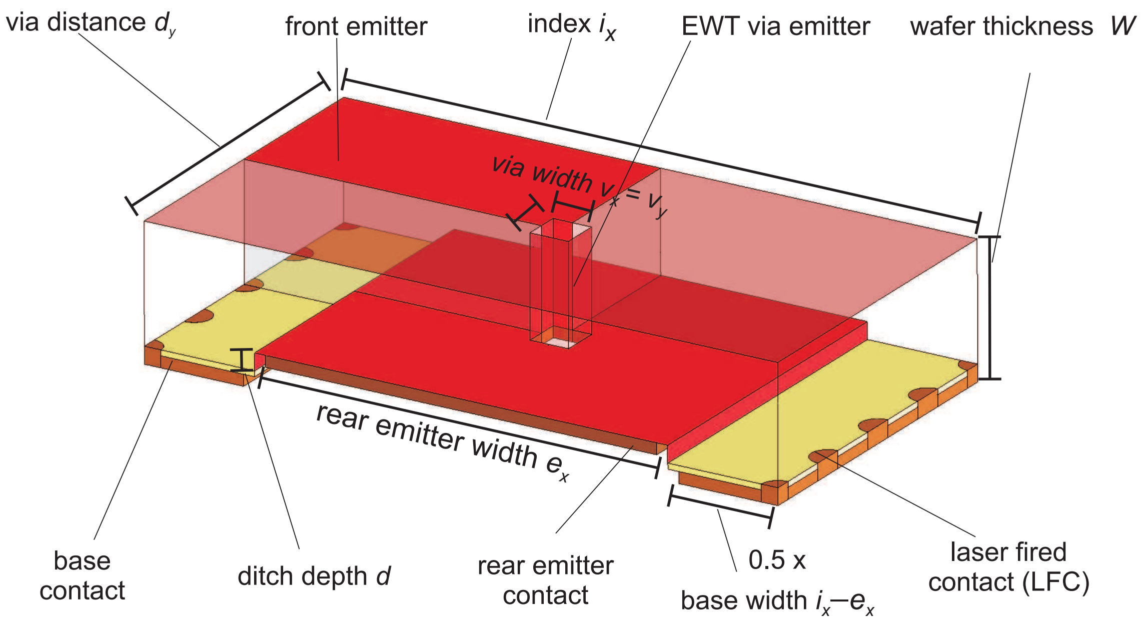

Figure 4.8: Unit of an EWT solar cell (not drawn to scale). The three-dimensional simulation domain of the EWT model used in this thesis comprises one quarter of this unit and is indicated by the non-translucent front emitter (upper left).

5 Didactical approach to EWT solar cells: One-dimensional model

5.1 Motivation

EWT solar cells are three-dimensional device structures. Their performance is influenced by a variety of three-dimensional effects such as lateral current transports of majority and minority carriers. With the following one-dimensional simulations, it is not claimed to precisely reproduce the three-dimensional devices. Instead, a one-dimensional model is beneficial for understanding the principles of EWT solar cell physics.

The front and rear emitters of EWT solar cells are connected by an EWT-via emitter. The uniqueness of this cell design is the existence of two possible current paths for the photogenerated minority carriers to the rear emitter contacts: either photogenerated carriers are transported as minority carriers through the base where they suffer recombination losses, or they are transported as majority carriers through the front and EWT-via emitter where they suffer resistive losses.

In particular, the basic interaction between the front and the rear emitter, both connected by an EWT-via resistance, can be described by one-dimensional device modeling. Furthermore, the model provides an insight into the voltage dependent minority carrier transport, which is one of the basic essentials to understand EWT solar cells. In previous literature, one-dimensional simulation of EWT cells focused on the impact of the EWT-via resistance on the I-Vcurve parameters [114]. The dependencies of V_{oc}, J_{sc} and FF on the EWT-via resistance were interpreted as simple resistive losses and neglected recombination effects.

In this chapter, one-dimensional simulations show that the FF behavior in EWT structures is influenced by resistive and recombination losses, both induced by the EWT-via emitter resistance. Furthermore, the impact of injection dependent bulk lifetimes on J_{sc}, MPP and V_{oc} is discussed since the good J_{sc}-current collection of EWT devices has raised the expectation for high-efficient mass-produced multicrystalline silicon (mc-Si) with relatively low carrier lifetimes [46]. This chapter is based on my publication in Ref. [118].

5.2 Experimental results of EWT cells

Despite the seemingly obvious advantages, EWT solar cells have at present not entered the stage of industrial mass production. This can be associated with the rather modest performance of EWT solar cells made from multicrystalline Si wafers. Such cells exhibit rather low efficiencies compared to their J_{sc}-V_{oc}-product [41, 128]. Thus it can be concluded that the fill factor (FF) of EWT solar cells is hampering the high performance [50] that is to be achieved for industrial mass production. Table 5.1 reports I-V-curve parameters of EWT solar cells under illumination where the bus bar regions have been shaded. This eliminates busbar-related series resistance effects which are particularly pronounced for non-optimized (relatively wide) busbars. The wafer resistivity is 1.5 Ωcm for the p-type mc-Si and the float-zone Si (FZ-Si) EWT solar cell.

Table 5.1: Measured parameters of the I-V-characteristics of two cells fabricated on 1.5 Ωcm mc- and FZ-Si under standard conditions (halogen lamp approximating the am1.5g spectrum, temperature=25°C).

wafer substrate	V_{oc} (mV)	J_{sc} (mA/cm^2)	FF (%)	η (%)	n_{MPP}
mc-Si	612	37	71.8	16.3	1.5
FZ-Si	627	39.2	75.5	18.6	1.25

Both devices are fabricated by the author of this thesis at the Institute of Solar Energy Research Hamelin (ISFH). The referring fabrication sequence is depicted in Fig. 6.1 and explained in the next chapter.

Injection dependent carrier lifetimes can cause effects on the fill factor [129]. In this specific case, the fill factor is reduced compared to the case of injection independent lifetimes if the lifetime decreases when going from higher carrier injection densities (i.e. V_{oc}-conditions) toward lower injection densities (maximum power voltage V_{mpp} and J_{sc}). Beside the effect of injection dependent-bulk lifetimes, EWT solar cells exhibit additional FF-losses that are lent on the device structure. A good indicator for fill factor losses is an ideality factor greater than unity. Formula 3.36 provides an expression of the ideality factor for a given ("local") position in the I-V-curve. We shall from hereon refer to this value as the "local ideality factor" in order to emphasize the voltage dependency of this quantity. Because the FF losses are caused by injection effects, their influence is quantified on the I-V-curve with the local ideality factor (see Eq. 3.36). The present analysis highlights the local ideality factor around MPP (n_{MPP}) in order to discuss its impact on the simulated I-V-curves.

5.3 Device model and simulation parameters

The device analysis is performed by means of the one-dimensional numerical device simulator PC1D [105]. The front and rear emitters are connected by an external resistance [114] which corresponds to the EWT-via resistance $R_{em,via}$ along the laser drilled and phosphorus diffused vias. The resistance of the EWT-via ($R_{em,via}$) depends on the device geometry and can be expressed by Eq. 4.6. Figure 4.7 illustrates a schematic cross section of an EWT solar cell and the corresponding PC1D model.

A reduction of $R_{em,via}$ is achieved by:

- reducing the EWT-via emitter sheet resistance R_{sq}, e.g. by a stronger phosphorus diffusion.
- using thinner wafers. Note, thin wafers with W<130 µm tend to break easily due to wafer handling. Today, silicon wafers with a thickness of 160 µm to 200 µm are commonly used in silicon wafer based photovoltaics.
- reducing the EWT unit area. This approach results in a higher EWT-via number per square centimeter.
- drilling more than one EWT-via per EWT unit area. This approach is related to a reduction of the EWT unit area. It results in increased process times for the laser drilling [39].
- processing wider EWT-vias by an increased etching time in KOH solution after laser drilling. However, the etching time in KOH solution is limited by the etching mask that defines the emitter and base regions at the rear side. The etching mask is not completely resistant against the etching solution but has a certain etching rate. Commonly applied etching times are about 15 min [36].

In mc-Si, the most abundant contaminant is iron that generates defects in the band gap and limits the cell efficiency [130]. Interstitial iron is effectively gettered by phosphorus diffusions in the highly diffused layer [131, 132]. However, iron-decorated defects are less effectively gettered and cause low bulk carrier lifetimes even after phosphorus gettering [133]. At elevated temperatures (T>400°C), the mobility of interstitial iron atoms is increased. Crystallographic defects can capture the atoms since they offer a lower energy sink than the interstitial position between atoms in the silicon crystal [134]. This can result in lower bulk lifetimes in area featuring a high density of crystallographic defects after the gettering process [133]. In the present simulation campaign, the recombination activity of iron-defect levels is approximated by choosing the Shockley-Read-Hall

(SRH) recombination parameters of interstitial iron [19, 135, 136]. The recombination at 2×10^{11} cm^{-3} interstitial iron atoms (typical value for boron-doped as-grown mc-Si) is modeled by setting the SRH recombination parameters to τ_n=10 µs, τ_p=7000 µs, and E_t-E_i=−0.182 eV, resulting in a strongly injection-dependent lifetime. As a reference, a "no iron" scenario is considered where the lifetime shows only small injection dependence. Here, τ_n=τ_p=380 µs and E_t-E_i=−0.182 eV is chosen to obtain the same V_{oc} as in the iron-dominated scenario. Figure 5.1 shows the resulting SRH lifetimes of both parameter settings as a function of the excess carrier density and the respective injection levels at J_{sc}, *MPP* and V_{oc}.

At J_{sc}, the local excess carrier density is mainly determined by the local photogeneration rates and current transports. The local current densities of electrons are defined by the product of local conductivity σ and the gradient of the electron quasi-Fermi level (QFL) (see Eq. 3.11). At the *pn*-junction, photogenerated minority carriers are driven by a large QFL gradient that results in a strong current transport and a low carrier density. More distant to the *pn*-junction, QFL gradients are smaller, the minority carrier transport is reduced and the local excess carrier density is higher. The locally differing gradients of QFL at J_{sc}-conditions are responsible for a wide injection range of excess carriers at J_{sc} conditions in Fig. 5.1. Note that the x-axis is plotted in a logarithmic scale.

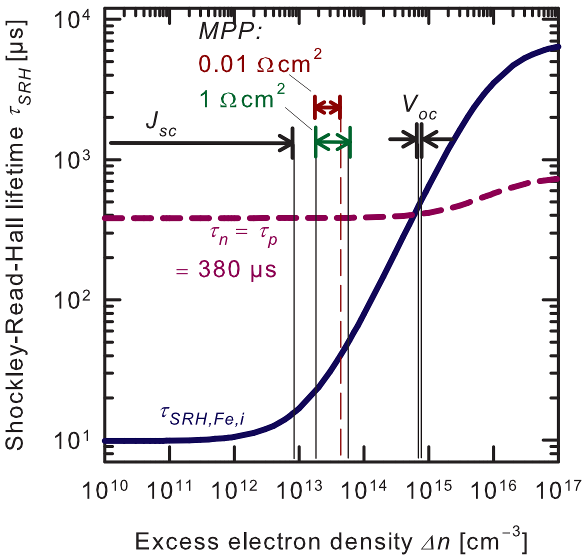

Figure 5.1: Injection-dependent SRH lifetime in 1.47 Ωcm *p*-type Si with an interstitial iron concentration of 2×10^{11} cm^{-3} and the reference scenario with τ_n= τ_p=380 µs. The injection ranges at J_{sc}, *MPP* and V_{oc} of both PC1D EWT simulation scenarios with $R_{em,via}$=0.01 Ωcm^2 and $R_{em,via}$=1 Ωcm^2 are indicated by arrow scales. The injection range at *MPP* is a function of the EWT-via resistance and differs for $R_{em,via}$=1 and 0.01 Ωcm^2. The injection ranges at J_{sc} and V_{oc} do not depend notably on the respective $R_{em,via}$.

At *MPP*, the carrier injection across the *pn*-junction and the excess carrier density in the base are increased compared to J_{sc}-conditions. The existing QFL gradients still drives the current transport. However, the absolute magnitude of the gradients decreases leading to a more narrow injection range of excess carriers.

At V_{oc}, the local carrier density is determined by the carrier injection across the *pn*-junction and the local photogeneration rate. QFL gradients converge to zero which leads to a more narrow injection range compared to the J_{sc}- and *MPP*-scenarios.

Note, at *MPP*, the range of the injection level within the base is larger for increased EWT-via resistances. In contrast to *MPP*, the injection ranges at short-circuit and open-circuit conditions are not affected by the EWT-via resistance, as will be explained in the following sections.

Realistic EWT-via resistances of fabricated EWT solar cells account for a range from 0.01 to 2 Ωcm^2 for EWT-via emitter sheet resistances between 8 and 200 Ω/□ depending on the geometry of the EWT-via as explained by Eq. 4.6 [114]. In the following discussions, this range is called "practical $R_{em,via}$ range". Common values for $R_{em,via}$ are about 0.2 Ωcm^2.

In the following simulations, the I-V-curve parameters are discussed as a function of the via resistance in the range between 10^{-3} and 10^4 Ωcm^2. A detailed analysis of the transport mechanism and the influence on V_{oc}, J_{sc} and FF is done by setting two representative values for $R_{em,via}$:

- $R_{em,via}$=0.01 Ωcm^2: This small value corresponds to a low level that that can be practically realized by phosphorus emitter diffusions with low sheet resistances. $R_{em,via}$=0.01 Ωcm^2 acts as reference and can be achieved by the exemplary EWT device parameters: R_{sq}=8 Ω/□, W=200 µm, v_x=75 µm, i_x=1000 µm and d_y=200 µm. In this scenario, the resulting number of EWT-vias per square centimeter is 500.

- $R_{em,via}$=1 Ωcm^2: This high value refers to an EWT device featuring weakly diffused EWT-vias and a strongly increased EWT-via distance d_y. It can be achieved by the following exemplary device parameters: R_{sq}=150 Ω/□, W=200µm, v_x=75 µm, i_x=1000 µm and d_y= 1000 µm. In this scenario, the resulting number of vias per square centimeter is 100.

The device modeling neglects lumped base or emitter series resistances. For the remaining simulation parameters see Tab. 5.2. Three dimensional device simulations that take into account lateral transport phenomenons such as resistive lateral base and emitter current flows are presented in the next chapters and will offer a more detailed analysis.

Table 5.2: PC1D simulation parameters.

Device parameters	Settings
wafer	200 µm thick, p-type, 1.47 Ωcm
emitter diffusion	phosphorus, 42 Ω/□, N_{peak}=3×10^{20} cm^{-3}, depth=350 nm, error function profile
surface recombination	neglected
material parameters	PC1D standard model for silicon
optical generation	PC1D standard model, AM1.5G spectrum

5.4 One-dimensional simulation results

Table 5.3 gives an overview of simulation results of the iron and "no iron" scenarios with $R_{em,via}$=1 and 0.01 Ωcm^2, respectively. The I-V-curve parameters are discussed separately in the following sections as a function of the bulk lifetime and $R_{em,via}$.

Table 5.3: PC1D simulation results of EWT solar cells.

$R_{em,via}$ (Ωcm^2)	τ_n, τ_p (µs)	J_{sc} mA/cm^2	V_{oc} (mV)	MPP (mV)	FF (%)	η (%)
0.01	380, 380 ("no iron")	40.9	642	561	83.4	21.9
1	380, 380 ("no iron")	40.9	641	548	80.1	21.2
0.01	10, 7000 (iron)	39.9	642	548	79.6	20.4
1	10, 7000 (iron)	39.9	641	534	77.4	19.8

5.4.1 Short-circuit current density

Figure 5.2 shows the simulated J_{sc} for both lifetime settings as a function of $R_{em,via}$ from 10^{-3} to 10^4 Ωcm^2. In the practical $R_{em,via}$ range, J_{sc} does not depend on the EWT-via resistance. At J_{sc}-conditions, the electron quasi-Fermi-level ($E_{F,n}$) in the solar cell base do not differ for $R_{em,via}$=1 Ωcm^2 and $R_{em,via}$=0.01 Ωcm^2 (see Fig. 5.3 for x-values greater than 0.4 µm). However, the front emitter potential in the 1 Ωcm^2 scenario (x<0.4 µm in Fig. 5.3) is increased and accounts for 36 mV due to the voltage drop along the EWT-via resistance. At J_{sc}, the slightly increased injection of electrons from the front emitter into the base and the injection of holes from the base into the emitter, does not affect the short-circuit current densities of the solar cell. This is so because of the local diode recombination current J_{rec} that depends exponentially on the voltage V (see Eq. 3.35). The saturation current density of the emitter J_0,e accounts for 290 fA/cm^2. In the 1 Ωcm^2 scenario, the resulting recombination current density of 1.1×10^{-9} mA/cm^2 is several magnitudes lower than the short-circuit current density.

The slope and magnitudes of both $E_{F,n}$ inside the base, and hence the referring gradients, are similar in both scenarios. Consequently, the spatial electron currents defined by the product of local conductivity σ and the gradient of $E_{F,n}$ are similar for both simulation settings, too.

Electrons diffuse from the point of highest electron concentration (point of the highest $E_{F,n}$ in Fig. 5.3), to both the front and the rear *pn*-junction along the gradients of the respective QFL. We define this point as demarcation point since it divides the electron transport in a front and rear collecting part. At short-circuit conditions, $E_{F,n}$ exhibits a strong gradient toward the front *pn*-junction with a demarcation point in a distance of 65 µm from the front of the cell (Fig. 5.3). The collected current density at the front *pn*-junction accounts for 36 mA/cm^2 and flows through the EWT-via emitter to the rear emitter contact. In the case of $R_{em,via}$=1 Ωcm^2, this leads to a voltage drop of 36 mV between front and rear emitter. In the case of $R_{em,via}$=0.01 Ωcm^2, this voltage drop accounts to a negligible 0.36 mV due to the lower resistance. As a consequence, the front emitter of the EWT cell operates at a higher potential than the rear emitter, with a pronounced potential difference for relatively large $R_{em,via}$ (shown in Fig. 5.3 for distances smaller than 0.4 µm).

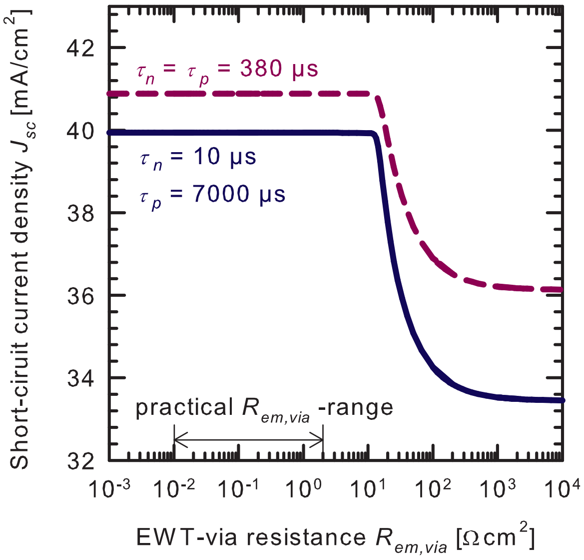

Figure 5.2: Simulated J_{sc} of the PC1D EWT structure in Fig. 4.7, as a function of $R_{em,via}$ with an interstitial iron concentration of $2{\times}10^{11}$ cm^{-3} and the reference scenario with τ_n=τ_p=380 µs. The practical $R_{em,via}$ range is indicated by arrows.

For voltage drops smaller than 520 mV between the front and rear emitter, recombination current densities remain below 1 mA/cm^2 (Eq. 3.35). Hence, there is no impact on J_{sc}. For voltage drops larger than 520 mV, which is the case for $R_{em,via}$>10 Ωcm^2 as shown in Fig. 5.2, the total recombination current density at the front pn-junction accounts for several mA/cm^2 and, hence, reduces J_{sc}. In practice, $R_{em,via}$>10 Ωcm^2 is not used for EWT solar cells since the gradient of $E_{F,n}$ flattens toward the front pn-junction and the EWT device starts converting to a back junction solar cell with floating emitter. Back junction devices put greater demands on bulk diffusion lengths and on the front side saturation current density [137].

Note, at higher externally applied voltages, the EWT-via resistance induces a potential distribution in the cell that causes recombination and a loss of extractable current. We will find in the subsequent paragraphs that this "resistance induced recombination" is also responsible for the low fill factors that are found in practice for EWT solar cells.

The absolute J_{sc}-difference between the iron-contaminated and the iron-free scenario in Fig. 5.2 is due to recombination losses in the bulk. At J_{sc}-conditions, the carrier density stays below 6×10^{12} cm^{-3}, as can be seen in Fig. 5.1. Consequently, the minority carrier lifetime in the iron-contaminated scenario is 15 µs and in the "no iron" scenario 380 µs (Fig. 5.1) with bulk diffusion length of 200 µm and 1020 µm, respectively. In both scenarios at J_{sc}-conditions, the demarcation point is situated at a distance of 65 µm to the front pn-junction. Electrons that are transported along the short current path to the front emitter suffer from low recombination losses that account for 0.36 mA/cm^2 and 0.01 mA/cm^2 in the iron and "no iron" scenario, respectively. Electrons that diffuse to the rear (with a current-density of 4 mA/cm^2) suffer from increased recombination losses along the 135 µm distance between the demarcation point and the rear pn-junction. These recombination losses are 0.62 mA/cm^2 in the iron and 0.03 mA/cm^2 in the "no iron" scenario. A conventional front junction solar cell would suffer higher recombination losses since the demarcation point is situated at the rear side of the cell. In this case, photogenerated electrons are forced to diffuse toward to the front pn-junction through the entire base, resulting in longer transport paths with increased recombination losses.

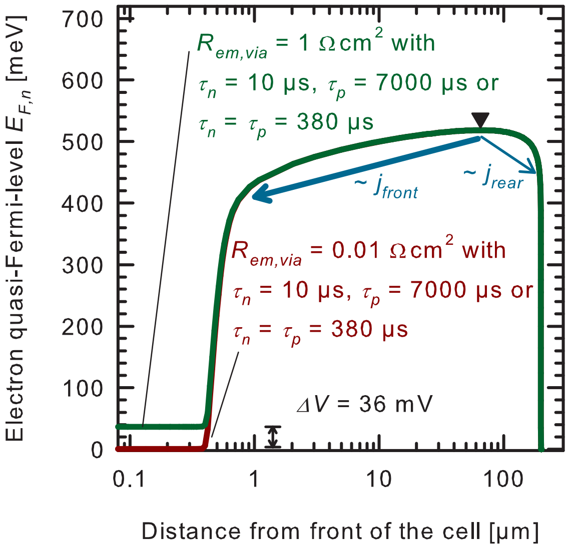

Figure 5.3: Simulated $E_{F,n}$ of the PC1D EWT structure in Fig. 4.7, with $R_{em,via}$=1 Ωcm^2 and $R_{em,via}$=0.01 Ωcm^2 at J_{sc}-conditions. Both simulation results hold for the iron- and "no iron" scenario, respectively. Departures of $E_{F,n}$ are caused by increased $R_{em,via}$. The demarcation point is marked as triangle.

The EWT cell behavior at short-circuit conditions is the main advantage over conventional front-junction cells: at short-circuit condition, the EWT cells undergo very low recombination losses, because the minority carriers are collected at both front and rear *pn*-junctions, which shortens their path-length to about half of the conventional cell. Hence, J_{sc} is less sensitive to low bulk lifetimes (low bulk diffusion lengths) e.g. in mc-Si wafers caused by iron- or chromium-decorated crystallographic defects [129, 22]. Furthermore, the absence of a front metalization grid eliminates shading losses.

5.4.2 Fill factor

Figure 5.4 compares the *FF* of the iron and "no iron" scenarios simulated with PC1D, both as a function of the EWT-via resistance.

EWT solar cells featuring EWT-via resistances in the practical range from 0.01 to 2 Ωcm^2 have slightly reduced *FF* values in this one-dimensional simulation study shown in Fig. 5.4. As an example, the reduction in *FF* for $R_{em,via}$=0.2 Ωcm^2 is 0.4 % absolute compared to the scenario with $R_{em,via}$=0 Ωcm^2.[1]

Figure 5.5 depicts the electron density profiles in the base, for the iron-free scenario with $R_{em,via}$=0.01 and 1 Ωcm^2 at two external voltages of 500 mV and 590 mV. A similar situation holds for the iron-contaminated scenario, and therefore is not shown here. The demarcation points of each electron density distribution are marked as black triangles. Increased EWT-via resistances shift the demarcation point toward the front *pn*-junction (compare both scenarios in Fig. 5.5 for $R_{em,via}$=1 Ωcm^2 and $R_{em,via}$=0.01 Ωcm^2 at V_{ext}= 500 mV). The recombination loaded current path for minority carriers through the base toward the rear *pn*-junction is extended, the minority carrier density is increased in the 1 Ωcm^2-scenarion. This effect leads to higher recombination losses. At higher external voltages (V_{ext}=590 mV in Fig. 5.5), the demarcation area is close to the front *pn*-junction and the carrier density is still increased. Minority carriers are forced to diffuse through the entire bulk to the rear emitter. They suffer enhanced recombination losses compared to the scenario with low $R_{em,via}$= 0.01 Ωcm^2. Consequently, increased EWT-via resistances increase the carrier density and force minority carriers to diffuse through the base and enhances bulk recombination losses at and beyond the maximum power point.

In the following analysis, recombination losses are separately quantified in the volume before the demarcation point ("front diode") and the volume behind the demarcation point ("rear diode"). These recombination losses are multiplied by the unit charge to obtain units of electric current. These currents are shifted by the respective recombination currents at V_{ext}= 0mV in order to calculate the local ideality factors which are used to analyse the *I*-*V*-curve (see explanation on page 19, Eq. 3.48).

In the iron-free scenario with nearly perfect via resistance ($R_{em,via}$=0.01 Ωcm^2), the front and rear emitters are connected to each other without notable resistive losses. Hence, both diodes operate at the same bias in the whole range between short and open-circuit (Fig. 5.7(a)). This has the following consequences:

- The demarcation line hardly moves in the entire injection range (see Fig. 5.5). As a result, the partitions of front and rear collecting electrons are constant. Figure 5.6 depicts the electron diffusion currents to the front and rear emitters between 400 mV and V_{oc}. For very low via resistances ($R_{em,via}$= 0.01 Ωcm^2) the internal current transport is stable and hardly varies for increasing external voltages.

---

[1] Note that the 1d- simulation campaign does not consider lateral current transports in the front emitter or in the bulk. Three-dimensional simulation results in the following chapters give a more detailed analysis considering further critical parameters, e.g. the base doping density, which are not discussed in this context.

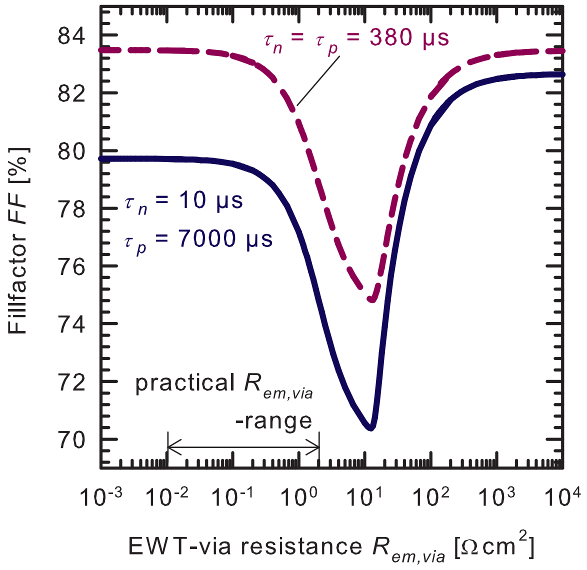

Figure 5.4: Simulated *FF* of the PC1D EWT structure in Fig. 4.7, as a function of $R_{em,via}$ with an interstitial iron concentration of $2{\times}10^{11}$ cm^{-3} (bold line) and the iron-free scenario (dashed line). The practical $R_{em,via}$ range is indicated by arrows.

- The cell operates as a near-perfect diode with an ideality factor $n_{MPP} \approx 1$ (Fig. 5.7(b)).
- The simulated *FF* of 83.4 % is close to the maximum achievable *FF* of 83.7 %, which is exclusively limited by V_{oc} with an ideality factor of unity in the total injection range [55].
- For a given operating condition (i.e. external voltage) the electron concentration varies throughout the cell, as it is illustrated in Fig. 5.1 for J_{sc}-, V_{mpp}- and V_{oc}-conditions. This range of electron concentration at V_{mpp} is smaller in case of low via resistances (Fig. 5.1). To illustrate this effect, compare both electron density profiles at V_{ext}=500 mV in Fig. 5.5.

In the iron-free scenario with an increased via resistance ($R_{em,via}$=1 Ωcm^2), the current flowing along the vias from the front to the rear causes a notable voltage drop between the front and rear p-n junctions. This has the following consequences:

- At external biases V_{ext}<500 mV, the front diode operates at a higher voltage than the rear diode, causing significantly higher excess carrier densities (see Fig. 5.5) and higher recombination current-densities in the front than in the rear diode (Fig. 5.8(a)).
- The increased operating potential of the front emitter is the reason for a broader range of injection levels at *MPP* for EWT devices featuring high EWT-via resistances (see Fig. 5.1).
- At V_{ext}>500 mV, the injection of electrons from the front emitter into the base increases and the demarcation point shifts toward the front emitter (Fig. 5.5). As a result, the current collected by the front diode decreases (Fig. 5.6) and so does the current through the EWT-vias since more electrons diffuse toward the rear *pn*-junction.
- Accordingly, the voltage drop across the EWT-vias decreases due to an ohmic behavior defined by: $U = R_{em,via} J_{via}$, where J_{via} is the current density transported along the EWT-via.
- Overall, the local bias of the front emitter increases at a slower pace than V_{ext}. As a result, the injection of electrons from the base into the emitter and of holes from the emitter into the base

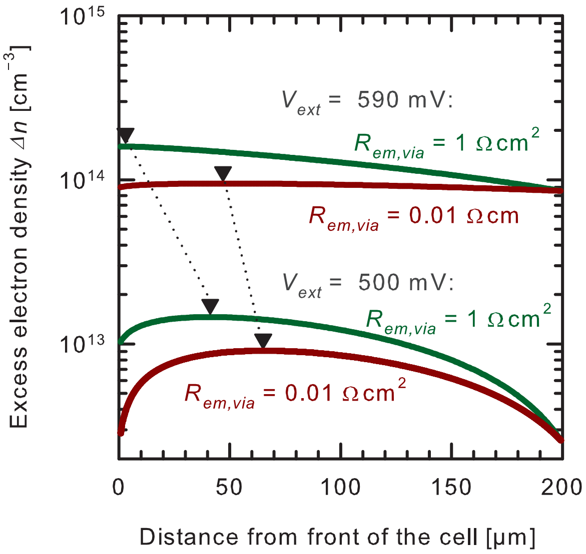

Figure 5.5: Simulated electron density distributions between the front (0 µm) and the rear (200 µm) of a rear-contacted EWT solar cell. Two cases, one with a nearly perfect EWT-via resistance ($R_{em,via}$=0.01 Ωcm^2), the other with an increased EWT-via resistance ($R_{em,via}$=1 Ωcm^2) are compared in the iron-free scenario. Triangles: Highest electron concentration density as demarcation point.

follows a non-ideal behavior with increasing V_{ext}. The result is a slowed-down recombination rate of the front diode. Thus, when the shifted recombination current is plotted against V_{ext}, a "shoulder" appears in the I-Vcurve of the front diode (Fig. 5.8). This shoulder is indicated by a guide-line in Fig. 5.8 that points to from the labeling "front diode" to the recombination characteristic. We refer to this specific shape as a "shoulder" since it is characterized by a slope section with a low gradient between two slopes sections with higher gradients at the left and at the right.

- The section of the front diode recombination at 550 mV exhibits a low gradient. As a consequence, the shifted total recombination is affected and its ideality factors are increased (n_{MPP}=1.22 (Fig. 5.8)). Finally, the FF is reduced to 80.10 %.

In this thesis we shall refer to this conglomeration of recombination effects due to $R_{em,via}$ as **"via-resistance induced recombination enhancement" (VIRE)** effect.

In the iron-contaminated scenario with nearly perfect EWT-via resistance ($R_{em,via}$=0.01 Ωcm^2), the dominant recombination losses are caused by interstitial iron.

- Here, the carrier lifetime increases with increasing excess carrier density Δn (Fig. 5.1), i.e. with increasing V_{ext}. The SRH recombination rate of interstitial iron $U_{Fe,i} = \frac{\Delta n}{\tau_{Fe,i}(\Delta n)}$ increases, too, but with a slower pace due to the increasing carrier lifetime. This leads to an non-ideal diode behavior (5.9(a)) with increased local ideality factors (5.9(b)). It is known that this causes a shoulder in the I-V-curve [129], generally at a different V_{ext} than the shoulder discussed above in the iron-free scenario. This shoulder is expressed by the peaks of the front and the rear diode in Fig. 5.9(b).
- The local ideality factors in the front and rear diode start increasing at similar V_{ext} since the excess carrier density is not increased by high $R_{em,via}$ in the front collecting part of the solar cell.

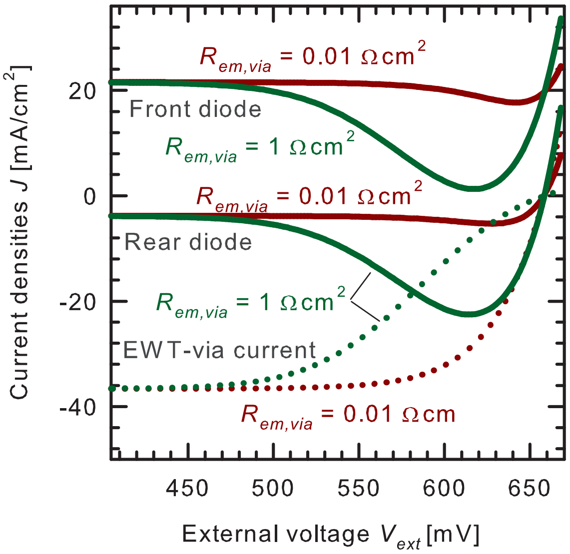

Figure 5.6: Electron diffusion currents within the front and rear diodes, respectively, taken at a distance of 1 µm from the front and the rear junction, respectively (dotted line), and the electron current along the EWT-vias (solid lines) as a function of the external voltage V_{ext} ($R_{em,via}$=1 and 0.01 Ωcm^2, τ_n=τ_p=380 µs). Positive signs indicate a current toward the front, negative signs toward the rear. The value of the diffusion current of the front diode is smaller than the EWT-via current since it is does not include photogenerated carriers within the first micrometer below the surface. The EWT-via current is composed of the total diffusion current in the front diode, including the photogenerated current in the first micrometer below the surface. For this reason, the value of the EWT-via current in the present figure is greater than the diffusion current in the front diode. For external voltage greater than 600 mV, the diffusion currents mainly recombine in the front and rear emitter and, hence, do not enter the external circuit.

- In this scenario, the local ideality factors are exclusively increased by the injection-dependent SRH recombination rate [129]. The *FF* is reduced to 79.6 % with n_{MPP}=1.41.

Finally, the scenario is discussed with an iron-contaminated base including an increased EWT-via resistance ($R_{em,via}$=1 Ωcm^2). The increase of Δn for increasing external voltages and the spatial distribution of Δn is influenced by the resistance of the EWT-via. Figure 5.1 shows that an increased EWT-via resistance leads to an expanded injection range at *MPP*. Hence, the two effects of iron and increased EWT-via resistance cause a superposed fill factor loss phenomenon.

The ideality factor of the front diode has a peak at 520 mV followed by a shoulder at 580 mV (Fig. 5.10(b)). The peak near 520 mV originates from the injection-dependent lifetime due to the iron contaminated base. Compared to the scenario with iron-contaminated base and a low EWT-via resistance (see Fig. 5.9), the local ideality factor of the front diode starts increasing at lower external voltages. This is so because of the higher EWT-via resistance that increases the local voltage at the front *pn*-junction and, hence, the excess carrier density inside the device (see Fig. 5.5). At V_{ext}= 520 mV, the local voltage and the carrier density at the front *pn*-junction accounts for 546 mV and 6.2×10^{13} cm^{-3}, respectively. In this injection range, the SRH lifetime increases at a high pace (see Fig. 5.1), and hence, the SRH recombination rate at a lower pace causing higher local ideality factors.

The excess carrier density at the rear *pn*-junction is not affected by the EWT-via resistance and accounts for 2.0×10^{13} cm^{-3} at V_{ext}=520 mV (see Fig. 5.5 for x-values at 200 µm). This is the same value at the front and rear *pn*-junctions in the scenarios with low EWT-via resistance ($R_{em,via}$=0.01

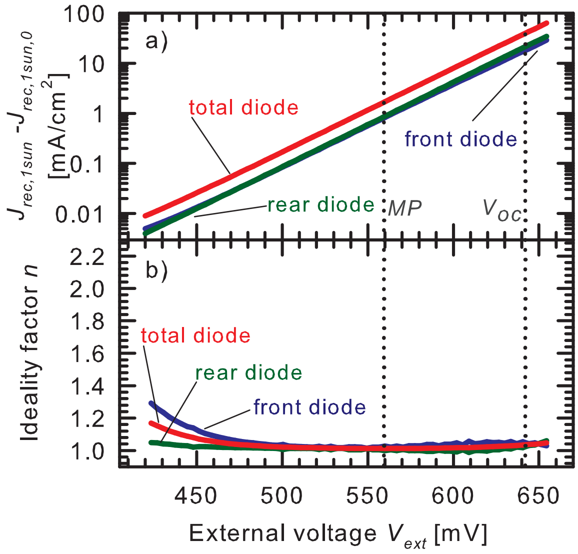

Figure 5.7: Calculated and shifted recombination current densities and local ideality factors of the PC1D EWT structure in Fig. 4.7, having nearly perfect EWT-via resistances ($R_{em,via}$=0.01 Ωcm^2) and no iron containing base.

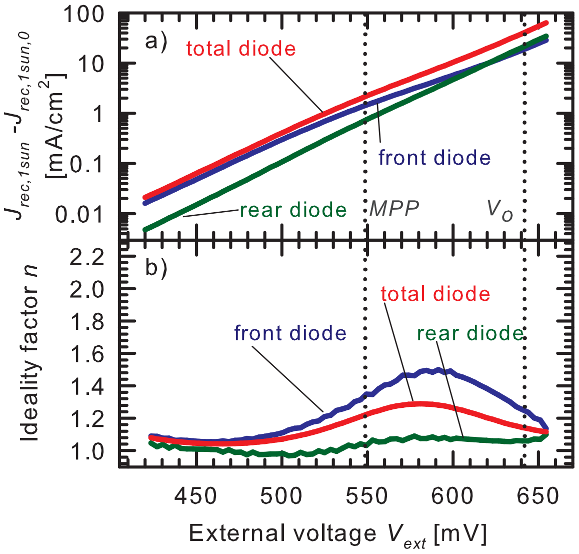

Figure 5.8: Calculated and shifted recombination current densities and local ideality factors of the PC1D EWT structure in Fig. 4.7, having increased EWT-via resistance ($R_{em,via}$=1 Ωcm^2) and no iron containing base.

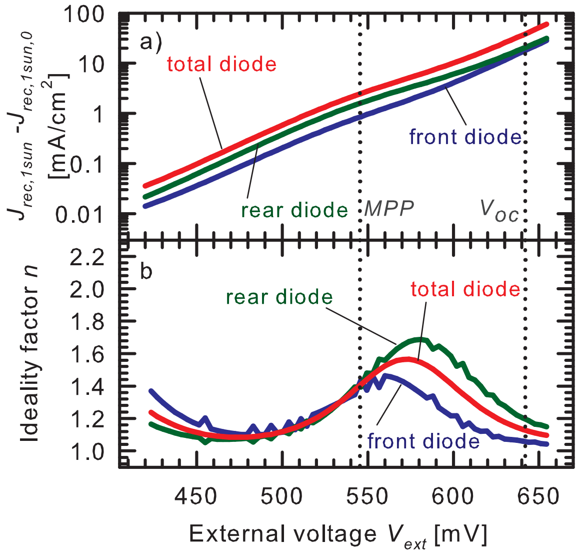

Figure 5.9: Calculated and shifted recombination current densities and local ideality factors of the PC1D EWT structure in Fig. 4.7, having nearly perfect EWT-via resistance ($R_{em,via}$=0.01 Ωcm^2) and iron containing base.

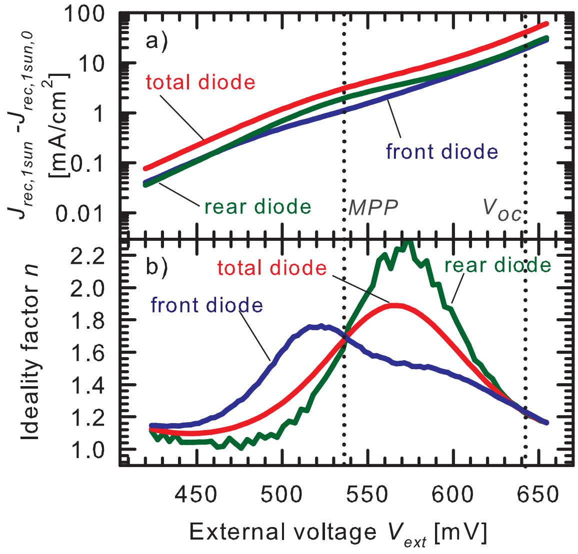

Figure 5.10: Calculated and shifted recombination current densities and local ideality factors of the PC1D EWT structure in Fig. 4.7, having increased EWT-via resistance ($R_{em,via}$=1 Ωcm^2) and iron containing base.

Ωcm). The excess carrier density in the rear collecting diode is increased by the stronger injection of electrons from the front emitter into the base. However, the absolute increase is lower than those of the front diode and the SRH lifetime starts increasing at higher external voltages. This can be observed by the peak of the local ideality factor which is shifted to higher external voltages (Fig. 5.10(b)).

The shoulder of the local ideality factor in the front diode near 570 mV originates from the VIRE effect. Actually, it is another peak superposed by the peak of the local ideality factor due to the iron contamination. The EWT-via current decreases at external voltages higher than 500 mV (Fig. 5.6). This causes a voltage drop adaption of the front *pn*-junction that accounts for 30 mV at V_{ext}=520 mV and 1 mV at V_{oc}. As a result, the local excess carrier density and the local recombination rates at the front *pn*-junction (front diode) increases at a slower pace than the external voltage.

- The front diode features two peaks. The first peak at V_{ext}=520 mV, which is due to the injection dependent bulk lifetime, and the second peak near V_{ext}= 570 mV, which is caused by the VIRE effect.
- In contrast to "no iron" scenarios, the losses in the rear diode dominate near *MPP* (Fig. 5.10) due to the decreased SRH lifetime.
- The rear diode reacts to the increased SRH lifetime at higher V_{ext} than the front diode due to the potential difference between the front and rear emitter, which causes a higher Δn in the front collecting volume. A pronounced peak arises in the ideality factor of the rear diode near 570 mV that dominates the overall characteristics.
- The fill factor is reduced to the value of 77.4 % with n_{MPP}=1.64.

5.4.3 Open-circuit voltage

At V_{oc}, the injection-level in the iron and in the "no iron" scenario is 6×10^{14} cm^{-3}. The SRH lifetime in the iron scenario is 380 µs (see Fig. 5.1). The SRH lifetime in the iron-free scenario is set as 380 µs, so similar V_{oc} are simulated in both scenarios at 1-sun illumination. In the present case, V_{oc} is mainly limited by the highly-doped front and rear emitters, both with a saturation current density $J_{0,e}$ of 290 fA/cm^2.

Figure 5.11 shows that V_{oc} slightly decreases by increasing the EWT-via resistance. Note that, even at V_{oc}-conditions, there is a non-negligible current flow from the front emitter through the EWT-via to the rear emitter [114]. The cumulative photogeneration accounts for 80% in the first 20 µm below the front side, and only 20% in the remaining back part of the solar cell. 15% of the photo current is generated in the first 330 nm below the front surface which means in the front emitter. The EWT-via emitter offers a possible current path for photogenerated carriers to the rear emitter resulting in a current flow between the front and rear side.

For both chosen lifetime settings, the currents are 2 mA/cm^2 for $R_{em,via}$=1 Ωcm^2 and 15 mA/cm^2 for $R_{em,via}$=0.01 Ωcm^2. In the case of $R_{em,via}$=1 Ωcm^2, the resulting voltage drop biases the front *pn*-junction potential compared to those at the rear side. Please compare both electron-quasi-Fermi levels $E_{F,n}$ in Fig. 5.12.

The reference point U = 0 mV is set at the rear emitter contact (at a distance of 200 µm from the front of the cell). The EWT-via resistance $R_{em,via}$=1 Ωcm^2 elevates the electron quasi-Fermi-level $E_{F,n}$ at the front and in the bulk of the solar cell. The injection of electrons from the bulk into the front emitter is increased. This leads to an increased recombination current density in the front emitter that lowers V_{oc}. However, this effect has a minor role on the V_{oc}-reduction as can be seen in Fig. 5.11. The largest deviation is about 1.6 mV between very low and very high EWT-via resistances.

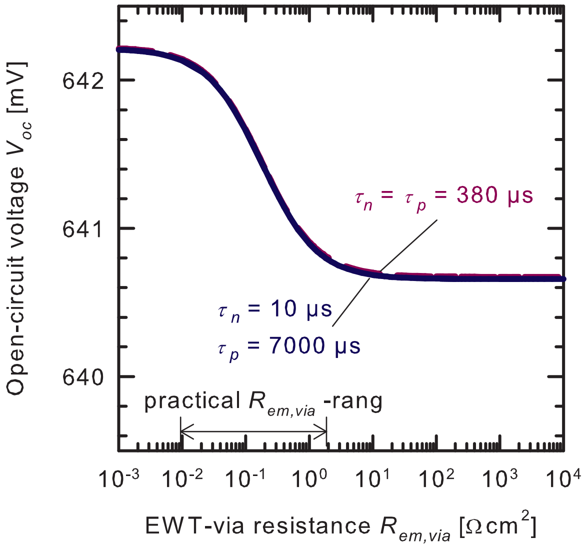

Figure 5.11: Simulated V_{oc} of the PC1D EWT structure in Fig. 4.7, as a function of $R_{em,via}$ with an interstitial iron concentration of $2{\times}10^{11}$ cm^{-3} and the reference scenario with $\tau_n{=}\tau_p{=}380$ µs. The practical $R_{em,via}$ range is indicated by arrows.

Note that the EWT-via current at V_{oc} does not enter the external circuit but mainly recombines as Auger recombination current in the rear emitter. If the SRH lifetime was very small at V_{oc}, the bulk would offer a sink for the recombination currents, more than the emitters. Consequently, electrons would be injected across the rear pn-junction into the bulk which would be the place of highest recombination. This scenario appears in one of the following simulation campaigns that feature three dimensions.

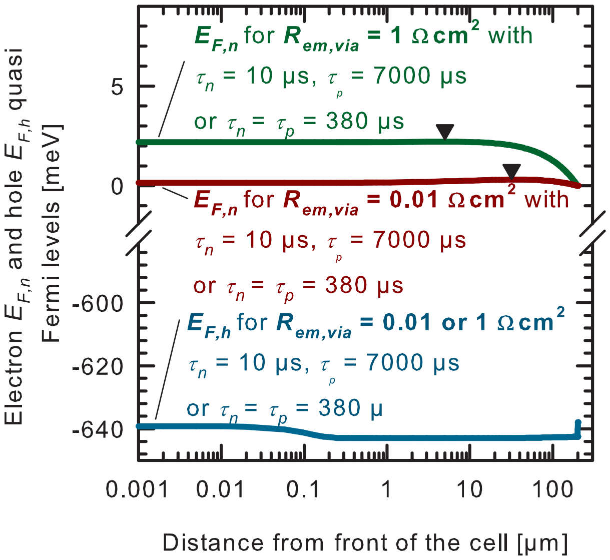

Figure 5.12: Simulated $E_{F,n}$ of the PC1D EWT structure in Fig. 4.7, with $R_{em,via}$=1 Ωcm^2 and $R_{em,via}$=0.01 Ωcm^2 at V_{oc}. The spatially-resolved position of $E_{F,n}$ is stimulated by $R_{em,via}$. The demarcation points are marked as triangles.

5.4.4 Cell efficiency

For EWT-via resistances $R_{em,via}$<0.1 Ωcm^2 and constant SRH lifetime parameters, there is no detrimental reduction of the *FF* or J_{sc}. The efficiency η (see Fig. 5.13) is affected by the high saturation current densities of the front and rear emitter ($J_{0,e}$=290 fA/cm^2) limiting V_{oc}. However, the EWT-via emitter resistance starts limiting the efficiency for $R_{em,via}$>0.1 Ωcm^2 by reducing the *FF*. An additional η -limitation for the iron-contaminated scenario is due to the reduced *FF* and increased recombination losses at short-circuit conditions. Both effects are caused by the strong injection dependent bulk lifetime of iron-decorated defects.

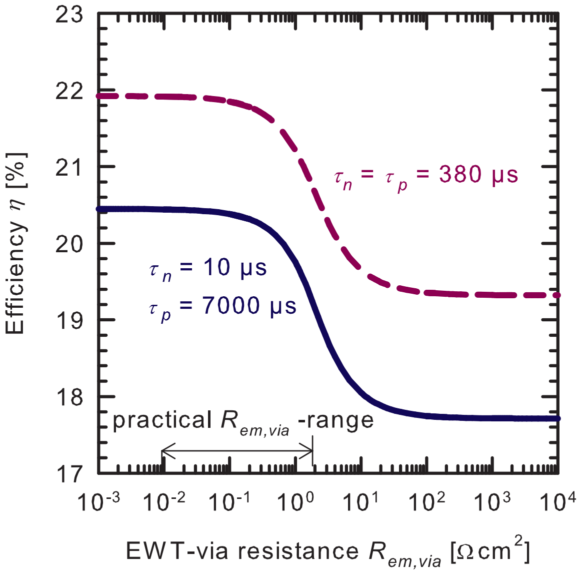

Figure 5.13: Simulated efficiency (η) of the PC1D EWT structure in Fig. 4.7, as a function of $R_{em,via}$ with an interstitial iron concentration of 2×10^{11} cm^{-3} and the reference scenario with τ_n=τ_p=380 µs. The practical $R_{em,via}$ range is indicated by arrows.

In the present one-dimensional simulation scenarios, the strongest impact of the VIRE-effect on the *FF* accounts for about 8% at EWT-via resistances of 10 Ωcm^2 (see Fig. 5.4). This value is beyond the practical $R_{em,via}$ of fabricated EWT solar cells. However, any $R_{em,via}$> 0.1 Ωcm induces a *FF*-reduction that limits the cell efficiency (see Fig. 5.4 and Fig 5.13). In this one-dimensional simulation study, the total voltage drop between front and rear emitter is induced by the EWT-via resistance. In two- or three dimensional scenarios, there are lateral current flows in the front emitter and in the bulk both inducing voltage drops and *FF*-losses. The present one-dimensional scenario does not consider lateral effects but defines the impact of the VIRE-effect which is, in this first chapter, exclusively induced by $R_{em,via}$.

If $R_{em,via}$>10 Ωcm^2, there will be no more current transport through the EWT-via at J_{sc}-conditions. All photogenerated minority carriers diffuse through the bulk. The EWT device changes to a back-junction solar cell which do not suffer from the VIRE-effect. Back junction devices exhibit *FF* comparable to those of ideal diodes. They do not suffer from crucial changes of internal currents in the one-dimensional device structure.

An amplified fill factor or efficiency loss in the iron scenario due to increased EWT-via-resistance is not observed. The VIRE effect increases the carrier densities in the base for external voltages between J_{sc} and V_{oc} compared to scenarios with very low $R_{em,via}$. Injection dependent SRH lifetimes react to the modified carrier densities. For high $R_{em,via}$, the increase of the SRH lifetime is at lower external voltages since respective carrier densities are higher compared to low $R_{em,via}$-scenarios. However, this shifting is low and the impact on the I-V-characteristic is not detrimental. The important aspect is to distinguish between the different impacts on the I-V-curve. The reason for high local ideality factors must be identified in order to distinguish between the different recombination loss mechanisms.

5.5 One-dimensional model of a front junction solar cell

The discussed one-dimensional simulation results reveal low FF of EWT solar cells in the scenario of high EWT-via resistances. The question arises if front junction (FJ) solar cells, commonly produced in the industry, suffer more or less from comparable device resistances than EWT solar cells. Figure 5.14 shows a sketch of the PC1D simulation domain that has been used for the calculation of front junction solar cells. All recombination and generation parameters are similar to those in the one-dimensional EWT model (see Tab. 5.2). Differences of the simulation results between the FJ and EWT cells are exclusively induced by the different device structure. Now, the lumped series resistance, formerly used as the EWT-via resistance in the EWT model, is situated at the front emitter. The total current of minority carriers collected at the front pn-junction is transported across this resistance. At the rear, we assume a non-contacted phosphorus diffusion in order to achieve similar saturation current densities in the EWT and FJ scenario.

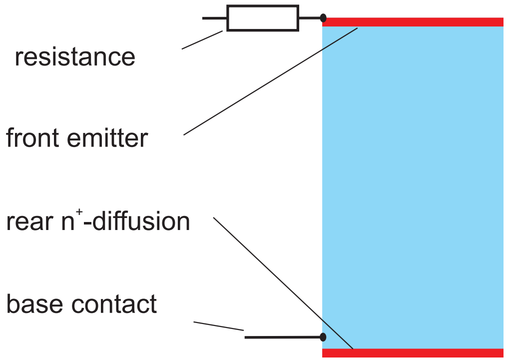

Figure 5.14: One-dimensional PC1D simulation model of a front junction solar cell (FJ). In order to obtain comparable recombination contributions compared to the PC1D EWT-device, a phosphorus diffusion is applied at the rear side. This diffusion exhibits similar recombination parameters than the front emitter. In the context of simulation results, the lumped series resistance at the front emitter has similar magnitudes than the EWT-via emitter resistance.

All the simulation results of the front junction devices are listed in Tab. 5.4. The differences between the simulated I-V-parameters of EWT and FJ devices are put in parentheses. The simulation results of the FJ devices are the reference points for the comparison of EWT and FJ cells. Negative (positive) signes indicate losses (gains) of the FJ device compared to the EWT device.

In the no-iron scenario (first and second row in Tab. 5.4), FJ devices exhibit slightly reduced J_{sc} (-0.5 mA/cm^2) compared to EWT cells due to the higher recombination at the phosphorus-diffused rear surface at V_{ext}=0 mV. Note that the phosphorus diffusion in the FJ scenario only increases the recombination and does not act as a collecting emitter for minority carriers. In the iron scenario (third and fourth row in Tab. 5.4), J_{sc} of the FJ devices is even stronger reduced. The FJ devices do not feature a both-sided minority carrier collection as it is the case in the EWT solar cell. The current paths of minority carriers in the base are comparatively longer since all the photogenerated minority are transported to the front pn-junction. Due to the long transport paths, recombination losses are increased in the base leading to lower J_{sc}.

Table 5.4: PC1D simulation results of front junction solar cells (FJ) that feature comparable bulk lifetimes and series resistances than the EWT solar cells. Deviations between FJ and EWT results are put in parentheses behind the referring I-V-parameters. The front junction simulation results are the reference point for the comparison.

$R_{em,via}$ (Ωcm^2)	τ_n, τ_p (µs)	J_{sc} mA/cm^2	V_{oc} (mV)	MPP (mV)	FF (%)	η (%)
0.01	380, 380 ("no iron")	40.4($-$0.5)	644(+2)	562(+1)	83.4($\pm$0)	21.7($-$0.2)
1	380, 380 ("no iron")	40.4($-$0.5)	644(+3)	526($-$22)	77.6($-$2.5)	20.2($-$1.0)
0.01	10, 7000 (iron)	38.8($-$1.1)	644(+2)	553(+5)	80.8(+1.2)	20.2($-$0.2)
1	10, 7000 (iron)	38.8($-$1.1)	644(+3)	521($-$13)	75.6($-$1.8)	18.9($-$0.9)

The V_{oc} in the FJ and EWT scenario is similar since the saturation current densities of all respective device components exhibit the same values. The difference of +2 mV is due to the contact positions in both scenarios. The FJ cell has its contacts at the front side, the place of the highest photogeneration and, hence, the highest splitting of the quasi-Fermi levels. In this FJ scenario, the splitting of the quasi-Fermi levels is similar to the V_{oc} at the external contacts. In the EWT scenario, the rear contacts are conductively connected with the front junction by the EWT-vias. The rear part of the EWT device has a lower quasi-Fermi level splitting (lower generation) resulting in a slightly lower V_{oc}. Due to the voltage drop along the front and rear emitter, a current flows along the EWT-via emitter at V_{oc}.

The former discussion showed that the front and rear collecting current path of an EWT solar cell exhibits a nearly perfect diode behavior for very low series resistances (R_s=0.01 Ωcm^2). The *FF* of the FJ device is similar to those of the referring EWT solar cell in the no-iron scenario with R_s=0.01 Ωcm^2.

In the EWT scenario at J_{sc}-conditions, about 10 % of the photogenerated current is collected at the rear *pn*-junction and, hence, does not suffer from resistive losses. As a consequence, the rear collecting diode of the EWT device exhibit a diode characteristic with local ideality factors around unity in the case of constant bulk lifetimes (see Figs. 5.7 (b) and 5.8 (b)). The small ideality factors indicate the non-disturbed diode behavior of the rear collecting part of the EWT solar cell. Since the total I-V-curve is calculated from the sum of the front and rear collecting diode, the EWT device with constant bulk lifetimes profits from its rear part in terms of a higher *FF* compared the FJ cell. The FJ device is more sensitive for increased lumped series resistances and exhibits a higher *FF*-loss than the EWT solar cell in the scenario of increased series resistances. All the current is collected at the front *pn*-junction and transported along the lumped series resistance. Hence, the impact of series resistances on the I-V-curve is comparatively stronger for FJ solar cells in the present simulation study. This result holds for the no-iron and iron scenario with R_s= 1 Ωcm^2 as depicted by the stronger reduced *FF* of the FJ device in the second and fourth row of Tab. 5.4.

In the iron scenario with R_s=0.01 Ωcm^2, the FJ device exhibits a comparatively higher *FF*. The front junction device grips the current and the voltage at the front side, the place of the highest carrier density. Hence, the SRH lifetime exhibits the highest values at the front side at which the respective SRH recombination exhibits its minimum impact on the I-V-characteristics in the iron scenario. Note that SRH recombination affects the I-V-characteristic and the *FF* in the present scenario with R_s=0.01 Ωcm^2. The EWT solare cell features its contacts at the rear side, the place of the lowest carrier density and, hence, the highest SRH recombination. Here, the impact of SRH recombination on the total I-V-charactistic is higher and the *FF* is reduced (third row in Tab. 5.4).

The simulated efficiencies of the FJ devices are always smaller than those of the respective EWT solar cells. Firstly, this is due to the reduced J_{sc}. Secondly, the simulated *FF* of FJ devices are smaller with the exception of the iron-scenario and R_s=0.01 Ωcm^2.

In practice, the fill factors of FJ solar cells are usually greater than those of EWT devices. The reason is simple: Front junction solar cells usually exhibit smaller series resistances than EWT devices. This is so because FJ cells often have short current paths for majority carriers. The one-dimensional PC1D model considers the series resistance as an input parameter. The more-dimensional geometry of the device is not respected. By means of PC1D, it is trivial to compare the FJ and EWT concept for similar R_s. Real FJ and EWT solar cells suffer from series resistances along the long transport paths of majority carriers which are different due to the varying geometries and solar cell concepts. In terms of efficiency evaluations, it is justifiable and important to discuss the advantages and disadvantages for each concept. PC1D can be used to describe basic mechanisms of solar cells. A more detailed analysis requests for more-dimensional simulation models that respect the geometry of the device.

5.6 Conclusion

The one-dimensional simulation model offers a qualitative but detailed analysis of the current-transport inside the solar cell. The key for understanding the behavior of EWT solar cells is the analysis of the minority carrier density and transport inside the bulk.

Low fill factors of EWT solar cells are induced by increased series resistances. The diffusion currents within the base region exhibit crucial changes between the front and rear collecting diodes in the present device modeling. These changing currents can be understood as a shift of the demarcation point toward the front *pn*-junction when going toward higher external voltages. The one-dimensional simulation domain respects the internal current transport which is is difficult to implement in an resistive network of diodes [111].

The present chapter discusses the **"*v*ia-resistance *i*nduced *r*ecombination *e*nhancement" (VIRE)** effect and its impact on the *I*-*V*-characteristic of EWT solar cells. The current density through the EWT-via (resistance) induces a voltage drop. The front emitter is on a higher potential than the rear emitter. Consequently the injection of electrons from the front emitter into the base as well as the injection of holes from the base into the front emitter is increased.

For higher external voltages, the demarcation line shifts toward the front *pn*-junction. The recombination loaded diffusion current through the solar cell base increases. The resistive loaded drift current through the EWT-via decreases. The approaching of the front emitter potential to the rear emitter potential with increasing V_{ext} causes a recombination characteristics with local ideality factors n>1 and, consequently, *FF*-losses.

As a result, the *FF* suffers from recombination losses and resistive losses. Furthermore, it is shown that J_{sc} and V_{oc} are hardly effected by the EWT-via emitter series resistance in a $R_{em,via}$ range practical to fabricated devices (phosphorus diffused emitters with a typical sheet resistance less than 200 $\Omega/\square$).

The shifting of the demarcation point due to the VIRE-effect strongly depends on the minority carrier density in the base. Three-dimensional simulations will verify this effect in the next chapter.

6 Investigations on the internal current transport of EWT devices by varying the wafer resistivity

6.1 Introduction

Currently, the emitter-wrap-through (EWT) design of Si solar cells is being intensively investigated as a promising concept for achieving improved cell efficiencies from cheap, low-quality Si materials.

Historically, an often used approach for increasing the *FF* and V_{oc} of EWT solar cells is the implementation of a deep phosphorus diffusion in the EWT-via and a weaker phosphorus diffusion in the front part [50, 49]. The deep diffusion decreases $R_{em,via}$, while the weak diffusion lowers $J_{0,front}$. In practice, no satisfactorily high *FF*-gains were achieved in this manner, and the efficiency was mainly improved by an increased V_{oc}. Firstly, the voltage drop along the EWT-via emitter is reduced. Secondly, the voltage drop along the front side emitter is increased which leads to the similar effect of high voltage drops along the emitter. Achievable *FF* gains by these strategies are rather small.

The previous chapter confirmed that experimentally achieved energy conversion efficiencies have stayed below the efficiency expectations derived from J_{sc}-V_{oc}-products. This is due to the typically low *FF* of EWT devices. In order to find an explanation for the low *FF*, two different EWT-via resistances were selected as simulation parameters. As a result, low *FF* of one-dimensional EWT devices could be explained by an increased $R_{em,via}$. However, the chosen value of 1 Ωcm^2 for $R_{em,via}$ was very large and did not represent typical experimental values that account for about 0.3 Ωcm^2.

In this chapter, fabricated EWT solar cells are analyzed in detail. A three-dimensional device model is applied to account for the limiting loss mechanisms. The wafer resistivity is identified as a critical parameter in order to improve the solar cell efficiency for EWT devices with point contacts at the base area. It is predicted that a proper adaption of wafer resistivity is more effective than lowering the resistance in the EWT-vias. Differences between one-dimensional and three-dimensional simulation results primarily arise due to the lateral transport of majority and minority carriers in the bulk. The investigated EWT cells feature a homogeneous emitter diffusion and a non-passivated rear emitter. The base area at the rear side is passivated by a layer of thermally grown silicon dioxide which exhibits a very low surface recombination velocity [138, 139, 82, 140]. This chapter is based on my publication in Ref. [36].

6.2 Solar cell fabrication

All EWT solar cells presented in this chapter are fabricated by an identical process sequence [50] depicted in Fig. 6.1.

(a) A 250 nm thick SiO_2 layer is thermally grown on both sides of the wafer at 1000 °C.

(b) At the front side, the SiO_2 layer is etched off in HF.

(c) Random pyramids are etched in a KOH-isopropanol solution to improve light trapping.

(d) At the front, a 100 nm thick silicon nitride layer (SiN) with a refractive index of 1.9 is deposited as a protecting layer for the random pyramids.

(e) At the rear side, the SiO_2 layer is ablated by laser power to structure the interdigitated emitter and base regions [141], and the EWT-vias are laser-drilled. The laser-damage in Si is removed in a 10 % KOH solution for 15 min at 90 °C, resulting in a 20 µm deep ditch. After etching, the vias are quadratic, with a width of 70 µm.

(f) The 100 nm thick SiN layer is removed in phosphoric acid.

(g) A phosphorus emitter with a sheet resistance of R_{sq}=50 Ω/□ is diffused at 880 °C with a $POCl_3$ diffusion in a tube furnace.

(h) At the front, a double layer of SiN is deposited to decrease the emitter saturation current [142] that accounts for about 300 fA/cm^2 in the present scenario. The refractive index is 2.4 in the first 10 nm to achieve good passivation properties, and 2.05 in the following 100 nm to obtain an antireflection coating. The deposition of SiN extend into the EWT-vias.

(i) At the rear, a 10 µm thick Al layer is evaporated, followed by a 300 nm thin layer of SiO_x, which acts as an etching barrier.

(j) The flanks between emitter and base are selectively etched off because they are less protected by the SiO_x layer, due to its columnar growth. This separates the emitter from the base regions [45, 39, 143].

(k) Local base contacts are formed by laser firing [144]. Finally, annealing at 360 °C on a hot plate improves the surface passivation at the Si-SiO_2-interface [145] and the contact resistance.

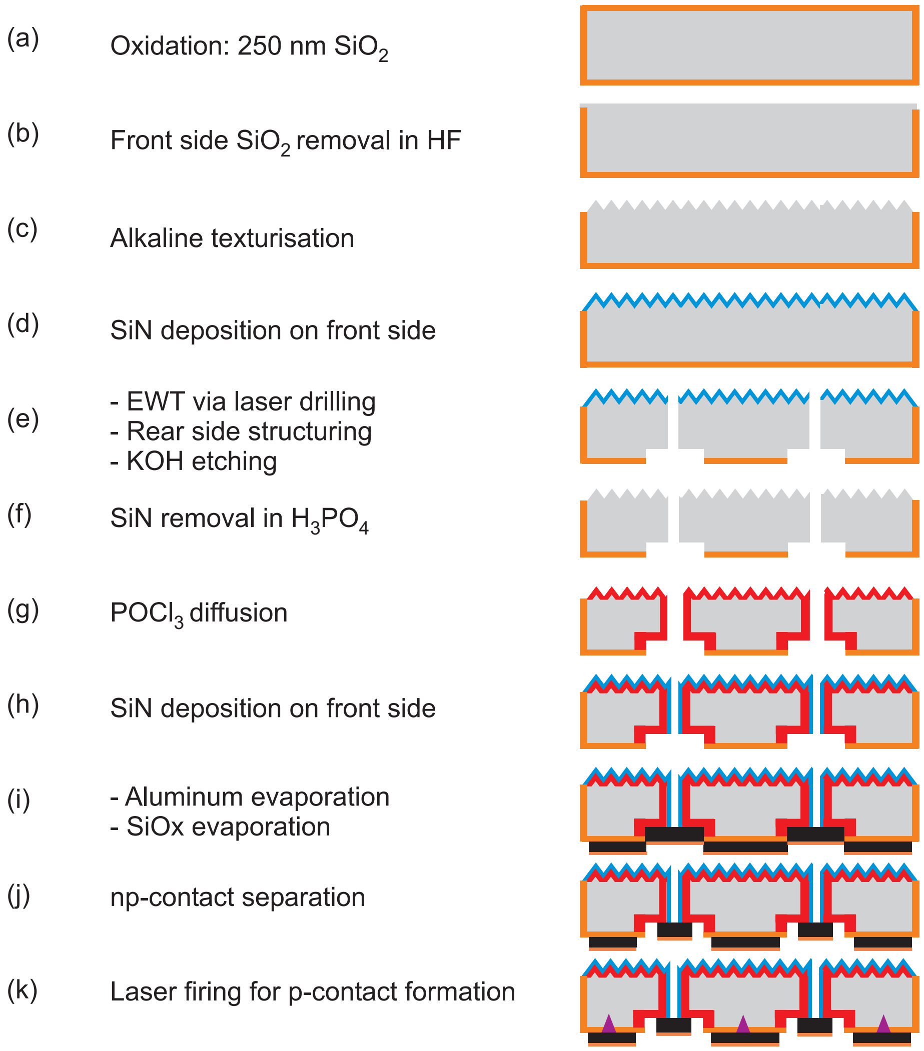

Figure 6.1: Fabrication sequence of boron-doped Cz-Si EWT solar cells presented in this chapter.

The local metal-semiconductor contact at the base area (laser-fired contacts) have been developed by Schneiderlöchner which is described in the following [144]. Onto the base area (and emitter area depending on the solar cell layout), a thin layer of aluminum (<=25 µm) is evaporated. A laser pulse is focused onto the surface. The laser energy heats the aluminum that melts together with the silicon wafer situated below. Depending on the laser pulse energy and aluminum thickness several laser pulses have to be applied in order to form one point contact. A thin layer (d<5 µm) of the melted and resolidified silicon beneath the aluminum features a certain aluminum dopant density. This aluminum doped silicon layer which is commonly called aluminum back surface field (BSF).

A technical drawing of an EWT structure is shown in Fig. 4.8. The unit cell of the EWT structure is comprised in the three-dimensional simulation domain (upper left quarter in Fig. 4.8) and can be pursued in space by mirroring the structure at the edges. The geometrical device parameters are listed in Tab. 6.1.

Table 6.1: Geometrical parameters of the EWT solar cells fabricated on p-type Cz-Si.

Device parameters	Settings
Index i_x	1150 µm
Rear emitter width e_x	750 µm
Base width $i_x - e_x$	400 µm
Distance d_y between EWT-vias	600 µm
EWT-via width $v_x = v_y$	70 µm
LFC diameter D_{LFC}	45 µm
Distance between LFC d_{LFC}	70 µm
Wafer thickness W	220 µm
Ditch depth d	20 µm
Cell area	2×2 cm^2

6.3 Solar cell characterization

Two EWT solar cells are examined, made from boron-doped Czochralski-grown (Cz) silicon wafers with a resistivity of 0.5 Ωcm and 5 Ωcm, respectively.

Using Thurber's dopant-resistivity relationship [146, 147] this corresponds to the dopant density N_A=3.3×10^{16} and 2.8×10^{15} cm^{-3}, respectively. All lifetimes of boron-doped Cz-Si wafers reported here refer to the degraded state after prolonged illumination. Hence, the lifetimes correspond to conditions in an illuminated photovoltaic cell module. The open symbols in Fig. 6.2 show the quasi-steady-state photoconductance decay [148] measurements of the effective excess carrier lifetime, τ_{eff}, of the 5 Ωcm and 0.5 Ωcm base, respectively. For these measurements, all dopant diffusions of the cell are etched off, and all surfaces are passivated with a SiN layer with a refractive index of 2.4. From these measurements, the Shockley-Read-Hall (SRH) lifetime in the bulk, τ_{SRH}, [14, 15] is extracted using Eq. 3.29. The applied surface lifetime τ_{surf} is calculated from Eq. (8) in Ref. [149]. The extracted τ_{SRH} values depend sensitively on τ_{surf} at injection densities Δn above 5×10^{14} cm^{-3}. In this Cz material, τ_{SRH} is modeled using Eq. 3.19. At Δn above 5×10^{14} cm^{-3}, the effective surface recombination velocity S_{eff}=11−15 cm/s is used, which is compatible with the S_{eff} measurements made in Ref. [87] on related material. The SiN layer also passivates the vias in the wafer [150] during our τ_{eff} measurements and has been considered in the choice of S_{eff}.

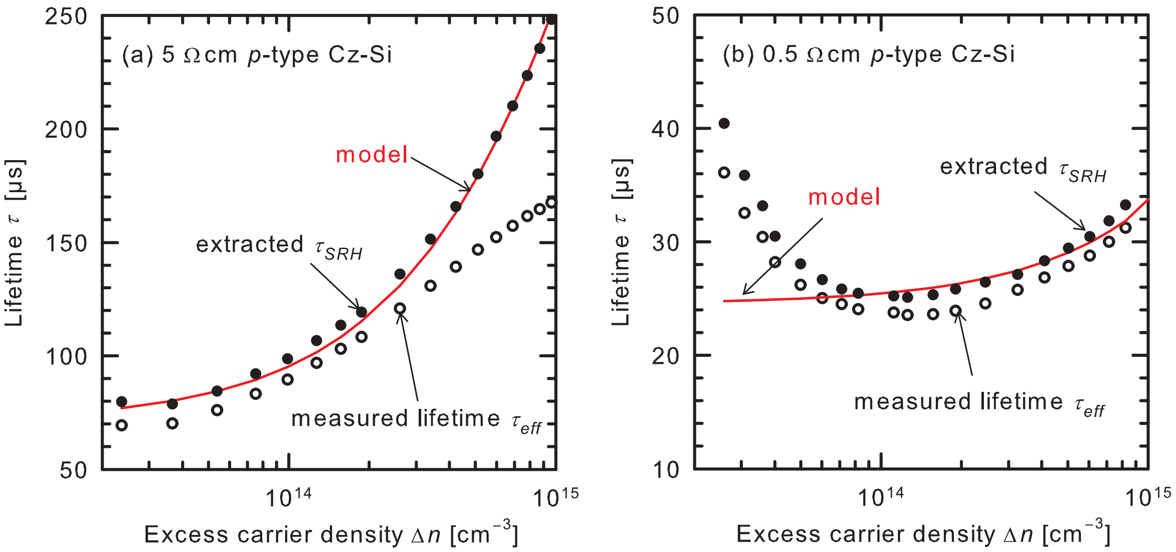

Figure 6.2: Measured effective excess carrier lifetime τ_{eff} (open circles) of the 5 Ωcm (a) and the 0.5 Ωcm (b) p-type Cz-Si EWT solar cells. The SRH lifetime in the bulk τ_{SRH} (closed circles), and a calculation of τ_{SRH} by means of Eqs. 3.29, 3.19, and 3.20, taking into account the lifetime limitation by the boron-oxygen complex (line).

The fits for τ_{n0} and τ_{p0} of Eq. 3.19 to τ_{SRH} (the lines in Figs. 6.2) and the resulting bulk diffusion lengths in low level injection calculated from $L_n = \sqrt{D_n \tau_n}$ are depicted in Tab. 6.2 for the 5 and 0.5 Ωcm wafers.

Figure 6.3 (panels (a) and (d)) shows the I-V-curves at 1 sun illumination or in the dark, respectively, and J_{sc}-V_{oc}-measurements at various light intensities, all measured at Institute for Solar Energy Research Hamelin (ISFH) at 25 °C with a halogen lamp approximating the am1.5g spectrum. Table 6.3 reports I-V-curve parameters of the EWT solar cells under illumination where the edges including the busbar regions have been shaded. This eliminates busbar-related series resistance effects which are particularly pronounced for non-optimized (relatively wide) busbars. The illuminated solar cell area accounts for 2×2 cm^2. The total solar cell area accounts for 2.5×2.5 cm^2. The J_{sc} is measured with an error of ±0.1 mA/cm^2, the V_{oc} with an error of ±1 mV and the FF with an error of ±0.1 %.

Table 6.2: Fitted SRH bulk lifetime parameters τ_{n0} and τ_{p0}, the fitted interstitial oxygen concentrations O_i for a gettering factor m=2 and the respective electron diffusion constants D_n (at a temperature of 25°C) for 5 and 0.5 Ωcm boron-doped Cz-Si wafers, respectively. The bulk diffusion lengths for electrons L_n in LLI are calculated using: $L_n = \sqrt{D_n \tau_{n0}}$.

ρ (Ωcm)	O_i (cm^{-3})	m (nondimensional)	τ_{n0} (µs)	τ_{p0} (µs)	D_n (cm/s)	L_n (µm)
5	8.4×10^{17}	2	70	700	32.6	477
0.5	5.3×10^{17}	2	20	200	23.1	215

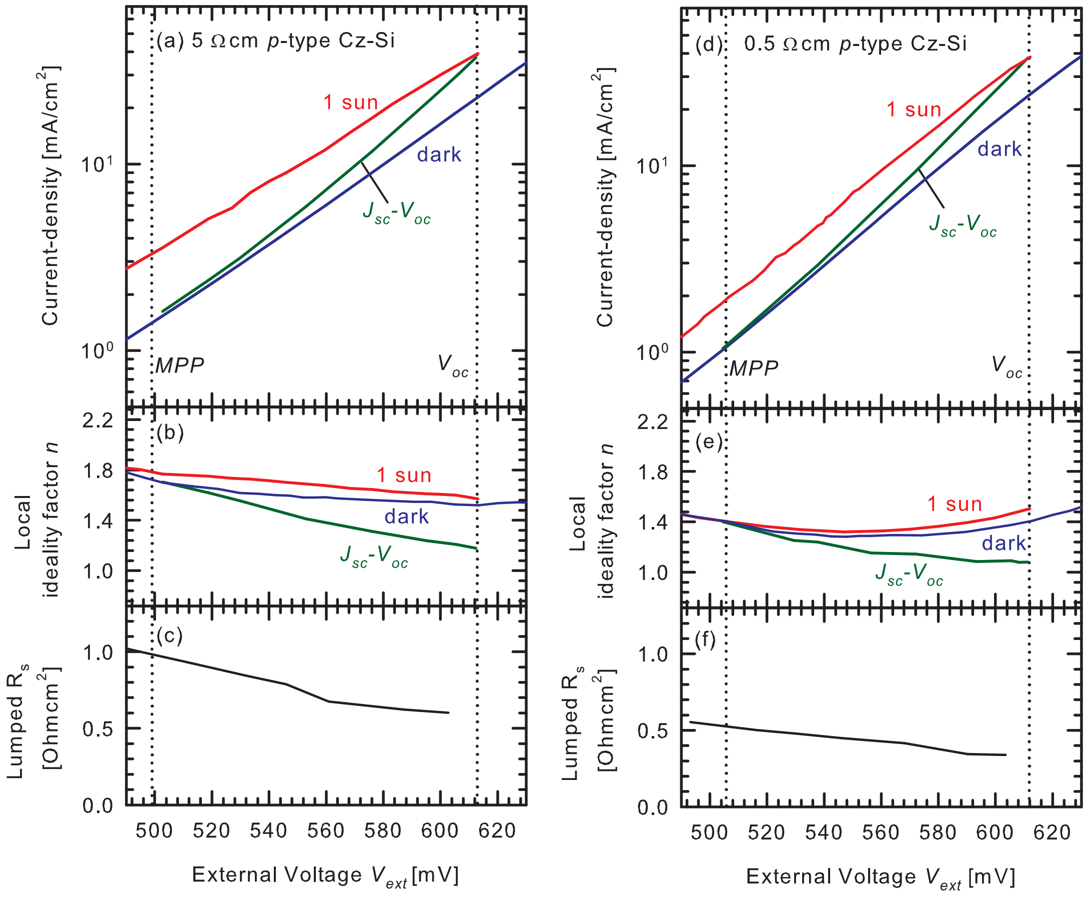

Figure 6.3: Top panels: measured I-V-characteristics under 1 sun illumination (shifted by J_{sc}), under dark conditions, and the J_{sc}-V_{oc}-values obtained under various illumination intensities of two EWT cells with the denoted base resistivity. Center panels: measured local ideality factors of the above I-V-characteristics. Bottom panels: lumped series resistance, extracted from the 1 sun and J_{sc}-V_{oc}-curves.

The center panels (b) and (e) of Fig. 6.3 contain the local ideality factors n, which indicate deviations from the ideal exponential behavior of the I-V-curve with n=1 and are calculated between two neighboring points, (J_1,V_1) and (J_2,V_2) using Eq. 3.36.

The bottom panels (c) an (f) of Figs. 6.3 show the lumped series resistance R_s. It is extracted from a comparison of the J_{sc}-V_{oc}- and the 1 sun I-V-curve by using Eq. 3.52.

The J_{sc} of both devices is not affected by the R_s values shown in the bottom panel of Fig. 6.3.

Table 6.3: Measured parameters shown without brackets and "edge-recombination-corrected" values shown in brackets of the I-V-characteristics of two cells fabricated on 0.5 and 5 Ωcm Cz-Si under standard conditions (halogen lamp approximating the am1.5g spectrum, temperature = 25 °C). The expression "edge-recombination-corrected" denotes the substraction of a a recombination current which is due to the laser damaged edges of the solar cells. More details are given in the text below.

ρ (Ωcm)	J_{sc} (mA/cm^2)	V_{oc} (mV)	J_{mpp} (mA/cm^2)	V_{mpp} (mV)	FF (%)	FF_{Pseudo} (%)	η (%)
5	39.6 (39.6)	613 (613)	35.9 (36.7)	499 (502)	74.8 (76.0)	79.6 (80.8)	18.2 (18.4)
0.5	38.7 (38.7)	612 (612)	36.2 (37.1)	506 (512)	79 (80.4)	81.4 (82.6)	18.7 (19.0)

The absolute series resistance is too low and does not have an impact on J_{sc} as explained by means of Fig. 3.3 on page 22. The V_{oc} of EWT solar cells slightly depends on the internal current flow along the EWT-via. At open-circuit conditions, internal currents flow between the photogeneration near the front surface and the recombination at the rear part of the EWT solar cell: these currents may attain significant magnitude along the EWT-vias. The last chapter identified the impact of the EWT-via resistance on the V_{oc} which is less than 2 mV. The produced voltage drop depends on the sheet resistance in the front and the via-emitter as well as on base dopant concentration and the cell geometry [151, 51]. Using the parameters in Tab. 6.1, the resistance of the EWT-via can be calculated by Eq. 4.6 [114] and accounts for 0.25 Ωcm^2 in both cells.

The panels (c) and (f) in Fig. 6.3 show the total lumped series resistance of both devices calculated by using Eq. 3.52. R_s accounts for 1 Ωcm^2 (0.5 Ωcm^2) of the 5 Ωcm (0.5 Ωcm) device at the maximum power point.

It is shown by means of numerical device modeling in section 6.5.3 that the internal current-flow from the front to the rear emitter at open-circuit condition causes a potential drop along the EWT-via of 3.5 mV in the 0.5 Ωcm cell. Hence, some moderate influence on the V_{oc} [51] and consequently on the J_{sc}-V_{oc}-curve should be expected.

The shunt resistance of both solar cells are higher than 5000 Ωcm^2 and, consequently, have no impact on the solar cell parameters.

6.4 Discussion of the EWT fill factor by means of a diode network

The effect of the lumped R_s on the FF is investigated by applying the model network depicted in Fig. 4.3. The SRH recombination parameters of the bulk (see Figs. 6.2(a) and (b)) and the experimental J_{sc} (Tab. 6.3) are used in order to model the illuminated I-V-curves of both solar cells by means of Eq. 4.2. The voltage dependent series resistances of the devices in Fig. 6.3 are set as input parameters for the modeling. The experimental open-circuit voltage of 612 mV (613 mV) for the 0.5 Ωcm^2 (5 Ωcm^2) device is calculated by considering the respective bulk recombination lifetimes in addition to a constant saturation current density $J_{0,const}$ of 1450 fA/cm^2 for both devices. The constant J_0 contribution respects the front and rear emitters, the passivated base area and the semiconductor-metal contacts at the rear side. The respective device components are similar in both solar cells. The resulting deviations between the experimental and the calculated V_{oc} are about 1 mV. All calculated I-V-parameters are depicted in Tab. 6.4.

Figures 6.3(b) and 6.3(e) show declining local ideality factors of both experimental J_{sc}-V_{oc}-curves for increasing external voltages. Such behavior points to a non-ideal recombination mechanism in the two cells. The J_{sc}-V_{oc}-curves are not or just hardly affected by series resistances that would disturb the ideal diode characteristic as it is the case in the present scenario. The observed behavior cannot be explained by phosphorus emitter recombination that usually exhibits constant local ideality factors of unity. Furthermore, the bulk-recombination due to the boron-oxygen complex would induce increased local ideality factors for increasing external voltages. For external voltages smaller than 540 mV, the dark and the illuminated I-V-characteristics are similarly affected by the high local ideality factors. The reason for this specific diode behavior is explained in the following.

Both devices are isolated by laser cutting from a larger wafer at the end of the process. In this fabrication step, the front emitter is damaged which leads to a recombination behavior with increased local ideality factors. Macintosh investigated front-junction solar cells that were cleaved from a large wafer at the end of the process [108]. Similar to the present scenario, these cells feature a non-passivated and damaged front emitter edge. The resulting recombination currents can be described by a diode with a constant local ideality factor of two (n=2) and a saturation current density of $J_{02,edge}$=1.5×10^{-8} A/cm [108]. The front emitter is a conductive channel that connects the device with the shaded and laser-damaged edges. Hence, the specific recombination is coupled

Table 6.4: I-V-parameters of the 0.5 and 5 Ωcm EWT devices calculated by means of the diode network in Fig. 4.3 (see Eq. 4.2). The experimental short-circuit current densities are used as input parameters in the applied model. The pseudo-FF is also calculated by means of the diode network with R_s=0. The experimental values as well as the "edge-recombination-corrected" values of both the cells are shown in Tab. 6.3. The calculated series resistance contributions of the respective device components are shown in Tab. 6.5.

ρ (Ωcm)	J_{sc} (mA/cm^2)	V_{oc} (mV)	J_{mpp} (mA/cm^2)	V_{mpp} (mV)	FF (%)	FF_{Pseudo} (%)	η (%)
5	39.6	613	37.4	491	75.5	81.3	18.3
0.5	38.7	613	36.8	519	80.3	83.0	19.1

to the remaining device recombination. As a result, the total I-V-curve is affected.

In order to estimate the impact of the laser-damaged edges on the I-V-parameters, we subtract the referring recombination from the illuminated 1 sun I-V-curve. First, we assume the recombination current of the damaged edge emitter to be independent of the remaining device recombination. The potential drop ΔV between the external circuit and the device edges is assumed to be: $\Delta V = JR_s$, where J is the device current under illumination and R_s the voltage dependent lumped series resistance of the 0.5 Ωcm or 5 Ωcm device depicted in Fig. 6.3. The saturation current density $J_{02,edge}$ is multiplied with the edge length of the solar cells (L_{edge}=4×2.5 cm) and divided by the total device area (A=2.5×2.5 cm^2) in order to obtain an area-averaged current density in units of mAcm^{-2}. The "edge recombination current density" $J_{rec,edge} = J_{02,edge}(e^{\frac{V_{ext}-RJ}{2V_{th}}} - 1)$ is subtracted from the illuminated 1 sun I-V-curve. Finally, we achieve two "corrected" I-V-curves for the two cells that are not affected by the laser-damaged edges. The short-circuit current density and the open-circuit voltage are similar with and without the laser-damaged edge emitter in both scenarios. The calculated and "corrected" FF of the 5 Ωcm and the 0.5 Ωcm device account for 76.0 % and 80.4 %, respectively. Compared with the experimental results of the illuminated I-V-curves in Fig. 6.3, the experimental FF of both devices are reduced by about 1% due to the damage at the emitter edge.

By means of the diode network calculated FF (Tab. 6.4) only deviate by about 0.5 % from the "$J_{rec,edge}$-corrected" FF. Hence, the FFs calculated by means of the diode model of Eq. 4.2 fit well to the results of both experimental I-V-curves without the impact of the edge recombination. As a result, the respective I-V-curve modeling by means of Eq. 4.2 allows the determination of EWT I-V-parameters with a good accuracy.

Table 6.5: Calculated series resistance contributions of the EWT solar cell fabricated on 5 Ωcm and 0.5 Ωcm p-type Cz-Si wafers: Parallel current path in front emitter: $R_{em,par}$ (Eq. 4.8); radial current path in front emitter: $R_{em,rad}$ (Eq. 4.13); current path in EWT-via emitter: $R_{em,via}$ (Eq. 4.6); vertical current path in base: $R^{LFC}_{base,ver}$ (Eq. 4.16); lateral current path in base: $R^{LFC}_{base,par}$ (Eq. 4.17); radial current path around LFC: $R^{LFC}_{base,rad}$ (Eq. 4.19).

ρ (Ωcm)	$R_{em,par}$ (Ωcm^2)	$R_{em,rad}$ (Ωcm^2)	$R_{em,via}$ (Ωcm^2)	$R^{LFC}_{base,ver}$ (Ωcm^2)	$R^{LFC}_{base,par}$ (Ωcm^2)	$R^{LFC}_{base,rad}$ (Ωcm^2)	$\sum R_s$ (Ωcm^2)
5	0.02	0.17	0.25	0.11	0.25	0.18	0.98
0.5	0.02	0.17	0.25	0.01	0.03	0.02	0.50

The impact of the injection dependent bulk lifetime due to the boron-oxygen complexes is also estimated by the application of the diode network. The J_{sc}-V_{oc}-curve represents the illuminated I-V-curve but freed from the influence of R_s at voltages where the superposition principle holds [103] and if the J_{sc} and V_{oc} values are not noticeably influenced by resistive losses. In the present case, the experimental J_{sc}-V_{oc}-curve is affected by the non-ideal recombination at the laser-damaged edges. For this reason, the pseudo fill factor of the experimental J_{sc}-V_{oc}-characteristics is reduced and accounts for FF_{pseudo} =79.6% (5 Ωcm cell) or 81.4% (0.5 Ωcm cell). In the following, we calculate the FF-loss which is exclusively based on the boron-oxygen complex and, hence, on the injection dependent bulk lifetime without the impact of the laser damaged emitter.

In the first step of our analysis, the lumped series resistance is set as zero (R_s=0) in Eq. 4.2. As a result, the diode network generates an illuminated I-V-curve without the impact of R_s. This characteristic represents the calculated J_{sc}-V_{oc}-curve that considers the injection dependent bulk recombination without the impact of series resistances (and without the impact of the edge recombination which is not considered in the diode network). The calculated pseudo-FF of these curves account for 81.3 % and 83.0 % for the 5 Ωcm and the 0.5 Ωcm device, respectively. In the next step, the injection dependent recombination current in the bulk is set as zero. In order to reproduce the experimental V_{oc}, a constant saturation current density J_0 of 2000 fA/cm^2 is inserted into Eq. 3.44. Using the calculated I-V-curve parameters of the diode with R_s=0, one obtains a FF=83.0 % by means of Eq. 3.46 for both solar cells. This certain FF denotes the highest value that can be achieved for an ideality factor of unity and the respective V_{oc}.

In the second stepf of our analysis, we discuss the calculated impact of the boron-oxygen complex on the I-V-characteristics of both solar cells. In the 0.5 Ωcm scenario, the excess carrier density Δn is about 6×10^{13} cm^{-3} at V_{oc} (Eq. 3.7). The SRH bulk lifetime is constant between J_{sc} and V_{oc} (see Fig. 6.2(b)). In the scenario with R_s=0, the SRH loss current increases with a constant local ideality factor n=1 between J_{sc} and V_{oc}. By means of the diode network calculated pseudo-FF accounts for 83 % and, hence, is similar to the FF-value of the cell which is exclusively limited by V_{oc} (83 %). Summarized, the boron-oxygen complex does not induce injection dependent carrier lifetimes between J_{sc} and V_{oc} in the 0.5 Ωcm-scenario. The FF-loss is marginal.

In the 5 Ωcm scenario, the excess carrier density Δn is comparatively larger and accounts for about 5.6×10^{14} cm^{-3} at V_{oc} (Eq. 3.7). The SRH bulk lifetimes increases from 70 µs at J_{sc} to 200 µs at V_{oc} (see Fig. 6.2(a)). Even in the scenario with R_s=0, the resulting SRH loss current increases in a sub-exponential pace with a local ideality factor greater than unity as explained in Ref. [25]. The calculated pseudo-FF of 81.3 % respects the impact of the boron-oxygen complex and is reduced by about 1.7 % absolute compared to the scenario of an ideal diode with a constant local ideality factor of n=1 (FF=83.0%).

The 5 Ωcm device additionally suffers from a low FF due to the increased wafer resistivity and the resulting resistive losses. The present issue is to identify the most detrimental R_s contributions in terms of FF-reductions.

Table 6.5 lists all series resistance contributions of the single device components that have been discussed in section 4.3.1 on page 28. The referring values are calculated be means of the geometrical device parameters depicted in Tab. 6.1.

In the front emitter, there is a parallel current component more distinct to the EWT-via ($\rightarrow R_{em,par}$, Eq. 4.8) and a radial component bordering the EWT-via ($\rightarrow R_{em,rad}$, Eq. 4.13). The same scenario holds for the current transport inside the base. Distinct or close to the LFC contacts at the rear side, we assume a parallel ($\rightarrow R^{LFC}_{base,par}$, Eq. 4.17) or a radial current flow ($\rightarrow R^{LFC}_{base,rad}$, Eq. 4.19). In context with the derivation of $R^{LFC}_{base,rad}$, the current crowding around the LFC point contact has been discussed. The resulting height of the current transport above the LFC is smaller than the wafer thickness. Simulation results, presented in the following sections, reveal the height of the current transport which is in the range of 10 to 20 µm. In the present calculation, we assume a height of 15 µm in order to respect the current crowding around the LFC point contacts.

In our model, the vertical component of the current transport inside the base is calculate by means of a one-dimensional transport ($\rightarrow R^{LFC}_{base,ver}$, Eq. 4.16). The EWT-via resistance $R_{em,via}$ is also based on a linear current transport and is calculated from Eq. 4.6.

Since the 0.5 and 5 Ωcm scenario feature similar geometries and emitter diffusions, the emitter resistances are similar. The current transport around and along the EWT-via results in a total emitter-R_s value of about 0.4 Ωcm^2. Using the diode network model in Fig. 4.3 (see Eq. 4.2), this relatively large value induces FF-losses of about 2 % in both scenarios compared to a diode scenario with R_s=0.

In the 0.5 Ωcm device, the sum of all base series resistances is small and account for about 0.06 Ωcm^2. Again, we apply the diode network model to estimate the FF-loss which is about 0.3 % due to the total base series resistance.

In contrast, the high base resistivity induces high resistive losses in the 5 Ωcm device. The sum of all base series resistance components is 0.54 Ωcm^2. The resulting FF-loss is about 3.2 % which is the reason for the large FF-differences between both devices.

The calculated total series resistances of 0.50 Ωcm^2 and 0.98 Ωcm^2 fit well to the experimentally derived lumped series resistance at MPP of 0.52 Ωcm^2 and 0.97 Ωcm^2 of the 0.5 Ωcm and 5 Ωcm device, respectively (Fig. 6.3). However, the lumped series resistance of the 5 Ωcm solar cell declines for increasing V_{ext}. This behavior is caused by the decreasing wafer resistivity which depends on the carrier density inside the base. Note that the wafer resistivity ρ (conductivity σ) is a function of the majority carrier density: $\rho = \sigma^{-1} = (q\mu(N_A + \Delta n))^{-1}$, with μ the mobility of the majority carriers, N_A the base doping density, q the elementary charge and Δn the excess carrier density. Hence, it is the sum of N_A and Δn that determines the wafer resistivity.

In the 5 Ωcm device , the base doping density N_A accounts for 2.8×10^{15} cm^{-3}. The excess carrier densities inside the base at J_{sc}, 500 mV and 610 mV, account for 1.1×10^{13} cm^{-3}, 2.0×10^{13} cm^{-3} and 5.0×10^{14} cm^{-3}, respectively. The resulting wafer resistivity at J_{sc}, 500 mV and 610 mV is 5 Ωcm, 4.9 Ωcm and 4 Ωcm, respectively. As a result of the increased density of majority carriers between the maximum power point and open circuit conditions, the wafer resistivity decreases by a factor of about 0.8 (−20 %). All derived single base series resistances, linearly depend on the wafer resistivity (see Eqs. 4.17, 4.19 and 4.15). Multiplying the factor of 0.8 with the analytically calculated base series resistances of the 5 Ωcm device depicted in Tab. 6.5, the total device resistance decreases from about 0.98 Ωcm^2 to 0.87 Ωcm^2, a difference of 0.11 Ωcm^2. The experimentally derived series resistance of the 5 Ωcm device declines from 1.00 Ωcm^2 at V_{ext}=500 mV to about 0.70 Ωcm^2 at V_{ext}=610 mV, a difference of 0.3 Ωcm^2. The analytical calculation does not fully explain the resistance decline. Note that the current crowding at the LFC point contact induces the highest resistive losses inside the device. Any changes of the local excess carrier density or displacements of the current transport into the LFC for increasing V_{ext} would result in different R_s-contributions of this device component. [1]

In the 0.5 Ωcm device, the base doping density N_A accounts for 3.3×10^{16} cm^{-3}. The excess carrier densities inside the base at J_{sc}, 500 mV and 610 mV, account for 1.3×10^{13} cm^{-3}, 1.6×10^{13} cm^{-3} and 5.6×10^{13} cm^{-3}, respectively. The resulting wafer resistivity is constant and accounts for

---

[1] The "firing" of LFC point contacts is a technological challenge. Too few laser pulses result in low or nonexistent contact resistances between the aluminum and the wafer substrate. Too many laser pulses can isolate the inner LFC contact area which would result in an LFC which is exclusively contacted at its outside perimeter. This situation would appear if the inner contact area is not covered by aluminum and does not exhibit an aluminum BSF. Furthermore, variations of applied laser parameters determine the contact topography and might have an influence of the voltage dependent R_s. Summarized, the semiconductor-aluminum contact resistance might depend on the injection regime in the scenario of LFC contacts. The field of semiconductor-metal contact is currently under investigtion and is not discussed in detail within this thesis.

0.5 Ωcm at all operating conditions. However, there is a small decline of the experimental lumped R_s shown in Fig. 6.3 ($\varDelta R_s$=0.15 Ωcm^2). Again, this behavior might be due to resistive losses at the LFC which are not analytically derived in this context.

The present chapter discusses two devices that feature a small EWT-index of 1150 µm. The smaller the EWT-index, the greater the time of laser-structuring processes [39]. In the majority of published cases, EWT solar cells feature indices greater than 1300 µm. These indices result in even larger resistive and FF losses than in the present scenario. Two important strategies can be applied to increase the FF. Firstly, the base dopant density is increased which leads to lower resistive losses and higher recombination losses based on the boron-oxygen complex. This strategy is applied in the present chapter. Secondly, a large area back surface field is integrated at the base area at the rear side. This BSF lowers the total base resistance even in the scenario of lowly doped substrates as discussed in the next chapter.

6.5 Device simulation

A description of the three-dimensional numerical EWT model is given in section 4.4.2 on page 37. The local base contacts are simulated by a boron doped Gaussian diffusion profile with a depth of 1.5 µm and a peak concentration of 3×10^{19} cm^{-3}. The simulated I-V-curve parameters are depicted in Tab. 6.6.

The applied three-dimensional model allows the discussion of single recombination current densities of the device. The total device volume is respected featuring all lateral current transports of minority or majority carriers. The model identifies the dominant loss currents of the device. In this section, we discuss the internal current transport of EWT devices associated with the single recombination currents.

Table 6.6: Simulated I-V-parameters of the 0.5 Ωcm and 5 Ωcm EWT devices calculated by means of the 3d numerical EWT SENTAURUS model. The FF gap of about 4 % between the experimental (see Tab. 6.3) and simulation results is due to resistive losses of the rear side metallization and due to the laser damaged edges of the fabricated devices. Both FF-loss mechanisms are not considered in the numerical model.

ρ (Ωcm)	J_{sc} (mA/cm^2)	V_{oc} (mV)	J_{mpp} (mA/cm^2)	V_{mpp} (mV)	FF (%)	η (%)
5	39.7	615	37.6	515	79.3	19.4
0.5	38.5	614	37.0	529	82.8	19.6

6.5.1 Short-circuit current-density

The short-circuit current-density J_{sc} is smaller than J_{gen} due to recombination losses. Our simulations yield J_{gen}=41.0 mA/cm^2 and show that J_{sc} is reduced primarily due to recombination in the front emitter and in the base:

$$J_{sc} \approx J_{gen} - J_{loss,e,front} - J_{loss,b} \tag{6.1}$$

The three-dimensional numerical EWT model simulates the J_{sc} with a precision of 0.2 mA/cm^2 (Tab. 6.6) compared to the experimental results of both solar cells (Tab. 6.3). The 50 Ω/□ front emitter has a phosphorus density at the surface of 2×10^{20} cm^{-3} and a junction depth of 350 nm and, according to our simulations, contributes to $J_{loss,e}$ =0.8 mA/cm^2 mainly via Auger recombination. Since both fabricated cells have the same emitter, variations in J_{sc} are mainly caused by recombination in the base. The simulations show that $J_{loss,b}$ accounts for 0.5 mA/cm^2 in the 5 Ωcm and 1.5 mA/cm^2 in the 0.5 Ωcm scenario.

6.5.2 Open-circuit voltage

Generally, V_{oc} is sensitive to the amount of recombination which, in turn, may be influenced by the transport properties of the free carriers. Considering the measured geometrical cell parameters (Tab. 6.1), the dopant diffusion profiles, together with the basic model parameters for Si (effective intrinsic density [62], mobility [127], Auger [70], and radiative [76] recombination), the SRH lifetime according to Eq. 3.19, and a recently established model for surface recombination [122, 126], the numerical simulation model reproduces the experimental V_{oc} with a precision of 3 mV without adjusting any parameters.

6.5.3 Loss mechanisms of the fill factor

The FF-loss due to the damaged edge emitter and the rear side metalization is not considered in the numerical EWT model. Hence, the simulated FF are greater than the experimental FF. The FF-difference of both devices between the simulation and the experimental (measured) results is similar and accounts for $\varDelta FF \approx 4$ %. By considering the edge recombination of the experimental devices, the absolute FF gap accounts for ≈ 3 % for both the cells. This result indicates that the laser-fired-point are simulated with a certain deviation. As mentioned above, the simulation model considers the LFC by a Gaussian diffusion profile which results in low ohmic contact resistance and guarantees a stable simulation model. However, the absolute differences between simulation and experiment are similar for both the cells fabricated on 0.5 and 5 Ωcm substrates. For this reason, the numerical model respects the specific loss mechanisms based on the internal current transports, the device resistances and recombination parameters, all of them existing in both solar cells

6.5.4 Simulated internal current transport and recombination currents

At short-circuit conditions, the minority electrons are collected from the base region by both the front and the rear emitter, and mainly due to diffusion. Therefore, the electron density profile has a distinct maximum within the base region, from where the electrons flow toward either the front or the rear junction. In the present three-dimensional scenario, this maximum shall be referred to as demarcation area, as shown in Fig. 6.4. When sweeping the external voltage from the short-circuit to the open-circuit condition, the demarcation area moves toward the front, because the rear collecting current path offers a lower resistance for the electron transport.

The influence on FF can be quantified by:

1. Integrating the Auger and SRH recombination rates separately in the front and rear collecting volume;

2. A multiplication by q, which turns these quantities into recombination currents; and

3. noting that they become directly comparable to the I-V-curve (i.e., the total recombination losses) if the 1 sun I-V-curve is shifted by J_{gen} into the first quadrant as is shown in the top panel of Fig. 6.5.

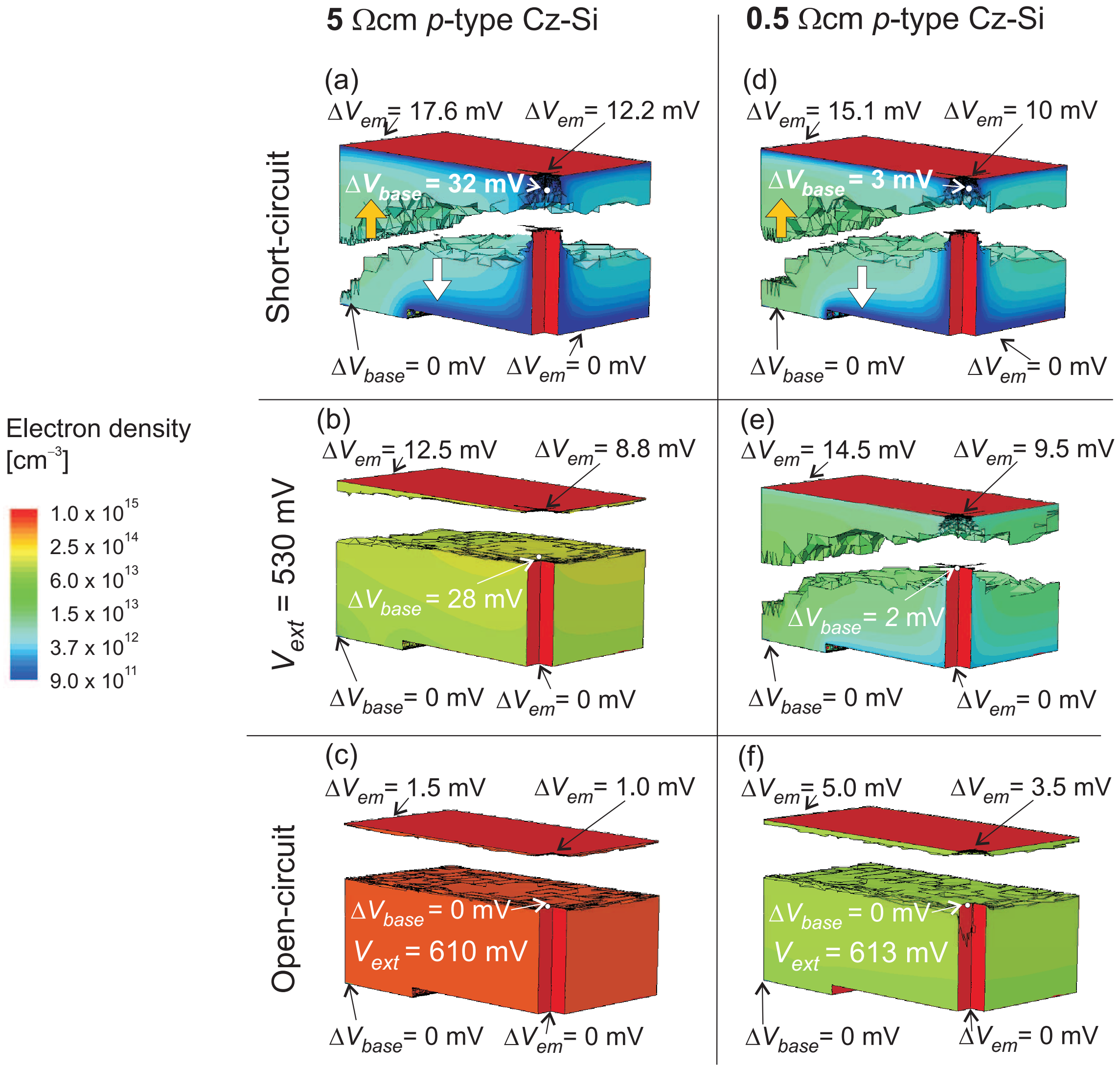

Figure 6.4: Simulated electron densities in the EWT solar cells. The domain is split into two regions at the location where the electron density in the base region is maximal, to visualize the demarcation area. This area divides the front collecting from the rear collecting part of the base, as indicated by the filled-in arrows in the upper panels. The left and right columns show the results for a base resistivity of 5 and 0.5 Ωcm, respectively. The three rows represent the operation conditions at short-circuit, at 530 mV and at open-circuit, respectively. Also indicated are the electric potentials V_{em} along the emitter and V_{base} in the base of the solar cell. The values of ΔV_{em} denote the voltage drop between the external voltage at the rear emitter contact and the front emitter (near the EWT-via and at the midpoint between neighboring EWT-vias). The values of ΔV_{base} denote the voltage drop between the external voltage at the rear base contact and the base near the EWT-via.

By means of the demarcation area, recombination losses can be analyzed in the front or rear collecting part of the solar cell. This offers the possibility to identify the part with the dominant losses that limit the EWT device efficiency. The greater the partition of a certain type of recombination on the total recombination current ($J_{rec,i}/J_{rec,total}$), the greater its impact on the shape of the I-V-curve and, hence, on the FF. An example is given in Fig. 3.2 on page 20.

The volume above the demarcation area is denoted as the front diode, and the volume below the demarcation as the rear diode. Since the position of the demarcation area depends on the external voltage, the volume of the front and rear collecting diodes is also a function of V_{ext}. As a result, the absolute recombination current densities of the front and rear collecting diode depend on the effective lifetime, the excess carrier densities **and on the volume** as explained by Eq. 3.38.

In order to discuss this fact, we assume three concrete examples:

1. We assume a constant effective lifetime and a constant diode volume for increasing external voltages. In the absence of series and shunt resistances, this results in a recombination characteristic with a constant local ideality factor since the excess carrier density exponentially increases with n=1.

2. We assume a constant effective lifetime and a diode volume that decreases for increasing external voltage. In the absence of series and shunt resistances, this results in a recombination characteristic with a local ideality factor greater than unity. The excess carrier density still increases with an exponential pace and a local ideality factor of unity. However, the total recombination current density is affected by the decreasing diode volume for increasing external voltages. As a result, the recombination current increases in a sub-exponential pace (n>1).

3. The inverse scenario is achieved by a diode volume that increases for increasing external voltage. Here, the local ideality factors of the total recombination current are greater than unity.

External voltage range from 0 to 400 mV

In this voltage range, the simulated recombination current densities of both solar cells in Figs. 6.5(a) and 6.5(c) remain horizontal. Both demarcation areas remain fixed at a position near the middle of the base (Fig. 6.4, upper row), and the SRH recombination losses have similar magnitudes in the cell's front and rear collecting regions (Figs. 6.5(a) 6.5(c)). Despite this, the front region contributes far more to J_{sc} (36 or 35.1 mA/cm^2 in the 5 or 0.5 Ωcm cell, respectively) than does the rear collecting part (3.6 mA/cm^2 in both cases). The referring values are indicated as EWT-via current which is the current collected by the front diode and transported through the EWT-via to the rear emitter. This implies that near short-circuit condition, both cells operate mainly as front collecting cells. The high current-densities, collected by the front emitter, cause potential drops. Apart from the drop along the front emitter toward the EWT-vias (approximately 6 mV) the drop along the via-emitter accounts for 12 mV in the 5 Ωcm and 10 mV in the 0.5 Ωcm scenario (see Figs. 6.4 (a) and (d)). Furthermore, the long current paths of majority carrier in the solar cell bulk induce voltage drops that account for 32 mV in the 5 Ωcm and 3 mV in the 0.5 Ωcm scenario. The relation of ten between both base voltage drops in the 5 Ωcm and 0.5 Ωcm scenario results from the two different base dopant densities (wafer resistivities) that also differ by a factor of ten.

External voltage higher than 400 mV

The front emitter still has a higher potential than the rear emitter. Because of the higher potential at the front emitter in both cells, the separation of the quasi-Fermi levels is larger at the front pn-junction than at the rear pn-junction near the metal contacts:

$$V_{ext} \approx E_{Fn,rear} - E_{Fp,rear} < E_{Fn,front} - E_{Fp,front} \tag{6.2}$$

where $E_{Fn,rear}$ and $E_{Fp,rear}$ denote the electron and the hole QFL, respectively, at the rear pn-junction near the metal contacts. Accordingly, the band bending across the pn-junction is smaller at the front, and more excess carriers Δn are injected across the front-junction into the base than from the rear emitter. This leads to a higher SRH rate $U_{SRH}=\Delta n/\tau_{SRH}$ within the front diode.

The 5 Ωcm cell is examined by means of Figs. 6.4 (left column), Figs. 6.5(a) and 6.5(b). At $V_{Shift,1}$ ≈440 mV (marked as black cross in Figs. 6.5(a) and 6.5(b)), the demarcation area starts

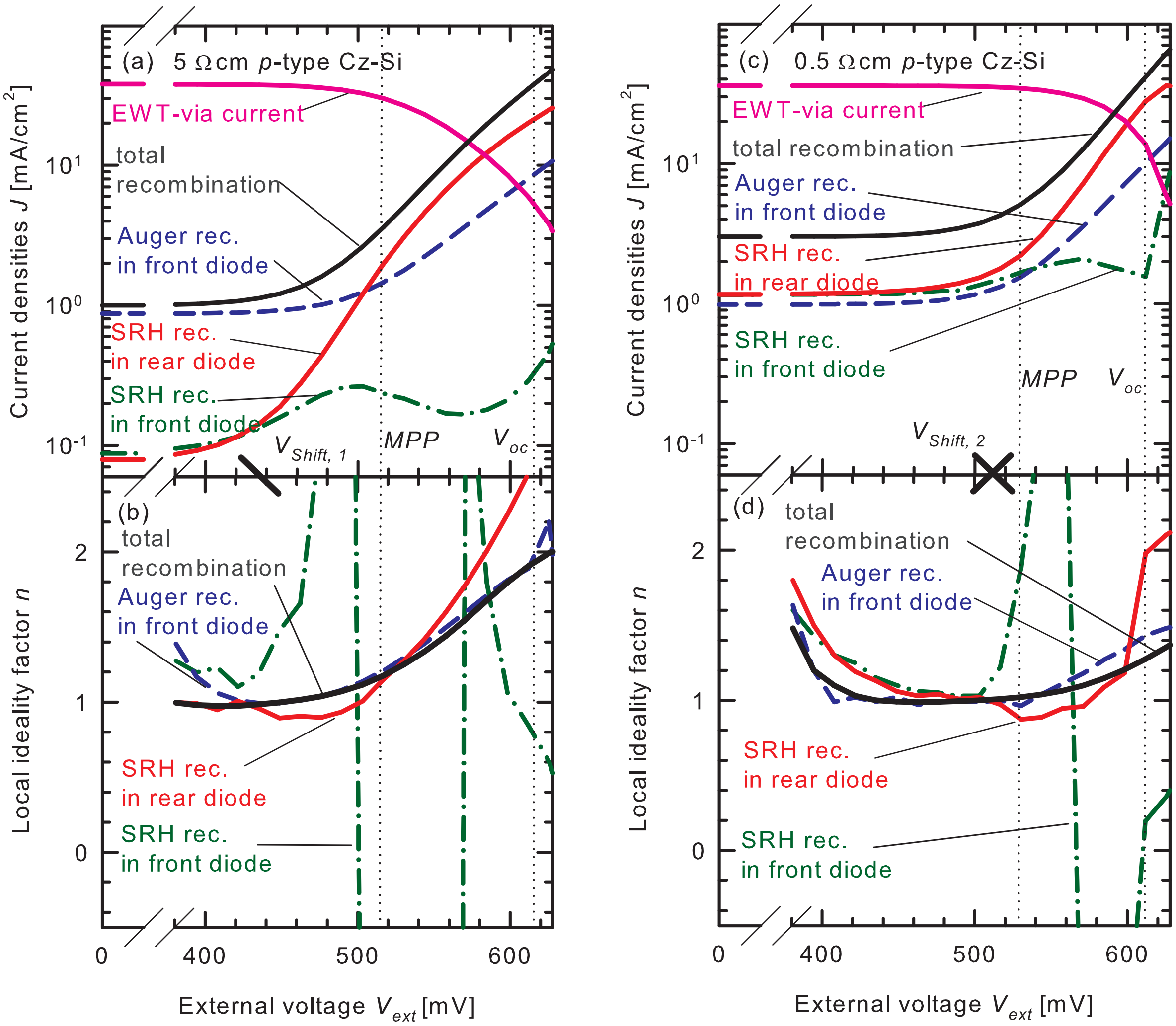

Figure 6.5: Simulated recombination losses (top panels) and local ideality factors of the recombination characteristics (bottom panels) of the EWT cells with a base resistivity of 5 Ωcm (left) or 0.5 Ωcm (right). The single recombination mechanisms (SRH in the front and rear collection regions, and Auger in the front emitter) can be directly compared to the main recombination losses in order to estimate the impact on the I-V-curve of the total device. To obtain the local ideality factors, each recombination current is shifted by its contribution at V_{ext}= 0mV as explained by Eq. 3.48. The sum of all shifted recombination currents results in the J_{sc}-shifted illuminated I-V-curve. Also shown is the current-density flowing from the front to the back of the cell through the EWT-via emitter and the external voltages V_{Shift} (marked as black crosses) at which the demarcation area in Fig. 6.4 begins to shift.

shifting toward the front emitter, and the front collecting volume decreases rapidly with increasing V_{ext}. As a consequence, the integrated recombination losses increase slowly. At a bias above 500 mV, the volume decreases so rapidly that the integrated recombination losses decrease even down to 8% of the total losses at *MPP*, leading to a negative ideality factor n of "SRH-front" in Fig. 6.5(b). In contrast, the rear collecting volume expands with increasing bias up to external voltages of 530 mV. Additionally, Fig. 6.5(a) shows that the SRH recombination in the 5 Ωcm EWT solar cell starts increasing at lower external voltages. The reason for this is that for a given external bias, the difference between the quasi-Fermi level of the minority carriers and the corresponding band edge $E_{F,n} - E_C$ in p-type Si is smaller in case of higher resistivity (e.g., 5 Ωcm) than those for lower resistivity (e.g., 0.5 Ωcm) and, consequently, Δn increases more strongly with increasing V

in high-resistivity material according to Eq. 3.8. If both the front and the rear *pn*-junction had the same potential, the shift in recombination from the front to the rear collecting diode would not affect the shape of the *I*-*V*-curve or the *FF* significantly.

Beside the EWT-via resistance, it is the base resistance that determines the carrier injection. In the 5 Ωcm scenario, the large voltage drop of 28 mV inside the base biases the barrier height at the front *pn*-junction. As a result, the carrier injection across the front *pn*-junction is increased compared to the 0.5 Ωcm scenario for external voltages smaller than V_{oc}. The adaption from high to low internal voltage drops inside the base results in the similar effect of non-ideal SRH and Auger recombination characteristics. A detailed analysis and improvement approaches are given in the next chapter.

The EWT-via resistance and the base resistance increases the front emitter potential and consequently the injection of electrons from the front emitter into the base as well as the injection of holes from the base into the front emitter.

Note that the voltage drop along the EWT-via and inside the base decrease with increasing V_{ext} (because less current flows through the via and through the base), which slows down the injection of excess carriers across the front *pn*-junction into the base (and into the rear collecting volume) with increasing V_{ext}.

Hence, the integrated SRH recombination in the rear collecting diode increases with respect to the external voltage V_{ext} at a slower pace (local ideality factor n>1) than would be expected from an ideal diode behavior with n=1. Consequently, the recombination characteristics of the 5 Ωcm EWT solar cell in Fig. 6.5 show local ideality factors higher than 1 for V_{ext}>500 mV.

Beside SRH recombination in the bulk, Auger recombination in the front collecting part (mostly in the front emitter) has a strong impact on the *I*-*V*-characteristics of our EWT cells (see Figs. 6.5(a) and 6.5(c)). The dependence of the Auger recombination rate on V is dominated by the injection of holes from the base into the front emitter. According to Eq. 3.14, it is the *eeh*-process that determines the recombination in the (front) emitter. The potential across the front junction increases at a slower pace than V_{ext}, and so does the Auger recombination rate due to a weaker injection of holes, as compared to the rear emitter. Again, this causes that also the Auger recombination in the front part of the device has a non-ideal relation with the external voltage V_{ext}. Since Auger recombination in the front emitter exhibits a large component of the total device losses with ideality factor values above 1, the total *I*-*V*-curve is affected. Figures 6.5(b) and 6.5(d) show that the Auger recombination current has n=2 at V_{oc} in the 5 Ωcm cell and n=1.4 at V_{oc} in the 0.5 Ωcm cell.

The Auger recombination in the rear collecting diode (not shown in Fig. 6.5) is dominated by the Auger recombination in the rear emitter. The rear emitter is directly contacted by the external contacts and consequently there is a lower potential difference between the external contact and the rear emitter. The resistive "decoupling" of the front emitter by the EWT-via resistance is therefore not present for the rear emitter. Consequently, the Auger recombination of the rear emitter exhibits a less disturbed recombination characteristic.

The 0.5 Ωcm EWT solar cell shows a different behavior due to is lower series resistance. Its demarcation area starts shifting at higher voltages (Fig. 6.4, right column) indicated by the increased $V_{Shift,2}$ =510 mV (Figs. 6.5(c) and 6.5(d)). The non-ideal recombination behavior of SRH and Auger recombination is observed by slightly enhanced local ideality factors for higher voltages V_{ext}>510 mV that are closer V_{oc}. The *I*-*V*-characteristics is less deformed and the *FF* is higher (see Tab. 6.3) compared to those of the 5 Ωcm cell.

6.5.5 Comparative simulation with lower EWT-via sheet resistances

In order to compare the impact of the EWT-via resistance on the *I*-*V*- curve parameters, we take the similar set of geometrical EWT device parameters as depicted in Tab. 6.1. The recombination parameters are equal, too. As the only difference, the EWT-via emitter sheet resistance is reduced from 50 to 15 Ω/□. In the case of 5 Ωcm and 0.5 Ωcm base resistivity, this leads to a *FF*-gain of 0.6 % absolute compared to the simulation results in Tab. 6.6. J_{sc} and V_{oc} are not affected by the modification of $R_{em,via}$. The impact of a slightly higher emitter recombination on the total *I*-*V*-characteristics is small since the EWT-via surface is only 5 % of the total emitter area of the device. However, reducing the base resistivity from 5 to 0.5 Ωcm causes a *FF* gain by about 3.6 % absolute, and is therefore a succesful strategy for improving the *FF*. Doping more highly reduces the transport losses of majority carriers.

6.6 Discussion of the minority carrier transport

In the following section, it is shown that decreasing the base resistivity has important consequences on the minority carrier density in the base which affects the current transport of carriers. In contrast, the implementation of a strong EWT-via diffusion hardly affects the carrier transport. An illustrative, one-dimensional network explaines the transport of minority carriers in the base of the EWT solar cells. The network is not qualified for a quantitative analysis of an EWT device. However, it improves the understanding of the transport mechanisms.

6.6.1 Resistive interpretation of the internal current transport

From the above discussion, it follows that the *FF* behavior is due to the high device resistances. The impact on the single recombination characteristics has been discussed by the evolution of the local ideality factors. The shifting of the demarcation area describes the internal current transport. To explain the shift in the demarcation area, it is analyzed in the following by means of analytical expressions, under which conditions photogenerated electrons are driven to the rear emitter contact either across the front or the rear collecting junction.

Generally, electron and hole currents are driven by the gradient of the quasi-Fermi-levels (see Eq. 3.11 [56]). This means that electron and hole currents are driven by the gradient of their concentration and by an electric field which is the gradient between two electrical potentials. In the case of an EWT solar cell fabricated on *p*-type silicon wafers, photogenerated electrons must be transported to the rear emitter contact. At short-circuit conditions, most electrons are collected at the front *pn*-junction and transported through the EWT-via emitter by the potential gradient (electric field) between front emitter (at a higher potential) and the rear emitter (at a lower potential).

The conductivity σ for electrons in the *p*-type base is a direct function of the electron density n:

$$\sigma = qn\mu_n, \tag{6.3}$$

with μ_n the electron minority carrier mobility. In the scenario of high electron carrier densities in the wafer, the base can offer a higher conductance σ (lower resistivity $\rho = 1/\sigma$) for the electron transport than the front and EWT-via emitter.

The conductivity for electrons in the *p*-type base is not ohmic. It exponentially depends on the electron carrier density n which is a function on the bias and the dopant density (see Eq. 3.6). As a result, the conductivity for electrons in the base at one defined voltage is higher in the 5 Ωcm device than in the 0.5 Ωcm device since the electron density is higher (see Eq. 3.8). At the same time, the recombination losses increase since electrons are minority carriers and can recombine in the bulk. On the other hand, a lowly doped bulk exhibits a high resistivity for majority carriers which leads to higher resistive losses for minority carriers and, hence, *FF*-losses. An illustrative view of the resistive network for minority carriers in EWT solar cells in shown in Fig. 6.6.

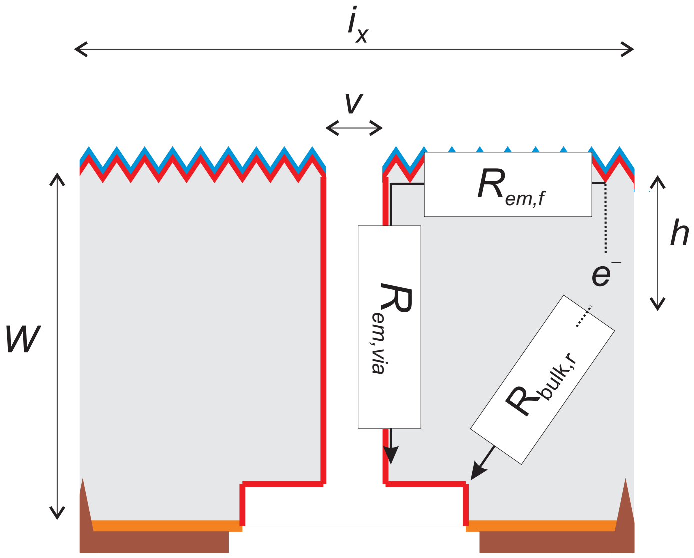

Figure 6.6: Equivalent circuit of resistances experienced by the electrons flowing through the front or rear collecting part in the EWT cell, where $R_{bulk,r}$ represent the minority carrier resistance.

It is assumed that electrons suffer from a lumped ohmic resistance in the front emitter and in the EWT-via emitter on their way to the rear emitter contact. When electrons flow across the front collecting current path, the resistance mainly depends on the front emitter and EWT-via emitter resistances. In the present solar cell fabrication, both emitter sheet resistances, R_{front} and R_{via}, are 50 Ω/□. The internal current transport of minority carriers has been divided in a path for electrons that diffuse to the front or rear emitter, respectively. The resistance of electrons in the rear collecting current path depends only on the non-ohmic minority carrier resistance $R_{bulk,r}$:

$$R_{bulk,r} = \left[\frac{W-h}{q\mu_n n i_x d_y} \right] i_x d_y \tag{6.4}$$

where $(W-h)$ is the distance between the point of photogeneration to the nearest point of the rear emitter. Equation 6.4 assumes a linear transport of minority carriers toward the rear emitter. It is a simplified scenario. Technologically, it can be achieved by a rear emitter that covers the largest part of the solar cell rear side. The lateral current flow of electrons would be zero since all minority carrier directly (vertically) diffuse toward the rear emitter.

The resistance of electrons in the p-type base is denoted as "minority carrier resistance" and influences the minority carrier transport in the bulk [152]. The dependence on the electron carrier density in Eq. 6.4 can be translated in a dependence of the external voltage V_{ext} at the pn-junction by using Eq. 3.8. Note that the electron density in the bulk is not constant for low voltages between J_{sc} and MPP. Hence, Eq. 6.4 is an approximation that holds for the scenario with equally distributed electron carrier concentrations in the base. This is the case for external voltage around MPP up to V_{oc}.

Figure 6.7 shows these calculated resistances of both current paths as a function of V_{ext} for an electron that is generated at a depth of 120 µm above the base contact. In the case of the 5 Ωcm-cell up to external voltages of 450 mV, the front collecting current path offers a lower resistance (black dotted line in Fig. 6.7) than the rear collecting path (black solid line), and hence electrons are preferably transported across the front emitter.

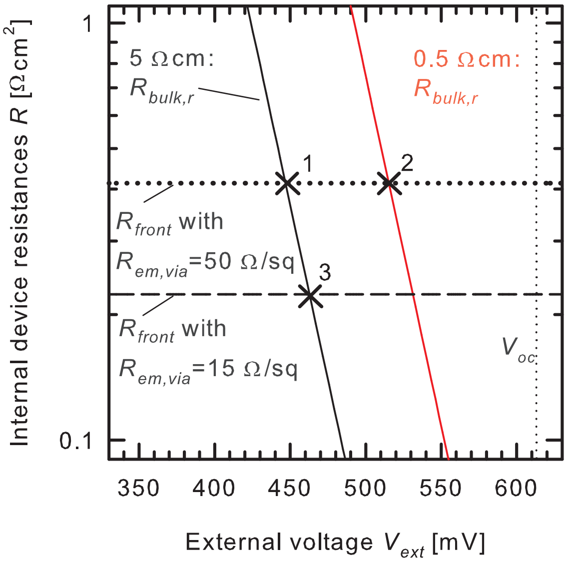

Figure 6.7: Calculated resistance of the front R_{front} and rear collecting current path $R_{bulk,r}$ in an EWT cell, shown in Fig. 6.6, with a base resistivity of 5 Ωcm (black) or 0.5 Ωcm (red) and for two different EWT-via sheet resistances of 50 and 15 Ω/□, as a function of V_{ext}. The two crosses 1 and 2 correspond to the V_{Shift} values in Fig. 6.5.

Equation 3.8 shows that the electron density in lowly doped (5 Ωcm) base material increases at a higher pace than in highly doped (0.5 Ωcm) base material with increasing V. For 5 Ωcm (0.5 Ωcm), at V_{ext}=450 mV (510 mV), the minority carrier resistance in the bulk $R_{bulk,r}$ becomes smaller than the sum of ohmic resistances of the front and EWT-via-emitter and electrons are preferably transported through the bulk to the rear contacts. These two intersections are marked as cross "1" for 5 Ωcm and cross "2" for 0.5 Ωcm in Fig. 6.7 and correspond to the external voltages $V_{Shift,1}$ in Fig. 6.5(a) and $V_{Shift,2}$ in Fig. 6.5(c) at which the demarcation areas begin to shift toward the front of the solar cell.

V_{Shift} can be pushed toward higher external voltages by two major ways (see Fig. 6.7):

- Reducing the emitter sheet resistance in the EWT-via and/or of the front emitter: As an example, the EWT-via emitter sheet resistance is reduced from 50 to 15 Ω/□ in Fig. 6.7).
- Reducing the wafer resistivity and consequently minority carrier density in the bulk (cross "1" to "2" in Fig. 6.7)

Reducing the emitter sheet resistance in the EWT-via has a moderate effect on V_{Shift} (compare cross "1" and "3" in Fig. 6.7). The minority carrier concentration in the bulk increases exponentially with the applied voltage. Consequently, the minority carrier resistance decreases exponentially since it is proportional to minority carrier concentration. The shift between cross 1 and 3 is very small. Highly diffused front emitters will reduce the voltage drop but exhibit large Auger recombination currents that reduce J_{sc} and V_{oc}. $R_{bulk,r}$ in Fig. 6.6 is the determining resistance for the current transport for minority carriers in EWT solar cells.

6.7 Conclusions

Experimental results of EWT solar cells have been reproduced by a diode network that considers the recombination loaded device components and the total device series resistance. High EWT device resistances have been identified to be responsible for typically low *FF*. One detrimental resistive contribution is caused by the lateral current transport of photogenerated majority carriers inside the base. The *FF* and the device efficiency of the solar cell featuring a highly doped wafer substrate (0.5 Ωcm) can be increased compared to those of the solar cell with a higher wafer resistivity (5 Ωcm). The efficiency improvement is mainly due to the lower resistive and lower resistance induced recombination losses of photogenerated majority and minority carriers around *MPP*, respectively.

The present advantage of highly doped Cz-Si wafers holds for the chosen geometries, the specific bulk lifetimes, the diffused phosphorus emitters and the applied passivation and contact schemes. As a disadvantage, highly doped Cz-Si wafers exhibit low bulk lifetimes that results in higher recombination currents at J_{sc}-conditions compared to scenarios with a lowly doped substrate and an increased τ_{bulk}. Consequently, the J_{sc} is lower in highly doped substrates (0.5 Ωcm) compared to the lowly doped scenario (5 Ωcm).

The internal current transport of EWT solar cells are discussed by means of a 3D numerical device model. The density of minority carriers determines the conductivity of the minority carrier transport inside the base. The external voltage bias the minority carrier density in the base and, as a consequence, the minority carrier resistance. For external voltages between *MPP* and V_{oc}, the carrier density is increased and the minority carrier resistance in the base is reduced compared to J_{sc}-conditions. A greater partition of photogenerated minority carriers is directly transported toward the rear collecting emitter. The demarcation area moves toward the front. A stabilization of the internal current transport is achieved by the application of highly doped wafer substrates. The respective solar cells exhibit lower carrier densities inside the base compared to EWT devices fabricated on lowly doped substrates.

7 Back surface fields: An approach for improving the fill factor and the efficiency of EWT solar cells

7.1 Introduction

The previous chapter discussed the relation between the base doping density, the internal current transport and the fill factor loss of EWT solar cells. High *FF* are achieved for low base resistivities that reduce the series resistances of long lateral transport path of majority carriers inside the base. However, doping more highly also leads to a stronger lifetime degradation via boron-oxygen complexes in boron-doped Cz-Si material.

An alternative strategy for increasing the *FF* is investigated in this chapter: the integration of a back surface field (BSF) constitutes an additional current path with a high conductivity, connected in parallel to the solar cell base. As an advantage, lowly-doped Cz-Si wafers can be used, which experience less lifetime degradation.

The following investigations expose the impact of a BSF on the majority carrier transport and on the minority carrier recombination losses. It is shown that the integration of a BSF reduces the resistive losses of majority carriers. As a consequence, the voltage drop inside the bulk is reduced. This leads to lower excess carrier densities and to lower recombination losses in the voltage range between 400 mV and V_{oc} compared to EWT solar cells featuring laser fired contacts.

Experimental results of EWT solar cells, fabricated on boron-doped Cz-Si wafers with two different base doping densities are discussed by means of the I-V-characteristics, the diode network depicted in Fig. 4.3 and three-dimensional SENTAURUS simulations.

7.2 Solar cell fabrication

All EWT solar cells in this chapter are fabricated by an identical process sequence depicted in Fig. 7.1. The fabrication process is not meant to be suitable for industrial production. Rather, it is chosen to be highly flexible and allows parallel processing of several small solar cells with a high number of process variations on a single wafer. As in the previous chapter, boron doped Cz-Si wafers are selected with two base resistivities of 0.8 Ωcm and 3.5 Ωcm, respectively. The two base resistivities represent a lower and an upper limit that is used for the fabrication of solar cells on boron-doped Cz-Si wafers. The right column in Fig. 7.1 depicts the process variation of EWT solar cells featuring a boron-diffused BSF. The left column in Fig. 7.1 depicts the process sequence where a line of LFC forms the contact between the solar cells bulk and the aluminum metalization [144], same as in the previous chapter. These solar cells do not incorporate any further BSF beside the small aluminum doped area around the LFC. To keep nomenclature simple, the solar cells featuring either laser fired contacts (LFCs) or a large-area boron-doped back surface field (BSF) are simply called "LFC" or "BSF solar cell". The geometrical device parameters are listed in Tab. 7.1. The process sequence is as follows and depicted in Fig. 7.1:

(a) SiN with a refractive index of 1.9 and a thickness of 100 nm is deposited on both sides of damaged-etched wafers.

(b) At the rear side of the BSF device precursors, square patterns with an area of 2.4×2.4 cm^2 are opened by pico-second (ps) laser radiation (λ=532 nm, τ_{pulse}=10 ps, $E_{pulse}=5\times10^{-6}$J) within the 2.5×2.5 cm^2 sized solar cells. The remaining 1 mm wide SiN diffusion barriers define non-diffused regions at the edges where the solar cells are separated by laser cutting at the end of the process. The laser damage is removed in aqueous KOH solution. The LFC device precursors remain non-opened.

(c) A BBr_3 diffusion at 890 °C provides a BSF with a sheet resistance of 75 $\Omega/\square$[1]. The rear side of the solar cells featuring LFCs is protected by the SiN diffusion barrier and remains non-diffused. Hence, every solar cell presented in this chapter has a similar thermal budget to avoid unwanted differences in the electronic properties of the devices.

(d) All SiN layers and BBr_3 diffusion residues are removed in hydrofluoric acid. Again, SiN with a refractive index of 1.9 and a thickness of 100 nm is deposited on both sides of the wafers.

(e) At the rear side, SiN is locally ablated by laser radiation to define the rear emitter pattern. At the front side, areas of 2.1×2.1 cm^2 are ablated by laser power to define the front emitter opening. EWT-vias are laser drilled by a disc-laser system (λ=1030 nm, τ_{pulse}=1 µs, $E_{pulse}=1.5\times10^{-3}$J). The laser damage in Si is removed in a 50 % KOH solution for 10 min at 90°C.

(f) A phosphorus emitter with a sheet resistance of R_{sq}=50 $\Omega/\square$ is diffused at 880 °C with a $POCl_3$ diffusion in a tube furnace.

(g) All diffusion residues and SiN layers are removed in 40 % HF solution.

(h) Al_2O_3 with a thickness of 20 nm is deposited at the rear side by means of plasma-assisted atomic layer deposition (ALD) [31], followed by an anneal in N_2 atmosphere at 400 °C for 15 min to activate the Al_2O_3 layer. An 80 nm thick SiN layer with a refractive index of 1.9 is deposited on top of the Al_2O_3 at the rear side acting as reflection layer to increase the generation current density.

(i) At the front, a double layer of SiN is deposited. The refractive index is 2.4 in the first 10 nm to achieve good passivation properties, and 2.05 in the following 80 nm to obtain an antireflection coating.

(j) Emitter contact openings are wet-chemically etched in 5 % HF. Therefore, a hotmelt ink is printed with an inkjet system. At the front, the hotmelt ink covers the entire surface to protect the dielectric passivation scheme. At the rear, 3 % of the emitter is kept open to etch off the Al_2O_3-SiN double layer. Additionally, the solar cells with a BSF obtain ps-laser contact openings at the boron-diffused surfaces with a partition of 3 %. Isopropanol dissolves the hotmelt ink at 55 °C.

(k) At the rear, a 13 µm thick Al layer is evaporated, followed by a 300 nm thin layer of SiO_x, which acts as an etching barrier.

(l) The flanks between emitter and base are selectively etched off [45] because they are less protected by the SiO_x layer due to its columnar growth. This separates the emitter from the base regions [39, 143].

(m) In the left column of Fig. 7.1, local base contacts [144] are formed by a nano-second slab-laser (λ=355 nm, τ_{pulse}=20 ns, $E_{pulse}=200\times10^{-6}$J). The single LFCs are shot in a line at the center of the base area.

(n) Finally, annealing at 320 °C for 1 min on a hot plate improves the surface passivation and the contact resistances.

---

[1] Hacke et al. proposed an industrial process sequence that features a boron-doped diffusion barrier. The barrier is used as a BSF diffusion source at the base area during a phosphorus emitter diffusion process [153]. The resulting BSF sheet resistance has been between 1000 and 2000 $\Omega/\square$ which hardly reduces the total base resistance.

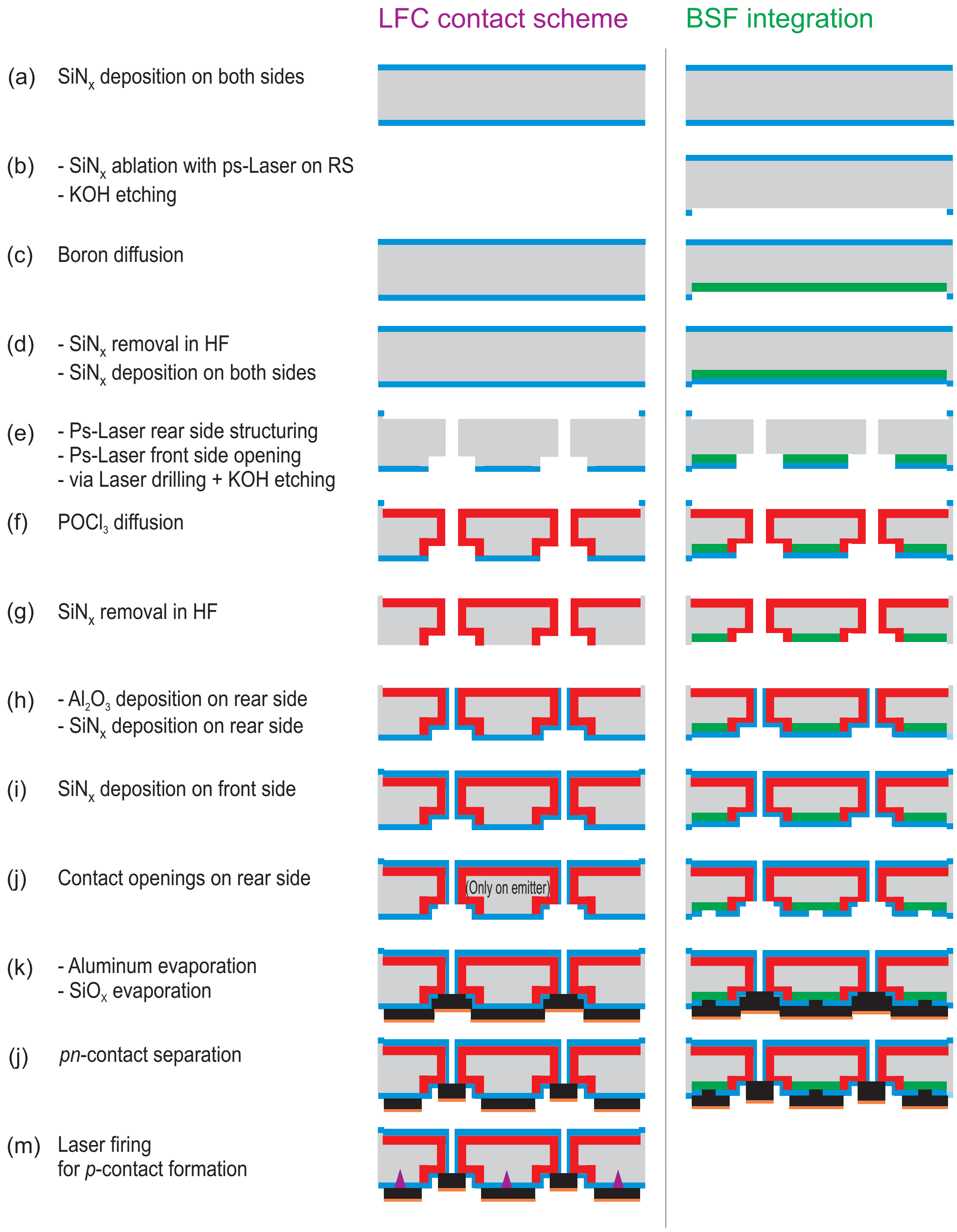

Figure 7.1: Fabrication sequence of p-type Cz-Si EWT solar cells having either a line of LFC at the center of the base area (left column), or a boron-diffused BSF that covers the entire base area (right column).

Table 7.1: Geometrical parameters of EWT solar cells fabricated on p-type Cz-Si having a BSF or LFCs.

General device parameters	Settings
Index i_x	1400 µm
Rear emitter e_x	700 µm
Base width $i_x - e_x$	700 µm
Distance d_y between EWT-vias	500 µm
EWT-via width $v_x = v_y$	85 µm
Wafer thickness W	180 µm
Ditch depth d	18 µm
Illuminated cell area	2 × 2 cm^2
Specific device parameters	**Settings**
BSF width b_{BSF}	700 µm
LFC diameter D_{LFC}	30 µm
LFC distance d_{LFC}	50 µm

7.3 Solar cell characterization

Four solar cells are examined, made from boron-doped Cz-Si wafers: the cells have either resistivities of 3.5 Ωcm or 0.8 Ωcm, and a BSF or LFC contact scheme, respectively, as shown in Fig. 7.1. As discussed in Section 6.3, bulk lifetimes of boron-doped Cz-Si wafers are limited by boron-oxygen complexes [25]. All solar cell parameters and measured lifetimes reported in this chapter refer to the degraded state and thus correspond to conditions under prolonged illumination. In order to determine the bulk lifetime of Cz-Si wafers after fabrication, all dopant diffusions are etched off, and all new surfaces are passivated with an Al_2O_3-SiN ($n_{SiN} = 1.9$) stack. Then, the samples are illuminated with light to degrade the lifetime after a possible regeneration process due to the temperature budget during the SiN deposition. Equation 3.29 is used to model the effective lifetime measured by means of QSSPC technique [148]. The effective surface recombination velocity of the Al_2O_3-passivation scheme is taken from Ref. [154]. Finally, equation 3.20 is used to calculate the injection-dependent τ_{SRH} recombination parameters of the bulk lifetime (shown in Tab. 7.2). The bulk diffusion lengths in low-level-injection (LLI) are calculated using $L_n = \sqrt{D_n \tau_n}$, where

Table 7.2: Fitted SRH bulk lifetime parameters τ_{n0} and τ_{p0}, the fitted interstitial oxygen concentrations O_i for a gettering factor m=2 and the respective electron diffusion constants D_n (at a temperature of 25°C) for 3.5 and 0.8 Ωcm boron-doped Cz-Si wafers, respectively. The bulk diffusion lengths for electrons L_n in LLI are calculated using: $L_n = \sqrt{D_n \tau_{n0}}$. All parameters have been achieved from boron-doped CZ-Si wafers that were exposed to the same high temperature steps of the solar cell process and after light-induced degradation as described in Refs. [26, 27].

ρ (Ωcm)	O_i (cm^{-3})	m (non-dimensional)	τ_{n0} (µs)	τ_{p0} (µs)	D_n (cm/s)	L_n (µm)
3.5	7.8 × 10^{17}	2	59	590	31.6	432
0.8	8.3 × 10^{17}	2	14	140	25.8	190

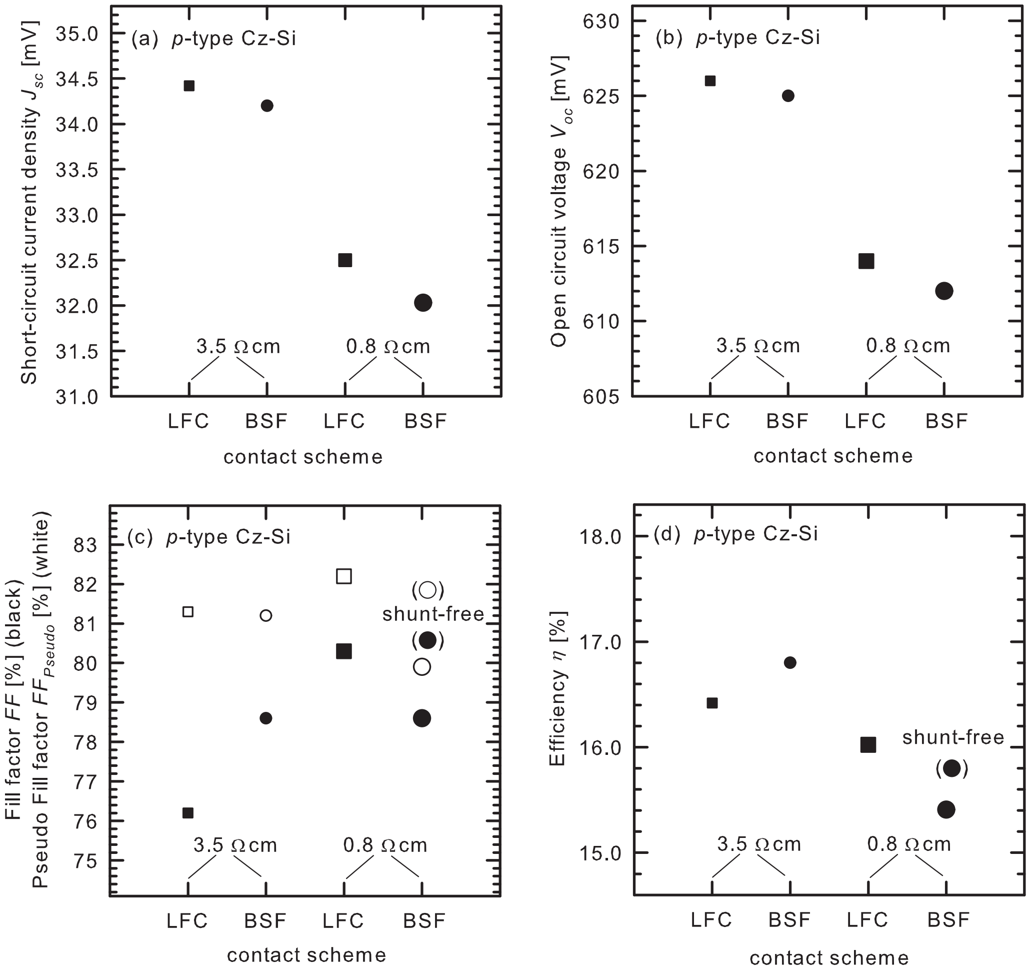

Figure 7.2: Experimental results of EWT solar cells, fabricated on boron-doped p-type Cz-Si wafers with a resistivity of 3.5 or 0.8 Ωcm, respectively. Both contact schemes, LFC or BSF, are indicated at the x-axis. The BSF device fabricated on 0.8 Ωcm p-type Cz-Si suffers from a shunt. In order to eliminate this technological issue, the shunt current is subtracted from the illuminated 1 sun I-V-curve and the J_{sc}-V_{oc}-characteristic. The resulting "shunt-free" FF, pseudo-FF and efficiencies are put in parenthesis.

D_n are the representative diffusion constants of electrons also shown in Tab. 7.2. The interstitial oxygen concentrations are calculated for a gettering factor of m=2, typically found in Cz-Si wafers after $POCl_3$-diffusion.

Figure 7.2 depicts the parameters of the experimentally achieved I-V-characteristics. All I-V-characteristics are measured at the Institute for Solar Energy Research Hamelin at 25°C. A halogen lamp approximating the am1.5g spectrum is applied for the illuminated and J_{sc}-V_{oc}-curves. The experimental J_{sc}-values are corrected by a spectral mismatch refinement [155, 99]. The J_{sc} is measured with an error of ±0.1 mA/cm^2, the V_{oc} with an error of ±1 mV and the FF with an error of ±0.1 %.

7.3.1 Short-circuit current-density

All experimental short-circuit current densities are reduced compared to J_{sc} of solar cells presented in the previous chapter. The reduction is due to the absence of a front side texturing. Reflection losses account for about 5 mA/cm^2 compared to the scenario of solar cells with wet-chemically etched random pyramids at the front side.

Figure 7.2(a) depicts a J_{sc}-gap of 2 mA/cm^2 between the 0.8 Ωcm and 3.5 Ωcm solar cells. 0.8 Ωcm Cz-Si wafers possess a higher density of boron-oxygen complexes and, hence, lower bulk lifetimes. The resulting bulk diffusion length of 190 µm is similar to the wafer thickness, causing significant recombination losses. The larger diffusion lengths of 432 µm in the 3.5 Ωcm scenario reduce SRH recombination losses at J_{sc} to a minimum as will be shown by simulation result in the next section.

Another reduction of J_{sc} is observed for both BSF solar cells compared to the respective LFC devices. The reason for this is the increased effective surface recombination velocity S_{eff} induced by the BSF. Hoex et al. investigated the effective surface recombination velocity of Al_2O_3 passivated non-diffused silicon wafers [31, 156]. Latest results showed values of S_{eff}≈6 cm/s on boron-doped FZ-Si wafers with a resistivity of 2 Ωcm [154]. The applied atomic layer deposition (ALD) technique for the deposition of Al_2O_3-layers is the same than those in the present solar cell process and, hence, results in similar S_{eff} for the non-diffused base areas of the LFC devices.

The boron-doped areas contribute to a higher recombination. Firstly, this is due to the Auger (and to a minor part SRH) recombination in the highly diffused layers. Secondly, the surface recombination velocity at highly diffused wafer surface is increased. Both effects result in an increased saturation current density and an increased effective surface recombination velocity of the boron-diffused layer. In the present scenario, the saturation current density of the BSF accounts for 50 fA/cm^2 measured by means of QSSPC techniques as described on page 13. For p-type semiconductors, the effective surface recombination velocity S_{eff} is given by Eq. 3.32. Using the dopant concentrations of both substrates and the saturation current density of the BSF $J_{0,BSF}$, the effective surface recombination velocities account for 13 cm/s and 60 cm/s for the 0.8 Ωcm and 3.5 Ωcm wafer, respectively.

S_{eff} is higher for the Al_2O_3-passivated boron-diffused BSF compared to the Al_2O_3-passivated non-diffused surface. Equation 3.32 defines a linear relation of S_{eff} and N_A. This is the reason for the wider J_{sc}-gap for both solar cells fabricated on 0.8 Ωcm Cz-Si wafers which have a five times higher doping density and, hence, a five times higher S_{eff} at the BSF compared to the 3.5 Ωcm Cz devices. In the 0.8 Ωcm scenario, S_{eff} is increased by the doping density which leads to stronger recombination losses of photogenerated minority carriers at V_{ext}=0 mV. A more extended discussion is given in the next section by means of simulated current transports.

7.3.2 Open circuit voltage

The emitters of the solar cells under consideration have all been diffused by the same process. It is therefore plausible to assume that all emitter saturation current densities are identical ($J_{0,em}$=300 fA/cm^2). Consequently, any deviations in V_{oc} must be mainly due to the bulk saturation current densities or the contact schemes.

The lower V_{oc} of both the 0.8 Ωcm solar cells in Fig. 7.2 (b) is a result of the low bulk lifetime. At V_{oc}, both the cells processed on 0.8 Ωcm Cz-Si wafers operate at a low injection level of 1.0×10^{14} cm^{-3} with a bulk lifetime of 15 µs. Both the cells fabricated on 3.5 Ωcm Cz-Si wafers operate at a higher injection level of 8.0×10^{14} cm^{-3} with a bulk lifetime of 157 µs. The respective excess carrier densities can be determined by using Eq. 3.8. Injection dependent bulk lifetimes are calculated by inserting the SRH parameters from Tab. 7.2 in Eq. 3.20. The V_{oc} of both 3.5 Ωcm devices profit from the increased lifetime, though, the doping density is five times lower than in the 0.8 Ωcm scenarios. In the present case, the bulk lifetime is injection-dependent. Hence, V_{oc} must be discussed as a function of the lifetime or, alternatively, as a function of an injection dependent J_0-contribution at a certain injection level.

In order to estimate the impact of the bulk recombination on the V_{oc} in the 0.8 Ωcm and 3.5 Ωcm scenario, we apply our diode model (see Fig. 4.3) with the respective analytical Eq. 4.2. All the solar cells featuring LFC or BSF are modeled with a constant saturation current density of 670 or

Table 7.3: Resistive-network modeling of I-V-parameters of the 0.8 Ωcm and 3.5 Ωcm EWT devices featuring LFC or BSF, respectively. The parameters are calculated by means of the diode network in Fig. 4.3. The short-circuit current densities are similar to the experimental values and are used as input parameters. The simulated I-V-parameters of the solar cells are depicted in Tab. 7.5.

ρ (Ωcm)	J_{sc} (mA/cm^2)	V_{oc} (mV)	J_{mpp} (mA/cm^2)	V_{mpp} (mV)	FF (%)	η (%)
3.5 (LFC)	34.4	623	32.5	508	77.2	16.5
3.5 (BSF)	34.3	622	32.6	518	79.4	16.9
0.8 (LFC)	32.5	614	30.9	520	80.5	16.1
0.8 (BSF)	32.0	613	30.5	522	81.2	15.9

720 fA/cm^2, respectively, plus the referring bulk recombination parameters depicted in Tab. 7.2. The higher constant J_0-contribution in the BSF scenario is due to the increased saturation current density of the BSF. The series resistances are taken from a comparison of the illuminated 1 sun I-V-curve and the J_{sc}-V_{oc}-curve, as depicted in Figs. 7.3 and 7.4. Note that the short-circuit current density of each device is set as input parameter. The model reproduces all V_{oc} with a precision of 3 mV (Tab. 7.3). A detailed explanation of recombination currents at V_{oc} is given in context of the simulation results in this chapter.

7.3.3 Fill factor

Figure 7.2 (c) depicts the experimental FF of the illuminated I-V-characteristics (black symbols), as well as the *pseudo*-fill factor, FF_{pseudo}, calculated by means of the J_{sc}-V_{oc}-characteristics (white symbols).

The BSF device fabricated on 0.8 Ωcm Cz-Si suffers from a shunt which is due to the emitter contact openings. A more profound discussion of this technological issue is given in Appendix A. The FF is reduced compared the LFC scenario which is not due to the integration of the BSF but due to this technological shunt issue. For this reason, the shunt current is modeled by means of a diode featuring a constant saturation current density and a constant local ideality factor. Then, the shunt current is subtracted from the referring 1 sun and J_{sc}-V_{oc}-curves in order to achieve characteristics that are exclusively affected by the device recombination and series resistance behavior (see Appendix A).

Both shunt-free FF are depicted as points put in parenthesis in Fig. 7.2 (c). In the following discussion, it is always referred to the shunt-free FF.

Figures 7.3 and 7.4 (panels (a) and (d)) show the I-V-curves at 1 sun illumination, in the dark, and the J_{sc}-V_{oc}-measurements for the 3.5 and 0.8 Ωcm solar cells, respectively. The center panels (b) and (e) of Figs. 7.3 and 7.4 contain the local ideality factors calculated by means of Eq. 3.36.

First, we discuss the pseudo-FF of all devices. The FF of an ideal diode calculated by means of Eq. 3.44 with R_s=0 and with a constant local ideality factor of unity is 83.4 % and 83.1 % for a V_{oc} of 625 mV (valid for both the 3.5 Ωcm solar cells) and 613 mV (valid for both the 0.8 Ωcm solar cells), respectively. The pseudo-FF of the 3.5 Ωcm and 0.8 Ωcm solar cells are 81 % and 82 %, respectively (see Fig. 7.2). Hence, the FF loss between the ideal reference scenario and the measured scenario is about 2.4 % and 1.1 % for the 3.5 Ωcm and 0.8 Ωcm devices, respectively.

The reason for the enhanced *pseudo*-FF reduction in the 3.5 Ωcm scenario is the injection dependent bulk lifetime between J_{sc} and V_{oc}. This effect is indicated by the increased local ideality factors (n≈1.2) of the J_{sc}-V_{oc}-characteristics in the voltage range between 500 mV and V_{oc} for the

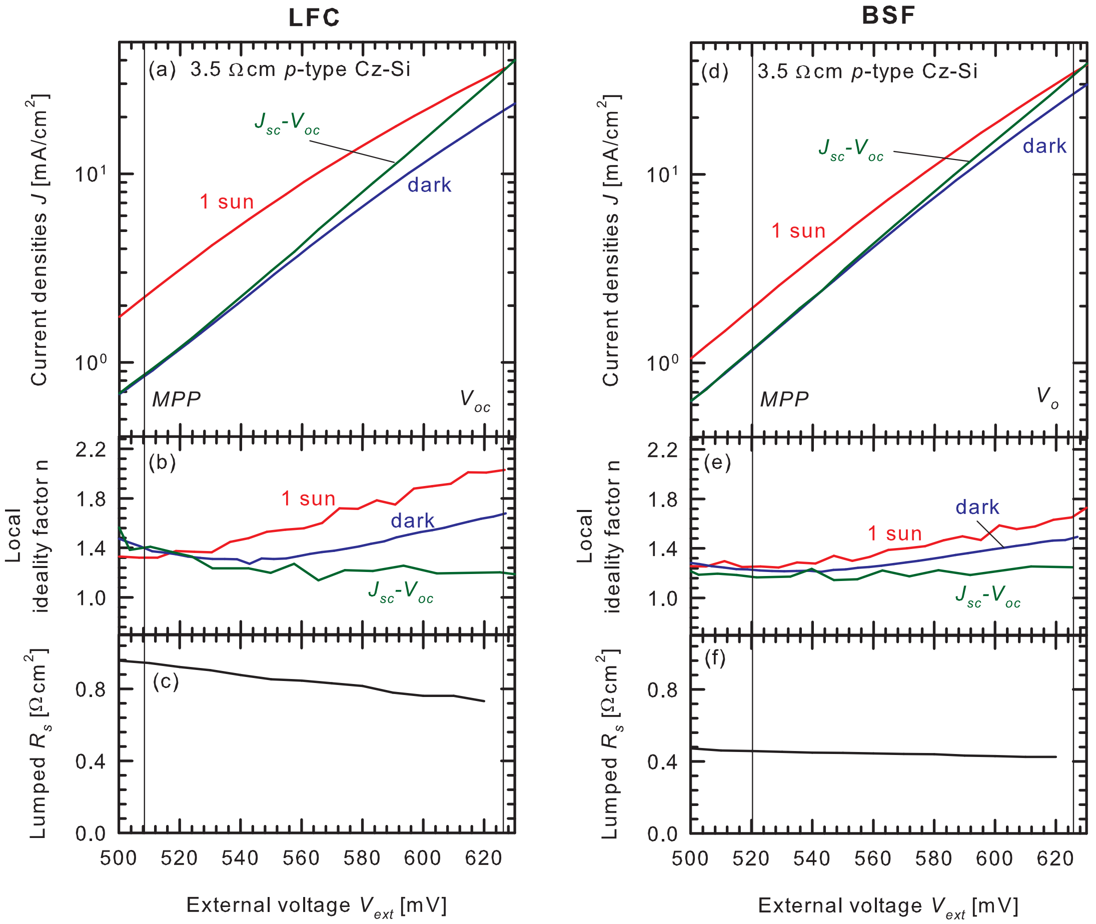

Figure 7.3: Top panels: measured I-V-characteristics under 1 sun illumination (shifted by J_{sc}), under dark conditions, and the J_{sc}-V_{oc}-values obtained under various illumination intensities for both EWT solar cells featuring LFCs (left part) or a BSF (right part), both fabricated on 3.5 Ωcm boron-doped Cz-Si. Center panels: measured local ideality factors of the above I-V-characteristics. Bottom panels: lumped series resistance, extracted from the 1 sun and J_{sc}-V_{oc}-curves.

LFC and BSF devices fabricated on 3.5 Ωcm Cz-Si (see Figs. 7.3 (b) and (e)).

The 0.8 Ωcm solar cells exhibits constant bulk lifetimes for injection ranges smaller than 1.0×10^{14} cm^{-3} ($\Delta n(V_{oc})$), as can be calculated by Eq. 3.20. As a result, the local ideality factors of the J_{sc}-V_{oc}-curves stay smaller than 1.2 between *MPP* and V_{oc} for both the LFC and BSF devices fabricated on 0.8 Ωcm Cz-Si (compare Fig. 7.4 (b) and (e)). Due to the constant bulk lifetimes, the *pseudo-FF* is only marginally reduced. The diode network depicted in Fig. 4.3 (see Eq. 4.2) is used for modeling the *pseudo-FF* and the respective I-V-curves. The calculated *pseudo-FF* (R_s=0) accounts for 81.5 % and 82.9 % in the 3.5 Ωcm and 0.8 Ωcm scenarios, respectively.

There is a difference of about 0.5 % (1 %) between the measured and the calculated pseudo-*FF* of the 3.5 Ωcm (0.8 Ωcm) devices.

These deviations are caused by small shunts which are not considered in the diode network. The local ideality factors of the J_{sc}-V_{oc}-curves in Figs. 7.3 and 7.4 are slightly increased for external voltages around and smaller than 500 mV which is due to these small shunts. Hence, the *FF*-reduction is based on a technical issue of the aluminum evaporation and the following annealing step. Annealing at low temperatures (e.g. T $<$ 250°C) would avoid this problem but does not improve (decrease) the contact resistances between the semiconductor and the aluminum. Finally, it is a compromise of decreasing the contact resistance and the generation of a shunt resistance at elevated temperatures. In the present solar cell process, tempering at 320 °C for 1 min on a hot

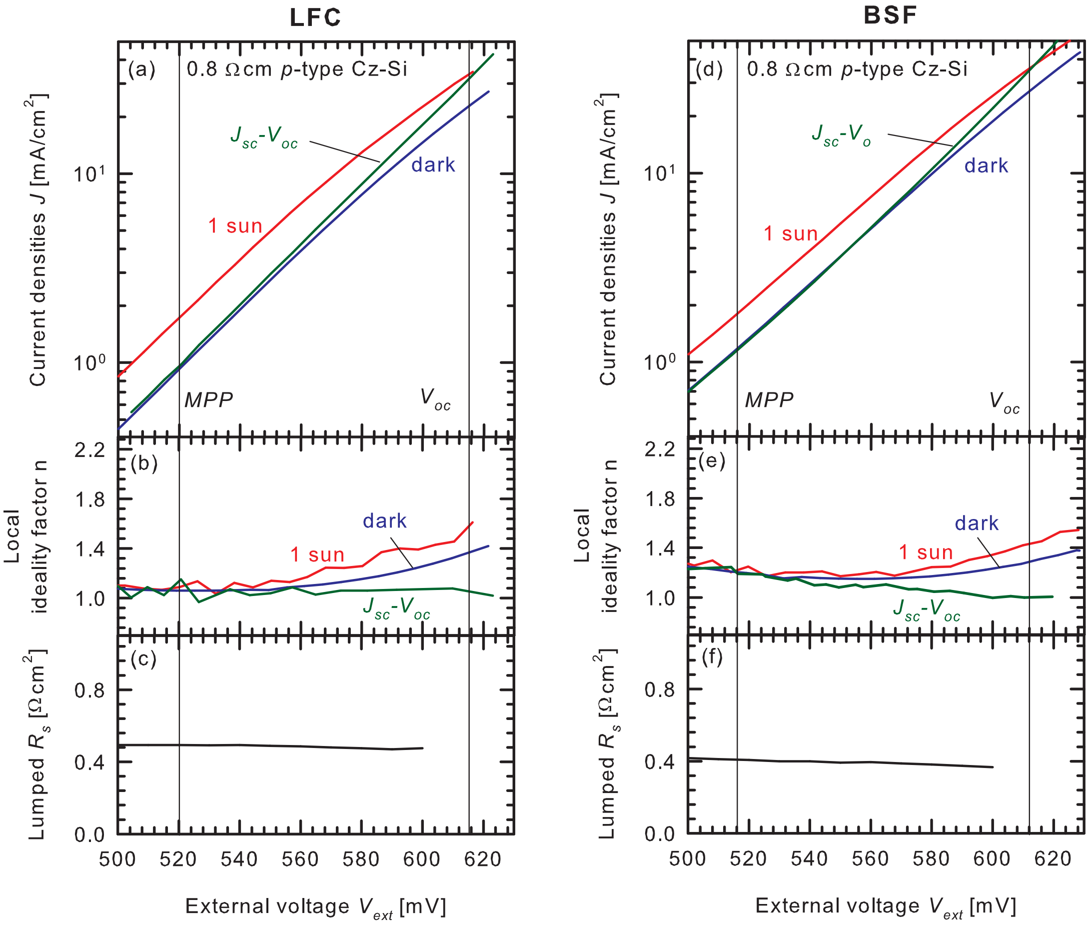

Figure 7.4: Top panels: measured I-V-characteristics under 1 sun illumination (shifted by J_{sc}), under dark conditions, and the J_{sc}-V_{oc}-values obtained under various illumination intensities for both EWT solar cell featuring LFCs (left part) or a BSF (right part), both fabricated on 0.8 Ωcm boron-doped Cz-Si. Center panels: measured local ideality factors of the above I-V-characteristics. Bottom panels: lumped series resistance, extracted from the 1 sun and J_{sc}-V_{oc}-curves.

plate has been identified to achieve the highest FF.

The FFs of the illuminated I-V-characteristics strongly depend on the wafer resistivities and the contact schemes. In the scenario of 3.5 Ωcm devices, the integration of a BSF increases the FF from 76.2 % (LFC device) to 78.6 % (BSF device). The FFs of 0.8 Ωcm EWT cells are rather insensitive for BSF integration. Here, FF is increased from 80.3 % (LFC device) to 80.6 % (BSF device) (Fig. 7.2).

The serie resistance along the vertical current transport inside the base ($R_{base,ver}$, Eq. 4.15) accounts for 0.06 Ωcm^2 and 0.01 Ωcm^2 in the 3.5 Ωcm and 0.8 Ωcm devices, respectively. The 0.8 Ωcm scenario exhibits a low magnitude of this series resistance contribution which is not a critical parameter in terms of FF losses. The small $R_{base,ver}$ value is based on the thin wafers that exhibit short vertical current transports in the range of 180 to 200 µm toward the base contacts [1].

The lateral current transport inside the base is one of the most critical issues in terms of resistive and FF losses of EWT solar cells. The discussion of the base resistances starts with the parallel current transport for both the 3.5 Ωcm solar cells. The respective series resistance $R_{base,par}$ accounts

---

[1] Industrial screen-printed silicon wafer based solar cells feature a full area aluminum BSF at the rear side. Hence, the current transport of majority carriers is vertical in the entire device except in the edge areas that feature no BSF. These solar cells are less sensitive for FF losses for a wide range of wafer resistivities.

for 0.29 Ωcm^2 and 0.08 Ωcm^2 in the LFC (Eq. 4.17) and BSF (Eq. 4.22) device, respectively. The BSF integration sustainably reduces the resistive loaded transport path of majority carriers inside the lowly doped base. The derivation of single R_s contributions anticipates the simulated trajectories of the internal current of EWT solar cells. The LFC device suffers from long current paths in the lowly doped base which is illustrated in Fig. 4.5. The implementation of a full-area BSF shortens the current transport inside the base and transports the current inside the highly-diffused back surface field to the base contacts as shown in Fig. 4.6. Note that the total length of the current path for majority carriers is not reduced by the BSF. It is only the length inside the base which is reduced. For this reason, the series resistance contribution of the parallel transport path is reduced in the BSF scenario. The BSF in the 3.5 Ωcm device sustainably reduces R_s without significantly increasing the surface recombination velocity at the base area. In the 0.8 Ωcm scenario, the resistive losses of the parallel transport inside the base are slightly reduced by the integration of a BSF ($R^{BSF}_{base,par}$=0.02 Ωcm^2) compared to the LFC device ($R^{LFC}_{base,par}$=0.07 Ωcm^2). However, the R_s-reduction is small and the strongly increased S_{eff} at the BSF compensates the positive effect on the FF by a reduced J_{sc} in the BSF compared to the LFC device.

The second part of the base resistance discussion focusses on the radial transport around the point contacts of the LFC devices. It has been mentioned above that the current of majority carriers inside the base is focused on the small area of the LFC. As a consequence, only a small part of the base volume contributes to the current transport which results in a high effective base sheet resistance around the LFC. A more detailed discussion is given in the context of Eq. 4.19 on page 32. Based on the three-dimensional simulation results, we assume the photogenerated current of the base to be collected in a height of W_{LFC}=15 µm above the LFC. The resulting $R^{LFC}_{base,rad}$ accounts for 0.13 Ωcm^2 and 0.03 Ωcm^2 in the 3.5 and 0.8 Ωcm LFC solar cell, respectively. The differing factor of about five is due to the linear relation between $R^{LFC}_{base,rad}$ and ρ (N_A), as defined by Eq. 4.19.

The majority carrier transport inside the BSF suffers from the series resistance $R^{BSF}_{BSF,par}$ which is calculated by means of Eq. 4.27. The respective resistance accounts for 0.07 Ωcm^2 in the 0.8 and 3.5 Ωcm BSF device.

The bottom panels (c) and (f) in Figs. 7.3 and 7.4 depict the lumped series resistance R_s of the 3.5 and 0.8 Ωcm devices, respectively. R_s is extracted from a comparison between the 1 sun and the J_{sc}-V_{oc}-curve by means of Eq. 3.52 [106, 107].

The 3.5 Ωcm BSF device exhibits a strongly reduced R_s compared to the respective LFC solar cell (compare panel (c) and (f) in Fig. 7.3). The R_s-contribution of the base is a critical factor in terms of FF losses of EWT solar cells fabricated on lowly doped substrates. The total device resistance is reduced from 0.93 Ωcm^2 in the LFC to 0.49 Ωcm^2 in the BSF scenario at MPP conditions (compare lower part in Fig. 7.3).

Both total R_s-values can be reproduced by adding the calculated resistance components shown in Tab. 7.4. In the 3.5 Ωcm LFC scenario, the deviation between the calculated and measured R_s accounts for 0.16 Ωcm^2. All R_s-deviations of the other devices are less than 0.1 Ωcm^2 between the measured and the calculated values.

The voltage dependent series resistance of the 3.5 Ωcm LFC device declines for increasing external voltages (Fig. 7.3(c)). This certain behavior has been discussed by means of an LFC contacted solar cell fabricated on a 5 Ωcm wafer in the previous chapter. The present 3.5 Ωcm BSF device exhibits a lumped R_s which only slightly declines (Fig. 7.3(f)). Both the cells fabricated on 0.8 Ωcm wafers exhibit a nearly constant lumped R_s (Fig. 7.4(c) and (f)). Hence, the stronger decline of the 3.5 Ωcm LFC device must be due to the point contact scheme combined with a lowly doped wafer substrate. In this chapter, we recapitulate a similar discussion in terms of carrier densities and wafer resistivities as presented in the last chapter.

Table 7.4: Calculated series resistance contributions of the BSF and LFC cells fabricated on 3.5 Ωcm and 0.8 Ωcm *p*-type Cz-Si, respectively: parallel current path in front emitter $R_{em,par}$ (Eq. 4.8), radial current path in front emitter $R_{em,rad}$ (Eq. 4.13), current path in EWT-via emitter $R_{em,via}$ (Eq. 4.6), vertical current path in base $R_{base,ver}$ (LFC device: Eq. 4.16; BSF device: Eq. 4.24), lateral current path in base $R_{base,par}$ (LFC device: Eq. 4.17; Eq. BSF device: 4.24), radial current path around LFC $R^{LFC}_{base,rad}$ (LFC-device: Eq. 4.19), parallel current path inside BSF $R^{BSF}_{BSF,par}$ (Eq. 4.27). The experimental R_s-values are shown in Figs. 7.3 and 7.4.

ρ (Ωcm)	$R_{em,par}$ (Ωcm^2)	$R_{em,rad}$ (Ωcm^2)	$R_{em,via}$ (Ωcm^2)	$R_{base,ver}$ (Ωcm^2)	$R_{base,par}$ (Ωcm^2)	$R^{LFC}_{base,rad}$ (Ωcm^2)	$R^{BSF}_{BSF,par}$ (Ωcm^2)	$\sum R$
3.5(LFC)	0.04	0.07	0.17	0.06	0.29	0.13	—	0.76
3.5(BSF)	0.04	0.07	0.17	0.06	0.08	—	0.07	0.49
0.8(LFC)	0.04	0.07	0.17	0.01	0.07	0.03	—	0.39
0.8(BSF)	0.04	0.07	0.17	0.01	0.02	—	0.07	0.38

In the 3.5 Ωcm LFC device, the base doping density N_A accounts for 4.0×10^{15} cm^{-3}. The excess carrier densities inside the base at J_{sc}, 500 mV and 625 mV, account for 8.2×10^{12} cm^{-3}, 1.4×10^{13} cm^{-3} and 5.6×10^{14} cm^{-3}, respectively. The resulting wafer resistivity at J_{sc}, 500 mV and 625 mV is 3.5 Ωcm, 3.5 Ωcm and 2.9 Ωcm, respectively. Due to the increased density of majority carriers between the maximum power point and open circuit conditions, the wafer resistivity decreases by a factor of 0.83 (-17 %). All single base series resistances contributions linearly depend on the wafer resistivity (see Eqs. 4.15, 4.19 and 4.17). Multiplying the factor of 0.83 with the analytically calculated total base series resistances of the 3.5 Ωcm LFC device at *MPP* (Tab. 7.4), the total device resistance decreases from 0.76 Ωcm^2 to 0.63 Ωcm^2, a difference of 0.13 Ωcm^2. The experimentally derived series resistance of the 3.5 Ωcm device declines from 0.93 Ωcm^2 at V_{ext}=500 mV to about 0.72 Ωcm^2 at V_{ext}=625 mV, a difference of 0.21 Ωcm^2. Similar to the previous chapter, the analytical calculation does not fully explain the resistance decline in the LFC scenario. Again, we assume that the injection-dependent R_s-behaviour might be due to LFC contact and a current crowding effect which differs for different V_{ext}.

The series resistance of the 3.5 Ωcm BSF device is discussed. The excess carrier densities inside the base at J_{sc}, 500 mV and 625 mV are about similar to the LFC scenario and, hence, result in similar wafer resistivities. Due to the increased density of majority carriers between the maximum power point and open circuit conditions, the wafer resistivity also decreases by a factor of 0.83 (-17 %). Multiplying this factor with the analytically calculated base series resistances of the 3.5 Ωcm BSF device at *MPP* (Tab. 7.4), the total device resistance decreases from 0.49 Ωcm^2 to 0.41 Ωcm^2, a difference of 0.08 Ωcm^2. The experimentally derived series resistance of the 3.5 Ωcm BSF device declines from 0.48 Ωcm^2 at V_{ext}=500 mV to 0.41 Ωcm^2 at V_{ext}=625 mV, a difference of 0.07 Ωcm^2. Hence, the analytically derived R_s-contributions quantitatively explain the behaviour of the lumped series resistance in the scenario of a BSF contact scheme.

Due to the highly doped BSF, the carrier density around the base point contacts just slightly increases for increasing V_{ext}. A possible impact of the injection regime on the semiconductor-metal contact resistance is minimized. Furthermore, the highly boron-doped BSF offers a higher conductivity and, hence, induces a modified current transport with a less developped current crowding effect compared to the LFC scenario featuring a lower doped wafer substrate above the base contacts.

Both the cells fabricated on 0.8 Ωcm wafer substrates exhibit constant lumped R_s for increasing V_{ext}. In this scenario, the excess carrier densities are low and in a more narrow range compared to the low wafer doping density. Hence, the impact of the excess carrier density on the wafer resistivity is small. The base series resistances are constant in the injection regime between MPP and V_{oc}.

The total device series resistance of the 0.8 Ωcm BSF device is slightly reduced compared to the LFC cell (please compare panel (c) and (f) in Fig. 7.4). However, even the 0.8 Ωcm device profits from a BSF integration in terms of FF-gains. The improvement is small since the base series resistances are negligible compared to the emitter series resistance which is the dominant factor for the FF-losses in the 0.8 Ωcm scenario. Similar to the 3.5 Ωcm scenario, it is possible to reproduce the measured series resistances around MPP in Fig. 7.4 with the sum of all calculated series resistances which is depicted in the right column of Tab. 7.4. They account for about 0.39 and 0.38 Ωcm^2 in the LFC and BSF scenario, respectively.

7.3.4 Efficiency

Solar cell efficiencies are the product of all three I-V-characteristics parameters: J_{sc}, V_{oc} and FF. The previous chapter exposed a small efficiency boost for EWT solar cells fabricated on highly boron-doped Cz-Si wafers. Beside the geometrical and diffusion parameters of a solar cell, this conclusion also depends on the specific interstitial oxygen concentrations O_i of Cz-Si wafers affecting all three I-V-parameters. O_i does not depend on the dopant concentration but on the crystal growth process. Hence, O_i is an individual parameter for all the different wafers used in the previous and present chapter.

In this chapter, O_i is higher in the highly doped (0.8 Ωcm) and lower in the lowly doped Cz-Si wafer (3.5 Ωcm) (see Tab. 7.2). In the previous chapter, O_i was lower in the highly doped (0.5 Ωcm) and higher in the lowly doped (5 Ωcm) Cz-Si wafers (see Tab. 6.2). As a consequence, both EWT solar cells fabricated on 0.8 Ωcm Cz-Si wafers in this chapter suffer from comparatively lower bulk lifetimes that reduce J_{sc} and V_{oc}. The higher recombination compensates the positive impact of a higher FF. In this chapter, efficiencies of both 0.8 Ωcm solar cells are the lowest ones in the experimental study (see Fig. 7.2). The implementation of a BSF further decreases the efficiency of the present solar cells fabricated on highly doped Cz-Si wafers.

In contrast, the BSF integration strongly increases the total conductivity of the 3.5 Ωcm EWT solar cell and boosts the FF. The efficiency of the 3.5 Ωcm BSF device is superior despite the fact that the BSF integration slightly reduces V_{oc} and J_{sc} compared to the LFC scenario (see Fig. 7.2). Hence, a high efficiency potential of EWT solar cells can be achieved for lowly or moderately boron-doped Cz-Si wafers.

Please be aware that these conclusions exclusively hold for boron-doped Cz-Si wafers that contain interstitial oxygen, i.e. oxygen-dimers. By removing or preventing boron-oxygen complexes, the bulk lifetime would increase strongly, leading to higher J_{sc}- and V_{oc}-values even in the scenario of highly doped Cz-Si wafers.

7.4 Device simulation

7.4.1 Model description

A detailed description of the 3d EWT SENTAURUS [119] model is given in Section 4.4.2. The physical models and input parameters are listed and referenced in Tab. 4.1. The recombination parameters of Al_2O_3-passivated boron doped surfaced are deduced from measurements discussed in Ref. [126].

Based on device symmetry, the minimum simulation domain is chosen, depicted in the top-left quarter of Fig. 4.8, which contains all the semiconductor features but neglects lateral currents within the Al finger along the metalized rear side of the cell. The photogenerated current-density J_{gen} is numerically simulated with SUNRAYS [124] using the am1.5g solar spectrum [101], the silicon absorption data from Ref. [125], and in-house ellipsometric measurements of the refractive indices and extinction coefficients of the Al_2O_3-SiN antireflection layer. In this way, the measured front reflectance spectrum is reproduced. The local laser fired base contacts are simulated with a boron-doped Gaussian diffusion profile having a depth of 1.5 µm and a peak concentration of 3×10^{19} cm^{-3}. The phosphorus emitters are approximated by a Gaussian profile with a peak concentration of 8×10^{19} cm^{-3} and a depth of 0.6 µm. The SRH surface recombination parameters of the emitter are set as S_h=16335 cm/s and S_n=163350 cm/s, respectively. The resulting saturation current density $J_{0,e}$ accounts for 300 fA/cm^2. This is similar to the experimental values achieved by passivating this specific emitter with SiN or Al_2O_3-SiN discussed in Section 7.2.

In the previous chapter, the EWT device has been split into a front and rear collecting diode along the demarcation area. Deviations of the ideal diode characteristic do not depend on the demarcation area which is the result and not the reason of the internal current distributions. In the following, carrier densities and recombination currents are discussed by means of the semiconductor energy bands. Auger and SRH recombination rates depend on the excess carrier densities Δn which are functions of the local voltages inside the device. Under illumination, the local voltage is higher than the external voltage. This is due to the series resistances that induce potential drops along the majority carrier Fermi levels. The series resistances and the resulting voltage drop adaptions cause FF-losses as described in Section 3.8 on page 20. The illustrative picture of the demarcation area is still used in this chapter in order to describe the internal current transports.

Table 7.5 shows the simulated I-V-parameters. The numerical model simulates the V_{oc} with an accuracy of 3 mV compared to the experimental V_{oc} depicted in Fig. 7.2. The simulated J_{sc} is increased compared to the experimental parameters with an error of 0.7 mA/cm^2 and 0.5 mA/cm^2 for the 0.8 Ωcm BSF and LFC device, respectively. The J_{sc} of both the 3.5 Ωcm devices is reproduced with an error less than 0.1 mA/cm^2. Experimental FF are smaller than the simulated FF and can be reproduced with an absolute deviation less than 1.6 % for all devices.

Table 7.5: Simulated I-V-parameters of the 0.8 Ωcm and 3.5 Ωcm EWT devices featuring LFC or BSF, respectively. Results are calculated by means of the three-dimensional EWT SENTAURUS model. The EWT simulation domain is depicted in Fig. 4.8. By means of the resistive-network modeled I-V-parameters of the solar cells are depicted in Tab. 7.3.

ρ (Ωcm)	J_{sc} (mA/cm^2)	V_{oc} (mV)	J_{mpp} (mA/cm^2)	V_{mpp} (mV)	FF (%)	η (%)
3.5 (LFC)	34.4	626	32.2	517	77.2	16.6
3.5 (BSF)	34.3	622	32.3	530	80.2	17.1
0.8 (LFC)	33.0	612	31.0	530	81.5	16.4
0.8 (BSF)	32.7	610	31.0	530	82.1	16.4

7.5 Simulation results: 3.5 Ωcm boron-doped Cz-Si device

The first part, both EWT solar cells fabricated on boron doped 3.5 Ωcm Cz-Si wafers are discussed.

7.5.1 External voltage range from 0 to 400 mV

Figures 7.5(a) and (b) depict the distribution of the hole quasi-Fermi level in the simulation domain and the hole current paths at J_{sc}-conditions for the LFC and BSF cell, respectively. For simplicity, the three-dimensional simulation domain is presented as a two dimensional side view. The yellow-black bars situated at the front emitter of each simulation domain in Fig. 7.5 denote the position at which the energy band schemes are extracted used in the following discussion. The current paths of photogenerated majority carriers are shown as trajectories between the front surface and the base

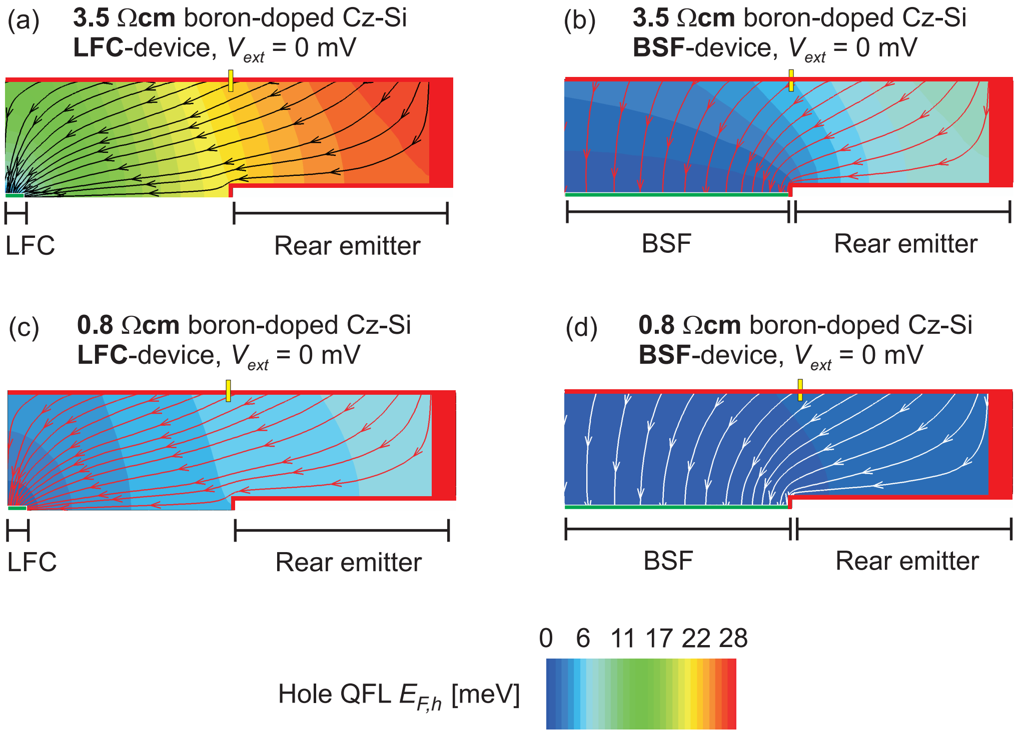

Figure 7.5: The hole QFL $E_{F,h}$ (shown in color) and the current trajectories of majority carriers in the 3.5 Ωcm LFC device (a), the 3.5 Ωcm BSF device (b), the 0.8 Ωcm LFC device (c) and the 0.8 Ωcm BSF device (d), all at V_{ext}=0 mV. The single current trajectories start below the front *pn*-junction with a lateral distance of 50 µm to each other. The yellow-black bars indicate the position across the front *pn*-junction where the band schemes are extracted depicted in Fig. 7.6.

contacts in the lower left corner. The current trajectories launch below the front *pn*-junction in a lateral distance of 50 µm to each other. Spatially higher densities of trajectories inside the base are related to higher local current densities.

Generally, the spatially resolved current flow of carriers $\vec{j}$ is described as the product of local conductivity σ with the gradient of the QFL ∇E_F (see Eq. 3.11). The LFC device exhibits long current paths for majority carriers inside the base. Photogenerated holes are forced to flow diagonally through the entire unit cell (Fig. 7.5 (a)). The highest current densities exist near the base contact at the lower left corner in Fig. 7.5 (a). The sum of all photogenerated majority carriers is focused on this area. It has been discussed in the context of the experimental results that the total base series resistance in the LFC device is the most detrimental factor in terms of *FF*-losses. Firstly, the series resistances induce higher ohmic power dissipation. Secondly, the resulting voltage drops lead to increased recombination compared to reference scenarios with R_s=0.

The integration of a BSF modifies the carrier transport. The base above the BSF, left hand side in Fig. 7.5(b), exhibits a current flow that is perpendicular (vertical) to the rear side of the device. Here, the majority carriers enter the BSF which has a lower resistance (R_{sq}=75 Ω/□) than the lowly doped solar cell base region (R_{sq}=194 Ω/□ for ρ=3.5 Ωcm and W=180 µm). This scenario can be understood in terms of an electronic network in which internal currents follow the path of lowest resistance [1]. The current of majority carriers above the rear side emitter, situated at the right hand side in Fig. 7.5(b), possesses a lateral vector component toward the BSF, a comparable

---

[1] The short and vertical current flow is a typical scenario also found in screen printed solar cells with an aluminum back surface field covering the entire rear side [157].

scenario as in the LFC device in Fig. 7.5(a). The majority carrier currents enter the BSF and are transported toward the rear base contacts. Compared to the LFC device, the BSF integration even results in longer current trajectories for photogenerated majority carriers. However, the resistive losses are reduced which is due to the high conductivity of the BSF as discussed by means of the analytically calculated R_s values in Tab. 7.4.

Generally, voltage is defined as the difference of two potentials. In the case of a semiconductor, the local voltage V_{local} is defined by $E_{F,n} - E_{F,h}$ devided by q. A potential drop is defined as the difference of one certain potential, e.g. of the hole QFL, $\Rightarrow \mathit{\Delta} E_{F,h}$ devided by q, at two points in the semiconductor. In the scenario of $\mathit{\Delta} E_F{>}0$, there is a potential gradient between these two points. Equally, a voltage drop can be defined by the difference of two voltages, e.g. of the local voltage V_{local} inside the base and the external voltage V_{ext} at the semiconductor-metal contacts.

In the case of an **illuminated** solar cell (see Fig. 7.5), photogenerated currents inside the device flow toward the semiconductor-metal contacts where they enter the external circuit. On this way due to series resistances of the device structure, the current induces a potential drop along the hole QFL $E_{F,h}$. This results in a voltage drop between the device and the external circuit. As a result, the local voltage inside the device is higher than the external voltage. The voltage drop depends on the solar cell geometry, the wafer resistivity and the implementation of additional current paths, e.g. front-surface [90] or back-surface fields. The modified current trajectories in the BSF scenario reduce the voltage drop along the hole QFL $E_{F,h}$ inside the device. To illustrate this effect, compare the colors of Figs. 7.5(a) and (b) which stand for the hole QFL.

Photogenerated electrons collected at the front pn-junction are transported long distances through the front and EWT-via emitter to the rear emitter contacts. Photogenerated hole carriers also cover a long distance until the reach the rear base contacts. Lowly doped Si (e.g. 3.5 Ωcm boron-doped Cz-Si) exhibits a low conductivity for the majority carrier transport inside the base and is more sensitive for resistive losses compared to the 0.8 Ωcm scenario. Large majority carrier currents at J_{sc} combined with long lateral current paths inside the lowly doped base result in increased gradients along $E_{F,h}$, and hence in increased local potential drops. The emitter and the base currents induce potential drops in the device and bias the barrier height at the pn-junctions. The potential drops affect the minority carrier recombination and the ohmic power dissipation. The carrier injection is increased across the pn-junction leading to higher Auger and SRH recombination losses. A discussion of the band schemes at the front pn-junction is presented in the following. Since the potential drop along the EWT-via and front emitter is similar in the LFC and BSF scenario for different V_{ext}, we focus the discussion on the potential drops inside base that strongly depend on the contact schemes. Voltage drops along the EWT-via and front emitter have similar consequences than voltage drops inside the base. In the following, the 3.5 Ωcm and 0.8 Ωcm devices are separately discussed. The specific FF-losses of each device in the 3.5 Ωcm and 0.8 Ωcm scenario are due to the current transport inside the base, the injection-dependent SRH recombination parameters of the bulk lifetime and Auger recombination.

Figure 7.6 depicts the semiconductor band schemes at the front pn-junction at V_{ext}= 0 mV, 530 mV and at V_{oc} of each solar cell. The band schemes are recorded within the first 1.5 µm beneath the front side in the center of the simulation domain which is indicated by a yellow-black bar in Fig. 7.5. The hole Fermi-level at the metalized base contacts is denoted as $E_{F,h}(rear)$. It is the reference point with 0 meV (0 mV) that refers to all potentials (voltages). The hole Fermi-level in a distance of 1.5 µm to the front side is denoted as $E_{F,h}(1.5 \mu m)$. The band schemes denote the semiconductor band energies in units of meV (see Fig. 7.6). The potential drops along the majority current paths have units of meV. The referring voltage drops for the electric current are exhibit units of mV.

At V_{ext}=0 mV, the 3.5 Ωcm LFC cell exhibits a large potential drop along $E_{F,h}$ that accounts for 23 meV near the front pn-junction (see Fig. 7.6(a)). The implementation of a BSF reduces the resistive losses of majority carriers and the potential drop along $E_{F,h}$ inside the base that only

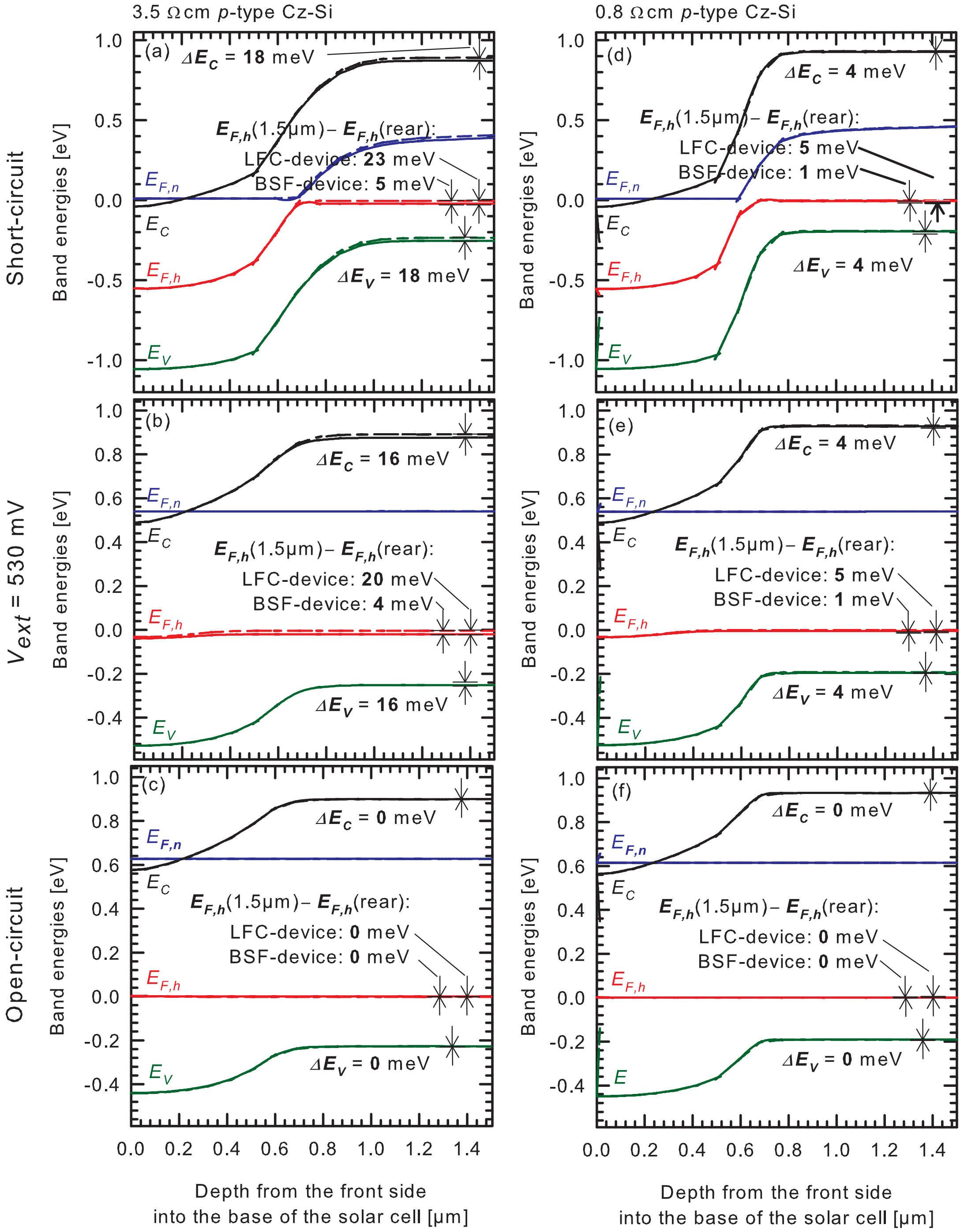

Figure 7.6: Semiconductor band schemes across the front pn-junction for the LFC and BSF devices processed on 3.5 Ωcm Cz-Si wafers (left column) and on 0.8 Ωcm Cz-Si wafers (right column). The band schemes are recorded within the first 1.5 µm beneath the front surface. The respective "cuts" are situated in the center of the simulation domain and are indicated as yellow-black bars in Fig. 7.5. The band schemes are shown for V_{ext}=0 (top panels), 530 mV (center panels) and at the referring V_{oc} of each solar cell (bottom panels). The hole Fermi-level at the base contact ($E_{F,h}(rear)$) is the fixed point with 0 meV that refers to all other potentials and voltages. Depicted potential drops along $E_{F,h}$ are recorded at a distance of 1.5 µm to the front surface and denoted as $E_{F,h}(1.5\mu m) - E_{F,h}(rear)$. Differences between the conduction and valence band energies in the LFC and BSF device are denoted as ΔE_C and ΔE_V, respectively.

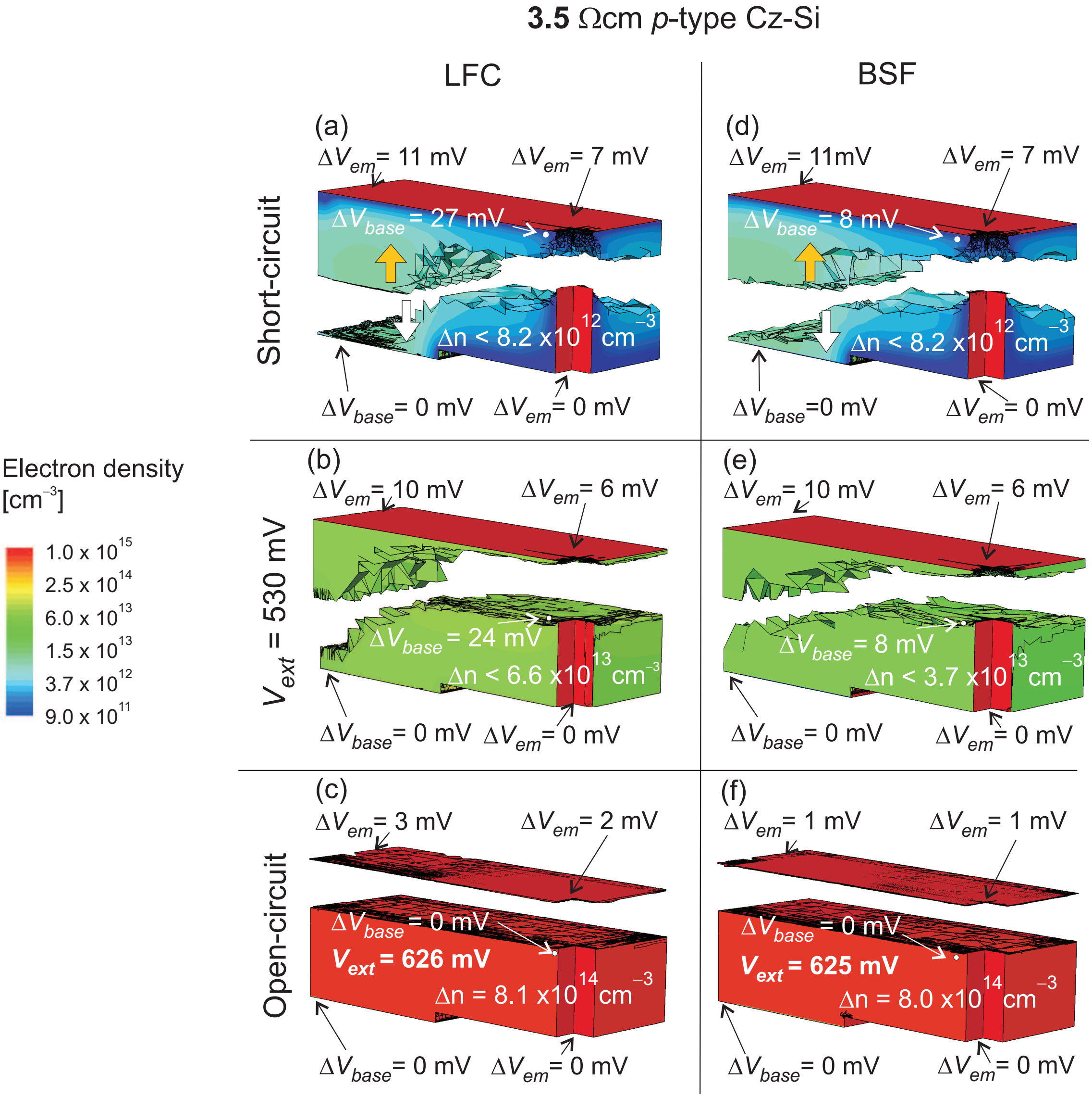

Figure 7.7: Electron distributions in the simulation domain of both 3.5 Ωcm EWT solar cells featuring either LFCs (left) or a BSF (right), at V_{ext}=0 mV (top panels), 530 mV (center panels) and for the respective V_{oc} of each solar cell (bottom panels). The simulation domains are split along the demarcation area at which the electron transport is separated into a front and rear collecting volume. The voltage drops V_{base} and V_{em} refer to the external voltages at the base or emitter contact, respectively.

accounts for 5 mV, also shown in Fig. 7.6(a). Consequently, the LFC device exhibits a lower barrier height at the front *pn*-junction, 18 mV less compared to the BSF scenario (see ΔE_C and ΔE_V Fig. 7.6(a)).

Figures 7.7(a) and (d) show the electron density distributions at V_{ext}=0 mV of both cells featuring either LFC or a BSF. In order to discuss the internal current transport, the simulation domains are split along the demarcation area.

Compared to the scenario in the previous chapter, the voltage drops of 7 mV at J_{sc} between front and rear emitter are reduced (compare upper row in Fig. 7.7 with Fig. 6.4 (a) on page 68). The reason is a reduction of the emitter resistance contributions as discussed in the context of the experimental *FF* on page 83. Between the rear contacts and the base near the EWT-via emitter, the potential drop along $E_{F,h}$ accounts for 27 mV and 8 mV in the LFC and BSF scenario, respectively (compare 7.7(a) and (d)).

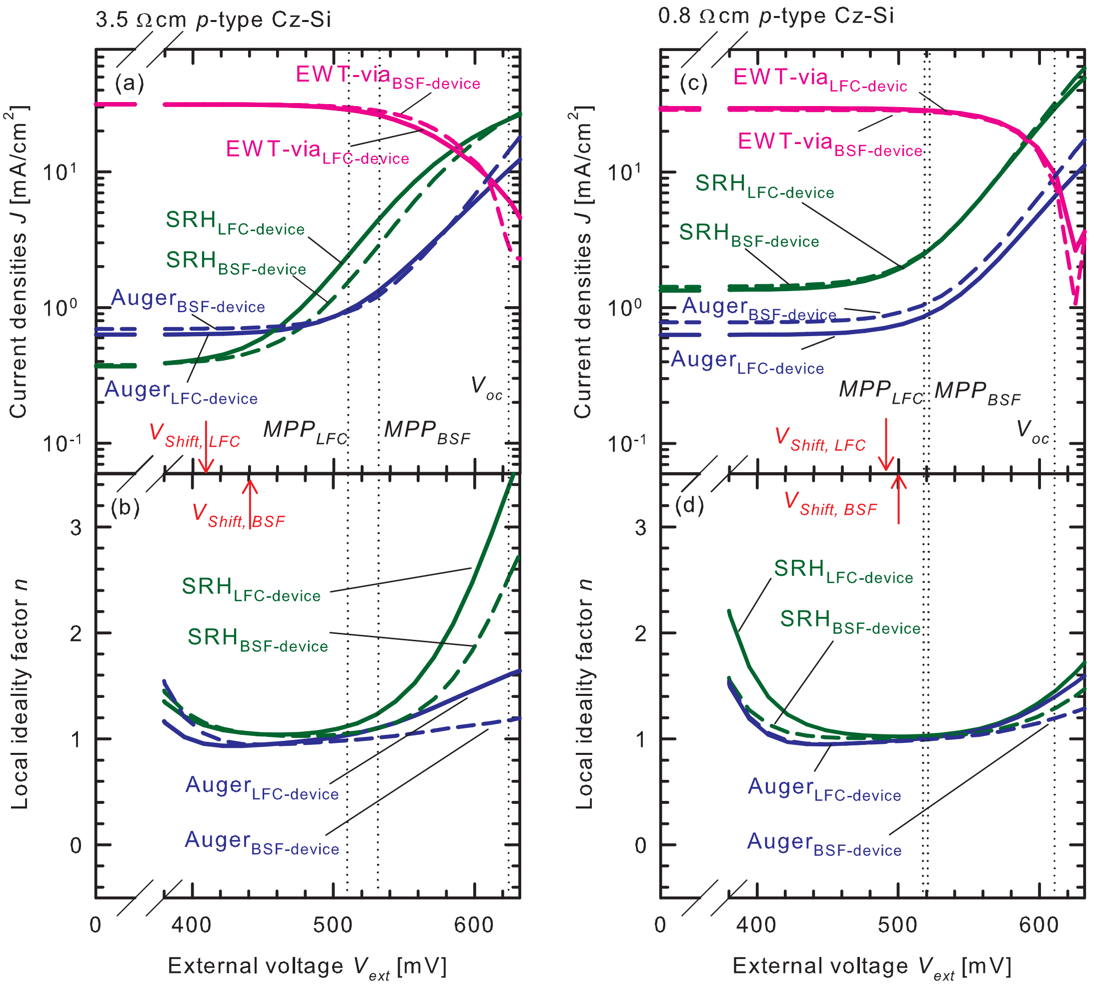

Figure 7.8: Simulated Auger and SRH recombination losses (top panels) and local ideality factors of the recombination characteristics (bottom panels) of the solar cell processed on 3.5 Ωcm Cz-Si wafers (left) or 0.8 Ωcm Cz-Si wafers (right). The simulation data for the LFC and BSF devices are plotted as solid and dotted lines, respectively. To calculate the local ideality factors, the SRH and Auger recombination currents are shifted by the referring recombination contributions $J_{rec,0}$ at V_{ext}=0 mV. A more detailed discussion is given in the context of Eq. 3.49 on page 19. Also shown is the current-density flowing from the front to the back of the cell through the EWT-via emitter and the external voltages V_{Shift} (marked as red arrows) at which the demarcation area in Figs. 7.7 and 7.9 begins to shift.

At V_{ext}=0 mV, the electron densities are similar in both solar cells. At J_{sc}-conditions, the potential drops do not induce higher carrier densities in the LFC compared to the BSF scenario. The excess carrier density is determined by the photogeneration. The injection of carriers across the pn-junction is comparatively small and can be neglected even in the LFC scenario that exhibits increased local voltages at the front pn-junction. This situation holds for V_{ext}=0 mV and will change by increasing the external voltage.

At V_{ext}=0 mV, the total recombination current density of both devices is dominated by Auger recombination, mainly in the front emitter. The BSF cell exhibits slightly higher Auger recombination losses (0.7 mA/cm^2) compared to the LFC cell (0.6 mA/cm^2) due to the highly doped back-surface field (see Fig. 7.8(a)). At the referring injection levels of about 8×10^{12} cm^{-3} at V_{ext}=0 mV, the bulk lifetime of 59 µs translates into long bulk diffusion lengths of 430 µm which is 2.4 times larger than the wafer thickness. SRH recombination losses inside the base are small and account for 0.4 mA/cm^2 in both devices (Fig. 7.8(a)). Recombination losses at the Al$_2$O$_3$-passivated non-diffused rear side (LFC-device) are negligible in terms of J_{sc}-reduction.

7.5.2 External voltage around 530 mV

The generation rate is still considerably larger than the recombination rate. The trajectories of the hole currents and their absolute values are similar as those at J_{sc}-conditions (see Fig. 7.5(a) and (b)). The potential drops along $E_{F,h}$ are marginally reduced. In the LFC (BSF) scenario, they account for 20 (4) meV across the front *pn*-junction as shown in Fig 7.6(b).

The excess carrier densities inside the bulk in both scenarios are strongly increased due to the injection of electrons across the *pn*-junction (Eq. 3.8). The enhanced potential drop of 16 meV in the LFC cell (20 meV−4 meV=16 meV) causes to a higher local voltage inside the device and at the front *pn*-junction compared to the BSF scenario. The barrier height at the front *pn*-junction is reduced and the injection of electrons from the emitter into the base is increased. A similar situation holds for the injection of holes from the base into the front emitter that is also increased at the front *pn*-junction of the LFC device.

The local voltage in a semiconductor is defined as the splitting of both QFL devided by q: $V_{local} = (E_{F,n} - E_{F,h})q$. The illuminated solar cells exhibit a higher voltage inside the device compared to the externally applied voltage. The local voltage can be written as: $V_{local} = V_{ext} + \varDelta V$, where $\varDelta V$ denotes the potential drop along $E_{F,h}$. Hence, the potential drop along $E_{F,h}$ causes to a higher local voltage which is induced by the resistive loaded current transport of majority carriers.

Equation 3.51 on page 21 defines the exponential relation between the increased carrier injection and the potential drop inside the device: $\varDelta n_{local}/\varDelta n = exp(\varDelta V/V_{th})$, where $\varDelta n$ is the excess carrier density in a reference scenario that exhibits no series resistance or, alternatively, a reduced series resistance in order to compare two different devices. In the next step, we use both potential drops along $E_{F,h}$ in the LFC and BSF scenario in order to estimate their impact on the carrier density inside the base. A potential drop of 20 mV (4 mV) in the LFC (BSF) device results in a 2.2 (1.2) times higher electron density compared to a reference scenario with $\varDelta V = 0$ mV. The carrier densities of the LFC and BSF device differ by a factor of 1.8 (=2.2/1.2) and account for 6.6×10^{13} cm^{-3} and 3.7×10^{13} cm^{-3} inside the base of the LFC and BSF device, respectively (see Figs. 7.7(b) and (d)).

The high voltage drop inside the LFC device induces higher electron densities and, consequently, enhanced SRH recombination currents ($U_{SRH} \propto \varDelta n$). The integration of a large-area BSF reduces the internal voltage drop in the base and the injection of excess carriers across the *pn*-junctions. SRH recombination in the BSF device is lower for external voltages between 420 mV and V_{oc}. At $V_{ext} = 530$ mV, the SRH recombination accounts for 4.5 mA/cm^2 and 2.7 mA/cm^2 in the LFC and BSF solar cells, respectively (see Fig. 7.8(a)). The relation of the SRH currents is 1.8 which is the factor for the different carrier densities in both devices. Note that the potential drop along $E_{F,h}$ biases the front and rear *pn*-junction. The voltage drop along the EWT-via and front emitter only biases the front *pn*-junction. Hence, the carrier injection is lower at the rear emitter since it is linked to the rear metal contacts without notable voltage drops along the emitter. However, the voltage drop inside the base has a similar effect on the carrier injection as discussed by means of the voltage drop at the front emitter.

Auger recombination, mainly caused by the highly doped emitter, is also biased by the internal voltage drops. The injection of holes from the base into the highly doped emitter and, consequently, the respective recombination losses are increased. The LFC device has a dielectrically passivated base at the rear side (negligible Auger recombination) which exhibits a smaller saturation current than the full-area BSF (increased Auger recombination). However, at external voltages around 530 mV, Auger recombination in the the LFC device (1.3 mA/cm^2) is greater than in the BSF device (1.2 mA/cm^2) (see Fig. 7.8(a)) due to the high base voltage drops and the higher carrier injection across the *pn*-junctions in the LFC scenario.

The higher electron density in the LFC device also has consequences on the current transport. For V_{ext}>408 mV, the minority carrier resistance in the base of the LFC scenario (see Eq. 6.4) starts being lower than the sum of the front and the EWT-via emitter resistances. The demarcation area shifts toward the front pn-junction marked by the arrow $V_{shift,LFC}$ in Fig. 7.8(a). In contrast, the current transport of photogenerated electrons is less affected inside the BSF device. A lower electron density at similar external voltages results in an increased minority carrier resistance for the electrons inside the base. The electron transport is stabilized toward the front pn-junction. The shifting of the demarcation area launches at a higher external voltage of 440 mV indicated as $V_{shift,BSF}$ in Fig. 7.8(b).

The smooth shape of the EWT-via current of the LFC device in Fig.7.8(a) is caused by the higher recombination and by the change of the internal current transport. At V_{ext}=0 mV, the EWT-via current accounts for 31.4 mA/cm^2 in the BSF and LFC scenario. At V_{ext}= 517 mV, the EWT-via current and the total recombination current density of the LFC (BSF) device accounts for 27.8 mA/cm^2 (29.4 mA/cm^2) and 4 mA/cm^2 (2.8 mA/cm^2). The difference between the LFC and BSF device recombination current is 1.2 mA/cm^2, whereas the difference of both EWT-via currents is larger and accounts for 1.6 mA/cm^2. The variation of 0.4 mA/cm^2 (1.6 mA/cm^2 $-$1.2mA/cm^2) is due to the shifting of the demarcation area. At V_{ext}=517 mV, a greater partition of photogenerated electrons are transported through the bulk toward the rear emitter in the LFC device compared to the scenario at J_{sc}-conditions. The EWT-via current of the BSF device has a more rounded shape. It strongly declines at higher external voltages near V_{oc}. In the BSF scenario, the shape and, hence the reduction of the EWT-via current is stronger affected by the recombination for increasing V_{ext} and less by the demarcation area shifting (see Fig.7.8(a)).

7.5.3 External voltages around V_{oc}

The gradients of the energy bands inside the base and the voltage drops between the device and the external circuit converge to zero. Between 530 mV and V_{oc}, the LFC (BSF) device passes through a potential drop adaption along $E_{F,h}$ from 20 meV (4 meV) to 0 meV at the investigated position at the front pn-junction (see Fig. 7.6(c)). The local voltage in both scenarios still increases by increasing V_{ext} between MPP and V_{oc}, but at a slower pace than V_{ext} itself. A stronger adaption of the local to the external voltage results in a stronger deviation of the carrier injection across the pn-junction. Local ideality factors of Auger and SRH recombination currents are increased. The perfect diode characteristic with n=1 is disturbed and the FF is reduced. In the LFC scenario, SRH and Auger recombination currents exhibit local ideality factors of 3.4 and 1.6, respectively (Fig. 7.8 (b) at V_{oc}). In the BSF scenario, SRH and Auger recombination currents are less affected by the lower voltage drop adaption and exhibit smaller local ideality factors of 2.5 and 1.2, respectively (Fig. 7.8 (b)).

The V_{oc} and the referring excess carrier densities are similar in the LFC and BSF device (see Figs. 7.7 (c) and (f)). At V_{oc}, SRH recombination, mainly based on bulk recombination, is similar in both devices and account for 24 mA/cm^2 (see Fig. 7.8 (a)). Auger recombination is slightly increased in the BSF device (12 mA/cm^2) compared to the LFC solar cell (10 mA/cm^2) which is due to the boron diffusion at the rear side. This is also the reason for a slightly smaller V_{oc} of -2 mV of the BSF solar cell (see Tab. 7.5).

7.6 Simulation results: 0.8 Ωcm boron-doped Cz-Si device

The second part, both EWT solar cells fabricated on boron doped 0.8 Ωcm Cz-Si wafers are discussed. Table 7.5 depicts the simulated I-V-parameters. In contrast to the 3.5 Ωcm scenario, a BSF marginally improves the FF of the EWT cell fabricated on 0.8 Ωcm Cz-Si wafer. A BSF reduces the J_{sc} (Fig. 7.2(a)) decreasing the efficiency of the 0.8 Ωcm device.

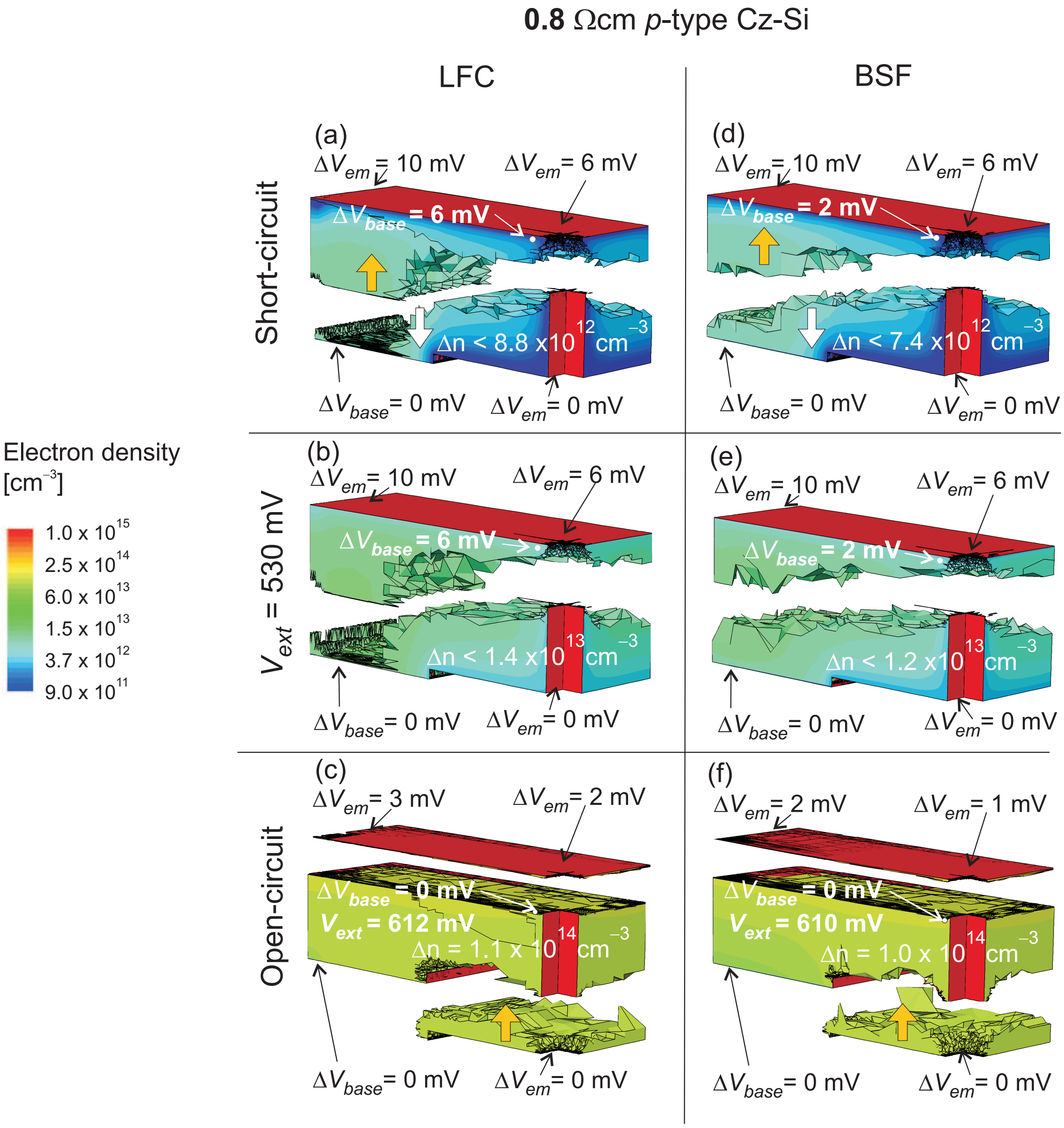

Figure 7.9: Electron distributions in the simulation domain of both 0.8 Ωcm EWT solar cells featuring either LFCs (left) or a BSF (right), at V_{ext}=0 mV (top panels), 530 mV (center panels) and for the respective V_{oc} of each solar cell (bottom panels). The simulation domains are split along the demarcation area at which the electron transport breaks into a front and rear collecting volume. The voltage drops V_{base} and V_{em} refer to the external voltages at the base or emitter contact, respectively.

7.6.1 External voltage range from 0 to 400 mV

Figures 7.5 (c) and (d) depict the distribution of the hole quasi-Fermi level in the simulation domain and the hole current trajectories at J_{sc}-conditions for the LFC and BSF device, respectively. The single trajectories launch near the front *pn*-junction with a lateral distance of 50 µm to each other. The trajectories in the 0.8 Ωcm cells are comparable to those in the referring 3.5 Ωcm devices. However, the maximum potential drops along $E_{F,h}$ are reduced between the rear base contacts and the bulk near the EWT-via emitter. The potential drops account for 6 meV in the LFC and 2 meV in the BSF simulation domain (see Figs. 7.5(c) and (d). Similar values are found at the front *pn*-junction where the potential drop along $E_{F,h}$ accounts for 5 meV and 1 meV in the LFC and

BSF scenario, respectively (see Fig. 7.6(d)).

The high boron-doping density of 0.8 Ωcm Cz-Si wafers increases the concentration of boron-oxygen complexes which results in a low bulk lifetime of 14 µs. The bulk diffusion length is 190 µm, and, hence is similar to the substrate thickness causing high SRH recombination currents that account for 1.4 mA/cm^2 in the LFC and BSF device (Fig. 7.8(c)).

The demarcation area near the full-area BSF is shifted toward the front emitter (Fig. 7.9(d)), whereas the demarcation area in the LFC device remains close to the Al_2O_3-passivated rear side (Fig. 7.9(a)). The effective surface recombination velocity in Eq. 3.32 is defined as the product of the base doping density N_A and the saturation current density J_0 of the respective surface. By substituting the wafer resistivity from 3.5 Ωcm (N_A=4.02×10^{15} cm^{-3}) to 0.8 Ωcm (N_A=1.93×10^{16} cm^{-3}), S_{eff} is amplified by a factor of five. Furthermore, the present BSF has an increased saturation current density ($J_{0,BSF} = 50$ fA/cm^2) compared to the dielectrically passivated rear side ($J_{0,Al2O3} < 10$ fA/cm^2). Hence, the BSF device fabricated on 0.8 Ωcm Cz-Si exhibits an S_{eff} of 50 cm/s, whereas S_{eff} of all other devices in this chapter are smaller than 12 cm/s. The recombination loaded surface causes a gradient in the electron QFL $E_{F,n}$. In the 0.8 Ωcm device, photogenerated electrons are driven to the BSF and recombine. Consequently, the demarcation area is more situated toward the front of the cell which indicates the higher recombination and the electron transport toward the BSF. The LFC and BSF device suffer from a simulated base area recombination current that accounts for 0.1 and 0.3 mA/cm^2, respectively (see Fig. 7.8(c)) [1].

7.6.2 External voltage around 530 mV

The spatially resolved transport of majority carriers is similar to the J_{sc}-scenario in Figs. 7.5(c) and (e). The base of both devices exhibit excess carrier densities Δn of about 1.2×10^{13} cm^{-3} (Fig. 7.9(b) and (e)). Compared to the 3.5 Ωcm scenario, the excess carrier density Δn is five times lower at external voltages between *MPP* and V_{oc} (Fig. 7.7 (b) and (e)) due to the five times higher wafer doping density (Eq. 3.8).

The demarcation areas in Figs. 7.9(b) and (e) marginally shift between 0 and 530 mV. The low carrier densities in the base induce high minority carrier resistances. The current of minority carriers is preferably transported toward the front *pn*-junction along the front and EWT-via emitter since they offer a lower resistance than the base of the solar cell. The EWT-via current is similar in both devices and starts declining due to the increasing total recombination but not due to demarcation area shifting (see Fig. 7.8(c)).

Inside the base, the potential drops along $E_{F,h}$ at the front *pn*-junction account for 5 meV and 1 meV in the LFC and BSF device, respectively (see Fig. 7.6(e)). Compared to a reference scenario with $\Delta V = 0$ mV, the carrier densities in the LFC and BSF device are increased by a factor of 1.2 and 1.0. Hence, both devices exhibit similar SRH recombination currents in the injection regime between *MPP* and V_{oc} (see Fig. 7.8(c)). Auger recombination is slightly increased in the BSF device (+0.2 mA/cm^2) due to the highly doped full-area back surface field. The marginal voltage drops of 4 mV inside the base of the LFC device does not induce an Auger recombination enhancement that would affect the *I*-*V*-curve as it has been the case in the 3.5 Ωcm scenario. Since the bulk lifetimes are constant and the voltage drop adaptions between J_{sc}- conditions and V_{ext}=530 mV are about zero, local ideality factors of all recombination current densities are close to unity (Fig. 7.8(d)).

---

[1] In the 3.5 Ωcm scenario, the recombination current density due to the BSF is less than 0.1 mA/cm^2. Any recombination at the dielectrically passivated non-diffused rear side of the LFC device does not affect J_{sc}.

7.6.3 External voltages around V_{oc}

In the present case of highly doped Si wafers, the implementation of a BSF marginally improves the device conductivity. The solar cell base operates at a narrow and defined voltage range even in the LFC scenario where $V_{local} \approx V_{ext}$. The BSF integration is disadvantageous for the device performance since it increases the total recombination without sustainably reducing the already small base series resistances and voltage drops.

The still existing EWT-via currents do not enter the external circuit at V_{oc}. Either, the currents recombine in the rear emitter (mainly Auger recombination) or, they are injected across the rear *pn*-junction and recombine in the base (mainly SRH recombination). The low bulk lifetime induces high SRH loss currents that account for about 27 mA/cm^2 at 612 mV. Compared to all other devices in this thesis, it is the highest SRH loss current in the respective voltage regime. The solar cell base offers a detrimental sink for the electron transport and electrons are injected across the rear *pn*-junction which is indicated by a yellow arrow in Figs. 7.9(c) and (d) [1].

The small adaption of the internal voltage drops inside the base from 5 meV (1 mV) in the LFC (BSF) device at *MPP* to 0 (0) mV at V_{oc} slightly affects the diode characteristics (Figs. 7.6 (e) and (f)). The voltage drop adaption along the EWT-via emitter from 6 mV at 530 mV to 1 mV at V_{oc} has a similar magnitude (see Figs. 7.6(e) and (f)). The higher voltage drop adaption inside the base of the LFC device results in slightly increased local ideality factors of the SRH and Auger recombination currents compared to the BSF scenario (see Fig. 7.8(d)). In the present scenario, the recombination of the BSF and LFC device has a diode characteristic with local ideality factors around unity. The total SRH recombination is strongly increased due to the low bulk lifetime compared to both 3.5 Ωcm devices. For this reason, V_{oc} (and J_{sc}) are lower which limits the efficiency even in the present case of low local ideality factors and high *FF*. Auger recombination is smaller and accounts for 9 mA/cm^2 and 6 mA/cm^2 for the BSF and LFC solar cells, respectively. The respective local ideality factors are close to unity.

7.7 Conclusion

A possible solution for improving the *FF* and the efficiency of EWT devices fabricated on lowly doped Cz-Si wafers (3.5 Ωcm) is the implementation of a BSF. A BSF constitutes an additional current path connected in parallel to the base. The BSF sustainably reduces the base series resistance and reduces voltage drops along the majority carrier current paths compared to a solar cell featuring LFC. A point-contact scheme (LFC) of the base results in higher series resistances, especially in the absorber that exhibits a low conductivity (3.5 Ωcm). Gradients of majority QFL are smaller in the BSF scenario which results in reduced ohmic power dissipation losses for external voltages between *MPP* and V_{oc} [152]. The injection of minority carrier densities across the *pn*-junctions is lower than those of a point-contacted solar cells at a defined external voltage. The BSF integration also reduces the magnitude of SRH recombination in the base and Auger recombination (mainly) in the emitter compared to those of the LFC device. Furthermore, all investigated recombination currents exhibit diode characteristics with local ideality factors closer to unity which is due to the lower voltage drop adaptions. The dilemma is cleared that high *FF* of EWT solar cells can be exclusively achieved by using highly doped Cz-Si wafers that suffer from strong bulk lifetime degradation. In the present chapter, an EWT solar cell processed on lowly doped Si wafer with integrated BSF exhibits the highest efficiency.

The passivation of boron-diffused surfaces by means of Al_2O_3 is a great progress in the development

---

[1] In the 3.5 Ωcm scenario, the SRH bulk lifetime is higher and the rear emitter offers a "deeper" sink for the electron recombination than the base. Hence, there is no carrier injection across the rear *pn*-junction at V_{oc}, see Fig. 7.7 (c) and (f).

of photovoltaics. Usually, diffused and passivated surfaces exhibit higher saturation currents than undiffused and passivated surfaces. The resulting saturation current of the Al_2O_3-passivated BSF only accounts for 50 fA/cm^2 in the applied process. This value is rather small for a 75 $\Omega/\square$ boron-diffusion that strongly decreases the device conductivity in the scenario of lowly doped Cz wafers. The effective surface recombination of the BSF is small for low and increased injection levels in the 3.5 Ωcm device. As a result, J_{sc} and V_{oc} are hardly affected compared to the LFC scenario.

A contrary situation holds for both the cells fabricated on highly doped Cz-Si wafers with a resistivity of 0.8 Ωcm. The BSF integration marginally reduces the already small base resistance. J_{sc} and V_{oc} suffer from recombination losses at the BSF compared to the LFC device that exhibits a lower recombination at the dielectrically passivated surfaces.

Laser-fired point contacts can be distributed more homogeneously at the base area at the rear side compared to the fabricated devices that exhibit a line of LFC. This would lead to shorter current paths of majority carriers inside the bulk and, consequently, smaller resistive and recombination losses. Note that laser-fired point contacts contribute to recombination losses at the base area. As a consequence, the number of LFC is limited in order to minimize its impact on V_{oc}. Furthermore, the series resistance contribution of the radial current transport around the LFC is high, as shown by the analytical calculations. Hence, this R_s-contribution will not be reduced by a more homogeneous distribution of LFC. However, more distributed LFC at the base area would be a first approach to achieve a potentially higher FF if this specific contact scheme is the preferred method of choice.

8 EWT solar cell fabricated on n-type Czochralski silicon

8.1 Introduction

The previous chapters investigated critical parameters that affect the I-V-characteristics of EWT solar cells. In terms of series resistances, the optimization strategy must comprise all single device components to achieve high fill factors.

Injection-dependent recombination rates of the wafer substrates represent a detrimental FF-loss mechanism and must be excluded. Auger recombination in the front emitter and low bulk lifetimes contribute to serious J_{sc}-losses, whereas V_{oc} is sensitive to all recombination currents inside the device.

In this chapter, the presented EWT device exhibits reduced recombination currents and a small total device series resistance. Phosphorus-doped n-type Cz-Si wafers are used as substrates in order to eliminate boron-oxygen complexes and the related SRH loss currents. As a result, moderately doped silicon wafers can be used that exhibit high bulk lifetimes and a feasible base conductivity. The saturation current of the applied 50 $\Omega/\Box$ boron emitter only accounts for 50 fA/cm^2 achieved by means of Al_2O_3-passivation techniques. Compared to SiN passivated, as-diffused phosphorus emitters with similar sheet resistances, the J_0-values of the Al_2O_3-passivated boron emitter is five times lower. The base series resistance is reduced by the implementation of a full-area phosphorus diffused BSF. Thermally grown SiO_2 passivates the BSF which results in saturation current densities of 120 fA/cm^2. The fabricated device has an efficiency of 21.6% and a fill factor of 80.8 %. To our knowledge, this is the highest FF of an EWT solar cell reported so far and the highest efficiency beside the result presented by Hermann in Ref. [37].

8.2 Solar cell fabrication

Figure 8.1 depicts the process of the n-type EWT solar cell. The as-cut wafer is etched in an aqueous KOH etching solution prior to the depicted fabrication steps in order to remove the saw damage. The wafer resistivity of 1.6 Ωcm (N_A= 3.0 × 10^{15} cm^{-3}) is a compromise between the highly doped 0.8 Ωcm and the lowly doped 3.5 Ωcm scenarios in the previous chapter. The geometrical device parameters are listed in Tab. 8.1.

(a) Both sides of the wafer are $POCl_3$ diffused with a sheet resistance of 75 $\Omega/\Box$ at 880°C in a tube furnace.

(b) SiN with a refractive index of 1.9 and a thickness of 100 nm is deposited at the rear side acting as a protection layer in the following texturization step. Random pyramids are etched in a KOH-isopropanol solution to improve light trapping.

(c) The SiN layer is removed in HF solution. A 350 nm thick SiO_2 layer is thermally grown on both sides of the wafer at 1000°C. A SiN layer with a refractive index of 1.9 and a thickness of 100 nm is deposited at the rear side. This SiO_2-SiN stack acts as an etching and diffusion barrier in the following KOH and high temperature processes.

(d) At the rear side, the SiO_2-SiN stack is structure by laser power to define the interdigitated emitter and base regions, and the EWT-vias are laser-drilled. The laser damaged Si is removed in aqueous KOH solution.

(e) At the front side, a frame of hotmelt solution is printed with an inkjet system. The SiO_2 layer is removed in HF solution within a window of 2.1×2.1 cm^2. The hotmelt is stripped in an aqueous KOH solution.

(f) A boron emitter with a sheet resistance of 50 Ω/□ is diffused at 890°C with a BBr_3 diffusion in a tube furnace. The emitter has a Gaussian like shape with a peak concentration of $1.0\times10^{20}cm^{-3}$ and a depth of 0.8 µm. The boron diffusion residues are removed in HF-solution. The SiN layer is etched off in phosphoric acid for 30 min at 140°C.

(g) A stack of plasma-assisted atomic layer deposited Al_2O_3 [31] and PECVD-SiN is deposited on both sides of the wafers followed by an annealing step at 400°C for 10 min in nitrogen atmosphere in a tube furnace. Al_2O_3 is a high quality passivation for boron-diffused silicon surfaces [158, 156]. Due to the increased temperature during the annealing step, the hydrogen atoms inside the SiN can diffuse toward the Si-SiO_2 and passivate defects [84]. The SiN-Al_2O_3 stack acts as an antireflexion or reflexion layer at the front or rear side, respectively.

(h) Pico-second laser power is locally applied to open the emitter and base area at the rear side with an area fraction of 3 %.

(i) Aluminum is evaporated and etched off between the base and emitter region for contact separation. Finally, annealing on a hot plate for 1 min at 300 °C improves the contact resistances.

Table 8.1: Geometrical parameters of the EWT solar cell fabricated on *n*-type Cz-Si. The EWT-via width is an averaged value. The real EWT geometry is shown as a scanning-electron microscope picture in Fig. 8.6.

Device parameters	Settings
Index i_x	1000 µm
Rear emitter width e_x	500 µm
Base width $i_x - e_x$	500 µm
Distance d_y between vias	500 µm
Averaged EWT-via width $v_x = v_y$	75 µm
Wafer thickness W	170 µm
Ditch depth d	20 µm
Illuminated cell area	2×2 cm^2

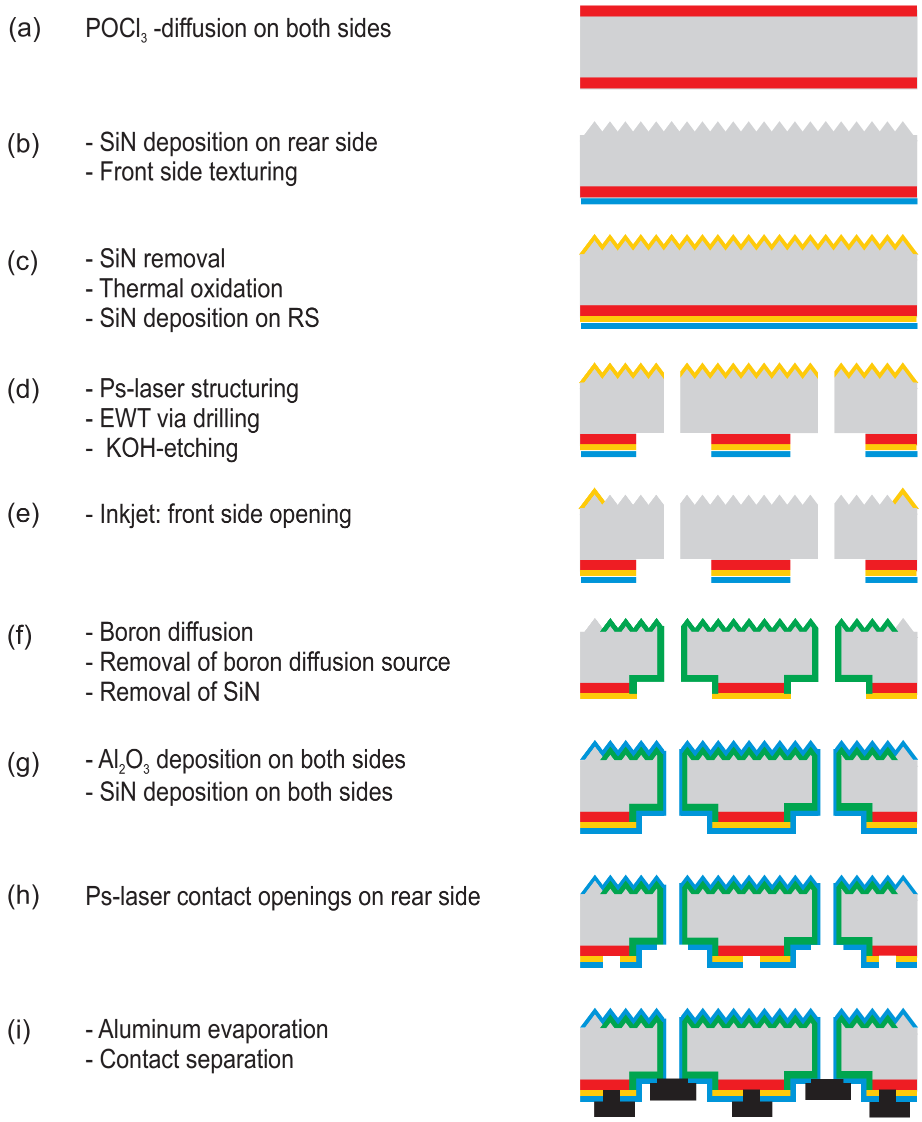

Figure 8.1: Fabrication sequence of the n-type Cz-Si EWT solar cell.

8.3 Experimental investigations

8.3.1 EWT-via emitter sheet resistance

The sheet resistance R_{sq} of the applied boron diffusion depends on the wafer topography. On a planar or textured wafer surface R_{sq} accounts for 50 $\Omega/\square$, whereas R_{sq} is increased to 110 $\Omega/\square$ in the EWT-via.

Fabrication of EWT-via emitter test samples

Figure 8.2 depicts a sketch of a test sample that has been used to determine the EWT-via sheet resistance. The edges of the via-drilled n-type Cz-Si wafer are masked by a SiN diffusion barrier. A boron diffusion is applied to the sample. On both sides of the wafer, aluminum with a thickness of 20 µm is evaporated through a mask that covers the wafer edges. Due to the diffusion barrier (⇒non-diffused edges) and the evaporation mask (⇒non-metalized edges), the edges remain non-conductive. There is no current flow along the wafer edges in the following analysis. A short etching step (t=2 min,T=70°C) in a solution containing phosphoric acid, nitric acid and acetic acid removes evaporated aluminum residues in the EWT-vias without removing the thick aluminum layer on both sides of the wafer.

Characterization of the EWT-via emitter sheet resistance

The total EWT-via emitter resistance is measured by a four point analysis between the front and rear side of the samples. At the front and rear side, one contact is applied to inject or collect the current, respectively. Another two contacts measure the voltage drop between the front and rear side as shown in Fig. 8.2. Currents injected into the sample are exclusively transported along the diffused EWT-vias. Lateral currents in the boron-diffused front and rear side can be neglected since the aluminum covers both sides of the sample. Hence, the front and rear side is assumed to be an equipotential surface. In consideration of the parallel connection of all EWT-vias, the resistance of one single EWT-via $R_{via,total}$ is calculated from:

$$R_{via,total} = N R_{total}, \tag{8.1}$$

where N is the number of EWT-vias of the test sample and R_{total} the measured (total) resistance between the front and rear side. The EWT-via emitter sheet resistance is calculated from:

$$R_{via} = \frac{N U R_{total}}{W}, \tag{8.2}$$

where U is the measured EWT-via perimeter and W the wafer thickness. In the present investigation, N=50, U=4×90 µm, W=160 µm and R_{total}=1 Ω, which results in an EWT-via emitter sheet resistance of 110 $\Omega/\square$.

BBr_3 diffusions are critical in terms of boron-rich layer formations suspected to generate crystallographic defects [159] and silicon wafer bulk lifetime degradations [160]. A minimization of deposition time of the boron diffusion source at moderate temperatures (e.g. T<900°C) prevent the formation of boron-rich layers. The applied deposition time for the solar cells and the test samples (45 min at 890°C) is a compromise in order to achieve feasible EWT-via sheet resistances without the effect of a possible bulk lifetime degradation. Longer deposition times would decrease the EWT-via resistance but carries with it the danger of boron-rich layer formations and, hence, bulk lifetime degradation.

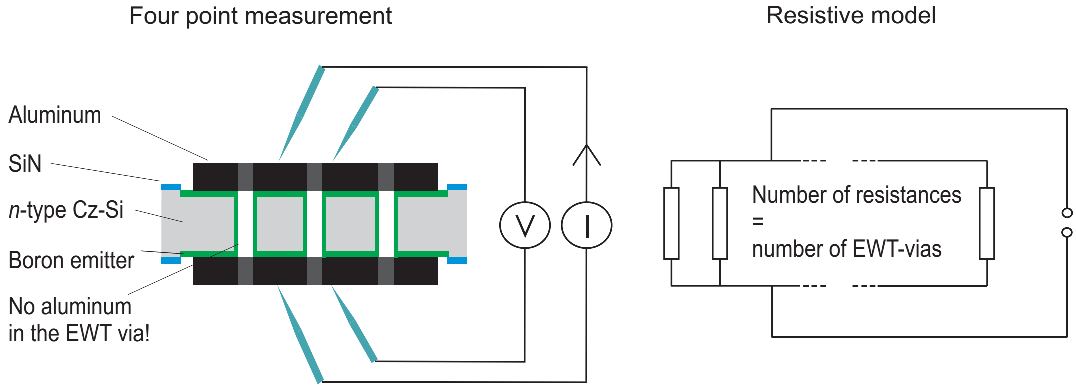
Four point measurement

Resistive model

Figure 8.2: Left: Test sample for the determination of the EWT-via sheet resistance. The boron diffusion inside the EWT-via connects the front and rear side. Aluminum is evaporated on both sides to contact the boron diffusion. Right: The respective resistive network is a parallel circuit of series resistances.

8.3.2 Boron emitter recombination

Boron diffusions are known for causing dislocations in the silicon crystal lattice [159]. A possible consequence could be injection dependent recombination currents of boron emitters with local ideality factors greater than unity due to defects near or inside the *pn*-junction region. As a possible result, the *FF* of the solar cells could be reduced [129].[1]

Fabrication of boron emitter test samples

In order to investigate this assumption, we fabricate reference samples on *n*-type Cz-Si wafers with a resistivity of 2.2 Ωcm. The first type of sample features two alkaline textured surfaces (random pyramids). The second type of sample features two untextured (planar) surfaces. All samples are boron-diffused in the same diffusion process of the solar cell and exhibit the same emitter sheet resistance (R_{sq}=50 Ω/□). The first and second type of sample is a reference for the textured and planar front and rear emitter of the solar cell, respectively. All samples are passivated with a stack of 20 nm Al_2O_3 (ALD) and 60 nm SiN (refractive index=1.9) on both sides of the boron-diffused wafer surfaces.

Boron emitter characteristics

Implied J_{rec}-V_{oc}-characteristics of the boron emitter samples are recorded by means of QSSPC techniques as described in Section 3.5 on page 3.34 [148]. J_{rec} is measured as a function of the implied voltage. In the next step, the measured recombination current is weighted by a factor $1/p$ that relates the recombination loaded area of the test sample to those of the referring device component. The bulk lifetime of the wafer is constant and exhibits values of 1000 µs as determined by an non-diffused and Al_2O_3-passivated sample. The measured recombination currents also comprise the bulk recombination that has a low magnitude. The stronger emitter recombination dominates the shape of the measured implied I-V-curves.

Concrete example: The solar cell features a textured and boron-diffused front side. The respective emitter test sample features a textured, boron-diffused front **and** rear side. The respective recombination of the sample is twofold increased compared to those of the solar cell. Hence, the weighting factor that relates the recombination of the solar cell to the recombination of the test sample is 1/2. In the case of a boron-diffused sample with planar wafer surfaces, the weighting $1/p$ is 1/4. Only 50 % of the solar cell rear side (planar surface) features a boron diffusion.

Figure 8.3 depicts the measured implied J_{rec}-V_{oc}-characteristics of the textured (red) and planar (green) boron-diffused and passivated samples, both plotted without the application of a weighting factor.

The solar cell presented in this chapter has a short-circuit current density of 40.4 mA/cm^2 at 1 sun illumination. Assuming this value, the implied V_{oc} of the textured and planar emitter sample accounts for 668 mV and 690 mV, respectively. The surface of the textured sample is increased by a factor of 1.22 compared to a planar surface. The respective recombination is higher for the textured than for the planar sample as shown in Fig. 8.3.

In order to calculate the area-weighted emitter recombination for the total device, the currents of the textured and planar sample are weighted by a factor of 1/2 and 1/4, respectively. Both weighted recombination currents are summarized (black curve in Fig. 8.3). The implied open-circuit voltage of the summarized emitter characteristics accounts for 670 mV at 1 sun illumination.

A reference recombination with a constant local ideality factor of unity (n=1) is depicted by

---

[1] The boron diffusion in the previous chapter has been applied to form a BSF on *p*-type substrate. In this scenario, there is no *pn*-junction and defects are less critical in terms of injection-dependent recombination rates [108].

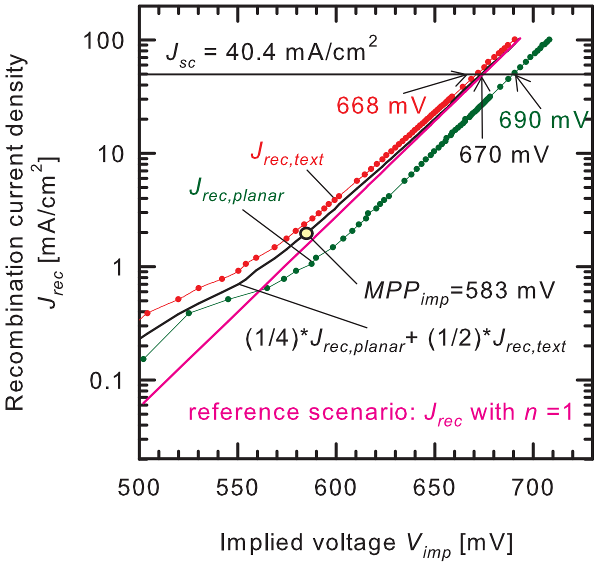

Figure 8.3: Implied I-V-characteristics of both-sided textured ($J_{rec,text}$) and planar ($J_{rec,planar}$) boron-diffused n-type Cz-Si wafers passivated by a 20 nm thick Al_2O_3-layer. The measured data points are connected by lines as guide for the eyes. In order to calculate the total emitter recombination of the device, the implied I-V-characteristics of the textured (planar) sample is weighted by a factor of 1/2 (1/4) (not shown in this figure). Then, both weighted recombinations are summarized in order to calculate a curve that represents the total emitter recombination of the device in the absence of series resistances. A reference characteristic with a constant local ideality factor of unity and a similar V_{oc} of 670 mV (pink color) is plotted to illustrate the deviated behaviour of the emitter recombination for implied voltages smaller than 630 mV.

a pink-colored line in Fig. 8.3. This reference characteristic has the same implied V_{oc} at 1 sun illumination that accounts for 670 mV. For voltages smaller than 630 mV, the emitter recombination deviates from those of an ideal diode. A possible reason is the existence of silicon lattice defects induced by the boron-diffusion [159]. A physical reason for this specific type of recombination is currently under investigation and is not investigated within this thesis.

As discussed above, the boron-emitter recombination exhibits an implied I-V-curve that deviates from the ideal diode characteristic. We apply our diode network depicted in Fig. 4.3 in order to calculate the FF-loss of the device which is based on the boron emitter recombination. The open-circuit voltage of the solar cell (661 mV) is achieved by summarizing the total emitter recombination (black solid line in Fig. 8.3) and the recombination current of an ideal diode with a constant saturation current density of 117 fA/cm^2 that represents the remaining recombination currents of the device (see Eq. 4.2). The experimental J_{sc} is used as an input parameter. The calculated *pseudo*-FF accounts for 83.1 %. The FF of an ideal diode with a constant local ideality factor of unity and a V_{oc} of 661 mV is 84 %. Hence, there is a reduction of 0.9 % due to the boron-emitter recombination.

8.4 Solar cell characterization

Table 8.2 depicts the experimental I-V-parameters of the n-type EWT solar cell. The I-V-curves, the respective local ideality factors and the series resistance calculated by a comparison of the J_{sc}-V_{oc}-curve and the illuminated 1 sun I-V-characteristics are depicted in Figs. 8.4(a), (b) and (c), respectively.

Table 8.2: I-V-parameters of the n-type EWT solar cell measured under standard conditions (halogen lamp approximating the am1.5g spectrum, temperature=25 °C).

J_{sc}	V_{oc}	J_{mpp}	V_{mpp}	FF	FF_{pseudo}	η
(mA/cm^2)	(mV)	(mA/cm^2)	(mV)	(%)	(%)	(%)
40.4	661	38.3	563	80.8	83.0	21.6

The J_{sc} is measured with an error of ±0.1 mA/cm^2, the V_{oc} with an error of ±1 mV and the FF with an error of ±0.1 %. For measuring the bulk lifetime, all dopant diffusions of the cell are etched off after the process, and all surfaces are passivated with a SiN layer (refractive index = 2.4). From these measurements, the SRH lifetime in the bulk is extracted using Eq. 3.29. The effective surface recombination velocity of referring SiN layers is 9 cm/s. Calculated bulk lifetimes account for 1000 µs and are constant in the entire injection regime between J_{sc} and V_{oc}.

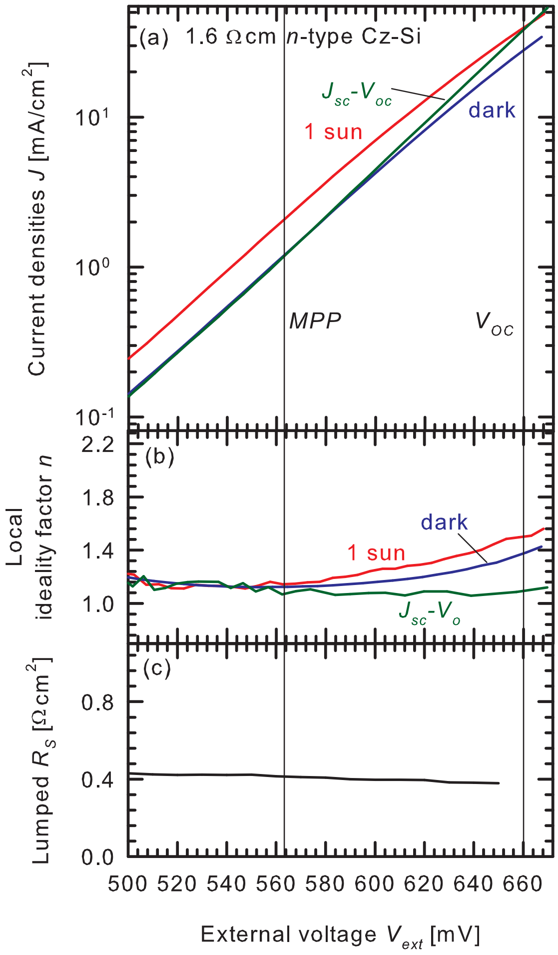

Figure 8.4: Top panels: measured I-V-characteristics under 1 sun illumination (shifted by J_{sc}), under dark conditions, and the J_{sc}-V_{oc}-values obtained under various illumination intensities for the EWT solar cell fabricated on 1.6 Ωcm n-type Cz-Si. Center panels: measured local ideality factors of the above I-V-characteristics. Bottom panels: lumped series resistance, extracted from the 1 sun and J_{sc}-V_{oc}-curves.

8.4.1 Short-circuit current

The experimental J_{sc} is 40.4 mA/cm^2, the highest value of all solar cells in this thesis. Figure 8.5 depicts the internal quantum efficiency (IQE) and the reflexion of the solar cell, both measured for the am1.5g spectrum.

The total reflexion losses in units of mA/cm^2 are calculated from:

$$J_{ref,loss} = q \int_0^{\lambda} R(\lambda)\phi(\lambda)d\lambda, \tag{8.3}$$

where $R(\lambda)$ is the wavelength dependent reflexion coefficient shown in Fig. 8.5, $\phi(\lambda)$ the spectrum of the photon flux and λ the wavelength of the incident light. For wavelengths greater than 1200 nm, silicon becomes transparent which defines the limit of photon wavelengths that can be absorbed. The respective reflexion losses account for 2 mA/cm^2 composed of 0.5 mA/cm^2 and 1.5 mA/cm^2 for wavelengths smaller and greater than 800 nm, respectively.

Silicon has an indirect band gap. The maximum energy of the valence band has another crystal momentum than the minimum energy of the conduction band. The minimum distance between the valence and the conduction band in silicon accounts for about 1.1 eV at 300 K. The generation of a free electron and hole carrier involves the absorption of a photon and the absorption or the emission of a phonon. The two-particle process including a phonon and a photon is less probable than a one particle absorption process (only one photon). The latter scenario exists in direct semiconductors, such as gallium arsenide, which have higher absorption coefficients compared to silicon. The higher the photon energy the higher the absorption coefficient and the probability for generating free electrons and holes in silicon.

The IQE is the relation between the number of photogenerated and collected carriers entering the external circuit solar to the number of photons absorbed inside the device. The absorption coefficient of silicon for the incident light strongly depends on the photon energy and, hence, on the wavelength. As an example, light with a wavelength smaller 600 nm (E>2.1 eV) is absorbed within the first 5 µm, whereas light with wavelengths of 1100 µm (E ≈1.1 eV) can pass several hundreds micrometers until it is absorbed.

The IQE of the n-type device is plotted as function of the wavelength in Fig. 8.5. In an ideal (virtual) case, the IQE would be constant and account for "1" which means that all photogenerated carriers are collected at the pn-junction and flow into the external circuit. A reduced IQE indicates recombination losses and/or losses based on free-carrier absorption.

Recombination losses are calculated by means of Eq. 3.11 in Ref. [99]. The respective losses for wavelengths smaller than 800 nm account for 0.6 mA/cm^2 which is mainly due to Auger recombination in the "bulk" of the front emitter and due to recombination losses at the passivated front side. It has been discussed in the context of the solar cell process that the present boron emitter exhibits a high surface concentration of 1.0×10^{20}cm^{-3}. Other solar cell developers applied drive-in steps at elevated temperatures (T> 850°C) in order to reduce the peak concentrations of their front emitters [40, 39, 161]. The consequence is a lower Auger recombination and a potentially lower surface recombination velocity of the passivated front side that sensitively reacts to high surface diffusion densities [142, 126]. The achieved gain of the short-circuit currents has been about 0.5 mA/cm^2 in the mentioned references. However, another high temperature step would complicate the already complex EWT process sequence discussed in this chapter. For this reason, we make a compromise of applying an already "good" emitter with a rather low saturation current density without further improvement steps.

Losses for wavelengths greater than 800 nm are caused by free-carrier absorption of the semiconductor, the aluminum metalization and the BSF. The BSF contributes to further recombination

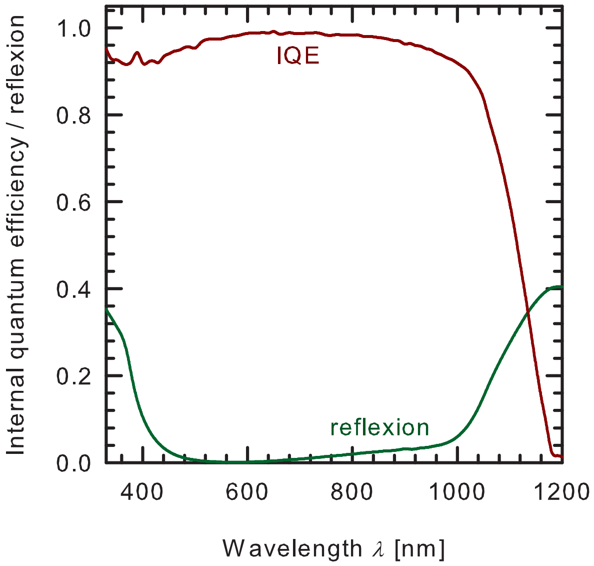

Figure 8.5: Internal quantum efficiency and reflexion of the n-type EWT solar cell.

losses of minority carriers which are photogenerated near the base area at the rear side. However, the respective losses are small. A virtual scenario would be a declining IQE in the wavelength range λ >800 nm. This behavior would indicate high surface recombination velocities at the base area and/or low bulk lifetimes. The present IQE exhibits a rathter constant section in the wavelength range up to 1000 nm. This behaviour indicates low J_{sc}-losses due to the BSF and the bulk of the solar cell. In the present scenario at J_{sc}-conditions, bulk recombination losses are marginal. The high bulk lifetimes (1000 µs) results in bulk diffusions lengths of 1077 µm which is 6 times larger than the wafer thickness. A detailed discussion of recombination losses is given in context with the simulation results.

8.4.2 Open circuit voltage

The experimental V_{oc} of the n-type device accounts for 661 mV. In the scenario of an ideal diode with a constant ideality factor of unity (n=1), the respective V_{oc} is defined for a total saturation current density of 270 fA/cm^2. The condition of n=1 does not hold for the n-type EWT device as indicated by the slightly increased local ideality factors of the J_{sc}-V_{oc}-characteristic in Fig. 8.4(b). In the injection range between 500 mV and V_{oc}, local ideality factors of the J_{sc}-V_{oc}-curve are between 1.0 and 1.2. However, the deviation of the local ideality factors is low. We give a V_{oc}-estimation by summarizing saturation currents measured by means of QSSPC techniques. For this reason, test samples have been fabricated that correspond to specific device components.

The boron emitter saturation currents on one textured or one planar surface account for 60 fA/cm^2 and 50 fA/cm^2, respectively. The BSF and bulk saturation current accounts for 120 fA/cm^2 and 10 fA/cm^2, respectively. 50% of the solar cell rear side features a boron-emitter or a BSF. Hence, the saturation currents of the rear emitter and the BSF must be area-weighted by a factor of 1/2. The sum of the bulk and surface saturation currents accounts for 155 fA/cm^2. The remaining difference of 115 fA/cm^2 is due to the contact openings [162, 163] and the recombination of the non-illuminated device area at the shaded edges that also contributes to the total recombination.

8.4.3 Fill factor

The *pseudo-FF* of the J_{sc}-V_{oc}-curve and the theoretical FF-limit of an ideal diode with a constant local ideality factor of unity and a V_{oc} of 661 mV accounts for 83.0 % and 84.0 %, respectively. Figure 8.4(b) depicts the local ideality factors of the J_{sc}-V_{oc}-curve. Local ideality factors larger than unity indicate deviations of the ideal diode behaviour.

It has been shown by means of the boron emitter characteristics that the referring recombination currents contribute to about 0.9 % of the FF-loss of the device. Hence, the 1% difference between the *pseudo-FF* and the maximum FF-limit can be explained by the non-ideal boron emitter recombination.

To our knowledge, the experimental *pseudo-FF* (83.0 %) and the FF of the 1 sun I-V-curve (80.8 %) are the highest results of an EWT solar cell that are found in literature so far. Similar to the approach in the previous chapter, we discuss the calculated series resistances of the device components in order to estimate their impact on the fill factor (Tab. 8.3).

Table 8.3: Calculated series resistance contributions of the EWT solar cell fabricated on 1.6 Ωcm *n*-type Cz-Si wafers: parallel current path in front emitter $R_{em,par}$ (Eq. 4.8), radial current path in front emitter $R_{em,rad}$ (Eq. 4.13), current path in EWT-via emitter $R_{em,via}$ (Eq. 4.6), vertical current path in base $R^{BSF}_{base,ver}$ (Eq. 4.24), parallel current path in base $R^{BSF}_{base,par}$ (4.24), parallel current path inside BSF $R^{BSF}_{BSF,par}$ (Eq. 4.27).

ρ (Ωcm)	$R_{em,par}$ (Ωcm^2)	$R_{em,rad}$ (Ωcm^2)	$R_{em,via}$ (Ωcm^2)	$R^{BSF}_{base,ver}$ (Ωcm^2)	$R^{BSF}_{base,par}$ (Ωcm^2)	$R^{BSF}_{BSF,par}$ (Ωcm^2)	$\sum R$ (Ωcm^2)
1.6	0.02	0.07	0.28	0.03	0.02	0.06	0.48

The geometrical device parameters determine the single R_s contributions. For this reason, we present a side-view of an EWT-via that has been recorded by a scanning-electron microscope (SEM). A similar EWT solar cell of this production series has been broken apart to get the wafer cross section. Note that the side-view is tilted. The depicted wafer thickness seems to be smaller than the real value of 170 µm. The EWT-via diameter is tapered near the front emitter and exhibits a wider opening at the rear. This is caused by the SiO_2 layer at the front side which has been grown prior the laser via-drilling and KOH-etching process. SiO_2 has a lower etching rate in KOH solution compared to silicon. Probably, the EWT-via opening at the front, surrounded by SiO_2, is a bottle neck for the exchange of the etching solutions and the etching products. In contrast, the rear side is not covered by a dielectric layer and, hence, exhibits a wider EWT-via width. The etching rate is lower near the front side which results in a smaller EWT-via diameter. The via-opening is square with a diameter that accounts for 50 µm at the front and 120 µm at the EWT rear emitter. We use the EWT-via geometry to calculate an averaged diameter ($\Rightarrow$ v=75 µm) used to calculate the EWT-via emitter resistance ($R_{em,via}$).

The calculated series resistance of the EWT-via ($R_{em,via}$=0.28 Ωcm^2) is the largest contribution of all device components (see Tab. 8.3). Primarily, this is caused by the high emitter sheet resistance of 110 Ω/□ and, secondarily, by the comparatively narrow EWT-via diameter. The second largest resistance contribution ($R_{em,rad}$=0.07 Ωcm^2) is due to the radial current transport inside the front emitter around the EWT-via. Note that the real EWT-via diameter of 50 µm at the front side has been respected to calculate this value. Figure 8.6 shows the cross section of an EWT-via taken by means of a scanning electron microscope.

Equation 4.2 is used to estimate the FF-loss based on the resistive loaded current transport in the emitter. We use the diode network in Fig. 4.3 that includes the boron-emitter recombination and the recombination described with a constant saturation current of 117 fA/cm^2 in order to

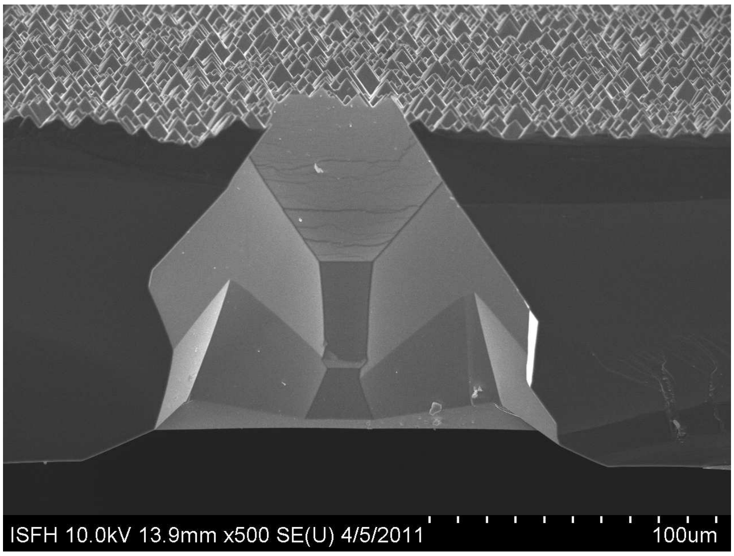

Figure 8.6: Cross section of an EWT-via recorded by a scanning-electron microscope. The front emitter (rear emitter) situated in the upper (lower) part of the photograph around the EWT-via features a textured (planar) surface.

achieve the experimental solar cell open-circuit voltage (661 mV). A total emitter resistance of 0.37 Ωcm^2 is considered that results in a calculated *FF* of 81.4 %. Assuming R_s=0 Ωcm^2 in the diode network, the *FF* accounts for 83.1 %. As a result, the emitter resistance contributes to a *FF*-loss of about 1.7 %. A similar operation is applied for the summarized base resistance (R_{base}=0.11 $\Omega\text{cm}^2 \Rightarrow FF_{calc}$=82.5 %) which results in a calculated *FF*-loss of 0.6 %. In the present scenario, the emitter resistance is the dominant parameter in terms of *FF*-losses.

The sum of all calculated series resistances is 0.48 Ωcm^2. This values agrees with the measured R_s of 0.43 Ωcm^2 around *MPP* as shown in Fig. 8.4. Again, we apply the diode network to calculate the *FF*. The model features the measured recombination currents of the passivated boron emitters and the passivated phosphorus BSF, as well as the experimental total series resistance at *MPP*. The calculated value of 80.9 % reproduces the experimental *FF* (80.8 %) with a small deviation of 0.1 %. Hence, the total device resistance reduces the *FF* by about 2.1 % compared to a virtual scenario with R_s=0.

Similar to the calculation in the previous chapter, we discuss the decline of the experimentally deduced series resistance of the solar cell between 500 mV and V_{oc} (see Fig. 8.4(c)). The base doping density accounts for 3.0×10^{15} cm^{-3}. The excess carrier densities inside the base at J_{sc}, *MPP* (561 mV) and V_{oc} (661 mV) account for 2.7×10^{13} cm^{-3}, 1.8×10^{14} cm^{-3} and 2.7×10^{15} cm^{-3}, respectively. The resulting base resistivity at J_{sc}, *MPP* and V_{oc} is 1.6 Ωcm, 1.5 Ωcm and 0.9 Ωcm, respectively. As a result of the increased density of majority carriers between the maximum power point and open circuit conditions, the base resistivity decreases by a factor of 0.6 (-40 %). The derived series resistances of the base components are proportional to the wafer resistivity (see Eqs. 4.22 and 4.24). Multiplying the factor of 0.6 with the analytically calculated base series resistances of the n-type device depicted in Tab. 8.3, the calculated total device resistance decreases from about 0.48 Ωcm^2 to 0.46 Ωcm^2, a difference of 0.02 Ωcm^2.[1] The experimentally derived series resistance of the n-type solar cells declines from 0.43 Ωcm^2 at V_{ext}=500 mV to about 0.39 Ωcm^2 at V_{ext}=661 mV, a difference of 0.04 Ωcm^2. The experimental and the calculated device resistances are hardly affected by the very small base series resistance contributions $R^{BSF}_{base,ver}$ and $R^{BSF}_{base,par}$ in Tab. 8.3. For this reason, the decline of the experimental and the calculated R_s is very small. However, the decline

---

[1] Note that the series resistances in Tab. 8.3 have been calculated for an excess carrier density of zero ($\Delta n = 0$).

can be explained (with an error of 0.02 Ωcm^2) by the increased majority carrier densities inside the base at elevated external voltages.

8.4.4 Efficiency

Investigations of laser-drilled boron diffused samples have revealed the high emitter sheet resistance in the EWT-vias. The series resistances are area-averaged values.. Reducing the EWT-via index and distance results in smaller resistances of all device components. The smaller the unit cell of the EWT device, the smaller the front emitter area that collects the photogenerated current which is transported through the EWT-via resistance. Hence, resistive losses are reduced for smaller EWT-distances and indices. This strategy has been applied in the present n-type EWT device. The experimental total R_s of 0.43 Ωcm^2 is comparatively small in the scenario of an EWT device that features long current paths for majority carriers. The strategy of reducing the geometrical device parameters is straightforward and easy to apply compared to the implementation of a further boron diffusion in order to decrease the EWT-via emitter sheet resistance.

Compared to all other devices in this thesis, the present bulk lifetime exhibits the highest value of 1000 µs. Note that in the case of n-type Cz-Si, the present bulk lifetime is comparatively small and can be outperformed by wafers featuring a higher quality. In this scenario, effective bulk lifetimes would be closer to the Auger recombination limit as described in Ref. [22]. However, the bulk saturation current density of about 10 fA/cm^2 is small compared to the total saturation current density of 270 fA/cm^2. Hence, an improvement must focus on the emitter, BSF and semiconductor-metal-contact recombination.

8.5 Device simulation

A detailed description of device modeling is given in Section 6.5. The simulated I-V-parameters are listed in Tab. 8.4. The generation current density is simulated by means of the ray tracing software SUNRAYS considering the reflexion and absorption data of all dielectric layers (J_{gen} ≈40.5 mA/cm^2). The numerical simulation model reproduces the experimental J_{sc} with a precision of 0.4 mA/cm^2 and the experimental V_{oc} with a precision of 2 mV. The simulated FF is higher (+1.0 %) compared to the experimental result. The boron-emitter recombination has an ideal diode characteristic (n=1) in the simulation model. FF-losses caused by the experimentally investigated non-ideal boron-emitter recombination are not considered. SRH lifetime parameters τ_n and τ_p are set as 1000 µs.

Table 8.4: I-V-parameters of the n-type EWT solar cell simulated by means of the three-dimensional EWT SENTAURUS model. The EWT simulation domain is depicted in Fig. 4.8.

ρ (Ωcm)	J_{sc} (mA/cm^2)	V_{oc} (mV)	J_{mpp} (mA/cm^2)	V_{mpp} (mV)	FF (%)	η (%)
1.6	40.0	659	37.8	571	81.8	21.6

8.5.1 Introduction

In the present n-type Si scenario, the FF-reduction is mainly based on resistive losses of majority carriers in the emitter. Auger recombination is primarily affected by an adaption of internal voltage drops between front and rear emitter. Secondarily, the smaller voltage drop inside the base also biases Auger recombination of the device. SRH recombination has a minor impact due to the high bulk lifetime.

Figure 8.7 shows the side view of the three-dimensional simulation domains at J_{sc}, MPP and V_{oc}. The voltage drops between the rear emitter contacts (rear base contacts) and the emitter positions (base positions) point to the referring areas (ΔV_{em} and ΔV_{base}). The BSF covers the lower left edge, the rear emitter the lower right edge of the simulation domain. Internal current trajectories of majority carriers (electrons) are similar to the BSF scenario shown in Fig. 7.5(b) and not depicted in the present figure. The voltage dependent EWT-via current, the recombination losses and the respective local ideality factors of the $J_{rec,0}$-shifted recombination characteristics are shown in Fig. 8.8.

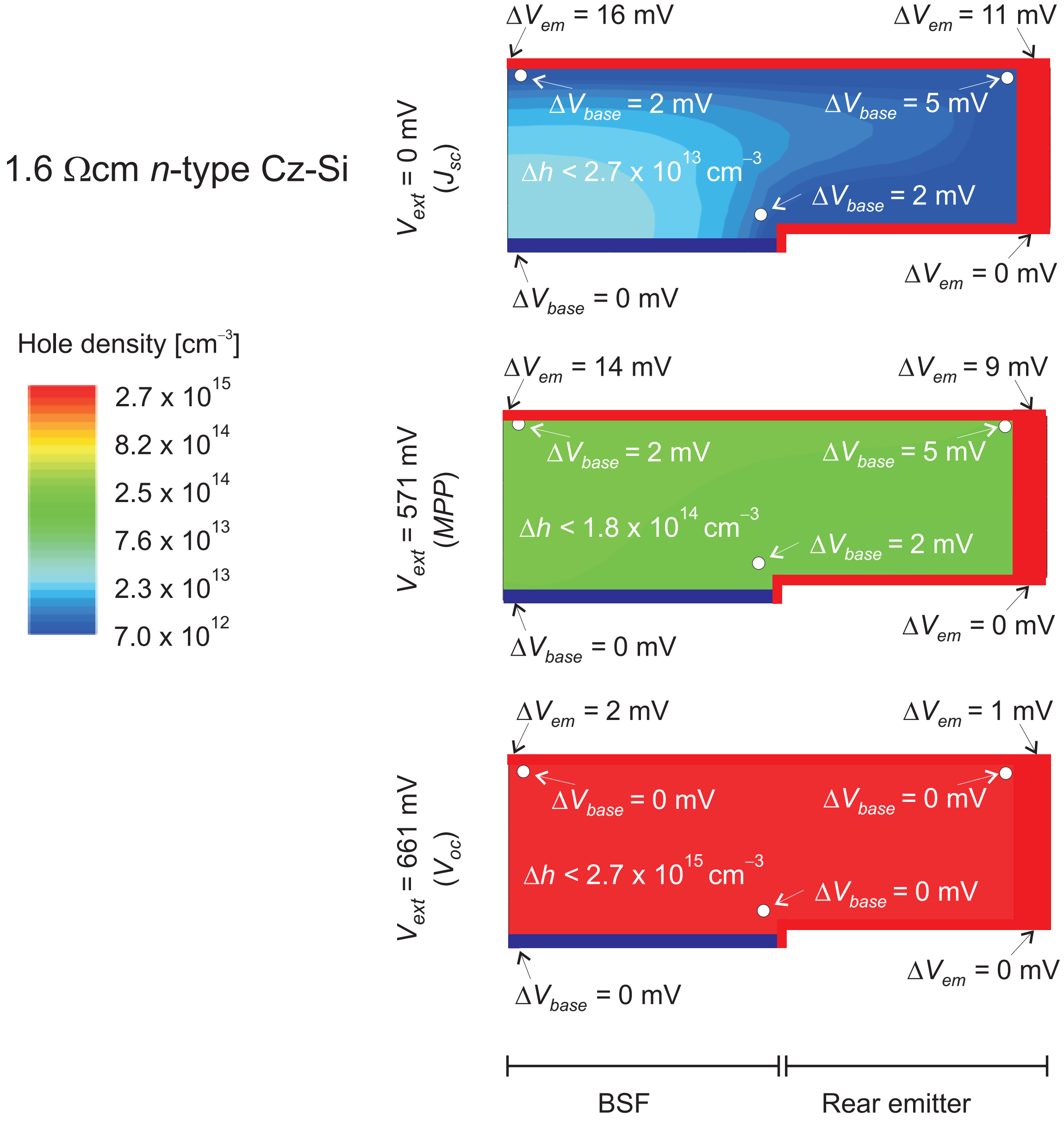

Figure 8.7: Voltage drop evolution and hole concentration inside the base at J_{sc}, MPP and V_{oc}. The moderate wafer resistivity of 1.6 Ωcm and the BSF reduce the voltage drop inside the base ΔV_{base} that only accounts for 5 mV at J_{sc}. The voltage drop between rear and front emitter ΔV_{em} accounts for 11 mV at J_{sc} due to the large EWT-via resistance of 0.28 Ωcm^2.

8.5.2 Short-circuit

At J_{sc}, 38 mA/cm^2 of photogenerated minority carriers (holes) are collected at the front pn-junction and transported through the EWT-via (Fig. 8.8(a)). Auger recombination, mainly in the front emitter, dominates the total loss current that accounts for 0.5 mA/cm^2. This loss current magnitude has been found by analyzing the internal quantum efficiency in the wavelength range up to 800 nm which is sensitive for recombination losses in the emitter (see Fig. 8.5). The EWT-via resistance of 0.28 Ωcm^2 induces a voltage drop ΔV_{em} of 11 mV between the front and rear emitter (Fig. 8.7(a)). The voltage drop inside the base ΔV_{base} only accounts for 5 mV between the rear base contact and the base volume near the EWT-via (Fig. 8.7(a)).

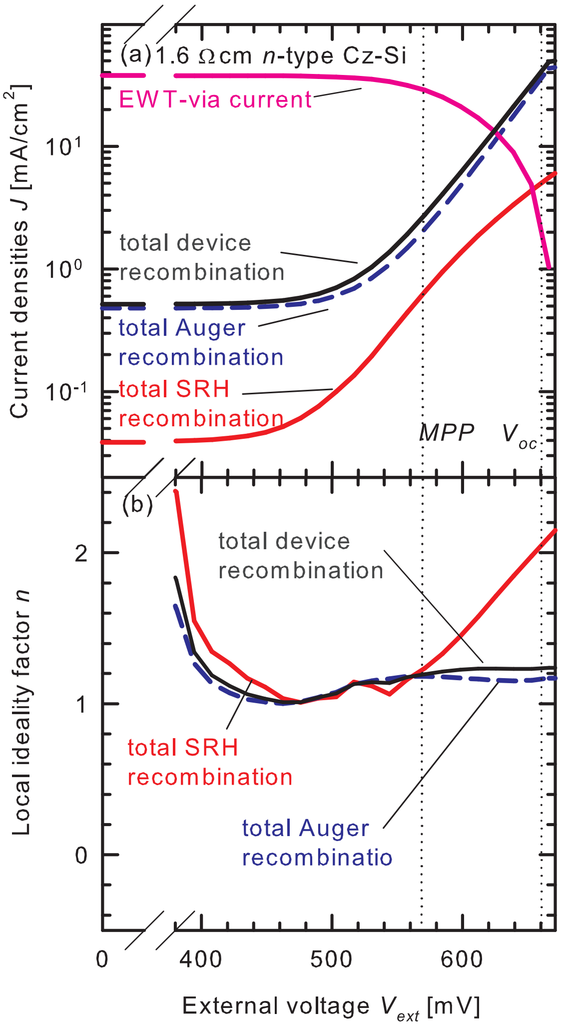

Figure 8.8: Simulated Auger and SRH recombination losses (a) and local ideality factors of the recombination characteristics (b) of the EWT device processed on 1.6 Ωcm n-type Cz-Si. To calculate the local ideality factors, the SRH and Auger recombination currents are shifted by the referring recombination contributions $J_{rec,0}$ at V_{ext}=0 mV. Also shown is the current-density flowing from the front to the back of the cell through the EWT-via emitter.

8.5.3 Maximum power point

At V_{ext}=571 mV (MPP), the minority carrier density in the base is sevenfold increased compared to the J_{sc}-scenario (Fig. 8.7(b)). The increasing carrier density results in a reduced resistance for the current transport of minority carriers (holes) through the base of the solar cell. The predominant part of photogenerated holes follow the path of lowest resistance which is still the front and EWT-via emitter (J_{via}=30.5 mA/cm^2). However, more holes are transported through the base at *MPP*-conditions compared the J_{sc}-scenario. The decline of the EWT-via current ($\Delta J_{via} = 7.5$ mA/cm^2 between J_{sc} and *MPP*) is greater than the increase of the total recombination ($\Delta J_{rec} = 1.8$ mA/cm^2 between J_{sc} and *MPP*) as shown in Fig. 8.8(a). The decreasing EWT-via current results in a reduced voltage drop between the front and rear emitter (11 mV at J_{sc}, 9 mV at *MPP*). Consequently, the local voltage of the front emitter increases at a slower pace than V_{ext} which leads to a lower injection of carriers compared to the scenario of a perfect diode with R_s= 0. As a result, the local ideality factors of Auger and SRH recombination are increased at *MPP* (n=1.2, see Fig. 8.8(b)).

At *MPP*, the total recombination (J_{rec}=2.3 mA/cm^2) is still considerably lower than the generation. The electron carrier currents inside the base exhibit a similar magnitude compared to J_{sc}-conditions. The induced potential drops ΔV_{base} are marginally affected by the recombination and account for 5 mV between the rear base contacts and the base volume near the EWT-via.

Note that the local voltage at the *pn*-junction biases the injection of carriers from the base into the emitter and from the emitter into the base. In the present scenario, the voltage drop along the EWT-via and front emitter accounts for 9 mV and 14 mV depending on the position at the front side of the solar cell. At the front *pn*-junction, the applied voltage is the sum of the external voltage and the emitter and base voltage drops of about 15 mV on an average. By using Eq. 3.51, the higher local voltage at the front *pn*-junction results in a carrier density and, hence, in a recombination current that is increased by a factor of about 1.8 compared to a reference scenario with R_s=0 and ΔV=0. Due to the high bulk lifetimes of 1000 µs, the low SRH recombination does not affect the shape of the total recombination or the *I*-*V*-curve at *MPP*. In contrast, Auger recombination is the dominant loss mechanism in the present scenario and accounts for about 2 mA/cm^2.

8.5.4 Open circuit

The minority carrier density in the base ($\Delta h = 2.7 \times 10^{15} cm^{-3}$) is fifteen-fold increased compared to the *MPP*-scenario (compare Figs. 8.7(b) and (c)).

The total recombination is dominated by Auger loss currents of 35.4 mA/cm^2. SRH recombination is about 5 mA/cm^2, sevenfold smaller than Auger recombination caused by the highly doped emitter and the phosphorus-doped BSF. The comparison emphasizes the advantage of *n*-type Cz-Si for the fabrication of high-efficient solar cells. An optimization can focus on the diffused and non-diffused surfaces. The bulk lifetime is not the dominant loss mechanism that limits the device efficiency. For this reason, the highest reported efficiencies, so far, refer to EWT devices that are fabricated on float-zone silicon wafers that also profit from very high bulk lifetimes. A list of published efficiencies is given in Chapter 2 on page 5 that reviews the historical context of EWT solar cells.

The small impact of SRH recombination on the *I*-*V*- characteristic is also found by considering the local ideality factors in Fig. 8.8(b). The low magnitude of SRH currents marginally affects the ideality factors of the total recombination. Auger recombination determines the shape of the device *I*-*V*-curve which is indicated by similar local ideality factors of Auger and the total recombination between *MPP* and V_{oc}.

At V_{oc}, the EWT-via current of 3 mA/cm^2 induces a voltage drop of 1 mV (Fig.8.7(c)). The EWT-via current recombines in the highly diffused rear emitter, mainly by Auger recombination. Due to the high bulk lifetime, there is no injection of hole carriers from the rear emitter into the base. This has been the case for low bulk lifetimes in the scenario of EWT solar cells fabricated on highly boron-doped Cz-Si wafers in the previous chapter.

8.6 Conclusion

The final chapter presents a solution to fabricate high-efficient EWT solar cells on n-type Cz-Si that respects the industrial needs of low-cost Si wafers. The laboratory process eliminates the critical loss mechanisms that have been identified in the previous chapters.

Despite a high EWT-via emitter sheet resistance of 110 $\Omega/\square$, we achieve the highest FF of 80.8 % that has been reported for an EWT-device so far. The applied diode network and the three-dimensional simulation provide a detailed analysis of the dominant loss mechanisms of the n-type device. The optimization strategy focus on a reduction of the entire device resistance. By identifying the high emitter sheet resistance in the EWT-via, a reduction of the EWT-via index and distance is a succesfull approach to reduce all series resistance contributions of the device.

Since the bulk lifetime is not limited by boron-oxygen complexes in n-type Cz-Si, SRH recombination is strongly reduced compared to the other devices fabricated on p-type Cz-Si in this thesis. The I-V-characteristic is dominated by Auger recombination losses based on the highly diffused boron emitter and phosphorus BSF.

A boron diffusion (BBr_3) has been applied for the emitter formation in a tube furnace. The emitter recombination characteristic contributes to a FF-loss of about 0.9 % which is investigated by means of the implied I-V-curve of test samples. The Al_2O_3-passivation of the emitter results in a saturation current density smaller than 60 fA/cm^2 despite the low sheet-resistance of 50 $\Omega/\square$ on textured and planar surfaces.

The EWT cell process includes characteristic fabrication steps such as laser-via-drilling and rear side structuring. Compared to an industrial cell process of a front and rear contacted device, the number of process steps is increased. As a consequence, the efficiency of EWT devices must be superior in order to guarantee a cost-effective process that can be scaled to industrial production. For this reason, n-type Cz-Si is an approach for high-efficient EWT devices which is difficult to achieve by low-cost Si wafer with low bulk lifetimes, e.g. mc-Si or boron-doped p-type Cz-Si.

9 Conclusion and perspective

The present thesis investigates loss mechanisms of EWT solar cells. A focus is set on the *FF* which has been the main issue limiting EWT efficiencies for the last 18 years.

A one-dimensional PC1D model gives a qualitative explanation of EWT specific efficiency losses. In the simulation scenario of an EWT-via resistance of 1 Ωcm^2 (0.01 Ωcm^2), the EWT-via current induces a voltage drop between the front and rear *pn*-junction that accounts for 36 mV (0.36 mV) in the injection range from J_{sc} up to *MPP*. The injection of minority carriers across the front *pn*-junction is increased by a factor of 4 in the 1 Ωcm^2 compared to the 0.01 Ωcm^2 device. In the 1 Ωcm^2 scenario, the higher recombination results in a reduced collection of minority carriers at the front *pn*-junction and, consequently, in a smaller majority carrier current along the EWT-via emitter. The adaption and the minority carrier injection from high voltage drops at *MPP* to low voltage drops at V_{oc} causes a recombination characteristic with local ideality factors greater than unity (n>1). The *FF*-loss accounts for -3.3 % compared to the reference 0.01 Ωcm^2 device. A reproduction of experimental values is difficult to achieve by means of this one-dimensional model. The more-dimensional current flow of majority and minority carriers is not respected. This leads to an undervalution of current-crowding effects that are identified in the following chapters. The PC1D model is a straight-forward method to give a didactical approach of the EWT-via specific loss mechanism. At the same time, it offers the risk that further losses, due to the more-dimensional EWT geometry, are not identified.

The first experimental loss analysis is a comparative discussion of two EWT solar cells featuring LFC contacts. The absorber of each device is the only differing parameter: 5.0 Ωcm or 0.5 Ωcm boron-doped Cz-Si. The cell fabricated on a lowly doped substrate (ρ=5.0 Ωcm) profits from a low density of boron-oxygen complexes and a rather high minority carrier lifetime of τ=70 µs at V_{ext}=0 mV. Recombination losses inside the base only account for 0.5 mA/cm^2 at J_{sc}-conditions. However, this device suffers from large base series resistances (R_{base}=0.54 Ωcm^2) which induce high internal voltage drops inside the base between J_{sc}- and *MPP*-conditions ($\Delta V \approx$30 mV). As a result, the *pn*-junction voltages and the minority carrier injection across the *pn*-junction are enhanced at *MPP*-conditions leading to high recombination losses despite the rather high bulk lifetime of 150 µs at *MPP*. At external voltages between *MPP* and V_{oc}, the voltage drops converge to zero inside the base and along the emitter causing a disturbed recombination characteristic compared to those of an ideal diode. The *FF* (74.8 %) is reduced which limits the total device efficiency (18.3 %) despite the high J_{sc} of 39.6 mA/cm^2. The second device fabricated on highly boron-doped Cz-Si wafers (ρ=0.5 Ωcm suffers from a high density of boron-oxygen complexes and a low bulk lifetime of τ=15 µs at V_{ext}=0 mV. Recombination losses inside the base account for 1.5 mA/cm^2 resulting in a smaller J_{sc} of 38.7 %. This device profits from a strongly reduced base series resistance ($R_{base} \approx$0.1 Ωcm^2) and, hence, lower resistive losses, reduced voltage drops and lower resistance-induced recombination losses. The *FF* and η account for 79.0 % and 18.7 %, respectively. The efficiency boost of 0.5% compared to the 5 Ωcm scenario is small. The application of highly boron-doped Cz-Si wafers increases the *FF* and, at the same time, reduces J_{sc}. Simply increasing the base dopant density is the wrong strategy for an efficiency gain of EWT solar cells. All *I*-*V*- parameters must be considered in order to optimize the efficiency. However, the experimental and theoretical results achieved in this chapter already identify the base series resistance as a critical parameter of EWT devices.

The second experimental approach is the integration of a back surface field in EWT devices fabricated on highly boron-doped (0.8 Ωcm) and lowly boron-doped (3.5 Ωcm) Cz-Si.[1] The applied BSF has a sheet resistance of 75 $\Omega/\square$ which is small (high) compared to the base sheet resistance of 195 (44) $\Omega/\square$ of the 3.5 (0.8) Ωcm device. A comparison of BSF device *I*-*V*-parameters and

---

[1] The respective devices do not exhibit a texturization at the front side. Compared to the experimental results described above, the J_{sc} and, hence, the η are smaller.

I-V-parameters of similar EWT devices featuring LFC (instead of a BSF) reveals a fill factor gain of +2.4 % (+0.3 %) and an efficiency boost of +0.4 % (−0.2 %) in the 3.5 Ωcm (0.8 Ωcm) scenario. In this approach, the lowly doped 3.5 Ωcm BSF device has the highest efficiency (η=16.8 %) due to the BSF. This cell profits from a reduced base series resistance compared to the similar LFC device ($R_{base,LFC} \approx$0.5 Ωcm^2 $\rightarrow$ $R_{base,BSF} \approx$0.2 Ωcm^2). Furthermore, the device profits from a higher bulk lifetime (59 µs) and low recombination losses at J_{sc}-conditions compared to the 0.8 Ωcm scenario (τ=14 µs). The relatively simple approach of BSF integration solves the issue of lowly-doped wafer substrates and the former consequence of high base series resistances. However, the application of boron-doped Cz-Si is not the right strategy for high-efficient solar cells. The injection-dependent bulk lifetime due to the boron-oxygen complexes remains a critical parameter in terms of FF-losses and total recombination losses that limit V_{oc}. Furthermore, the as-diffused phosphorus emitter (50 Ω/□) passivated by PECVD silicon nitride has a high saturation current of 300 fA/cm^2. This limits the maximum V_{oc} to 660 mV and contributes to recombination losses of about 0.6 mA/cm^2 in the front emitter at J_{sc}-conditions. The bulk lifetime and the high saturation currents of the phosphorus emitters are limiting factors improved in the following approach by the application of high-quality, n-type Si absorbers and emitters that exhibit lower recombination.

The third experimental approach comprises the application of phosphorus-doped 1.6 Ωcm n-type Cz-Si. The respective wafers do not suffer from boron-oxygen complexes and exhibit an injection-independent bulk lifetime of 1000 µs. A 50 Ω/□ p-type boron-emitter is diffused in a BBr$_3$ tube furnace and passivated with aluminum oxide (atomic layer deposition) which results in a saturation current density of 50 fA/cm^2. Total device recombination losses only account for 0.5 mA/cm^2 at J_{sc}-conditions which results in a short-circuit current density of 40.4 mA/cm^2. In contrast to the boron-emitter on a planar or textured surface, the EWT-via emitter has a sheet resistance of 110 Ω/□. This is a rather high and critical value in terms of resistive losses along the current path of majority carriers in the EWT-via emitter. The applied strategy for decreasing the referring resistance is a reduction of the EWT-via distance and of the EWT-via index. As a result, a smaller amount of current is transport through the EWT-via (compared to the other experimental scenarios in this thesis) which results in a small area-averaged EWT-via resistance of 0.3 Ωcm^2. The fill factor loss accounts for 1.2 % due to the EWT-via emitter resistance. A phosphorus-diffused BSF with a sheet resistance of 75 Ω/□ is passivated by thermally grown silicon dioxide and exhibits a saturation current density of 120 fA/cm^2. The total base series resistance only accounts for 0.1 Ωcm^2($\Rightarrow \mathit{\Delta FF} = -0.5$ %). The fabricated solar cell has the highest FF of all EWT devices (FF=80.8 %) that have been reported so far and a V_{oc} of 661 mV. The efficiency is 21.6 %.

What is the perspective of EWT solar cells?

I try to answer this question by a discussion of previous and present results and by my experience of the current state of laboratory process.

EWT devices offer a high efficiency potential that has been shown by many photovoltaic scientists in the past and in the present thesis. However, since their first presentation in 1993 by Gee et al., a long-term industrial production has not been realized yet.

One of the motivations for developing this solar cell has been the issue of very short minority carrier diffusion lengths in substrates that were produced 20 years ago. By means of the EWT design, high short-circuit currents could be (and can be) achieved even for lower absorber material qualities. Todays absorber materials (e.g. mc-Si) exhibit higher minority carrier diffusion lengths. However, the argument of high short-circuit current densities still remains due to the front and rear collecting pn-junction and the low recombination losses at J_{sc}. Even though, this argument is not as important as it was in the past.

The FF issue has been solved by theoretical and experimental investigations in this thesis. Hence, a limiting factor could be eliminated. The V_{oc} of the n-type solar cell is still low compared to other front junction devices that feature a boron-emitter [158]. The enhanced and high saturation current density of the boron-emitter and phosphorus BSF, respectively, limit the device efficiency in this thesis. These two parameters must be optimized if the *n*-type EWT device is transfered into industrial production. I estimate that these two parameters can be improved by simple technological approaches, e.g modified boron- and phosphorus diffusion processes. Due to the limited time of this thesis, the final optimization has not been done.

I expect the extensive EWT process as the most critical "parameter" in terms of an industrial transfer. The present *n*-type process features more than 30 steps on a laboratory scale. Accordingly, the number of broken precursors is high. Efforts have to be done in order to simplify the process, to reduce the number of process steps and, finally, to reduce the costs per kilo Watt peak. A potential approach could be the combination of high temperature steps to define a BSF and an emitter at the same time. Alternatively, the contact opening sequence could be used to define a BSF by means of laser power and a diffusion source that is deposited onto the surface.

A final technical assessment of the *n*-type EWT solar cell should be done by a fabricated solar cell module. Firstly, this module has to show superior efficiencies compared to the present industrial modules. Secondly, the long-term stability in terms of its efficiency and endurance has to be demonstrated. The applied technology of evaporated aluminum contacts offers several advantages like the sophisticated contact separation and very low metal-semiconductor contact resistances as shown in this thesis. In terms of connection methods by means of tin-lead or other soft solder techniques which are the present standard, (evaporated) aluminum does not have the long-term capability to fulfill the hard requirements of PV modules. The atmospheric oxygen reacts with the aluminum and generates an aluminum oxide layer that grows into the surface. This thin layer avoids the generation of an intermetalic phase between the solder paste and the aluminum during the thermal soldering treatment. A possible solution could be a modification of the evaporated aluminum layer with other metallic layers on top, an alternative connection method, e.g. by means of laser power to weld the cell interconnections or the application of a completely different metalization technique like screen printing pastes. The later approach would change the entire solar cell process.

Bibliography

[1] C.Z. Zhou, P.J. Verlinden, R.A. Crane, R.M. Swanson, R.A. Sinton, and CA SunPower Corp., Sunnyvale. 21.9% efficient silicon bifacial solar cells. In *Proc. 26th IEEE PVSC, Anaheim, CA , USA*, 2002.

[2] M. A. Green. Crystalline and thin-film silicon solar cells: state of the art and future potential. *Solar Energy*, 74:181–192, 2003.

[3] A. Metz. *Neuartige höchsteffiziente Silicium-Solarzellen mit schräg im Hochvakuum aufgedampften Al/SiO$_x$/n-Si-Tunnelkontakten.* PhD thesis, Gottfried Wilhelm Leibniz Universität Hannover, 2000.

[4] D.D. Smith and J.M. Gee. Review of back contact silicon solar cells for low cost application. In *Proc. 16th EUPVSEC, Glasgow, United Kingdom*, page 1104, 2000.

[5] G. Beaucarne and E. van Kerschaver. Back-contact solar cells: a review. *Prog. Photovolt. Res. Appl.*, 14:107–123, 2006.

[6] R.M. Swanson, S.K. Beckwith, R.A. Crane, W.D. Eades, Young Hoon Kwark, R.A. Sinton, and S.E. Swirhun. Point-contact silicon solar cells. *IEEE T. Electron. Dev.*, 31:661–664, 1984.

[7] R. M. Swanson. Point-contact solar cells: Modeling and experiment. *Solar Cells*, 17:85–118, 1986.

[8] N.-P. Harder, V. Mertens, and R. Brendel. Buried emitter solar cell structures: Decoupling of metallisation geometry and carrier collection geometry of back contacted solar cells. *phys. stat. sol. (RRL)*, 2:148–150, 2008.

[9] S.R. Wenham, C.B. Honsberg, and M.A. Green. Buried contact silicon solar cells. *Sol. Energy Mater. Sol.*, 34:101–110, 1994.

[10] Solar cell, http://en.wikipedia.org/wiki/solarcell, june 2011. via Internet, June 2011.

[11] B. Lenkeit. *Elektronische und strukturelle Eigenschaften von Plasma-Siliziumnitrid zur Oberflächenpassivierung von siebgedruckten, bifazialen Silizium-Solarzellen.* PhD thesis, Gottfried Wilhelm Leibniz Universität Hannover, 2002.

[12] J. Zhao, A. Wang, and M.A. Green. 24.5% efficiency silicon PERT cells on MCZ substrates and 24.7% efficiency PERL cells on FZ substrates. *Prog. Photovolt. Res. Appl.*, 7:471–474, 2000.

[13] S.W. Glunz. *Ladungsträgerrekombination in Silicium und Silicium-Solarzellen.* PhD thesis, Fakultät für Physik der Albert-Ludwigs-Universität Freiburg i. Brsg., 1995.

[14] W. Shockley and W.T. Read. Statistics of the recombinations of holes and electrons. *Phys. Rev.*, 87:835–842, 1952.

[15] R.N. Hall. Electron-hole recombination in germanium. *Phys. Rev.*, 87:387, 1952.

[16] D. Macdonald, A. Cuevas, and J. Wong-Leung. Capture cross sections of the acceptor level of iron-boron pairs in *p*-type silicon by injection-level dependent lifetime measurements. *J. Appl. Phys.*, 89:7932–7939, 2001.

[17] D. MacDonald. *Recombination and Trapping in Multicrystalline Silicon Solar Cells.* PhD thesis, Australian National University, 2001.

[18] D. Macdonald and A. Cuevas. Validity of simplified Shockley-Read-Hall statistics for modeling carrier lifetimes in crystalline silicon. *Phys. Rev.*, 67:1–7, 2003.

[19] D. Macdonald and L.J. Geerligs. Recombination activity of interstitial iron and other transition metal point defects in p- and n-type crystalline silicon. *Appl. Phys. Lett.*, 85:4061–4063, 2004.

[20] J.E. Birkholz, K. Bothe, D. MacDonald, and J. Schmidt. Recombination parameters of iron-boron pairs in boron-doped crystalline silicon. In *Proc. 20th EUPVSEC, Barcelona, Spain*, 2005.

[21] J.E. Birkholz, K. Bothe, D. Macdonald, and J. Schmidt. Electronic properties of iron-boron pairs in crystalline silicon by temperature- and injection-level-dependent lifetime measurements. *J. Appl. Phys.*, 97:103708, 2005.

[22] J. Schmidt, R. Krein, K. Bothe, G. Pensl, and S. Beljakowa. Recombination activity of interstitial chromium and chromium-boron pairs in silicon. *J. Appl. Phys.*, 102(12):123701, 2007.

[23] R. Krain. Rekombinationsaktivität von interstitiellem Chrom und Chrom-Bor-Paaren in kristallinem Silizium. Master's thesis, Institut für Solarenergieforschung Hameln/Emmerthal, 2006.

[24] J. Czochralski. Ein neues Verfahren zur Messung der Kirstallisationsgeschwindigkeit von Metallen. *Z. phys. Chem.*, 92:219–221, 1918.

[25] J. Schmidt, A. Cuevas, S. Rein, and Glunz S. W. Impact of light-induced recombination centres on the current-voltage characteristic of Czochralski silicon solar cells. *Prog. Photovolt: Res. Appl.*, 9:249–255, 2001.

[26] J. Schmidt, C. Berge, and A. Aberle. Injection level dependence of the defect-related carrier lifetime in light-degraded boron-doped Czochralski silicon. *Appl. Phys. Lett.*, 73:2167, 1998.

[27] J. Schmidt and A. Cuevas. Electronic properties of light-induced recombination centers in boron-doped Czochralski silicon. *J. Appl. Phys.*, 86(6):3175–3180, 1999.

[28] K. Bothe, R. Hezel, and J. Schmidt. Understanding and reducing the boron-oxygen-related performance degradation in Czochralski silicon solar cells. *Solid-State Phenomena*, 95-96:223–228, 2003.

[29] K. Bothe, R. Sinton, and J. Schmidt. Fundamental boron-oxygen-related carrier lifetime limit in mono- and multicrystalline silicon. *Prog. Photovolt. Res. Appl.*, 13:287–296, 2005.

[30] H. Plagwitz. *Surface passivation of crystalline silicon solar cells by amorphous silicon films.* PhD thesis, Gottfried Wilhelm Leibniz Universität Hannover, 2007.

[31] B. Hoex, S.B.S. Heil, E. Langereis, M.C.M. van de Sanden, and W.M.M. Kessels. Ultralow surface recombination of c-Si substrates passivated by plasma-assisted atomic layer deposited al_2o_3. *Appl. Phys. Lett.*, 89:042112, 2006.

[32] O. Breitenstein, J.P. Rakotoniaina, M.H. Al Rifai, and M. Werner. Shunt types in crystalline silicon solar cells. *Prog. Photovolt. Res. Appl.*, 12:529–538, 2004.

[33] K. Ramspeck. *Characterization techniques for silicon solar cells and material using an infrared-camera based approach.* PhD thesis, Gottfried Wilhelm Leibniz Universität Hannover, 2009.

[34] F. Clement. *Die Metal Wrap Through Solarzelle - Entwicklung und Charakterisierung.* PhD thesis, University of Freiburg, 2009.

[35] P.J. Cousins, D.D. Smith, Hsin-Chiao Luan, J. Manning, T.D. Dennis, A. Waldhauer, K.E. Wilson, G. Harley, W.P. Mulligan, and CA USA SunPower Corp., San Jose. Generation 3: Improved performance at lower cost. In *Proc. 35th IEEE PVSC, Honolulu, HI, USA*, 2010.

[36] C. Ulzhöfer, P.P. Altermatt, N.-P. Harder, and R. Brendel. Loss analysis of emitter-wrap-through silicon solar cells by means of experiment and three-dimensional device modeling. *J. Appl. Phys.*, 107:104509 –104509–12, 2010.

[37] S. Hermann. *ISFH Annual Report 2007.* ISFH, 2008.

[38] A. Schönecker, H.H.C. de Moor, A.R. Burgers, A.W. Weeber, J.W. Hoornstra, C. Sinke, P.-P. Michiels, and R.A. Steeman. An industrial multi-crystalline EWT solar cell with screen printed metallization. In *Proc. 14th EUPVSEC, Barcelona, Spain*, page 796, 1997.

[39] P. Engelhart. L*asermaterialbearbeitung als* S*chlüsseltechnologie zum* H*erstellen rückseitenkontaktierter* S*iliciumsolarzellen.* PhD thesis, Gottfried Wilhelm Leibniz Universität Hannover, 2007.

[40] S. Hermann, P. Engelhart, N.-P. Harder, B. Fischer, R. Meyer, and R. Brendel. 21%-efficient emitter wrap-through RISE solar cell on large area. In *Proc. 22nd EUPVSEC, Milan, Italy*, page 970, 2007.

[41] D. Kray, J. Dicker, S. Rein, F.-J. Kamerewerd, D. Oßwald, E. Schäffer, S.W. Glunz, and G. Willeke. High-efficiency emitter-wrap-through cells. In *Proc. 17th EUPVSEC, Munich, Germany*, 2001.

[42] D.M. Chapin, C.S. Fuller, and G.L. Pearson. A new silicon *p-n* junction photocell for converting solar radiation into electrical power. *J. Appl. Phys.*, 25(5):676–677, 1954.

[43] G. J. Pack. U.S. patent no. 3903427, 2 September 1975.

[44] R.N. Hall and T.J. Soltys. Polka dot solar cell. In *Proc. 14th IEEE PVSC, San Diego, CA*, page 550, 1980.

[45] R.A. Sinton, P. Verlinden, D.E. Kane, and R.M. Swanson. Development efforts in silicon backside-contact solar cells. In *Proc. 8th EUPVSEC, Florence, Italy*, page 1472, 1988.

[46] J.M. Gee, W.K. Schubert, and P.B. Basore. Emitter wrap-through solar cell. In *Proc. 23rd IEEE PVSC, Louisville, KY*, page 265, 1993.

[47] S.W. Glunz, J. Dicker, D. Kray, J.Y. Lee, R. Preu, S. Rein, E. Schneiderlöchner, J. Sölter, W. Warta, and G. Willeke. High-efficiency cell structures for medium-quality silicon. In *Proc. 17th EUPVSEC, Munich, Germany*, 2001.

[48] W. Neu, A. Kress, W. Joos, P. Fath, and E. Bucher. Low cost multicrystalline back contact silicon solar cells with screen printed metallization. *Sol. Energy Mater. Sol.*, 74:139, 2002.

[49] D. Kray, J. Dicker, D. Osswald, A. Leimenstoll, S.W. Glunz, W. Zimmermann, K.-H. Tentscher, and G. Strobl. Progress in high-efficiency emitter-wrap-through cells on medium quality substrates. In *Proc. 3rd WCPEC, Osaka, Japan*, page 1340, 2003.

[50] P. Engelhart, A. Teppe, A. Merkle, R. Grischke, R. Meyer, N.P. Harder, and R. Brendel. The RISE-EWT solar cell - a new approach towards simple high efficiency silicon solar cells. In *Proc. 15th PVSEC, Shanghai, People's Republic of China*, page 802, 2005.

[51] P. Hacke, J.M. Gee, M. Hilali, J. Dominguez, H. Dundas, A. Jain, G. Lopez, B. Fischer, and B.L. Sopori. Current status of technologies for industrial emitter wrap-through solar cells. In *Proc. 21st EUPVSEC, Dresden, Germany*, page 761, 2006.

[52] P. Hacke, J. Gee, P. Kumar, J. Howarth, V. Gonzales, L. Pratt, C. Strumpel, J. Dominguez, J. Franklin, G. Lopez, C. Corwine, L. Dawson, and Advent Solar Inc. Albuquerque NM USA. Optimized emitter wrap-through cells for monolithic module assembly. In *Proc. 34th IEEE PVSC, Philadelphia, PA, USA*, 2009.

[53] N. Mingirulli, D. Stuewe, J. Specht, A. Fallisch, and D. Biro. Screen-printed emitter-wrap-through solar cell with single step side selective emitter with 18.8 % efficiency. *Prog. Photovolt. Res. Appl.*, doi: 10.1002/pip.1022, 2010.

[54] S. Hermann, A. Merkle, C. Ulzhöfer, S. Dorn, I. Feilhaber, M. Berger, T. Friedrich, T. Brendemühl, N.-P. Harder, L. Ehlers, K. Weise, R. Meyer, and R. Brendel. Progress in emitter wrap-through solar cell fabrication on boron doped Czochralski-grown silicon. *Sol. Energy Mater. Sol.*, in press, 2011.

[55] M.A. Green. *Solar Cells.* The University of New South Wales, Sydney, Australia, 1992.

[56] M.A. Green. *Silicon Solar Cells.* The University of New South Wales, Sydney, Australia, 1995.

[57] P. Würfel. *Physik der Solarzelle*, volume 2. Spektrum, 2000.

[58] S.M. Sze. *Semiconductor Devices, Physics and Technology.* John Wiley, 1985.

[59] S.M. Sze. *Physics of Semiconductor Devices.* John Wiley, 2nd edition, 1981.

[60] M.A. Green. Intrinsic concentration, effective densities of states, and effective mass in silicon. *J. Appl. Phys.*, 67:2944–2954, 1990.

[61] A. B. Sproul and M. A. Green. Improved value for the silicon intrinsic carrier concentration from 275 to 375 K. *J. Appl. Phys.*, 70:846–854, 1991.

[62] P.P. Altermatt, A. Schenk, F. Geelhaar, and G. Heiser. Reassessment of the intrinsic carrier density in crystalline silicon in view of band-gap narrowing. *J. Appl. Phys.*, 93(3):1598–1604, 2003.

[63] N. P. Harder, R. Gogolin, and R. Brendel. Trapping-related recombination of charge carriers in silicon. *Appl. Phys. Lett.*, 97:1.3490240, 2010.

[64] D. Macdonald and A. Cuevas. Trapping of minority carriers in multicrystalline silicon. *Appl. Phys. Lett.*, 74(12):1710–1712, 1999.

[65] H. Neuhaus. *Electrical Characterisation of Crystalline Silicon for Thin-filmSolar Cells.* PhD thesis, University of New South Wales, 2002.

[66] D.M. Caughey and R.E. Thomas. Carrier mobilities in silicon empirically related to doping and field. In *Proc. IEEE*, page 2192, 1967.

[67] J.M. Dorkel and P. Leturcq. Carrier mobilities in silicon semi-empirically related to temperature, doping and injection-level. *Solid-State Electron.*, 24:821–825, 1981.

[68] M.S. Tyagi and R. Vanoverstraeten. Minority-carrier recombination in heavily-doped silicon. *Solid-State Electron.*, 26:577–597, 1983.

[69] J. Dziowior and W. Schmid. Auger coefficients for highly doped and highly excited silicon. *Appl. Phys. Lett.*, 31(5):346–348, 1977.

[70] P.P. Altermatt, J. Schmidt, G. Heiser, and A.G. Aberle. Assessment and parameterisation of coulomb-enhanced Auger recombination coefficients in lowly injected crystalline silicon. *J. Appl. Phys.*, 82(10):4938–4944, 1997.

[71] A. Hangleiter and R. Häcker. Enhancemet of band-to-band Auger recombination by electron-hole correlations. *Phys. Rev. Lett.*, 65(2):215–218, 1990.

[72] J. Schmidt, M. Kerr, and P.P. Altermatt. Coulomb-enhanced Auger recombination in crystalline silicon at intermediate and high-injection densities. *J. Appl. Phys.*, 88(3):1494–1497, 2000.

[73] M.J. Kerr and A. Cuevas. General parameterization of Auger recombination in crystalline silicon. *J. Appl. Phys.*, 91(4):2473–2480, 2002.

[74] W.P. Dumke. Spontaneous radiative recombination in semiconductors. *Phys. Rev.*, 105:139–144, 1957.

[75] P.P. Altermatt, F. Geelhaar, T. Trupke, X. Dai, A. Neisser, and E. Daub. Injection dependence of spontaneous radiative recombination in crystalline silicon: Experimental verification and theoretical analysis. *Appl. Phys. Lett.*, 88:261901, 2006.

[76] T. Trupke, M.A. Green, P. Wuerfel, P.P. Altermatt, A. Wang, J. Zhao, and R. Corkish. Temperature dependence of the radiative recombination coefficient of intrinsic crystalline silicon. *J. Appl. Phys.*, 94(8):4930–4937, 2003.

[77] J. Schmidt and K. Bothe. Structure and transformation of the metastable boron- and oxygen-related defect center in crystalline silicon. *Phys. Rev. B*, 69:024107, 2004.

[78] D.W. Palmer, K. Bothe, and J. Schmidt. Kinetics of the electronically stimulated formation of a boron-oxygen complex in crystalline silicon. *Phys. Rev. B*, 76:035210, 2007.

[79] S. Rein and S.W. Glunz. Electronic properties of the metastable defect in boron-doped Czochralski silicon: Unambiguous determination by advanced lifetime spectroscopy. *Appl. Phys. Lett.*, 82(7):1054–1056, 2003.

[80] T. Suzuki, N. Isawa, Y. Okubo, and K. Hoshi. Cz silicon crystals grown in a transverse magnetic field. *Semiconductor Silicon 1981*, Electrochemical Society, Pennington:90–100, 1981.

[81] S.W. Glunz, S. Rein, J. Knobloch, W. Wettling, and T. Abe. Comparison of boron- and gallium-doped *p*-type Czochralski silicon for photovoltaic application. *Prog. Photovolt. Res. Appl.*, 7:463, 1999.

[82] A.G. Aberle, S. Glunz, and W. Warta. Impact of illumination level and oxide parameters on Shockley-Read-Hall recombination at the Si-Sio$_2$ interface. *J. Appl. Phys.*, 71:4422–4431, 1992.

[83] J. Schmidt. *Untersuchungen zur Ladungsträgerrekombination an Oberflächen und im Volumen von kristallinen Silicium-Solarzellen.* PhD thesis, Gottfried Wilhelm Leibniz Universität Hannover, 1998.

[84] Y. Larionova, V. Mertens, N.-P. Harder, and R. Brendel. Surface passivation of n-type Czochralski silicon substrates by thermal-SiO_2/ plasma-enhanced chemical vapor deposition SiN stacks. *Appl. Phys. Lett.*, 96:032105, 2010.

[85] T. Lauinger, J. Schmidt, A.G. Aberle, and R. Hezel. Record low surface recombination velocities on 1 Ωcm p-silicon using remote plasma silicon nitride passivation. *Appl. Phys. Lett.*, 68:1232, 1996.

[86] M.J. Kerr. *Surface, Emitter and Bulk Recombination in Silicon and Development of Silicon Nitride Passivated Solar Cells.* PhD thesis, Australian National University, 2002.

[87] M.J. Kerr and A. Cuevas. Recombination at the interface between silicon and stoichiometric plasma silicon nitride. *Semicond. Sci. Technol.*, 17(2):166, 2002.

[88] J. Schmidt, B. Veith, and R. Brendel. Effective surface passivation of crystalline silicon using ultrathinA l_2O_3 films and Al_2O_3/SiN_x stacks. *phys. stat. sol. (RRL)*, 9:287–289, 2009.

[89] F. Granek, C. Reichel, M. Hermle, D.M. Huljic, O. Schultz, and S.W. Glunz. Front surface passivation of n-type high-efficiency back-junction silicon solar cells using front surface field. In *Proc. 22nd EUPVSEC, Milan, Italy*, 2007.

[90] F. Granek, M. Hermle, D.M. Huljic, O. Schultz-Wittmann, and S.W. Glunz. Enhanced lateral current transport via the front n^+ diffused layer of n-type high-efficiency back-junction back-contact silicon solar cells. *Prog. Photovolt: Res. Appl.*, 17:47–56, 2008.

[91] H. Nagel, C. Berge, and A.G. Aberle. Generalized analysis of quasi-steady-state and quasi-transient measurements of carrier lifetimes in semiconductors. *J. Appl. Phys.*, 86:6218–6221, 1999.

[92] R.A. Sinton, A. Cuevas, and M. Stuckings. Quasi-steady-state photoconductance: A new method for solar cellmaterial and device characterization. In *Proc. 25th IEEE PVSC, Washington DC, USA*, 1996.

[93] R.A. Bardos, T. Trupke, M.C. Schubert, and Roth.T. Trapping artifacts in quasi-steady-state photoluminescence and photoconductance lifetime measurements on silicon wafers. *Appl. Phys. Lett.*, 88:053504, 2006.

[94] J.A. Hornbeck and J.R. Haynes. Trapping of minority carriers in silicon. I. p-type silicon. *Phys. Rev.*, 97(2):311–323, 1955.

[95] A. Cuevas, M. Stocks, D. Macdonald, M. Kerr, and C. Samundsett. Recombination and trapping in multicrystalline silicon. *IEEE T. Electron. Dev.*, 46(10):2026–2034, 1999.

[96] P. Pohl, J. Schmidt, K. Bothe, and R. Brendel. Mapping of trap densities and energy levels in semiconductors using a lock-in infrared camera technique. *Appl. Phys. Lett.*, 87:14104, 2005.

[97] J. Schmidt, K. Bothe, and R. Hezel. Oxygen-related minority-carrier trapping centers in p-type Czochralski silicon. *Appl. Phys. Lett.*, 80:4395–4397, 2002.

[98] M. Schubert and W. Warta. Prediction of diffusion length in multicrystalline silicon solar cells from trapping images on starting material. *Prog. Photovolt: Res. Appl.*, 15:331–336, 2006.

[99] B. Fischer. *Loss analysis of crystalline silicon solar cell using photoconductance and quantum efficiency measurements.* PhD thesis, University of Konstanz, 2003.

[100] A. Cuevas and R.A. Sinton. Prediction of the open-circuit voltage of solar cells from the steady-state photoconductance. *Prog. Photovolt. Res. Appl.*, 5:79–90, 1997.

[101] International electrotechnical commission, standard iec 60904-3,edition 2.0, april 2008.

[102] F.A. Lindholm, J.G. Fossum, and E.L. Burgess. Application of the superposition principle to solar-cell analysis. *IEEE T. Electron. Dev.*, 26:165–171, 1979.

[103] S.J. Robinson, A.G. Aberle, and M.A. Green. Departures from the principle of superposition in silicon solar cells. *J. Appl. Phys.*, 76:7920–7930, 1994.

[104] N.G. Tarr and D.L. Pulfrey. The superposition principle for homojunction solar cells. *IEEE T. Electron. Dev.*, 27:771–776, 1980.

[105] D.A. Clugston and P.A. Basore. PC1D version 5: 32-bit solar cell modeling on personal computers. In *Proc. 26th IEEE PVSC, Anaheim, CA, USA*, pages 207–210., 1997.

[106] A.G. Aberle, S.R. Wenham, and M.A. Green. A new method for accurate measurement of the lumped series resistance of solar cells. In *Proc. 23rd IEEE PVSC, Louisville, KY*, page 133, 1993.

[107] M. Wolf and H. Rauschenbach. Series resistance effects on solar cell measurements. *Advanced Energy Conversion*, 3:455–479, 1963.

[108] K.R. McIntosh. *Lumps, humps and bumps: Three detrimental effects in the current-voltagecurve of silicon solar cells.* PhD thesis, University of New South Wales, 2001.

[109] H. Knauss, W. Jooss, S. Roberts, T.M. Bruton, R. Toelle, P. Fath, and E. Bucher. Emitter wrap through solar cells using electroless plating metallisation. In *Proc. 17th EUPVSEC, Munich, Germany*, page 1731, 2001.

[110] S. Eidelloth. Untersuchung von laserinduzierten schädigungen bei der strukturierung von siliziumwafern für hocheffizienz-solarzellen. Master's thesis, Fachhochschule Münster, 2006.

[111] D.D. Smith, J.M. Gee, M.D. Bode, and Jimeno J.C. Circuit modeling of the emitter-wrap-through solar cell. *IEEE T. Electron. Dev.*, 46:1993–1999, 1999.

[112] R.R. King and R.M. Sinton, R.A. Swanson. Studies of diffused phosphorus emitters: Saturation current, surface recombination velocity, and quantum efficiency. *IEEE T. Electron. Dev.*, 37:365–371, 1990.

[113] N. Mingirulli. *Fabrication and Characterization of Emitter-Wrap-Through Cells.* PhD thesis, Universität Konstanz, 2009.

[114] J. Dicker. *Analyse und Simulation von hocheffizienten Silizium-Solarzellenstrukturen für industrielle Fertigungstechniken.* PhD thesis, University of Konstanz, 2003.

[115] M.M. Hilali, P. Hacke, and J.M. Gee. Two-dimensional modeling of EWT multicrystalline silicon solar cells and comparison with the IBC solar cell. In *Proc. 4th IEEE WCPEC, Waikoloa, Hawaii*, 2006.

[116] W. van Roosbroeck. Theory of flow of electrons and holes in germanium and other semiconductors. *Bell Syst. Tech. J.*, 29:560–607, 1950.

[117] A. Kress. *Emitterverbund - Rückkontaktsolarzellen für die industrielle Fertigung.* PhD thesis, University of Konstanz, 2001.

[118] C. Ulzhöfer, S. Hermann, N.-P. Harder, P.P. Altermatt, and R. Brendel. The origin of reduced fill factors of emitter-wrap-through-solar cells. *phys. stat. sol. (RRL)*, 2:251, 2008.

[119] *Sentaurus, Manual Version 2008.09, Synopsys Inc., Mountain View,CA, 2008.*

[120] A. Schenk. Finite-temperature full random-phase approximation model of band gap narrowing for silicon device simulation. *J. Appl. Phys.*, 84:3684–3695, 1998.

[121] P.P. Altermatt, G. Heiser, A.G. Aberle, A. Wang, J. Zhao, S.J. Robinson, S.J. Bowden, and M.A. Green. Spatially resolved analysis and minimisation of resistive losses in high-efficiency Si solar cells. *Prog. Photovolt. Res. Appl.*, 4:399–414, 1996.

[122] P.P. Altermatt, J.O. Schumacher, A. Cuevas, S.W. Glunz, R.R. King, G. Heiser, and A. Schenk. The extraction of the surface recombination velocity of Si:P emitters using advanced silicon models. *J. Appl. Phys.*, 92:3187–3197, 2002.

[123] K.R. McIntosh and L.P. Johnson. Recombination at textured silicon surfaces passivated with silicon dioxide. *J. Appl. Phys.*, 105(12):124520, 2009.

[124] R. Brendel. Sunrays: a versatile ray tracing program for the photovoltaic community. In *Proc. 12th EUPVSEC, Amsterdam, Netherlands*, page 1339, 1994.

[125] M.A. Green. Self-consistent optical parameters of intrinsic silicon at 300 K including temperature coefficients. *Sol. Energy Mater. Sol.*, 92:1305, 2008.

[126] P.P. Altermatt, H. Plagwitz, R. Bock, J. Schmidt, R. Brendel, M.J. Kerr, and A. Cuevas. The surface recombination velocity at boron-doped emitters: Comparison between various passivation techniques. In *Proc. 21st EUPVSEC, Dresden, Germany*, page 647, 2006.

[127] D.B.M. Klaassen. A unified mobility model for device simulation - I. model equations and concentration dependence. *Solid-State Electron.*, 35:953, 961, 1992.

[128] C. Peters, P. Engelhart, M. Hlusiak, R. Wade, R. Jesswein, D. Rychtarik, J.W. Müller, C. Ulzhöfer, S. Spätlich, T. Neubert, N.-P. Harder, C. Schmiga, D. Kray, A. Grohe, and S.W. Glunz. ALBA - development of high-efficiency multi-crystalline Si EWT solar cells for industrial fabrication at Q-cells. In *Proc. 23th EUPVSEC, Valencia, Spain*, pages 1010–1013, 2008.

[129] D. Macdonald and A. Cuevas. Reduced fill factors in multicrystalline silicon solar cells due to injection level dependent bulk recombination lifetimes. *Prog. Photovolt: Res. Appl.*, 8:363–375, 2000.

[130] A. A. Istratov, T. Buonassisi, R. J. McDonald, A. R. Smith, R. Schindler, J. A. Rand, J. P. Kalejs, and E. R. Weber. Metal content of multicrystalline silicon for solar cells and its impact on minority carrier diffusion length. *J. Appl. Phys.*, 94:6552, 2003.

[131] A. Bentzen. *Phosphorus diffusion and gettering in silicon solar cells.* PhD thesis, Faculty of mathematics and natural sciences department of physics, Oslo, 2006.

[132] S.A. McHugo, H. Hieslmair, and E.R. Weber. Gettering of metallic impurities in photovoltaic silicon. *Appl. Phys. A*, 64:127–137, 1997.

[133] C. Ulzhöfer, B. Wolpensinger, and J. Schmidt. Understanding the lifetime evolution in n-type multicrystalline silicon during phosphorus gettering and hydrogenation. In *Proc. 23rd EUPVSEC, Valencia, Spain*, 2008.

[134] R. Krain, S. Herlufsen, and J. Schmidt. Internal gettering of iron in multicrystalline silicon at low temperature. *Appl. Phys. Lett.*, 93:152108, 2008.

[135] A.A. Istratov, H. Hieslmair, and E.R. Weber. Iron and its complexes in silicon. *Appl. Phys. A*, 69:13–44, 1999.

[136] J. Schmidt. Effect of dissociation of iron-boron pairs in crystalline silicon on solar cell properties. *Prog. Photovolt. Res. Appl.*, 13:325–331, 2005.

[137] N.-P. Harder, V. Mertens, and R. Brendel. Numerical simulations of buried emitter back-junction solar cells. *Prog. Photovolt: Res. Appl.*, 17:253–263, 2009.

[138] A.G. Aberle, S.W. Glunz, A.W. Stephens, and M.A. Green. High-efficiency silicon solar cells: Si-SiO_2 interface parameters and their impact on device performace. *Prog. Photovolt. Res. Appl.*, 2:265–273, 1994.

[139] A.G. Aberle, P.P. Altermatt, G. Heiser, S.J. Robinson, A. Wang, J. Zhao, U. Krumbein, and M.A. Green. Limiting loss mechanisms in 23 % efficient silicon solar cells. *J. Appl. Phys.*, 77:3491–3504, 1995.

[140] P.E. Gruenbaum, J.Y. Gan, and R.M. Swanson. Use of ultrathin oxides and thin polycrystalline silicon films for stable high-efficiency silicon solar cells. *Appl. Phys. Lett.*, 58:945–947, 1991.

[141] P. Engelhart, N.-P. Harder, R. Grischke, A. Merkle, R. Meyer, and R. Brendel. Laser structuring for back junction silicon solar cells. *Prog. Photovolt. Res. Appl.*, 15:237–243, 2007.

[142] M.J. Kerr, J. Schmidt, and A. Cuevas. Surface recombination velocity of phosphorus-diffused silicon solar cell emitters passivated with plasma enhanced chemical vapor deposited silicon nitride and thermal silicon oxide. *J. Appl. Phys.*, 89:3821–3826, 2001.

[143] German, 2004, Patent-Kontakttrennung, DE 10 2004 050 269.2.

[144] E. Schneiderlöchner, R. Preu, R. Lüdemann, S.W. Glunz, and G. Willeke. Laser-Fired Contacts (LFC). In *Proc. 17th EUPVSEC, Munich, Germany*, pages 1303–1306, 2001.

[145] H. Yano, F. Katafuchi, T. Kimoto, and H. Matsunami. Effects of wet oxidation/anneal on interface properties of thermally oxidized SiO_2/SiC MOS system and MOSFET. *IEEE T. Electron. Dev.*, 46:504–510, 1999.

[146] W.R. Thurber, R.L. Mattis, Y.M. Liu, and J.J. Filiben. Resistivity-dopant density relationship for phosphorus-doped silicon. *J. Electrochem. Soc.*, 127:1807–1812, 1980.

[147] W.R. Thurber, R.L. Mattis, Y.M. Liu, and J.J. Filiben. Resistivity-dopant density relationship for boron-doped silicon. *J. Electrochem. Soc.*, 127:2291–2294, 1980.

[148] R.A. Sinton and A. Cuevas. Contactless determination of current-voltage characteristics and minority-carrier lifetimes in semiconductors from quasi-steady-state photoconductance data. *Appl. Phys. Lett.*, 69:2510–2512, 1996.

[149] A.B. Sproul. Dimensionless solution of the equation describing the effect of surface recombination on carrier decay in semiconductors. *J. Appl. Phys.*, 76:2851–2854, 1994.

[150] N. Mingirulli, D. Biro, R. Preu, S.W. Glunz, and S. Riepe. Method for determination of recombination activity of cylindric conduction channels for back-contacted solar cells. *Appl. Phys. Lett.*, 91(18):183512, 2007.

[151] J. Dicker, J. Sölter, J.O. Schumacher, S.W. Glunz, and W. Warta. Analysis of rear contacted solar cell structures for cost-effective processes and materials. In *Proc. 28th IEEE PVSC, Anchorage, AL*, page 387, 2000.

[152] R. Brendel, S. Dreissigacker, N.-P. Harder, and P.P. Altermatt. Theory of analyzing free energy losses in solar cells. *Appl. Phys. Lett.*, 93:173503, 2008.

[153] P. Hacke, J.M. Gee, M.W. Sumner, J. Salami, and C. Honsberg. Application of a boron source diffusion barrier for the fabrication of back contact silicon solar cells. In *Proc. 31st IEEE PVSC, Coronado Springs Resort, USA*, 2005.

[154] B. Hoex, J. Schmidt, P. Pohl, M. C. M. van de Sanden, and W. M. M. Kessels. Silicon surface passivation by atomic layer deposited Al_2O_3. *J. Appl. Phys.*, 104:044903– 044903–12, 2008.

[155] D.L. King and B.R. Hansen. A sensivity analysis of the spectral mismatch correction procedure using wavelength dependent error sources. In *Proc. 22nd IEEE PVSC, Las Vegas*, 1991.

[156] B. Hoex, J. Schmidt, R. Bock, P.P. Altermatt, M.C.M. van de Sanden, and W.M.M. Kessels. Excellent passivation of highly doped *p*-type Si surfaces by the negative-charge-dielectric Al_2O_3. *Appl. Phys. Lett.*, 91:112107, 2007.

[157] J.G. Fossum, R.D. Nasby, and S.C. Pao. Physics underlying the performance of back-surface-field solar cells. *IEEE T. Electron. Dev.*, 27, 4:785–791, 1980.

[158] J. Benick, B. Hoex, M.C.M. van de Sanden, W.M.M. Kessels, O. Schultz, and S.W. Glunz. High efficiency *n*-type Si solar cells on Al_2O_3-passivated boron emitters. *Appl. Phys. Lett.*, 92:253504, 2008.

[159] P.J. Cousins and J.E. Cotter. The influence of diffusion-induced dislocations on high efficiency silicon solar cells. *IEEE T. Electron. Dev.*, 53:457–464, 2006.

[160] M.A. Kessler, T. Ohrdes, B. Wolpensinger, and N.-P. Harder. Charge carrier lifetime degradation in Cz silicon through the formation of a boron-rich layer during BBr_3 diffusion processes. *Semicond. Sci. Technol.*, 25:055001, 2010.

[161] D. Kray. *Hocheffiziente Solarzellenstrukturen für kristallines Silicium-Material industrieller Qualität.* PhD thesis, University of Konstanz, 2005.

[162] S. Hermann, T. Neubert, B. Wolpensinger, N.-P. Harder, and R. Brendel. Process characterisation of picosecond laser ablation of SiO_2 and SiN_x layers on planar and textured surfaces. In *Proc. 28nd EUPVSEC, Valencia, Spain*, 2008.

[163] S. Hermann, N.-P. Harder, R. Brendel, D Herzog, and H. Haferkamp. Picosecond laser ablation of SiO_2 layers on silicon substrates. *Appl. Phys. A*, 99:151–158, 2010.

A Measured *IV*-curves of full area BSF cell fabricated on 0.8 *Ω* cm boron-doped Cz-Si

The impact of back-surface fields on the *I*-*V*-characteristics of EWT solar cells has been discussed by means of a process that features a laser contact opening sequence. Pico-second laser power is used to ablate the dielectric passivation layers prior to the metalization depicted in Fig. 7.1.

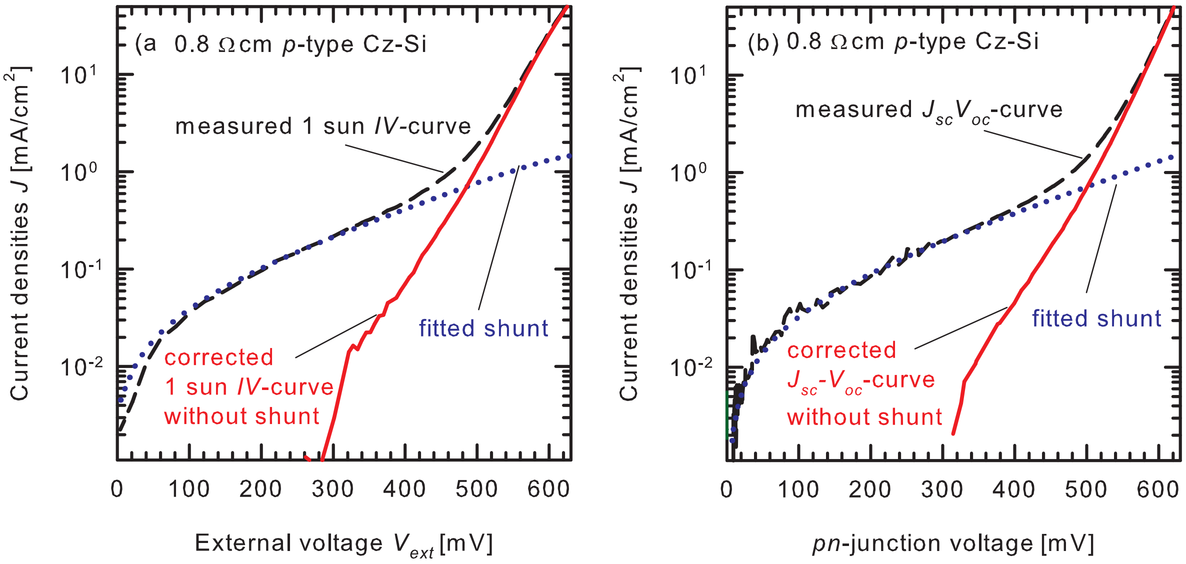

Figure A.1: (a) 1 sun *I*-*V*-characteristics and (b) J_{sc}-V_{oc}-characteristics of the BSF solar cell fabricated on 0.8 Ωcm boron-doped Cz-Si. The fitted shunt current is subtracted from the measured curves. The corrected, "shunt-free" curves respect the recombination behaviour of the device components without the impact of the technological shunt issue.

The device fabricated on 0.8 Ωcm boron-doped Cz-Si suffers from a shunt which is due to a bad alignment during the laser-ablation. As a result, small areas of the phosphorus-doped emitter have been treated by the laser power at the rear side. Since the emitter is as-diffused without any further temperature treatments (e.g. drive-in processes, oxidation steps, etc.) the *pn*-junction depth is narrow and accounts for about 500 nm in the present scenario. Pico-second laser power is known to be critical in terms of *pn*-junction damages induced by laser treatment. Hermann et al. investigated this effect that is identified as a recombination mechanism with a high local ideality factor [162]. This certain type of recombination reminds on a shunt that causes a shoulder in the *I*-*V*-curves at small external voltages. Note that shunts also exhibit diode like recombination characteristics as described in Ref. [32].

In order to eliminate this technological issue of the present solar cell, the recombination current (shunt) is subtracted from the measured illuminated 1 sun *I*-*V*- and the J_{sc}-V_{oc}-characteristics. Finally, solar cell characteristics are calculated that are exclusively affected by the single device component recombination and series resistivity behavior.

Figures A.1(a) and (b) depict the J_{sc}-shifted illuminated 1 sun *I*-*V*- and the J_{sc}-V_{oc}-characteristics, respectively. The shunt current is modeled by a diode that features a constant saturation current density of $J_{0,shunt}$=0.042 mA/cm² and a constant ideality factor $n_{shunt} = 6.8$. Under illumination, the series resistance (R_s≈0.4 Ωcm²) must be considered in order to respect the voltage drop between the external circuit and the solar cell (Fig. 7.4).

The measured and the calculated *I*-*V*-parameters of the referring solar cell are listed in Tab. A.1. The J_{sc} and the V_{oc} is not affected by the misalignment of the pico-second laser ablation. It is the

FF of the illuminated I-V-curve and the pseudo-FF of the J_{sc}-V_{oc}-characteristic that suffer from the pico-second laser contact openings.

Table A.1: I-V-parameters of the EWT solar cell featuring a BSF, fabricated on 0.8 Ωcm Cz-Si wafers. First row: measured values. Second row: without the impact of shunt currents (shunt-free).

scenario	J_{sc} (mA/cm^2)	V_{oc} (mV)	FF (%)	pseudo-FF (%)	η (%)
measured	32.0	612	78.6	79.9	15.4
shunt-free	32.0	612	80.6	81.8	15.8

B List of publications

B.1 Refereed journal papers

1. C. Ulzhöfer, S. Hermann, N.-P. Harder, P. P. Altermatt, R. Brendel. The origin of reduced fill factors of emitter-wrap-through-solar cells. *phys. stat. sol. (RRL)*, 2:251, 2008.
2. C. Ulzhöfer, P. P. Altermatt, N.-P. Harder, R. Brendel, Loss analysis of emitter-wrap-through silicon solar cells by means of experiment and three-dimensional device modeling. *J. Appl. Phys.*, 107:104509-104512, 2010.
3. F. Kiefer, C. Ulzhöfer, T. Brendemühl, N.-P. Harder, R. Brendel, V. Mertens, S. Bordihn, C. Peters, J.W. Müller, High efficiency n-type emitter-wrap-through silicon solar cells. *IEEE Journal of Photovoltaics*, Vol. 1, pp. 49-53, 2011.
4. S. Hermann, A. Merkle, C. Ulzhöfer, S. Dorn, I. Feilhaber, M. Berger, T. Friedrich, T. Brendemühl, N.-P. Harder, L. Ehlers, K. Weise, R. Meyer and R. Brendel. Progress in emitter wrap-through solar cell fabrication on boron doped Czochralski-grown silicon. *Sol. Energy Mater. Sol.*, DOI: 10.1016/j.solmat.2010.12.004.
5. C. Schinke, D. Hinken, K. Bothe, C. Ulzhöfer, A. Milsted, J. Schmidt, R. Brendel. *Proc. 1st International Conference on Crystalline Silicon Photovoltaics (SiliconPV 2011), Energy Procedia 8, Elsevier;* Eds. S. W. Glunz, A. G. Aberle, R. Brendel, A. Cuevas, G. Hahn, J. Poortmans, R. Sinton, A. Weber, 147-152, Freiburg, Deutschland, 2011.

B.2 Refereed conference papers

1. C. Ulzhöfer, B. Wolpensinger, J. Schmidt. Understanding the lifetime evolution in n-type multicrystalline silicon during phosphorus gettering and hydrogenation. *Proceedings of the 23st European Photovoltaic Solar Energy Conference*, Valencia, Spain, 2008.
2. C. Ulzhöfer, S. Hermann, N.-P. Harder, P. P. Altermatt, R. Brendel. VIRE-EFFECT: Via-Resistance induced recombination enhancement - The origin of reduced fill factors of emitter wrap through solar cells. *Proceedings of the 24st European Photovoltaic Solar Energy Conference*, Hamburg, Germany, 2009.
3. C. Peters, P. Engelhart, M. Hlusiak, R. Wade, R. Jesswein, R. D. Rychtarik, J.W. Müller, C. Ulzhöfer, S. Spätlich, T. Neubert, T. N.P. Harder, C. Schmiga, D. Kray, A. Grohe, S. W. Glunz. ALBA-Development of high-efficiency multi-crystalline Si EWT solar cells for industrial fabrication at Q-Cells. *Proceedings of the 23st European Photovoltaic Solar Energy Conference*, Valencia, Spain, 2008.
4. R. Brendel, S. Dreissigacker, C. Ulzhöfer, N.-P. Harder, and P. P. Altermatt. Free energy loss analysis for solar cells. *Proceedings of the 18th NREL Workshop on Crystalline Silicon Solar Cells and Modules*, Vail, Colorado, 2008.
5. R. Ferré, N.-P. Harder, W. Mühleisen, S. Herlufsen, C. Ulzhöfer, M. C. Schubert, R. Wade, V. Mertens, R. Brendel. Bulk lifetime enhancement by firing steps in back contacted multicrystalline silicon solar cells. *Proceedings of the 25st European Photovoltaic Solar Energy Conference*, Valencia, Spain, 2010.
6. I. Köhler, W. Stockum, A. Meijer, C. Ulzhöfer, A. Merkle, H. Plagwitz, B. Terheiden. A new advanced material for removing edge shunts in silicon solar cells. *Proceedings of the 22st European Photovoltaic Solar Energy Conference*, Milan, Italy, 2007.

B.3 Given talks

1. C. Ulzhöfer, Defektgeneration durch Hochtemperaturprozesse, 25th February 2008, Silicon Forest, Falkau, Germany.
2. C. Ulzhöfer, B. Wolpensinger and J. Schmidt, Understanding the lifetime evolution in n-type mc-Si during P-gettering and hydrogenation, 1st September 2008, 22nd EUPVSEC, Valencia, Spain.
3. C. Ulzhöfer, Reduzierte Füllfaktoren in EWT-Solarzellen, 3rd March 2009, Silicon Forest, Falkau, Germany.
4. C. Ulzhöfer, S. Hermann, N.-P. Harder, R. Brendel and P.P. Altermatt, The Origin of Reduced Fill Factors of Emitter-Wrap-Through-Solar Cells, 21st September 2009, 24th EUPVSEC, Hamburg, Germany.
5. C. Ulzhöfer, P.P. Altermatt, Fill factor losses of emitter wrap through solar cells, 16th November 2009, Meeting of the Scientific Advisory Board of the ISFH, Hameln, Germany.

C Danksagung

Eine Dissertation kann nur in guter Zusammenarbeit mit Vorgesetzten, Kollegen, Familie und Freunden entstehen. Ich danke hiermit:

- Meinen Eltern, die mich all die Jahre unterstützt und nur selten gesehen haben. Durch ihre Hilfe wurde vieles einfacher.
- Prof. Dr. Nils-Peter Harder für die Unterstützung während meiner Dissertation in all den Jahren, die erfolgreiche Zusammenarbeit im ALBA-Projekt und die vielen inspirierenden Gespräche in seiner Arbeitsgruppe. Wir haben viele Lösungen gefunden.
- Prof. Dr. Rolf Brendel für die Anstellung am ISFH und die wissenschaftliche Unterstützung. Sein Vertrauen in mich war der Anfang dieser Arbeit.
- Dr. Pietro P. Altermatt für die Unterstützung, die Korrekturen und die gute Stimmung bei unseren Gesprächen, sowie Bettina Wolpensinger für die Arbeiten am REM und die vielen schönen Momenten mit der ganzen Familie.
- Prof. Dr. Jan Schmidt und Dr. Karsten Bothe für die vielen Diskussionen und Antworten gerade in den Anfangsmonaten meiner Doktorarbeit.
- Allen Gruppen- und Abteilungsleitern am ISFH. Diese sind: Dr. Carsten Hampe, Dr. Thorsten Dullweber, Dr. Rüdiger Meyer, Dr. Heiko Plagwitz, Dr. Bernhard Fischer, Dr. Enrique Garralaga, Dr. Rolf Reinecke-Koch, Dr. Marc Köntges und Dr. Barbara Terheiden.
- Dipl. oec. Wolfgang Gaßdorf für die klare Organisation am ISFH. Jeder Doktorand profitiert davon.
- Ralf Gogolin, Michael Kessler und Dr. Sonja Hermann für die enge Zusammenarbeit, die gegenseitige Unterstützung und die Freude, die wir bei den Grillabenden teilen durften.
- Anja Lohse und Tobias Neubert, die neben der Projektarbeit viel Unterstützung für meine Doktorarbeit geleistet haben. Ohne ihre Hilfe wären viele Ergebnisse nicht zustande gekommen.
- Meinen Kollegen Till Brendemühl und Fabian Kiefer, denen ich viel Erfolg für die weitere Projektarbeit bzw. Promotion wünsche.
- Agnes Merkle, die mich in den ersten Wochen sehr detailliert in die Solarzellen-Fabrikationsprozesse eingelernt hat.
- Allen Mitarbeiter von Q-Cells für die gute Zusammenarbeit im ALBA-Projekt: Dr. Jörg Müller, Dr. Christina Peters, Dr. Verena Mertens, Stephan Bordihn, Robert Wade, Markus Hlusiak und Reik Jesswein.
- Allen Diplomanden, Doktoranden, wissenschaftlichen Angestellten und ehemaligen Kollegen am ISFH, die mit mir zusammengearbeitet haben und von denen ich viel lernen konnte: Stefan Eidelloth, Dr. Robert Bock (vielen Dank), Dr. Ulrich Eitner, Marco Ernst, Sebastian Gatz, Felix Haase, Udo Römer, Sandra Herlufsen, David Hinken, Hendrik Holst, Jörg Käsewieter, Rafael Krain, Dr. Yevgeniya Larionova, Dr. Bianca Lim, Christoph Mader, Jens Müller, Dr. Klaus Ramspeck, Dr. Peter Pohl, Dr. Andreas Wolf, Silke Steingrube, Tobias Ohrdes, Florian Werner, Dimitri Zielke, Boris Veith, Carsten Schinke, Frank Heinemeyer, Rene Hesse, Jan Hensen, Joachim Otto, Dr. Robby Peibst und Helge Hannebauer.
- Den beiden Elektroingenieuren Martin Wolf und Arne Schmidt für ihre hervorragende Arbeit im Charakterisierungslabor.

- Den technischen Angestellten für die Unterstützung im Labor: Marita Steinhof, Sarah Spätlich, Miriam Berger, Susanne Mau, Daniel Münster, Cornelia Marquardt, Nadja Braun, Peter Giesel, Iris Kunze und Lotte Ehlers.
- Den hausinternen Technikern und Ingenieuren Andreas Treder, Johannes Schlieker, Hans Thulke, Michael Weiß, Willy Giesecke und Stefan Beisse für die tolle Arbeit und Instandhaltung im ISFH-Technologiepark.
- Den Verwaltungsangestellten für ihre Unterstützung in sämtlichen verwaltungstechnischen Dingen: Heidi Paldino, Mareike Meißner, Iris Berger, Marion Brucksch, Sonja Helbig, Kathrin Depping, Simone Lücking und Carina Faulhaber.
- Thomas Kriegisch für die Unterstützung bei der Erstellung der 3d-EWT-Zeichnung (Fig. 4.8).
- Den folgenden Mitarbeitern des ISE für die gute Zusammenarbeit im ALBA-Projekt: Dr. Daniel Kray, Dr. Andreas Grohe, Christian Schmiga, Dr. Stefan Glunz, Marc Rüdiger, Dr. Martin Hermle und Dr. Martin Schubert.

D Wissenschaftlicher Werdegang

Persönliche Daten

Name	Christian Ulzhöfer
Anschrift	Kurt-Lutz-Str. 9, 97877 Wertheim, Deutschland
Geburtsdatum	22. August 1979
Mobiltelefon	+49 (0) 15 11 74 39 39 8
E-Mail	christian.ulzhoefer@web.de

Schule

1986-1990	Grundschule, Wertheim/Wartberg
1990-1999	Dietrich Bonhoeffer Gymnasium, Wertheim

Zivildienst

1999-2000	Rotes Kreuz, Wertheim/Tauberbischofsheim

Studium

2000-2002	Grundstudium Physik Julius-Maximilians-Universität, Würzburg
2002-2003	1. Jahr Hauptstudium Physik Julius-Maximilians-Universität, Würzburg
2003-2004	2. Jahr Hauptstudium Physik Université Joseph Fourier, Grenoble (Frankreich) Drei monatige Forschungsarbeit am CNRS, Grenoble (Centre National de la Recherche Scientifique) mit dem Thema "Tiefe Störstellen in der Bandlücke von GaN-Verbindungen"
2004-2005	Abschließendes Semester einschließlich Diplomprüfung
2005-2006	Diplomarbeit, Lehrstuhl für Technische Physik, Würzburg Thema: "Abstimmbare InP-Halbleiterlaser mit integriertem Wellenlängenmonitor auf Basis Photonischer Kristalle"

Promotion

2006-2011	Anstellung am ISFH (Institut für Solarenergieforschung Hameln) Thema: Verlustanalyse von EWT-Solarzellen